Technische Universität München
TUM School of Engineering and Design

Design and Comparison of Configurations and Subsystems for Fixed-Wing Electric Vertical Takeoff and Landing Unmanned Aerial Vehicles

Philipp Peter Stahl

Vollständiger Abdruck der von der TUM School of Engineering and Design der Technischen Universität München zur Erlangung eines

Doktors der Ingenieurwissenschaften (Dr.-Ing.)

genehmigten Dissertation.

Vorsitz: Prof. Dr. phil. Ilkay Yavrucuk

Prüfer*innen der Dissertation:

1. Prof. Dr.-Ing. Mirko Hornung
2. Prof. Dr.-Ing. Florian Holzapfel

Die Dissertation wurde am 06.02.2023 bei der Technischen Universität München eingereicht und durch die TUM School of Engineering and Design am 11.10.2023 angenommen.

Abstract

Small multirotor drones are established tools for surveying, inspection and photography today. For more demanding applications of the future like surveillance or cargo transport, fixed-wing aircraft with vertical takeoff and landing capability are preferred because they offer higher ranges, flight times and speeds in addition to being independent of takeoff and landing infrastructure. The possible arrangements and types of lifting surfaces and powertrains lead to a variety of proposed aircraft layouts.

Therefore, eleven fully electric, 5 kg heavy representatives of this hybrid aircraft type are compared quantitatively and objectively in terms of their flight performance and cost-effectiveness using a multidisciplinary conceptual aircraft design and optimization tool chain. Among them are two new configurations which are proposed by the author.

Furthermore, aircraft type specific issues are investigated and corresponding solutions for flight performance enhancement are proposed. This includes the experimental assessment and reduction of drag generated by lift rotors that are stopped in wing-borne flight, the measurement of the thrust loss caused by objects inside the rotor slipstream and hybrid architectures of high-power and high-energy battery types.

The evaluation shows that the proposed rotor alignment system which turns the stopped rotor to a low drag position can increase the range by up to 17%. The benefit of hybrid battery architectures is very case sensitive, but ranges between 3 and 15% range improvement for the example scenario. When comparing the cost of an exemplary survey mission, there are only marginal differences among the configurations due to the dominance of pilot labor cost. The achievable ranges however differ by up to 21%. The newly proposed configurations are, also in terms of maximum flight time, among the best performers.

Finally, the implementation and flight testing of the two proposed configurations not only prove their feasibility but also serve to validate the aircraft design tool chain.

Kurzfassung

Kleine Multikopter-Drohnen sind inzwischen etablierte Werkzeuge für die Vermessung, Inspektion und Fotografie. Für zukünftige anspruchsvollere Anwendungen wie Luftaufklärung oder Frachttransport werden senkrechtstartfähige Tragflächenflugzeuge bevorzugt, da sie höhere Reichweiten, Flugzeiten und Geschwindigkeiten bieten und dennoch unabhängig von Start- und Landeinfrastruktur sind. Die möglichen Anordnungen und Typen von Tragflächen und Antrieben führen zu einer Vielzahl von in Fachkreisen vorgeschlagenen Flugzeugkonzepten.

Daher werden elf vollelektrische, 5 kg schwere Vertreter dieses hybriden Flugzeugtyps unter Zuhilfenahme einer multidisziplinären Flugzeugvorentwurfs- und Optimierungswerkzeugkette quantitativ und objektiv auf ihre Flugleistung und Wirtschaftlichkeit hin verglichen. Darunter befinden sich auch zwei neue Konfigurationen, die vom Autor vorgeschlagen werden.

Darüber hinaus werden flugzeugtypenspezifischen Fragestellungen untersucht und entsprechende Lösungen zur Verbesserung der Flugleistung vorgeschlagen. Dazu gehören die experimentelle Erfassung und Verringerung des Luftwiderstands von im Tragflächenflug gestoppten Hubrotoren, die Messung des durch Propellerstrahlverblockung verursachten Schubverlusts und hybride Architekturen aus Hochleistungs- und Hochenergiebatterien.

Die Auswertung zeigt, dass das vorgeschlagene Rotorausrichtungssystem, das den angehaltenen Rotor in eine Position mit geringem Luftwiderstand dreht, die Reichweite um bis zu 17% erhöhen kann. Der Mehrwert von hybriden Batteriearchitekturen hängt stark vom Einzelfall ab, liegt aber für das Beispielszenario zwischen 3 und 15% Reichweitensteigerung. Beim Vergleich der Kosten für eine beispielhafte Vermessungsmission gibt es nur marginale Unterschiede zwischen den Konfigurationen, was auf die Dominanz der Lohnkosten des Piloten zurückzuführen ist. Die erzielbaren Reichweiten unterscheiden sich jedoch um bis zu 21%. Die vom Autor vorgeschlagenen Konfigurationen gehören auch in Bezug auf die maximale Flugzeit zu den Besten.

Der Bau und die Flugerprobung der beiden vorgeschlagenen Konfigurationen beweisen zuletzt nicht nur ihre Machbarkeit, sondern dienen auch der Validierung der Flugzeugentwurfskette.

Acknowledgements

This thesis was made possible by a large number of people, whom I would like to sincerely thank at this point.

First and foremost to mention is Prof. Dr.-Ing. Mirko Hornung who gave me the opportunity to work at his chair and to do my doctorate under his supervision. He provided the advice, infrastructure, financial means and freedom that enabled the investigations, prototype setups and knowledge exchange required for the completion of this thesis.

Dr.-Ing. Christian Rößler always had an open ear for my questions and gave helpful assessments and advice.

My colleagues at the Institute of Aircraft Design provided constant support, were open to discuss and share their opinions, and created an excellent working atmosphere. This was especially true for my fellow members of the VTOL group Sebastian Oberschwendtner, Thomas Seren and Christian Rieger as well as my longtime office mates Moritz Thiele and Franz Sendner.

Many students contributed to this work in the form of student theses, assistant jobs and internships. In particular, there is Maximilian Gschwandtner who reliably supported the VTOL group for many years.

Such work is not possible without the support from the private environment. Therefore, I owe special thanks to my parents and family who enabled the way to this thesis. My girlfriend Kira always had my back and gave up many hours of our time together to be put into this thesis.

Table of Contents

List of Figures

List of Tables

List of Symbols and Abbreviations

Abbreviations

AoA	angle of attack
BAT	battery
BPMS	battery power management system
c	cruise/wing-borne flight state
cc	cruise climb flight state
cd	cruise descent flight state
CFD	computational fluid dynamics
CG	center of gravity
CONOPS	concept of operations
cpt	cruise powertrain
CTOL	conventional takeoff and landing
dmpt	dual-mode powertrain
DoD	degree of discharge
EASA	European Union Aviation Safety Agency
ESC	electronic speed controller
eVTOL	electric vertical takeoff and landing
F3F, F3B, F3J	remote control glider competition classes
fc	fast cruise flight state
FCC	flight control computer
FOV	field of view
GCS	ground control station
GNSS	global navigation satellite system
h	hover flight state
hc	hover climb flight state
hd	hover descent flight state
hpt	hover powertrain
htp	horizontal tailplane
ICAO	International Civil Aviation Organization
IMU	inertial measurement unit
INS	inertial navigation system
LOS	line of sight
MRO	maintenance, repair, overhaul
MTBF	mean time between failures
MUX	multiplexer
NASA	National Aeronautics and Space Administration
OEI	one engine inoperative
qX..., qP...	aircraft configurations, see section 3.1
RC	remote control
rpm	revolutions per minute, rotational frequency
SGL	single

SoC	state of charge
SORA	specific operational risk assessment
SPRT	separate battery architecture
STOL	short takeoff and landing
SUV	sport utility vehicle
tpt	tilt powertrain
TUM	Technical University of Munich
tV..., tA...	aircraft configurations, see section 3.1
UAS	unmanned aerial system
UAV	unmanned aerial vehicle
VTOL	vertical takeoff and landing
vtp	vertical tailplane

Greek Symbols

α	angle of attack	[rad]
β	sideslip angle	[rad]
δ	tilt/deflection angle; ratio	[rad;−]
η	efficiency	[−]
Γ	circulation	$[\frac{m^2}{s}]$
γ	rotor azimuth angle	[rad]
μ	electric motor friction constant	[−]
ω	angular velocity	$[\frac{rad}{s}]$
ρ	air density	$[\frac{kg}{m^3}]$
σ	sensitivity	[−]
φ	bank angle	[rad]

Latin Symbols

AR	aspect ratio	[−]
DL	disk loading	$[\frac{N}{m^2}]$
FM	figure of merit	[−]
LD	glide ratio	[−]
rps	revolutions per second, rotational frequency	[Hz]
A	disk area; cross section area	[m^2;m^2]
a_{ax}	axial induction factor	[−]
a_{tan}	tangential induction factor	[−]
B	width	[m]
b	span	[m]
b_{bat}	battery technology curve parameter	[−]
c	chord length; cost	[m;€]
c_τ	wall shear coefficient	[−]
c_f	skin friction coefficient	[−]
c_P	power coefficient	[−]
c_Q	torque coefficient	[−]
c_T	thrust coefficient	[−]

c_V	tail volume coefficient	[−]
c_D	global/3D drag coefficient (e.g. of aircraft)	[−]
c_d	local/2D drag coefficient (e.g. of airfoil)	[−]
c_L	global/3D lift coefficient (e.g. of aircraft)	[−]
c_l	local/2D lift coefficient (e.g. of airfoil)	[−]
D	aerodynamic drag	[N]
d	diameter; distance	[m;m]
E	energy; Young's modulus	[J or W h;Pa]
e	Oswald efficiency; relative error; gravimetric energy density	$[-;-;\frac{\mathrm{J}}{\mathrm{kg}}$ or $\frac{\mathrm{W\,h}}{\mathrm{kg}}]$
f	factor	[−]
G	shear modulus	[Pa]
g	gravitational constant	$[9.81\frac{\mathrm{kg\,m}}{\mathrm{s}^2}]$
H	outer height	[m]
h	altitude; inner height	[m;m]
I	electric current	[A]
J	advance ratio; inertia	$[-;\mathrm{kg\,m}^2]$
k_m	motor size constant	$[\mathrm{Nm}/\sqrt{\mathrm{W}}]$
k_Q	electric motor torque constant	$[\frac{\mathrm{N\,m}}{\mathrm{A}}]$
L	lift	[N]
m	mass	[kg]
n	integer amount	[−]
n_z	load factor	[−]
P	power	[W]
p	static pressure; propeller pitch; probability; gravimetric power density; roll rate	$[\mathrm{Pa;m};-;\frac{\mathrm{W}}{\mathrm{kg}};\frac{\mathrm{rad}}{\mathrm{s}}]$
Q	torque	[N m]
q	dynamic pressure	[Pa]
R	tip radius; ohmic resistance; specific gas constant	$[\mathrm{m};\Omega;287\frac{\mathrm{J}}{\mathrm{kg\,K}}]$
r	(normalized) radius	[m;−]
Re	Reynolds number	[−]
S	reference surface	$[\mathrm{m}^2]$
s	range	[m]
T	thrust; temperature	[N;K]
t	time; thickness	[s or h;m]
U	voltage	[V]
v	velocity	$[\frac{\mathrm{m}}{\mathrm{s}}]$
W	work	[J]
w	wind velocity	$[\frac{\mathrm{m}}{\mathrm{s}}]$
Y	side force	[N]
y	spanwise coordinate	[m]
z	(vertical) distance	[m]

Subscripts

0	zero lift, thrust, airspeed or load condition

ax	axial
bat	battery
$blown$	operating in propeller wake
c	cruise/wing-borne flight state
$cabl$	cabling
cc	cruise climb flight state
cd	cruise descent flight state
$ctrl$	control
eff	effective
el	electric
ESC	electronic speed controller
fc	fast cruise flight state
fus	fuselage
h	hover flight state; horizontal
hc	hover climb flight state
hd	hover descent flight state
$heat$	heating
in	inflow; incoming
ind	induced
$inst$	installation
$interf$	interference
lam	laminar
max	maximum
min	minimum
$misc$	miscellaneous
mot	motor
nac	nacelle
$prop$	propeller
$pwtr$	powertrain
$pyld$	payload
$rand$	random
ref	reference
rot	rotor
$struct$	structural
sw	swirl
sys	systems
$turb$	turbulent
v	vertical
$xsect$	cross-section

1 Introduction

1.1 Problem Statement and Motivation

The added value of unmanned aerial vehicles has become obvious for a wide range of industries, so their use is expanding rapidly. The global drone market is estimated to double its 20 billion US$ market volume of 2020 until 2025. Major user industries are energy, agriculture and construction. Transportation is expected to join these by 2025 (Drone Industry Insights 2020). Today's typical applications include surveying, inspection, film and photography as well as mapping and observation (Kortas et al. 2019). With the legal basis for these applications now being largely laid out (JARUS 2019, EASA 2020), a former key barrier is removed.

Unmanned aerial vehicles (UAV) with takeoff masses between 5 and 25 kg are sufficient for most applications to carry the required sensor payload and communication equipment for a reasonable amount of time. Multicopters are currently the most commonly used type of UAV. On the one hand, they impress with their vertical takeoff and landing capability (VTOL), which makes them largely independent of takeoff and landing infrastructure. Furthermore, they score with the simplicity and robustness of their electric drive systems (eVTOL).

To open up further applications with higher range and flight time requirements or to increase productivity at reduced cost, hybrids of multicopters and fixed-wing aircraft, so-called *fixed-wing VTOL* aircraft, are increasingly being investigated and used. With their wing-borne flight mode, they enable lower power consumption at higher flight speeds, while maintaining the necessary infrastructure independence through VTOL capabilities.

Similar aircraft concepts are also considered for the potential future market of man-carrying urban and regional air transport, colloquially known as *air taxis*.

A wide range of layouts is conceivable to exhibit fixed-wing aircraft with VTOL capabilities. These can differ, for example, in the arrangement of wings and stabilizers or in the type and location of the powertrains.

Correspondingly, the variety of proposed fixed-wing VTOL aircraft designs is large. A general consensus of a "best" aircraft configuration comparable to today's airliner architecture has not yet been manifested.

The question for the "best" aircraft configuration usually also stands at the beginning of most aircraft design projects. In this conceptual design phase, aircraft modeling methods are used that cope with the low initial amount of information, but allow to quickly iterate on a lot of parameters to narrow down the interesting design space.

In the course of the evolution of an aircraft class, besides the vehicle configuration itself, also subsystems emerge that solve aircraft class specific problems. Historical examples are the pressurized cabins of passenger transport aircraft to enable flight at favorable altitudes, cable cutters on helicopters or so-called "bug wipers" that remove the contamination on the wing leading edge of sailplanes to preserve laminar airflow and thus low drag.

1.2 Objectives and Limitations

This thesis aims to contribute to the development of the vehicle class of small unmanned fixed-wing VTOL aircraft. This shall be realized by reaching the following objectives:

- The setup of a validated conceptual design methodology which allows an objective and quantitative comparison of different fixed-wing VTOL configurations.
- The comparison metric when looking for a "best" aircraft is a central question in itself. Besides flight performances like endurance or range, the economic performance shall be compared. For the latter, a suitable metric must be identified.
- The comparison shall include new aircraft configurations and performance-promoting subsystems which the author proposes based on his investigations.
- The feasibility and effectiveness of the proposed aircraft and subsystems shall be demonstrated in flight.

From these objectives, the following central research question and further sub-questions derive:

How is the flight performance and economy of small fixed-wing electric VTOL UAV affected by overall aircraft layout and specific subsystems?

- What are key drivers for the flight performance and economy?
- Which aircraft configurations can address and mitigate these sensitivities?
- Which aircraft subsystems address and contribute to mitigate these sensitivities?
- How is a fair comparison and performance assessment of different aircraft configurations and subsystems performed?
- What is the quantitative performance benefit caused by the choice of aircraft configuration or usage of the above-mentioned subsystems?

To narrow down the field of research, the following limitations are made:

- The proposed methods and system solutions are valid for maximum aircraft takeoff masses between approximately 2 and 50 kg.
- All powertrains are electric and solely powered by batteries. Only fixed-pitch propellers and rotors are used.
- The considered aircraft are monoplane configurations with a conventional arrangement of lifting surfaces (main wing in front of empennage). Flying wings, tailsitters or tiltwing configurations are not examined.
- The economic evaluation is restricted to survey missions.

1.3 Structure of the Work

Chapter 2 states the operational concept and key design considerations for small fixed-wing VTOL UAV in typical applications.

Chapter 3 reviews existing types of fixed-wing VTOL UAV and groups them. Two new aircraft configurations are proposed. Furthermore, two subsystems are presented that aim to mitigate aircraft type specific performance barriers:

- the reduction of aerodynamic drag caused by rotors that are stopped during wing-borne flight
- the idea of using hybrids of high-power and high-energy battery types is adapted to the powertrain architectures of fixed-wing VTOL aircraft to increase the resulting energy density of the battery system

Chapter 4 presents the multidisciplinary conceptual design tool chain which allows the flexible implementation of different aircraft configurations for their performance and economy comparison. It employs comprehensible methods and reduces necessary input information. Experiments have been conducted to derive models for

- the thrust loss that is caused by objects in the slipstream of a rotor
- the aerodynamic drag of hover rotors that are stopped for wing-borne flight

Chapter 5 compares the eleven implemented aircraft configurations when optimized for range, endurance and minimal cost per surveyed area based on breakdowns of mass, drag, power, energy and cost. Also the effect of the proposed subsystems is presented.

Chapter 6 presents the prototypes and test flight approach used for inflight validation. Besides a description of the prototypes' flight characteristics, the flight performance is plotted against the predictions of the design tool chain.

Chapter 7 concludes the thesis and provides ideas for further research.

Literature and market reviews are performed at the beginning of each chapter.

2 Operations and Design Considerations

The basis for aircraft and system design is the knowledge about operations and their environment. Furthermore, this chapter is intended to create a basic understanding for the requirements, trade-offs and sensitivities of fixed-wing VTOL aircraft design in order to better justify and assess the developments in the following chapters.

The presented considerations are limited to the special items relevant for the configuration layout and subsystem design of unmanned fixed-wing VTOL aircraft. What is valid for conventional fixed-wing aircraft design otherwise also applies here.

2.1 Mission and Design Implications

The range of applications listed in chapter 1 can be condensed to *survey* and *transport* tasks. Survey hereby refers to any kind of mission that uses a sensor payload to gather information of the ground.

Both applications can widely be described by a generalized mission whose altitude and airspeed profiles are depicted in fig. 2.1. Key parameters for each phase of this generalized mission and the implications on aircraft design are explained in the following. Refer to table 4.1 for a list of exemplary quantitative requirements that serve as inputs for the design toolchain of chapter 4.

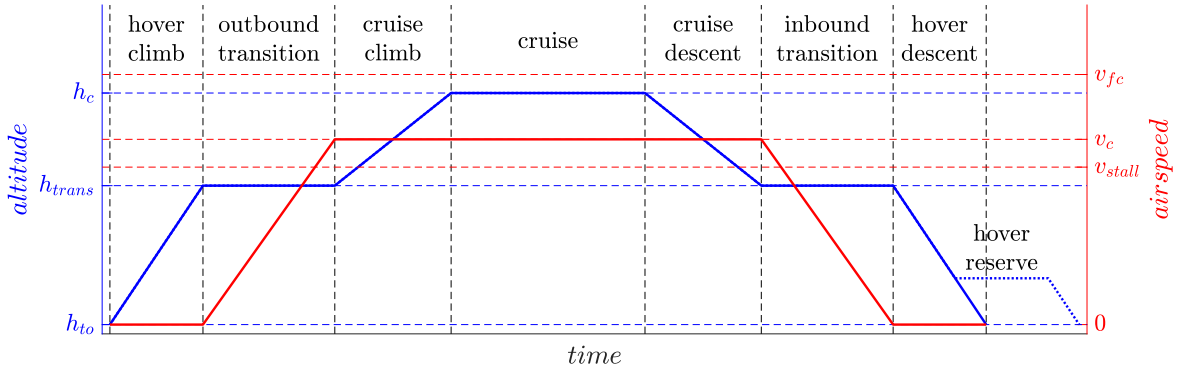

Figure 2.1: Mission profile

2.1.1 Vertical Takeoff and Landing, Hover Climb and Descent

To fulfill the purpose of VTOL, the aircraft must be able to get airborne and land by itself within a lateral space of approximately two to four times the aircraft dimension.

First of all, a powertrain is required that can generate a vertical thrust of at least the weight of the aircraft. If required, that must also be the case under certain powertrain failure conditions.

Furthermore, the dimensions of the landing pad size and vertical flight corridor are determined by the geometric size of the aircraft, the precision of the navigation solution, the flight control algorithms, the maneuverability of the aircraft, the gust conditions and the required safety margins. The aircraft designer hereby can mainly influence the geometric size of the aircraft and its maneuverability.

Further limitations to the geometric aircraft size can be introduced by legal considerations like the widely adopted JARUS (2019). Here, among others, the width and mass of the aircraft determines the prerequisites to obtain operational authorization. Important for aircraft design is that this width includes rotors that exceed the wingspan.
The requirements for maneuverability in hover flight can be imposed in the abstracted form of translational and rotational accelerations or velocities. Examples are roll rate, pitch rate acceleration or vertical acceleration. Likewise, the aircraft can be required to compensate the forces and moments of certain gust forms like a crosswind gust.
To generate the required control moments, the powertrains are distributed on the aircraft with lever arms to the center of gravity (CG). It is economic to use multiple instances of the same powertrain. Given an equal thrust share among these instances, that will lead to symmetric powertrain locations with regard to the aircraft's CG.
The aircraft structures need to be sized for the loads, but also for the added mass and inertia which the powertrains introduce. The structural stiffness must be adequate to avoid critical vibration and resonance. That includes flutter in wing-borne flight.

After takeoff at altitude h_{to}, the aircraft climbs to the transition location at altitude h_{trans}. Its minimum altitude is defined by the height of surrounding obstacles. The minimum deployment altitude of a parachute system can be determining as well. It must be noted that parachute systems that can be deployed at high wing-borne airspeeds exhibit drastically increased deployment heights compared to multicopter parachute systems.
High climb and descent rates generally shorten the duration of the highly energy-consuming hover flight phase. Powertrain mass and power consumption typically limit the maximum design climb rate. The maximum descent rate can be restricted by excessive vibration that occurs if the aircraft enters its own rotor wakes.
Vertical speeds can also be chosen to minimize the noise exposure time. Hover flight is especially critical as it represents the flight state with the highest thrust but lowest distance to people on the ground. For operations in urban areas, noise may be a major design requirement for the powertrain and its placement on the airframe to not compromise public acceptance.
For test and apprentice flights, for unplanned scenarios like a blocked landing pad as well as for cargo winching, the hover duration can exceed what is needed for nominal operation. Very often, thermal limits of the powertrain respectively its cooling represent the main restriction for maximum hover time. For normal missions, the total duration of all hover flight segments together is however less than one minute.

2.1.2 Outbound and Inbound Transition

During the outbound transition, the aircraft's source of lift force switches from the rotors to the wing. Therefore, the aircraft has to gain velocity. With more and more lift produced by the wing, the thrust on the vertical lift powertrains can gradually be reduced. Once stall airspeed v_{stall} is

exceeded by a sufficient margin, the powered lift component can be switched off. The inbound transition performs these steps in reversed order to switch from wing-borne to hovering flight.
During transition, the required control moments can be complex. That results from the constantly changing mutual influence of wings, empennage and rotor downwash. The aircraft designer needs to conservatively plan for control margins and try to minimize the flow interactions.
The non-axial airflow into the rotors leads to asymmetrical thrust and periodic blade load fluctuations. This can lead to vibration or critical structural loads for the rotor blades and their mounts. The operational authorization can require the transition to be performed within a specified area on the ground. Powertrain thrust, aircraft mass, wing size, etc. must be selected accordingly to meet this virtual runway requirement.

2.1.3 Cruise Climb and Descent

Changes between transition and cruise altitude h_c are performed in fully wing-borne mode as higher climb rates with less power consumption can be achieved. Traffic avoidance maneuvers can define the minimums for climb and descent rate.

2.1.4 Cruise

The wing-borne cruise allows to fly at higher airspeed and significantly lower power consumption than in hovering flight. As a result, considerably higher distances can be covered. The powertrain must only provide the thrust to overcome the aerodynamic drag of the aircraft. That is around one magnitude lower than the aircraft weight respectively the vertical powertrain thrust. This difference in thrust and inflow airspeed represents contrary design conditions for the powertrain. The lower propulsive power of wing-borne flight typically leads to a lower noise signature as well.

The cruise trajectory for a survey mission is the result of the strategy for the task (e.g. search and mark task vs. imaging task), the shape of the survey area, sensor choice, aircraft design and wind conditions. The airspeed and altitude is usually defined by the characteristics of the optical payload and the required image resolution. The survey pattern poses requirements to the turn radius and roll rates. Precise trajectory following and attitude stabilization improve the orthogonality of the images and minimize the necessary overlap between the stripes. The field of view (FOV) of the electro-optical sensor payload must not be compromised by nacelles, rotors or the landing gear.

For transport missions, the airspeed and route during the cruise segment are optimized according to payload mass, time, meteo conditions and legal aspects. The size of approvable flight corridors and traffic avoidance maneuvers define the maximum radii for turns and holding patterns as well as minimum turn rates. The upper limit for the cruise altitude is often set for traffic segregation reasons. Some legal drone classes indirectly limit the maximum airspeed in cruise by imposing kinetic energy limits.

For long range missions, it can be beneficial if the cruise flight can be continued despite an actuator or powertrain failure. When using the hover powertrain in this failure scenario, many emergency

landing spots along the route must be identified upfront due to the short range in hover flight mode. Nevertheless, the hover powertrain can effectively be used to recover from unusual cruise flight attitudes or stall. Its start-up time must be reasonably short therefore.

2.1.5 Turnaround

Turnarounds are required between flights. Especially in high volume operations, the aircraft design must allow for a fast and comfortable, yet safe conduction of the required actions like payload or battery exchange.

Transport payloads are located near the aircraft's CG to mitigate balance shifts with frequently changing or deployed cargo. Nevertheless, the hover powertrains and wing-borne longitudinal stability need to tolerate a certain uneven load distribution. Rotors, nacelles or other aircraft parts inside the access area of battery and payload will hamper fast turnarounds and increase the risk of structural damage. Some cargo drones are designed to interact with dedicated parcel stations that automatically perform the turnaround actions (DHL 2016, UPS 2019, Amazon 2016, Matternet 2020).

Survey payloads are less frequently changed than cargo. The focus here is on the battery exchange and data transfer.

2.2 Performance Drivers and Design Trade-Offs

A performance measure for an aircraft is its range. A simple range equation for electric fixed-wing VTOL aircraft is developed in the following to highlight the main performance drivers and sensitivities.

The mission is condensed to static hover flight and horizontal wing-borne cruise. The electric power drains from the battery in cruise P_c and hover P_h are

$$P_c = \frac{mgv_c}{LD\eta_{pwtr}} \text{ with } \eta_{pwtr} = \eta_{prop}\eta_{mot}\eta_{ESC}\eta_{cabl}\eta_{bat} \tag{2.1}$$

$$P_h = \frac{mg}{FM}\sqrt{\frac{DL}{2\rho}} \text{ with } FM = FM_{rotor}\eta_{mot}\eta_{ESC}\eta_{cabl}\eta_{bat} \tag{2.2}$$

Note that the common rotor figure of merit FM also includes powertrain efficiencies here. The cruise power loading $\frac{P_c}{mg}$ mainly depends on airspeed v_c, glide ratio LD and overall powertrain efficiency η_{pwtr}. Disk loading DL, overall figure of merit FM and air density ρ determine the hover power loading $\frac{P_h}{mg}$. Hover flight usually exhibits the higher power consumption.

Vertical takeoff and landing are assumed to last for t_h. The energy E_c that is left in the battery after hover can be used to cover distance s in cruise flight.

$$E_c = E_{bat} - E_h = e_{bat}m_{bat} - t_hP_h \tag{2.3}$$

$$s = v_ct_c = v_c\frac{E_c}{P_c} \tag{2.4}$$

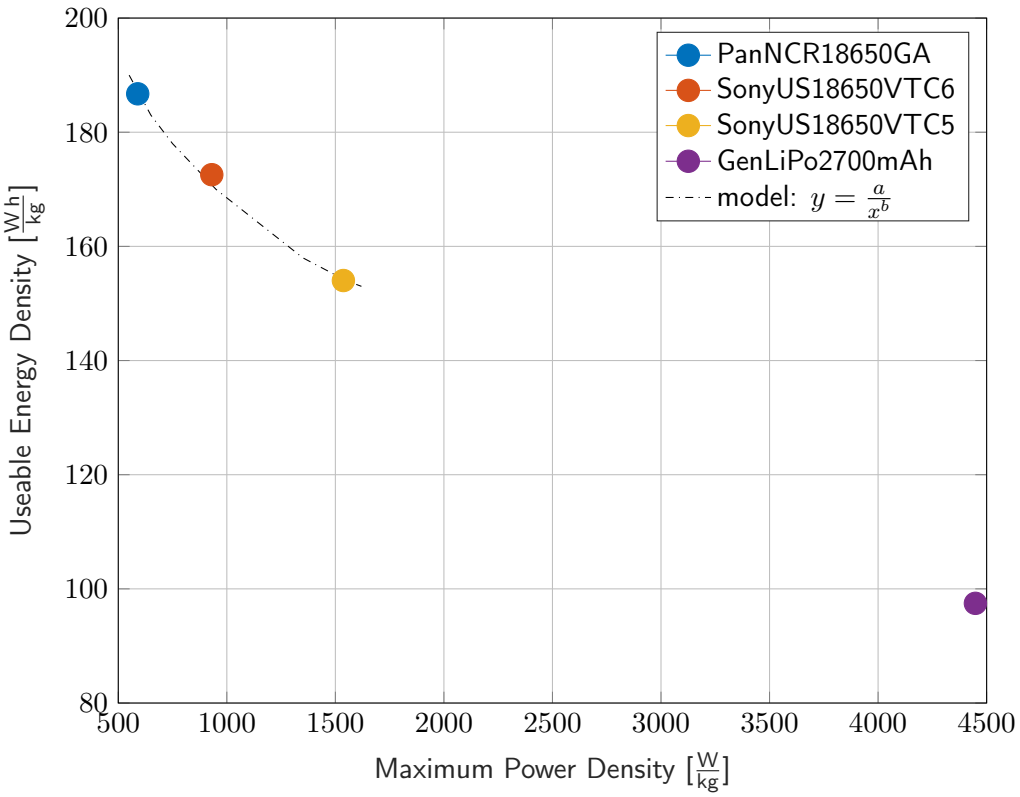

Figure 2.2: Maximum power density vs. nominal energy density for state-of-the-art batteries (on pack level and using only 80% of nominal capacity)

The fact that the maximum power capability for a given battery mass $p_{bat} = \frac{P}{m_{bat}}$ limits the battery's gravimetric energy density e_{bat} is shown in fig. 2.2. This dependency is relevant as significantly different battery power requirements can result from the typical ranges of fixed-wing VTOL aircraft design parameters. Furthermore, in the required range of specific battery power, battery cell types are available in close spacing. This is a prerequisite to make practical use of this dependency.

A simple exponential model is fitted to approximate the state-of-the-art battery technology in the relevant range of specific power:

$$e_{bat} = e_{ref} \left(\frac{p_{ref}}{p_{bat}} \right)^{b_{bat}} \quad \text{with } e_{ref} \approx 670 \ \frac{\text{W h}}{\text{kg}}, \ p_{ref} = 1 \ \frac{\text{W}}{\text{kg}}, \ b_{bat} \approx 0.2 \tag{2.5}$$

Rearranging the above equations yields

$$s = LD \ \eta_{pwtr} \left(C_1 \ e_{ref} \ DL^{-\frac{b_{bat}}{2}} \ FM^{b_{bat}} \left(\frac{m_{bat}}{m} \right)^{1+b_{bat}} - \ C_2 \ DL^{\frac{1}{2}} \ t_h \ FM^{-1} \right) \tag{2.6}$$

$$\text{with } C_1 = \frac{{p_{ref}}^{b_{bat}} (2\rho)^{\frac{b_{bat}}{2}}}{g^{1+b_{bat}}} \tag{2.7}$$

$$\text{and } C_2 = \frac{1}{\sqrt{2\rho}} \tag{2.8}$$

The second term in the brackets represents the range penalty due to the energy consumption of

the hover phase. For long missions with minimum hover time, this second term may be neglected. The battery mass m_{bat} as a fraction of the total aircraft mass m can be expressed as a residual:

$$\frac{m_{bat}}{m} = 1 - \frac{m_{pyld}}{m} - \frac{m_{sys}}{m} - \frac{m_{struct}}{m} - \frac{m_{pwtr}}{m} \tag{2.9}$$

The factorization of eq. 2.6 allows to identify potential design drivers. For functions of the type $f(x) = kx^n$, the exponent n is a measure of the sensitivity σ for relative variations around a design point x_0.

$$\sigma = \frac{\frac{\Delta f}{f_0}}{\frac{\Delta x}{x_0}} = f'(x_0)\frac{x_0}{f_0} = knx_0{}^{n-1}\frac{x_0}{kx_0{}^n} = n \tag{2.10}$$

Table 2.1 indicates the range increase for a 1% increase of each design variable.

Table 2.1: Range increase for a 1% increase of major fixed-wing eVTOL design variables. Only effects of eq. 2.6 and exemplary battery parameters are assumed, hover energy is neglected

design variable	range increase [%]
battery mass fraction $\frac{m_{bat}}{m}$	$\approx$ 1.2
aerodynamic efficiency LD	1
powertrain efficiency in cruise η_{pwtr}	1
reference battery energy density e_{ref}	1
powertrain figure of merit in hover FM	$\approx$ 0.2
disk loading DL	$\approx$ − 0.1

The figures emphasize the mass sensitivity of battery electric VTOL aircraft. Each mass reduction in payload, systems, structure or powertrains (compare eq. 2.9) will increase the battery mass fraction and enable an overproportional range increase. Aerodynamic efficiency LD, cruise powertrain efficiency η_{pwtr} and the reference energy of the battery technology model e_{ref} show proportional range influence. It is noteworthy that the design variables of the hover powertrain DL and FM influence range in wing-borne flight. Only if the battery energy density would be independent of the power density (battery energy lapse parameter $b_{bat} = 0$), their influence would vanish.

Equation 2.6 and table 2.1 neglect obvious dependencies among the design variables, of which the following exemplary design trade-offs arise:

- How does the mass fraction of the powertrain $\frac{m_{pwtr}}{m}$ change with its design parameters DL, η_{pwtr} and FM?
- How much does the cruise powertrain efficiency η_{pwtr} degrade if the powertrain is more optimized towards the contradictory operating condition of hover flight, e.g. by improving DL or FM?

- How much does the aerodynamic efficiency LD suffer if rotors are enlarged respectively DL is reduced? The rotor alignment subsystems developed in section 3.2 try to mitigate this conflict.
- How can the sensitivity on the battery energy density lapse b_{bat} be reduced? Section 3.3 therefore looks into different battery architectures.

How well these design trade-offs are solved by the different aircraft configurations of chapter 3 is answered in chapter 5.

3 eVTOL UAV Configuration and Subsystem Development

With the operation and performance background of chapter 2 in place, aircraft configurations and subsystems are presented that aim to solve the specific trade-offs of electric fixed-wing VTOL aircraft. The insights gained in this chapter feed into the aircraft modeling of chapter 4. This finally allows to quantify the performance impact of the configuration and subsystems in chapter 5.

3.1 Review, Grouping and Proposal of eVTOL Aircraft Configurations

This chapter provides an overview over existing fixed-wing VTOL aircraft configurations from which representatives are chosen for further investigation. Newly developed configurations are part of the selection as well.

Among the winged VTOL aircraft, the common classification into *vectored thrust* and *lift+cruise* is made. Aircraft of the *vectored thrust* class use the same powertrains in both hover and cruise flight. These powertrains are referred to as *dual-mode powertrains* (short: dmpt) or *tilt powertrains* (short: tpt) in this thesis.
Lift+cruise configurations use dedicated and independent powertrains for hover and cruise propulsion. These single purpose powertrains are referred to as *hover powertrains* (short: hpt) and *cruise powertrains* (short: cpt).
The investigated aircraft are grouped into families. For the families, there are common or specific options to create family derivatives (see fig. 3.1). A common option is for example the usage of full span trailing edge flaps (option *_flap*). The specific features are introduced in the following chapters together with principal information on the aircraft families.

The scheme to name families and options is taken from the program code of chapter 4. In the first two letters, the number of powertrains and their locations is contained. For example, in *tA*, the t stands for tri (three) powertrains that are located at the corners of a triangle that rests on its base edge. The capital letter A resembles the shape of this triangle. For qP must be known that the four (quad) powertrains are located at the endpoints of a + sign. The letter P represents the plus sign. The definition of powertrain locations is associated with a top view of the aircraft with its nose pointing up. The meaning of the other letters is explained in the family chapters.

Example UAV designs for each family are given within their chapters. Like for the early V/STOL concepts (AHS 2017), the Vertical Flight Society maintains a collection of manned eVTOL developments on their website (VFS 2017, Hirschberg 2018). These can mostly be assigned to the presented families as well.

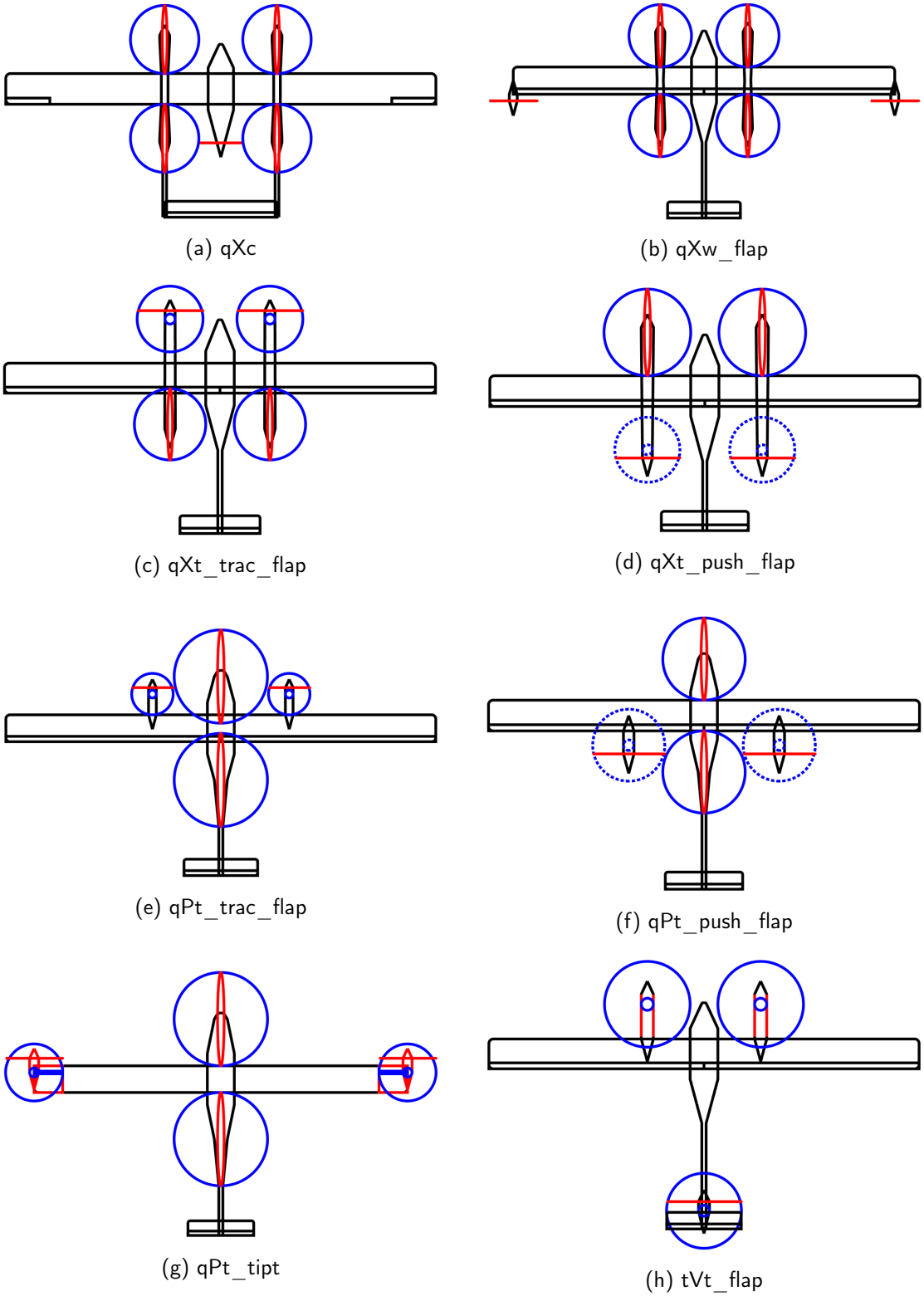

(a) qXc

(b) qXw_flap

(c) qXt_trac_flap

(d) qXt_push_flap

(e) qPt_trac_flap

(f) qPt_push_flap

(g) qPt_tipt

(h) tVt_flap

Figure 3.1: Investigated aircraft families with their derivatives. Red lines show position of rotors/propellers in cruise flight, blue lines show position in hover flight. Dotted lines indicate operation as pusher in hover.

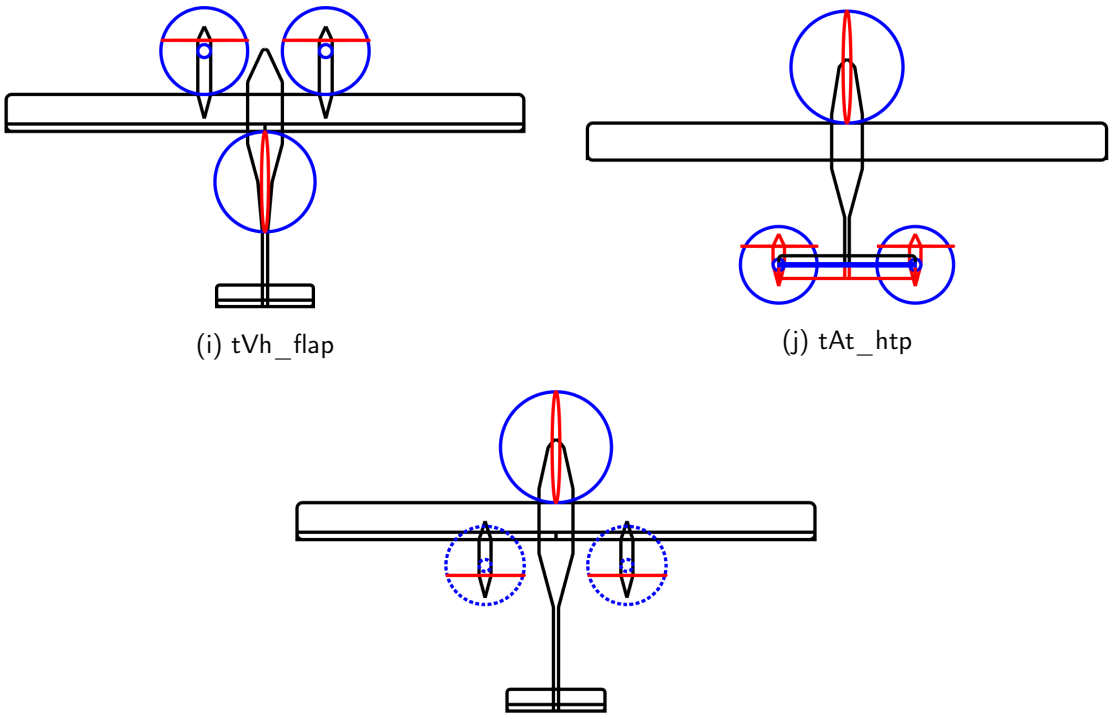

(i) tVh_flap

(j) tAt_htp

(k) tAt_wing_flap

Figure 3.1: Investigated aircraft families with their derivatives. Red lines show position of rotors/propellers in cruise flight, blue lines show position in hover flight. Dotted lines indicate operation as pusher in hover.

3.1.1 qXc

The *qXc* configuration (see fig. 3.1a, *c* for center cruise powertrain) ranges among the most popular fixed-wing VTOL configurations. Example products are ALTIUAS (2020) or JOUAV (2020). It uses a conventional twin-boom pusher aircraft and adds a quadrocopter in X-orientation to the

Figure 3.2: Representative of the qXc configuration: JOUAV CW-25E

wings of the aircraft. Hover and cruise powertrains are used in their dedicated flight phases exclusively. Placing the cruise powertrain at the nose or tail of a single fuselage is a popular alternative (ArcturusUAV 2017, JOUAV 2020, PhoenixWings 2020) but comes with challenges for the FOV or CG. The independence of hover and cruise propulsion makes redundancy considerations straightforward.

3.1.2 qXw

The *qXw* configuration (see fig. 3.1b, *w* for wingtip cruise powertrain) uses a conventional single-fuselage aircraft and adds a quadrocopter in X-orientation. A pair of cruise powertrains is attached to the wingtips. This allows to enhance yaw authority by the usage of differential thrust. At the same time, the powered wing-borne flight can usually not be continued in an one engine inoperative (OEI) scenario. Propeller efficiency gains respectively induced drag reduction can be achieved as the propeller swirl interacts with the wingtip vortex (Veldhuis 2005, Snyder & Zumwalt 1969, Miranda & Brennan 1986, Snyder 1967, Patterson & Bartlett 1987, Stokkermans et al. 2019, Dimchev 2012). HORYZN (2020) proposed this configuration.

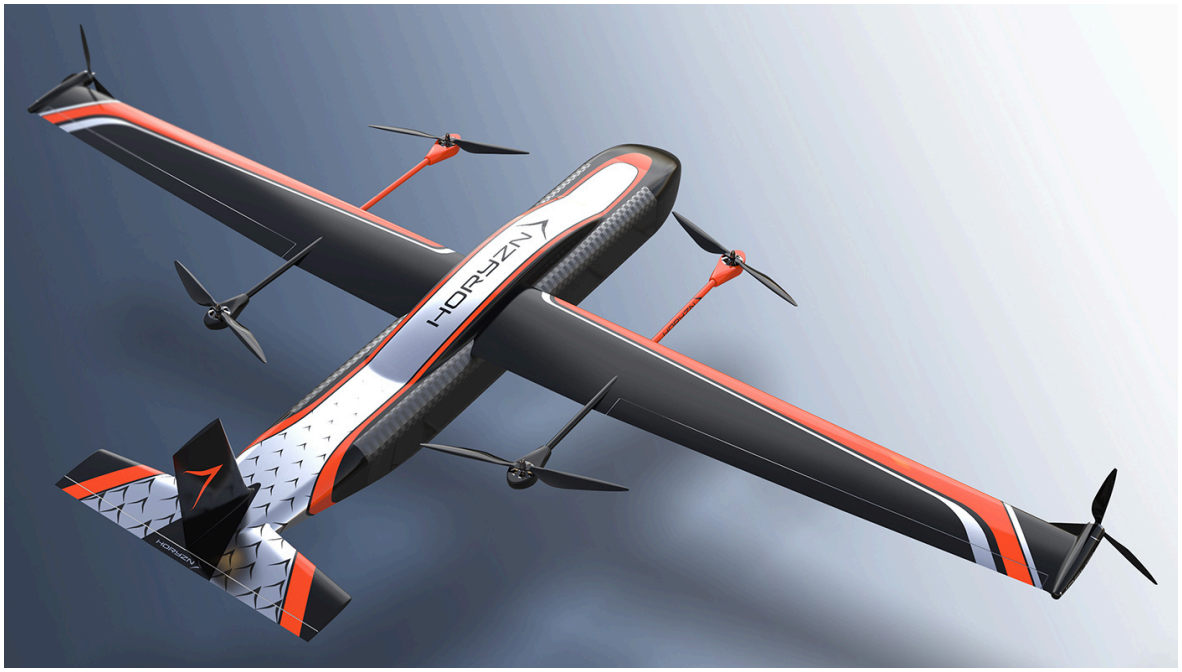

Figure 3.3: Representative of the qXw configuration: Horyzn Silencio Gamma

3.1.3 qXt

The *qXt* configurations (see figs. 3.1c and 3.1d, *t* for tilt powertrain) have two tiltable powertrains in either tractor (_trac) or or pusher (_push) arrangement in front respectively behind the wing. The opposite powertrains are solely used for hover and are stopped during cruise flight. Aircraft control in cruise uses conventional control surfaces. In hover, the conventional quadrocopter control principle is supported by the tilt capability. Vertical Aerospace (2020) uses the *qXt_trac* configuration.

Figure 3.4: Representative of the qXt_trac configuration: Vertical Aerospace VA-X4 (manned)

3.1.4 qPt

The *qPt* configurations (see figs. 3.1e to 3.1g, *t* for tilt powertrain) were developed in the course of this thesis. Prototypes were built and taken to flight at the Institute of Aircraft Design at Technical University Munich (TUM) (see fig. 3.5). Newman et al. (2015) proposed a similar aircraft.

It is based on a conventional wing-tail configuration. Two hover-only powertrains are attached on top of the fuselage before and aft of the wing. They provide the majority of lift thrust at favorable efficiency. By 120° tiltable powertrains are mounted to the wing at an arbitrary spanwise position either in front (_*trac*) or behind (_*push*) the wing. A third version (_tipt) uses tiltable wingtip segments to mount the powertrain. The wing powertrains are vertical in hover flight to support lift and slightly tilt for yaw control. Their hover thrust contribution is widely independent of the powertrains' lever arm proportions. In wing-borne flight, the fuselage powertrains are stopped and the wing powertrains point forward for thrust and yaw control. The low thrust share in hover allows to optimize these powertrains for the cruise condition at minor detrimental impact

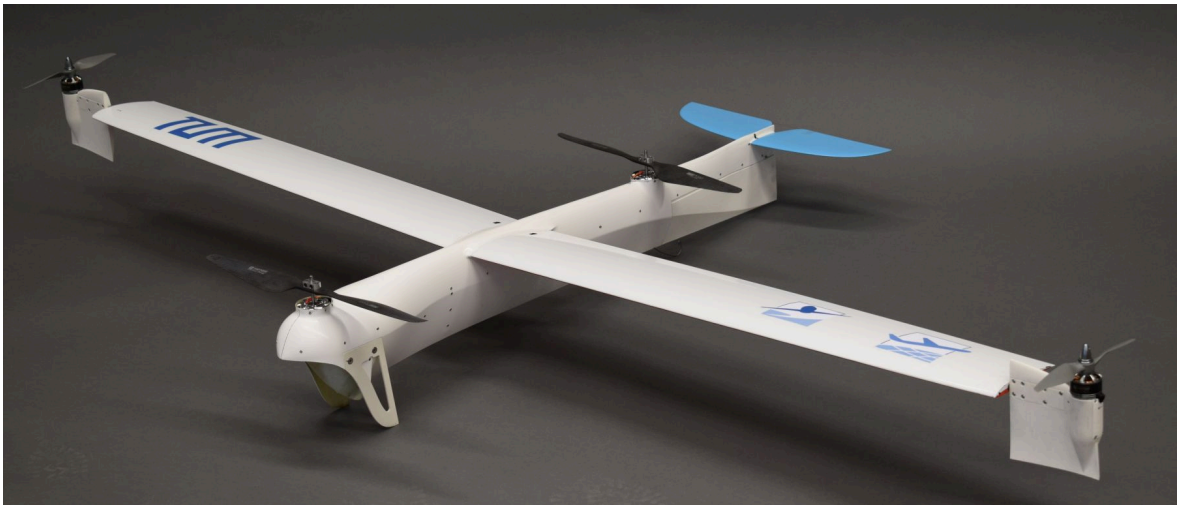

Figure 3.5: qPt_tipt prototype of the Institute of Aircraft Design/TUM

on overall hover efficiency. Roll control is achieved by the antisymmetric deflection of either the conventional ailerons or the wingtip segments. The downwash blocking caused by the wide fuselage is disadvantageous for hover efficiency. The presence of rotors at the main fuselage complicates the integration of systems and payload.

As three different dmpt options are available in this aircraft family, their specific characteristics shall be highlighted in the following. The stated applies likewise for other configurations that use one of the dmpt types.

Tractor Tilt Powertrain *_trac*

Tractor tilt powertrains are the most common type of dmpt. In wing-borne flight, the propeller operates in undisturbed air which avoids noise and efficiency degradation. The propeller slipstream however causes a disturbance of the wing's lift distribution and scrubbing drag over the downstream wing section and nacelle (due to increased dynamic pressure and turbulent airflow). In hover or transition flight, the propeller downwash hits the wing with a negative angle of attack and produces negative lift. The distance between powertrain tilt mechanics and aerodynamic control surface usually prohibits to drive both with a single actuator.

Pusher Tilt Powertrain *_push*

Figure 3.6 shows a tiltable pusher powertrain that was developed to drive control surface and tilt mechanism with a single actuator. Due to their proximity, a simple push rod is sufficient. The linkage implements nonlinear kinematics that limit the downward deflection of the aileron. The depicted design is located at the wingtip, but can likewise be adapted for more inboard positions. While the mass and cost of an additional aileron actuator can be saved, the failure of the tilt actuator will affect multiple systems. The pusher arrangement of the propeller avoids scrubbing drag. If located at the wingtip, the same extent of beneficial interaction of propeller swirl and wingtip vortex as for tractor layouts is evident (Miranda & Brennan 1986). In hover operation,

Figure 3.6: Pusher tilt powertrain of the qPt_push prototype

the blocking of the propeller on the inflow side is less critical in terms of thrust degradation (see section 4.9.1.2). In cruise, propeller efficiency, blade stress and noise are negatively affected by the wake of the wing, especially when a control surface is deflected (Channa 2015, Taylor 1968, Wilson 1942, Harmon 1941). Low-drag laminar flow wings however mitigate the causal wake velocity bucket (Pifer & Bramesfeld 2012). Spacing trailing edge and propeller plane further apart helps to even out the wake velocity distribution (Nakayama 1985) but conflicts with propeller ground clearance and inertial loads.

Tractor Tilt Wingtip _*tipt*

Figure 3.7 depicts an exemplary design for a tractor tilt wingtip. The complete unit is tilted around a hollow shaft by a single actuator that is placed in the nacelle behind the motor. The diameter of the drive shaft must be chosen to provide adequate strength, stiffness and room for cables. Its integration within the wing loft limits the usage of high aspect ratios, low taper ratios and thin airfoils. The tilt wingtip's shaft location and mass distribution is crucial for low actuation forces and sufficiently high flutter onset airspeed. The occurrence of gap flow for larger deflection angles degrades the control surface efficiency. Unlike the _*trac* arrangement, tilting the complete wing section together with the propeller slipstream avoids negative lift in hover operation.
A study on design solutions for the tractor tilt wingtip is performed in Fröhlich (2017).

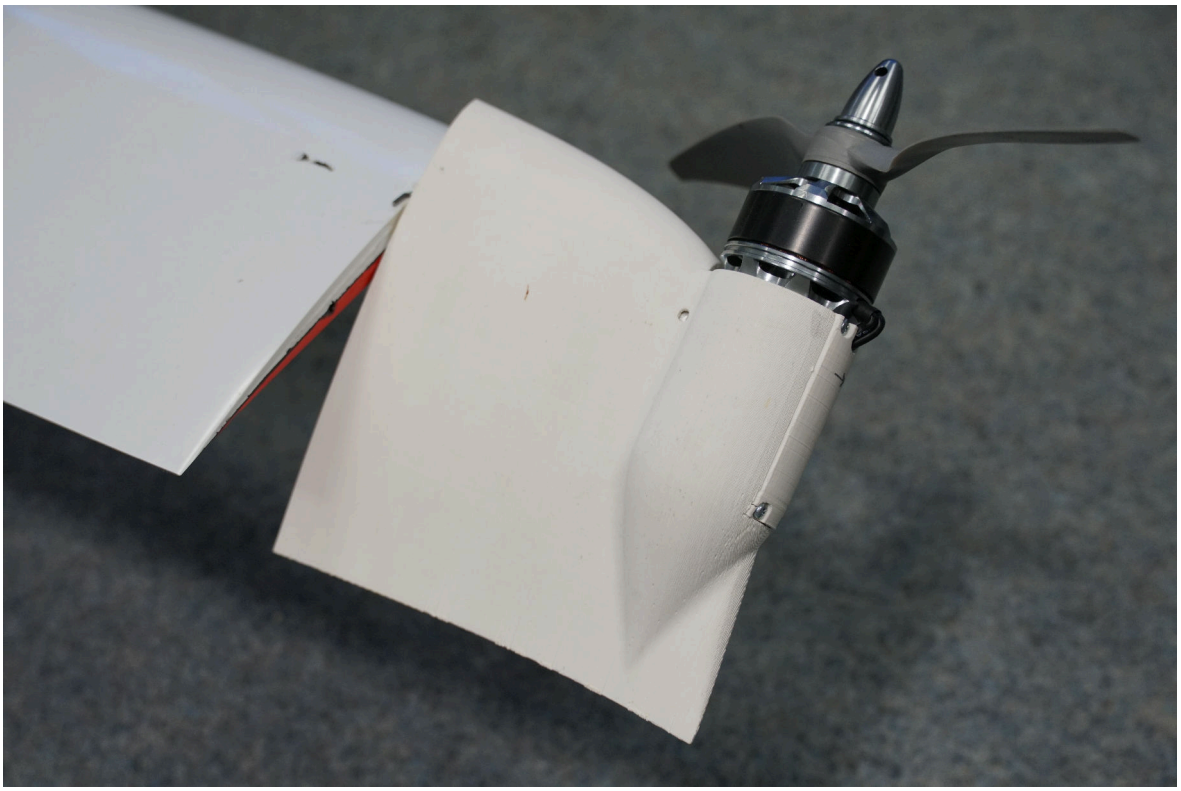

Figure 3.7: Tractor tilt wingtip of the qPt_tipt prototype

3.1.5 tVt

The *tVt* configuration (see fig. 3.1h, *t* for tilt powertrain at the aft location) is e.g. used by Quantum Systems (2020) or Kapetair (2020). It uses two tiltable powertrains in front of the wing and one tiltable powertrain mounted on top and in front of the vertical tailplane. In nominal operation, the front powertrains are only used in hover and transition. Their tilting is essential for yaw control in hover. In cruise flight, the motor axes are tilted horizontally to fold and attach the rotors to the nacelle for drag reduction. Cruise thrust is generated by the rear powertrain. In case of its failure, the hover powertrains can be activated to continue powered flight. Conventional control surfaces are used.

Figure 3.8: Representative of the tVt configuration: Quantum Systems Vector with powertrains in hover position

3.1.6 tVh

FlightWave (2019), despite being a flying wing, or Foxtech (2020) are implementations of the *tVh* configuration (see fig. 3.1i, *h* for hover powertrain at the aft location). The rear powertrain is only active in hover. The two front powertrains are attached in front of the wing and can tilt between vertical and horizontal. Yaw control in hover requires tilting of these powertrains around the vertical position. Conventional aerodynamic control surfaces are used in cruise. The rudder can be augmented by differential thrust of the horizontally tilted powertrains in cruise.

Figure 3.9: Representative of the tVh configuration: Foxtech Nimbus V2

3.1.7 tAt

Another development in the course of this thesis are the *tAt* configurations (see figs. 3.1j and 3.1k, *t* for tilt powertrain at the aft locations). It was found that this configuration is covered by a patent by North et al. (2018).

The goal with *tAt_htp* is to use the minimum number of five control effectors (powertrains or actuators) on a conventional wing-empennage configuration. The control principle in hover is equal to the tVh configuration, but the tilt powertrains are attached to the horizontal tailplane (*_htp*). Due to the lever arm proportions, the rear powertrains provide less lift thrust in hover. This allows to better optimize them for the wing-borne flight condition. In cruise flight, the front rotor is stopped. The rear powertrains tilt horizontally together with the elevons to which they are connected. Differential thrust and a large vertical tail are used to omit the rudder control surface. Due to the elevons, the wing must not necessarily have ailerons. However, a design trade-off between controllability, longitudinal stability and aerodynamic drag arises as the span of

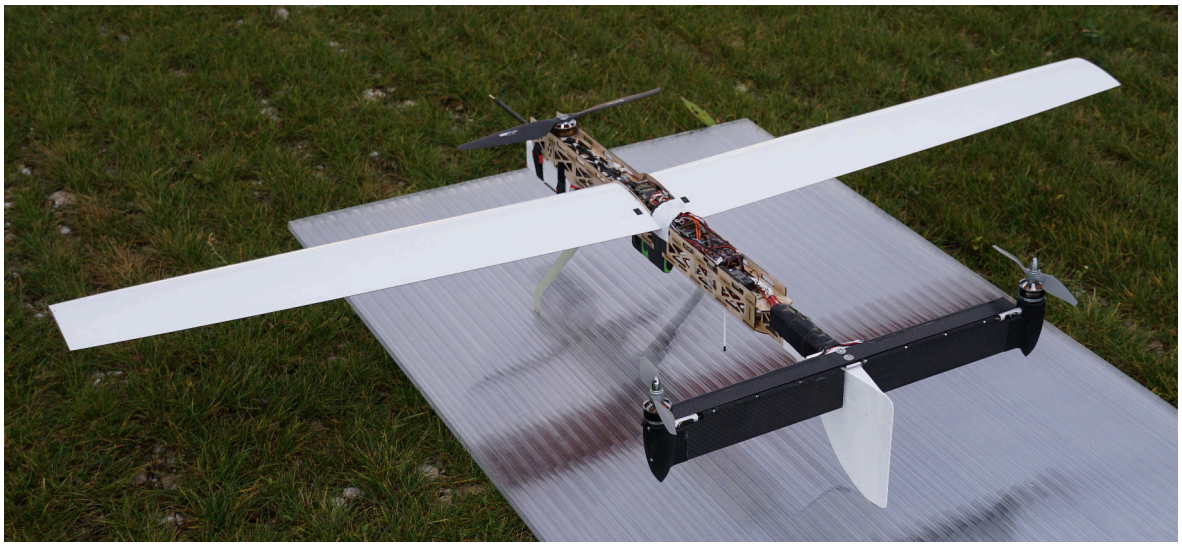

Figure 3.10: tAt_htp prototype

Figure 3.11: Tiltable powertrain on the horizontal tailplane of the tAt_htp prototype

the horizontal tailplane defines the lever arm of the tilt powertrains and elevons. The wing can be unmounted for hover-only missions.
A flying prototype was built and proved the general feasibility of this configuration (see fig. 3.10). The tilt powertrain mechanism (see fig. 3.11) is widely similar to the tractor tilt wingtip design (see fig. 3.7). Related design considerations are documented in Tiesler (2019*a*,*b*).

On the *tAt_wing* derivative, the rear powertrains are located at the trailing edge of the wing (*_wing*). A design like in fig. 3.6 can be used to drive powertrain tilting and aileron deflection with only one actuator.

3.2 Stopped Rotor Drag Reduction

The majority of the aircraft configurations presented in section 3.1 feature hover powertrains that are stopped for wing-borne flight. With a share of around 10% of the total aerodynamic drag (Stahl & Hornung 2020), the stopped rotors can considerably degrade the aerodynamic efficiency of VTOL aircraft. This is confirmed by Bacchini et al. (2021) who performed wind tunnel measurements on an entire aircraft of qXc configuration. He finds an 8% degradation in maximum glide ratio when airflow-parallel rotors are added to a baseline model, and a 30% degradation when rotors are mounted perpendicular to the airflow.
Motivated by that, this chapter presents three systems that aim to reduce the drag of stopped rotors by

- aligning the rotor parallel to the airflow
- retracting the rotor into the fuselage
- folding the rotor parallel to the airflow

Parts of these approaches are already published in Blaim (2017) and Stahl, Seren, Roessler & Hornung (2018).

3.2.1 Identification of Concepts

The process that led to the three investigated systems starts at the following goals and requirements:

- Reduce the aerodynamic drag of the stopped rotor at minimal system mass and power consumption to increase the net performance benefit.
- The simple and robust system shall use off-the-shelf powertrain components.
- The generation of hover thrust must not be impaired:
  - Lift and control performance, especially rpm envelope, angular acceleration, free rotor in- and outflow and cooling must be unaffected.
  - Failures may not lead to an inoperative hover powertrain system as its reliable performance is highly critical for a safe landing.

– The activation timespan between stopped rotor state and operative state must be short enough to use the hover powertrain for recovery from unusual wing-borne attitudes.

In a next step, essential subfunctions of a stopped rotor drag reduction system are identified. Table 3.1 summarizes the considered solutions for each of these subfunctions. These solutions stem from existing motor gliders and fixed-wing VTOL designs (LZ Design 2020, Pätzold 2014, Litherland et al. 2017, Krossblade Aerospace 2020, CompositAirplanes 2020, Akaflieg Berlin 2020, Schempp Hirth 2020). Additionally, own ideas are included. By combining solutions, a system concept is formed. The solutions for each of the three presented stopped rotor drag reduction systems can be found in one column of the table.

Table 3.1: Morphological box with design solutions for stopped rotor drag reduction systems

		rotor alignment	**rotor folding**	**rotor retraction**		
		Solutions				
Functions	drag reduction	rotor aligned with airflow	rotor in-plane folding	rotor rests in recess	rotor tilted + folded	rotor housed inside doors
	movement into storage compartment	no movement		threaded shaft + bidirectional rotation	lift of rotor + spring	rotor on pivoted arm
	rotor azimuthal positioning	precise stop	wind vane	rotor stop pin	motor position control	
	shaft-rotor torque transmission	bolted		friction/clamping	form fit	
	position sensing	hall switch	motor current	limit switch	rotary encoder	none

Prototype implementations of each system are described in more detail in the following three chapters.

3.2.2 Rotor Alignment

Rotor alignment means that the spanwise coordinate of a two blade rotor is positioned parallel to the incoming airflow.

The few available systems on the market which are capable of rotor alignment operate the motor in a position control mode. Standard electronic speed controllers (ESC) are however only capable of rpm control, not rotary position control. They neither have the software nor the required position feedback sensor installed.

The approach here (see fig. 3.12) is to precisely stop the motor at the desired position from a low rpm rotation. The ESC-inbuilt motor brake is triggered after a short time delay when having passed the hall switch. If the hall switch does not report the correct position of the stopped rotor,

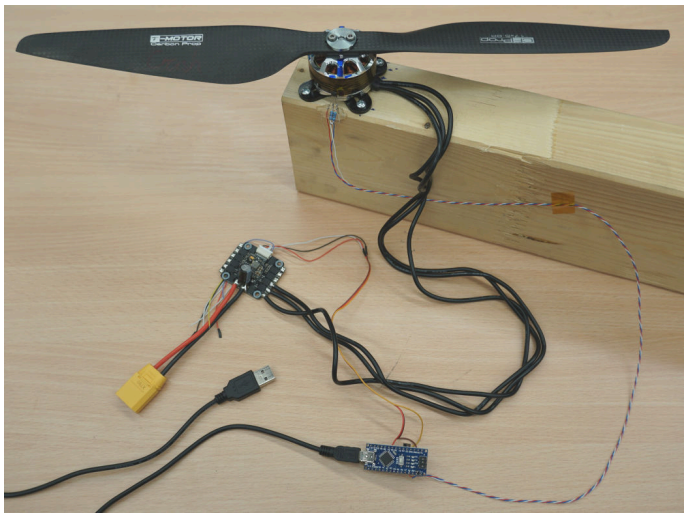

(a) From top to bottom: 17 in rotor, 400 rpm/V motor, ESC with BLHeli32 firmware (Skaug 2020), Arduino microcontroller

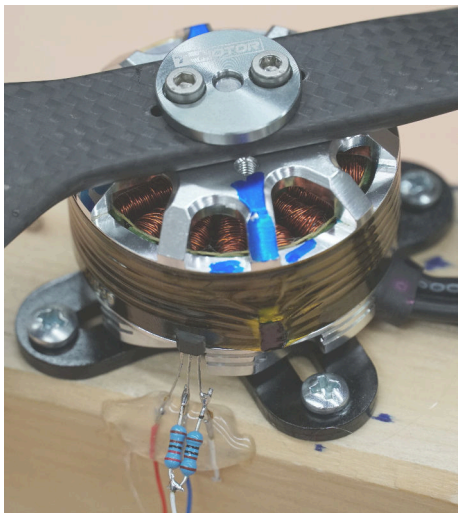

(b) Hall sensor and magnet application to the motor

Figure 3.12: Development setup for rotor positioning by precise stopping

another positioning sequence is started by the managing microcontroller. This is also the case if the desired rest position is lost. The time delay between sensor pass and brake activation is tuned automatically based on the alignment success rate.

Apart from the microcontroller as a potential node of hard- or software failure, the powertrain performance and reliability is unchanged. Entering nominal ESC operation with <1 s delay satisfies the requirement of a fast return to operational mode. During testing, 70% of the performed positioning procedures took less than 4 s between initial positioning command and successfully aligned rotor. It was found that there are positions in which the motor comes to rest with higher probability e.g. due to a major cogging torque step. Those positions must be used for the desired aligned rotor position. A low minimum rpm of the ESC is beneficial for repeatable positioning. Flight tests show that the positioning procedure is not relevantly affected by airflow. A downside of this approach is that only the cogging torque of the motor holds the rotor in its aligned position. Motors with high cogging torque (typically small, high rpm motors) are therefore preferred, or the holding force must be augmented externally e.g. by a pair of magnets. During the test flights, the rotor was pushed away from its aligned position approximately every half hour of flight such that a repositioning was initiated. The retrofitted microcontroller, hall sensor and magnet add a mass of below 10 g which means a relative mass increase of 4.7% for the tested powertrain (rotor, motor, ESC, cabling).

3.2.3 Rotor Retraction

Figure 3.13 gives an overview of the rotor retraction system. For drag reduction, the two-blade rotor (2) is aligned parallel to the airflow and additionally retracted into a recess (1) on the fuselage back. A structurally favorable, closed fuselage hull is present. The rotor is mounted on a threaded

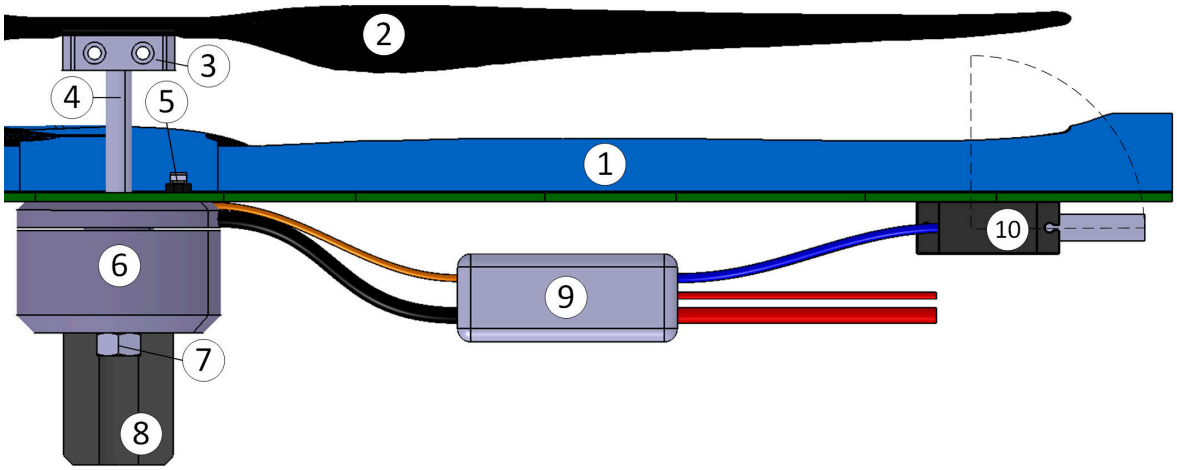

Figure 3.13: Schematic of the rotor retraction system in extended state

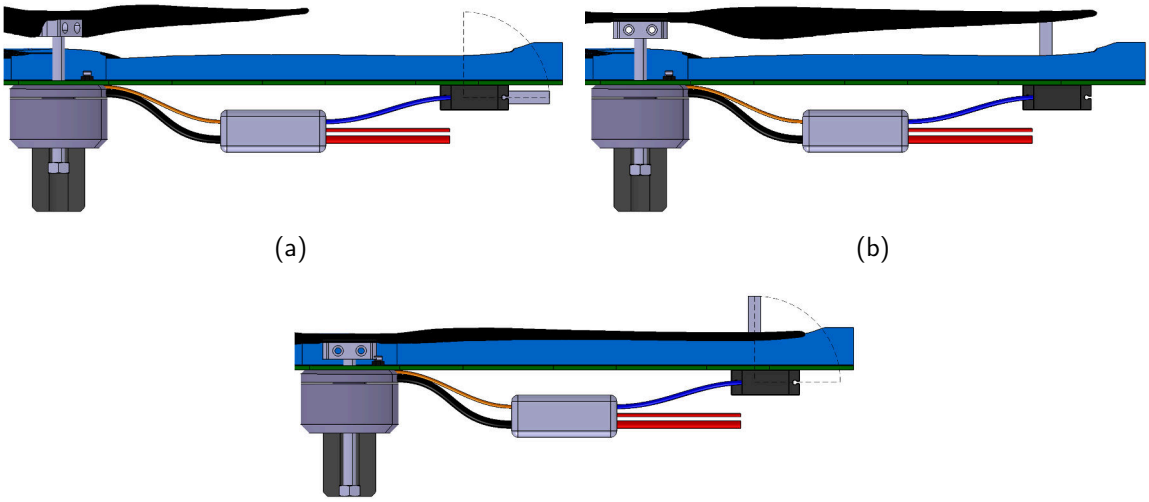

(a) (b)

(c)

Figure 3.14: Retraction sequence

shaft (4) with a connector (3). A limit switch (5) is integrated on the stator surface of the brushless outrunner electric motor (6). The motor is bolted to the fuselage structure. A hollow shaft with inside thread depicts the counterpart for the threaded shaft whose travel is limited by a lock nut (7). A hollow foam or rubber cylinder (8) attached to the motor's rotating bell applies friction to the shaft. (9) houses a microcontroller board to control the extension and retraction sequence as well as the ESC. The sequence control board uses the limit switch feedback and the throttle command signal to control the rotor stop pin actuation (10) and the ESC. The ESC is capable of a bidirectional motor operation and active motor RPM deceleration.

In normal operation, the rotor operates in the extended state depicted in fig. 3.13. The rotor stop pin is short enough to not hamper the rotor operation even in case of an actuator failure in vertical pin position. Clamping between the lock nut and the rotor bell transmits the motor's angular acceleration and deceleration torque on the threaded shaft. The throttle command is passed through the sequence controller to the ESC. The retraction sequence is triggered by a

throttle command lower than a threshold value. The motor then settles a predefined rpm and abruptly stops the motor. The inertial torque loosens the clamping between lock nut and rotor bell and the rotor's left-over kinetic energy dissipates in friction between the lock nut and the hollow cylinder. Due to the thread, the revolutions until the rotor has stopped lead to a translation of the rotor towards the fuselage (see fig. 3.14a). By the choice of friction torque and initial rotor rpm, the translation is adjusted such that the rotor plane moves within the rotor stop pin length. Once a sufficient period of time has passed to ensure the rotor has stopped, the rotor stop pin is moved into the rotor plane. Slow reverse motor rotation is initiated. The friction torque between hollow cylinder and lock nut rotates the rotor until one blade's trailing edge hits the stop pin. The rotor blades are then exactly positioned above the rotor recess (see fig. 3.14b). Friction is chosen high enough to reliably move the rotor against all disturbances like airflow or contamination. Due to

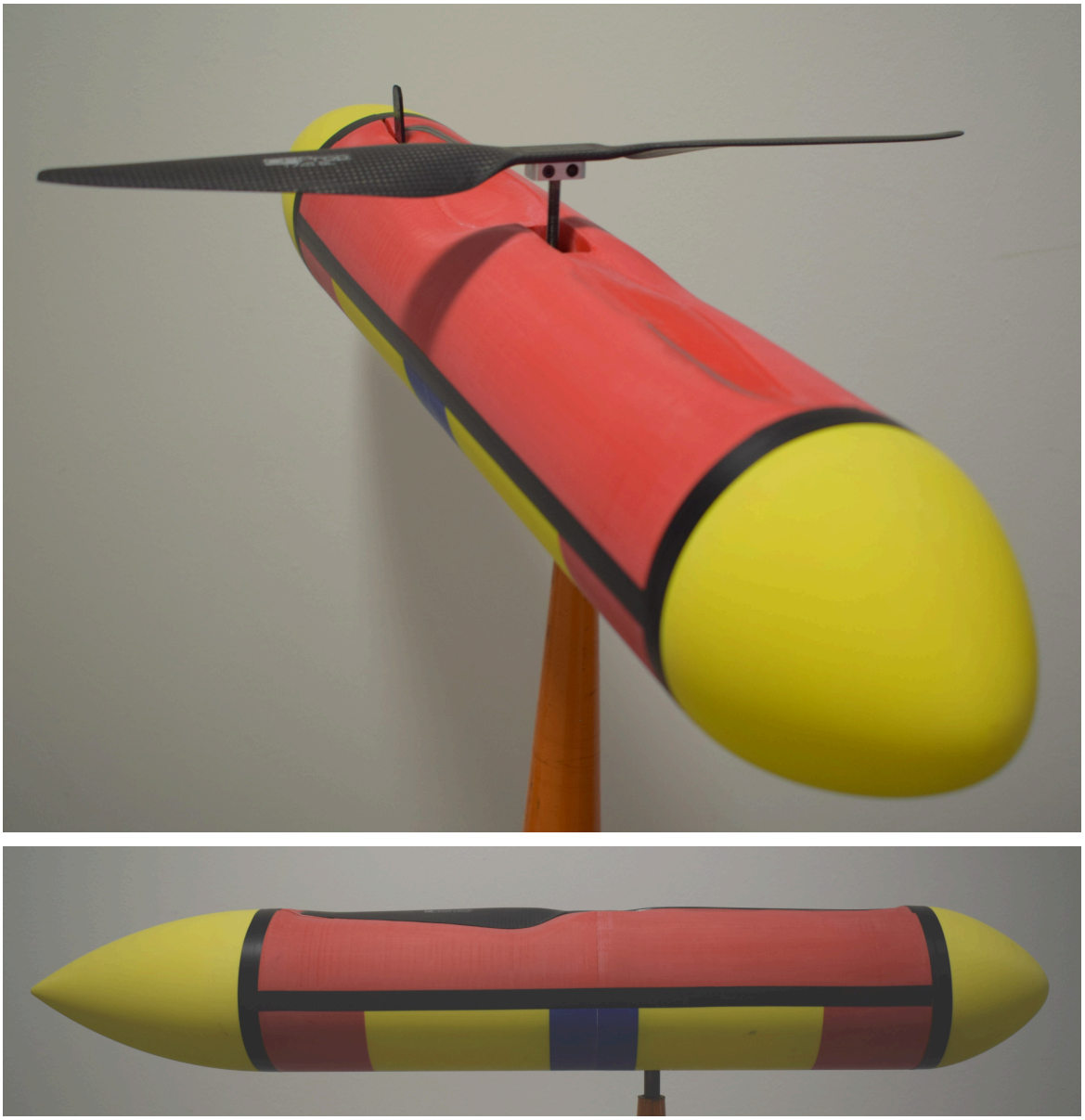

Figure 3.15: Rotor retraction system prototype

the relative rotation between the stopped rotor and the electric motor, the rotor moves towards its recess. The translation is stopped by the limit switch feedback when the rotor is fully retracted in its recess (see fig. 3.14c). Optional cooling air inlets are then closed by the rotor blades. To finish the retraction sequence, the rotor stop pin is pivoted inside the fuselage. Due to the thread, no torque respectively power is required to hold the rotor's fully retracted state. The extension sequence can be triggered any time during the retraction process. In this case, the stop pin is commanded into its retracted state and the motor adopts the extension RPM. First due to the rotor being stopped by the recess edges, then due to rotor inertial torque and finally due to the rotor drag torque, a relative rotation between electric motor and threaded shaft lets the rotor translate away from the fuselage. In case of an inoperative rotor stop pin in vertical position, the stopped rotor extends until it is free from the stop pin. The rotor extension movement is stopped when the lock nut contacts the electric motor bell at the fully extended state. The kinetic energy of the relative rotation is stored in the clamping between lock nut and motor bell. The extension rpm is chosen such that sufficient clamping is achieved. Furthermore, the extension rpm must be lower than the initial retraction rpm to guarantee a reliable loosening of the clamping. The sequence control board switches to throttle command passthrough mode after a preprogrammed timespan for the extension process.
Figure 3.15 illustrates the development prototype in extended and retracted state.
Wind tunnel tests simulating inflight airflow conditions up to $30\,\frac{\mathrm{m}}{\mathrm{s}}$ proved the robustness of the operation principle. The time to extend the rotor to full operation is 3.6 s and 6.8 s to retract. For larger systems, issues are likely to arise from the threaded shaft with regard to inappropriate centering and stress concentrations. Also considerable wear of the friction element was evident. The mass increase due to the mechanism is 25.3 g respectively 12% of the baseline powertrain mass.

3.2.4 Rotor Folding

Here, the blades of the stopped rotor are pivoted by the wind force around axes parallel to the motor shaft (see fig. 3.16). After the majority of motor stops, the pivoted blades are not aligned with the fuselage axis at first. But wind force on the blades turns the motor against its cogging torque into the airflow-parallel position. During hover flight test, a significant increase in vibration coming from the rotor was evident. The likely reason is the unconstrained asymmetric lead-lag movement of the blades that moves the overall rotor CG off the center axis. Asymmetric lift during transition intensifies this effect. After stopping the rotor in wing-borne cruise flight, the blades easily fold under the wind force. However to overcome the cogging torque and turn the motor into the desired position, an airspeed increase beyond cruise airspeed was required. An inherent drawback with regard to aerodynamic drag is the large frontal area of the folding hinges (see fig. 3.17).

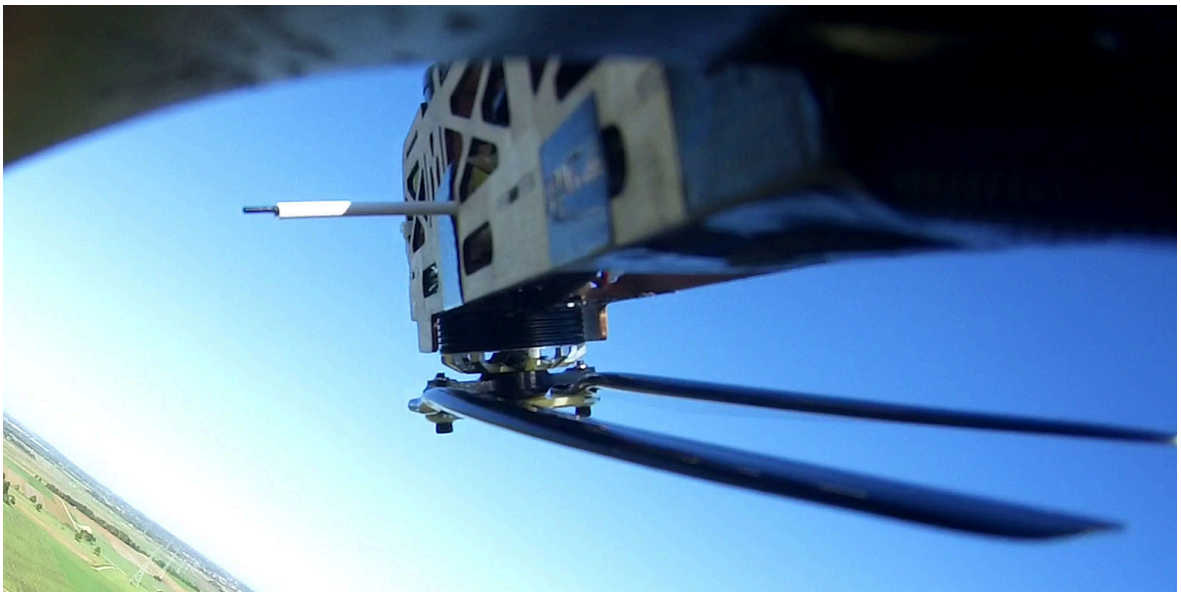

Figure 3.16: Folded rotor in flight

Figure 3.17: Comparison of folding rotor mount (left) and conventional rotor mount (right), both for a pusher arrangement

3.2.5 Review

The wind tunnel investigation of section 4.8.4 shows that an alignment of the rotor parallel to the airflow achieves the major drag saving. Compared to that, only small additional drag reductions can be gained by a retraction or housing of the rotor. Further, section 5.2.1 models the impact of the presented rotor retraction and rotor alignment systems on the range of different fixed-wing VTOL aircraft configurations.

Accordingly, rotor alignment turns out to be the superior approach for the drag reduction of a stopped rotor. The small additional drag saving of rotor retraction cannot compensate the

system's significantly higher mass and complexity. If the payload, flight control system and the aircraft itself can cope with the higher level of vibration, rotor folding can be a viable, most simple approach.

3.3 Battery Architectures

Figure 3.18 shows the inherent trade in battery design between energy density and power density for different battery types. The dashed vertical lines represent typical power requirements for the different flight phases of a fixed-wing VTOL aircraft. Suitable battery types must be able to provide the high power requirement of hover climb or transition. Battery types with high energy density however cannot supply that. The time share of the high power VTOL phases is typically less than 10% of the overall mission time. Hence, only a small portion of the energy must be provided at the highest discharge rate. This opens up the opportunity to compose a battery system of multiple batteries which are each tailored to the different power and energy requirements. The potential is to maximize the overall energy density of the battery system. Stahl & Hornung (2020) already published parts of the presented approach. Becker et al. (2018) performed a similar study for battery architectures comparable to BPMS BAT 1 and BPMS BAT 2 (see fig. 3.19) on electric cars. Besides the identification of a mass saving potential of up to 20% for high range, high

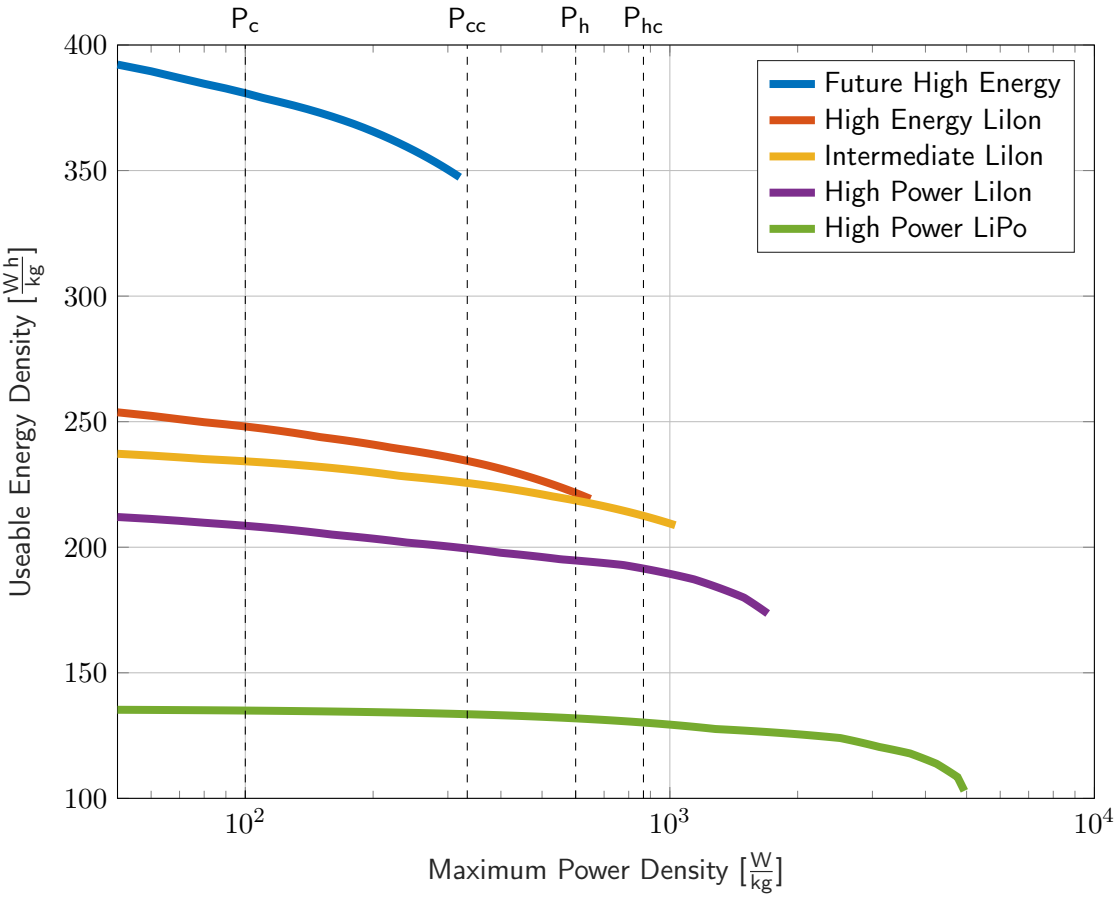

Figure 3.18: Energy density vs. power density for different battery types (cell level) and typical fixed-wing VTOL UAV power consumptions in cruise, cruise climb, hover and hover climb

power cars like SUVs, the usage of combinations of two standard battery cell types across the manufacturer's complete portfolio could simplify the supply chain. Due to the high energy/low power battery type in the system, a complete recharging will take longer. Zimmermann et al. (2016) reviewed topologies for battery-battery hybrid storage systems. Foxtech (2018) commercially offers a battery multiplexer for drones to switch between high power and high energy batteries.

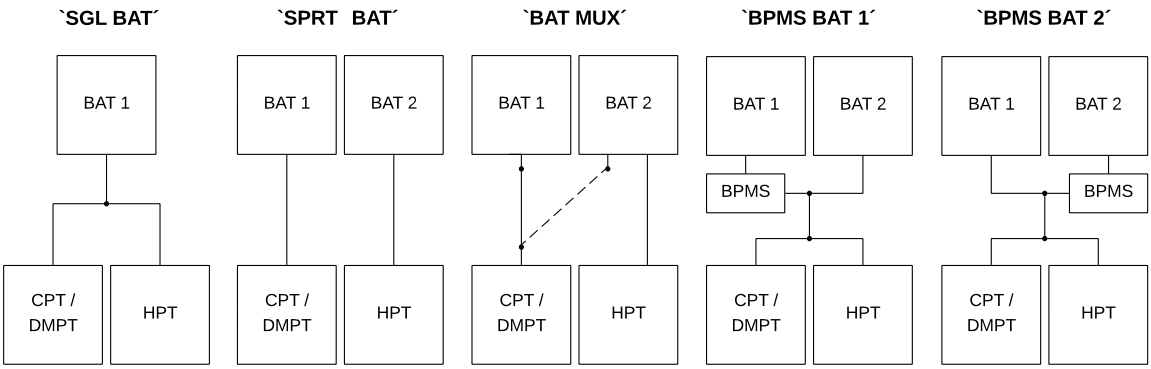

Figure 3.19: Investigated battery architectures

Figure 3.19 illustrates the studied battery architectures. The considered battery architectures combine a maximum of two batteries with two powertrain groups. The batteries are characterized by their energy and power density. BAT 1 owns the higher energy density while BAT 2 owns the higher power density. HPT, DMPT and CPT are the abbreviations for hover, dual-mode and cruise powertrain.

- SGL BAT uses a single battery of one battery type that supplies both hover and cruise power requirements of all powertrains. This is the simplest and most common implementation of a battery power supply. Other than all other architectures, all energy could be spent in the high power phases. Hence, it provides the highest flexibility for applications with extended hover times.
- SPRT BAT uses separate batteries for the cruise and hover powertrain. Due to its lower power drain, the cruise powertrain is connected to the high energy battery. It represents the simplest two-battery architecture.
- BAT MUX extends the latter architecture by a multiplexer switch to enable energy crossfeed. According to the power capability, a crossfeed is only possible from the high power battery to the cruise powertrain. Redundancy in the energy supply of the cruise powertrain is introduced. An additional switching device must be considered in the cost, mass and failure probability breakdown.
- BPMS BAT 1 uses a battery power management system (BPMS) that is connected to the high energy battery (analog to Gao et al. (2005)). It limits the power drained from the high energy battery to the allowed rate. The rest of the required power is provided by the high power battery. With that, a maximum in energy for all powertrains and flight phases can be

stored weight-efficiently in the high energy density battery. The battery power management system could further be used to recharge the high power battery during low power flight phases. Again additional cost, mass and failure modes have to be considered. Losses in the battery power management system reduce the energy that is usable from the high energy battery.

- BPMS BAT 2 moves the battery power management system to the high power battery. It limits the maximum power drain of the high energy battery to the allowed maximum by controlling the power contribution of BAT2. Compared to BPMS BAT 1, less energy passes through the battery power management system. Associated losses are reduced. An attempt to prove the feasibility of this type of battery power management system is made in Nagel (2020).

An advantage of either BPMS is that the share of power between the batteries is independent of the powertrain architecture.

In principle, all dual battery architectures allow recharging the high power battery from the high energy battery using an onboard battery charger. Also different voltage levels for BAT1 and BAT2 could be used in some architectures. Both is however not considered here.

As a dual battery system contains high energy batteries, its recharge time is increased. The reason is that similar to the discharge rate, also the allowed recharge rate of high energy batteries is reduced compared to high power battery types. The increased charge times as well as the general handling of two instead of one battery may be detrimental to the practicability.

The modeling of the batteries and topologies is further addressed in section 4.11.5. A computational study on the aircraft performance impact of the different battery architectures is presented in section 5.2.2.

4 Conceptual Design Tool Chain

To be able to compare the various fixed-wing VTOL UAV configurations of section 3.1 in terms of their mission performance, an aircraft design tool chain is implemented. Its features and methods are presented in the following. Stahl et al. (2019) provides insights into an early version of this tool.

4.1 State of the Art and Capability Gaps

Conceptual design is the first phase of traditional aircraft design. Different aircraft layouts and subsystem options are evaluated to select the most promising configuration which is further elaborated in the following design phases. Only minimal information on the mission and vehicle is available in first place. Yet a large extent of the project and vehicle life cycle cost is determined in this early phase. Rather low fidelity but time-efficient methods are used to model the different aspects of vehicle and operation. This allows to perform a great number of design runs with the many open design parameters. By that, the required vehicle size, subsystem specifications and cost characteristics can be narrowed down. It is common practice that these design runs are automated and use optimization algorithms to efficiently yield the interesting design space.

Fixed-wing VTOL design or analysis (e.g. in Bacchini & Cestino (2019), Palaia et al. (2021)) widely employs conventional conceptual design methods as they are summarized in fixed-wing aircraft or helicopter design standard literature (Raymer 1992, Roskam & Lan 1997, Leishman 2017, Johnson 2013). That concerns for example the sizing of wing and tail for sufficient lift and stability in cruise flight, the drag of lifting surfaces and fuselages, the power requirement of hovering rotors, mass estimates for aircraft systems and structure, mission performance and the aircraft's life cycle cost. Many regression based methods for aerodynamic drag, component masses and cost are however not applicable for the very small aircraft size investigated in this thesis. This can be attributed to the significantly lower Reynolds number and more laminar airflow respectively the different materials, construction techniques and design standards. Gundlach (2012) provides suitable weight estimation relationships for UAV. In his UAV design framework, Roessler (2012) approaches the mass estimation problem with an analytical sizing of the wing's primary structural elements for the given aerodynamic loads and desired deformation limits. Further, he selects commercially available products of electric motors and actuators from a database that contains precise masses. A key difference also in the powertrain modeling techniques is whether the efficiencies of components are estimated by fixed values or derive from analytically matched operating parameters of battery, ESC, electric motor and propeller (Drela 2005, Faulhaber 2020, Lundström et al. 2010, Gong et al. 2018). The available methods are further discussed in the individual chapters.

Complete tool chains are used in Tyan et al. (2017), Ozdemir et al. (2014), Serrano (2018) for the conceptual design of small unmanned fixed-wing VTOL UAV with fully electric powertrains. The Institute of Aircraft Design/TUM started their eVTOL UAV frameworks with Schwank (2016).

Seren (2017, 2018), Seren et al. (2019) continuously matured this. Methods like powertrain component matching, vortex lattice methods for lifting surfaces, automated component arrangement for weight and balance gives this tool high fidelity in scales of conceptual aircraft design, but at cost of high computational effort. Only few aircraft configurations are implemented to date. An existing in-house fixed-wing UAV design tool (Roessler 2012) has been modified for the fixed-wing VTOL configurations qXc, qXt, qPt by Karpfinger (2018*a*) as well. Previous work on implementing VTOL powertrain performance measurements and controllability in hover flight (Kolb 2018) is included there. It employs methods of similar fidelity level as Seren et al. (2019).

For the envisioned purpose of configuration comparison, the following shortcomings in existing design methods and tool chains can be assessed.

- Control authority in hover is insufficiently evaluated in the conceptual design tools. In this regard, the thrust-to-weight ratio of the entire powertrain in hover flight is the only determining parameter. It is however set by an input requirement, independently from obvious aspects like powertrain lever arms, vehicle inertia or wind conditions. For a configuration comparison, the impact of powertrain arrangement must be covered.
- A solution to inadequate models for structural mass is the above-mentioned analytical sizing for loads. This must be refined to cover the impact of the configuration's different powertrain locations and masses. The fuselage, nacelles and tail surfaces hence need to be included in this method.
- A matching of powertrain components is required to cover the impact of the widely different operating points in hover and wing-borne flight. However if datasets of dedicated motors and propellers are used for that, a bias can be introduced by the different technology levels and quality of the individual components. A motor, propeller and ESC model is required that incorporates the physical dependencies on operating conditions but exhibits identical efficiency levels.
- A geometry-based, time-efficient propeller model is missing that is valid in the hover and wing-borne regime to allow the analysis of dual-mode powertrains.
- A life cycle cost model for survey tasks with unmanned electric fixed-wing VTOL aircraft is missing and must be set up. The differences in configurations must be incorporated here as well.
- Analytical approaches for the thrust degradation caused by blocked rotor slipstreams and the aerodynamic drag of stopped rotors need to be validated.
- The data structure and framework of the tool must handle the different configurations without special cases.

The first two capability gaps are also identified by McDonald (2018) for the design of manned electric fixed-wing VTOL aircraft.

4.2 Program and Data Structure

Maximizing endurance or range for a given takeoff mass is a typical setup for the aircraft design task in the present class and size of aircraft. This enables the program sequence as shown in fig. 4.1. The principal idea is to subtract all component masses from the target total aircraft mass until only the battery mass remains. From this energy equivalent, all energy shares of prescribed mission segments e.g. hover climb or wing-borne climb are subtracted. The remaining energy is spent on the wing-borne cruise segment from which the endurance or range can be calculated. The component masses derive from structural components or systems that are sized to meet the prescribed mission requirements (e.g. stall speeds, climb rates, transition/cruise altitude). Mission specifications and requirements are stated in a common input file. Configuration input files describe the aircraft configuration by e.g. specifying the number or type of powertrains. The individual aircraft are described by a few basic parameters like configuration type, aspect ratio, airfoil, rotor/propeller size, etc.

Either a 'design of experiments' strategy or a genetic optimization algorithm is used to generate the parameter combinations to find a 'best' aircraft. The tool allows to define target functions for this search containing aircraft, performance, mission or cost properties.

Compared to other aircraft design tool chains, the program structure tends to avoid iteration loops at the cost of increased filter effort to sort out invalid configurations. Checks to skip the calculation of invalid configurations take place as early as possible in the program sequence to minimize computational effort.

All data is stored in intuitive structs that mimic the structural and systems architecture of the aircraft (see fig. 4.2). An SI unit system is used for the calculations. MATLAB as a widespread, powerful and well maintained engineering programming language is used.

4.3 Mission Profile

Figure 2.1 shows the segments of which the mission is composed. After hover takeoff at altitude h_{to}, the aircraft vertically climbs to transition altitude h_{trans} to be clear of obstacles. During transition, airspeed is increased beyond stall airspeed v_{stall} to cruise airspeed v_c. In- and outbound transition are only considered by an estimate power requirement composed of static hover and maximum available forward thrust, but not in terms of energy consumption or flight mechanics. Cruise altitude h_c is reached with a wing-borne climb at v_c. Cruise is the longest flight phase. It can, dependent on the application, contain a prescribed portion of turns or loiter. Flight at fast cruise airspeed v_{fc} is a requirement but is not considered as a dedicated flight phase with energy consumption. Cruise descent, inbound transition and hover descent are performed in a reverse manner to the previous flight states. In case of a landing site blockage which is discovered just in the hover descent phase, energy for a reserve hover of prescribed timespan is preserved. Cruise duration is a calculation result. All other segment durations are defined by altitudes and climb rate requirements. The ICAO standard atmosphere with a prescribed temperature offset is used.

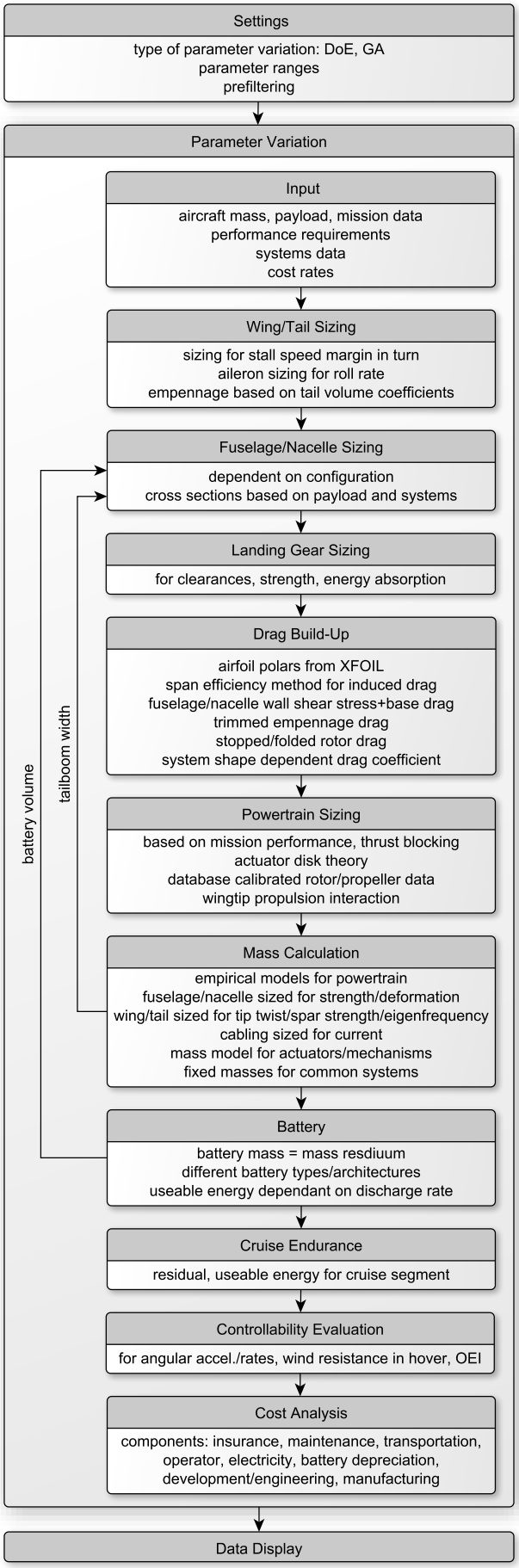

Figure 4.1: Program sequence and methods overview

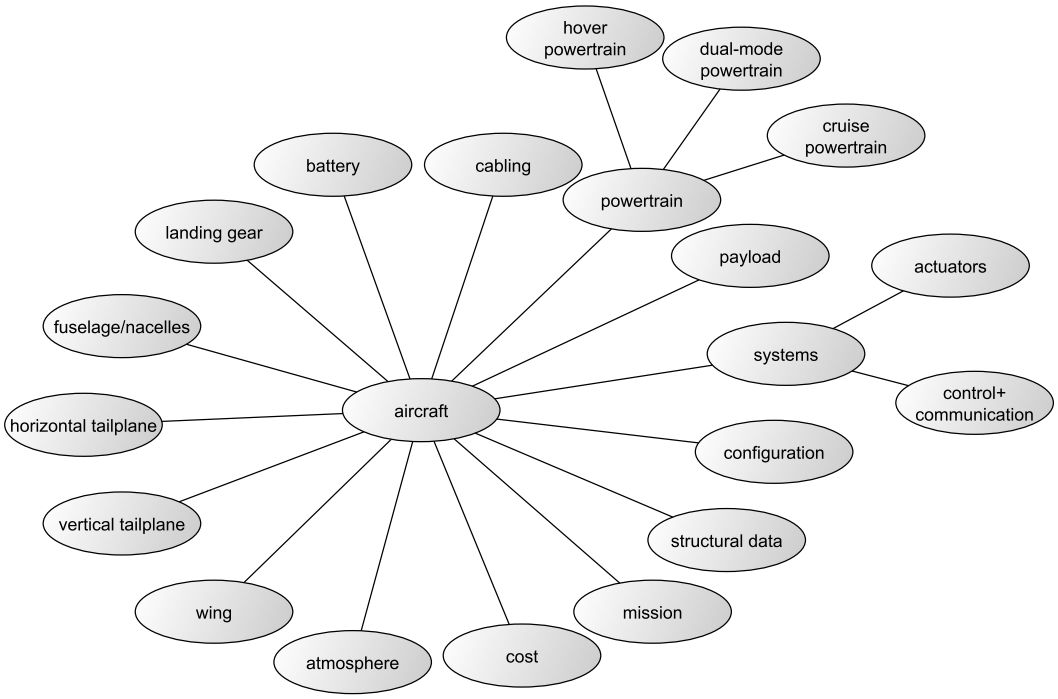

(a) High-level fields of the aircraft data structure

(b) Examples for the data structure

parameter	aircraft number	system	sub-system	property	flight phase
wing area	ac(1).	wing.		S	
wing lift coefficient in cruise	ac(2).	wing.		cL.	c
disk load of hover powertrain in hover	ac(3).	pwtr.	hpt.	DL.	h
time between big overhauls	ac(4).	cost.	maint.	tbo_big	
climb rate requirement in cruise climb	ac(5).	msn.		hdot.	cc

Figure 4.2: Aircraft data structure

4.4 Requirements Input and Parameter Variation

Major inputs and requirements can be taken from table 4.1. Table 4.2 lists the reasonable minimum number of parameters to be altered within an aircraft optimization and comparison task. Each parameter combination represents a unique aircraft. The parameter combinations are generated using either of the following two approaches:

- Design of Experiments

  The parameter vectors are combined in a full factorial manner. Unreasonable, invalid or redundant parameter combinations are removed in a second step (e.g. removing the variation of a dual-use propeller diameter for a qXc configuration). The core program sequence is then executed for every parameter combination without feedback of the results. This approach is mainly used for sensitivity studies. Sorting for the desired property (e.g. cruise endurance) allows to find the best aircraft among the discrete parameter combinations that were defined by the user.

Table 4.1: Major input variables/requirements and exemplary values

parameter	value	unit
aircraft total mass	5	kg
payload mass	0.8	kg
airspeed in fast cruise	35	$\frac{m}{s}$
duration hover reserve	30	s
altitudes takeoff/transition/cruise	450 / 500 / 750	m MSL
climb rates hc/hd/cc/cd	3 / -1 / 3 / -3	$\frac{m}{s}$
vertical acceleration in hover	1.125	$\frac{m}{s^2}$
time for $\pm 20^\circ$ angle to angle (roll/pitch/yaw)	0.7 / 0.7 / 1.1	s
gust velocity	8	$\frac{m}{s}$
min. roll rate in cruise	70	$\frac{^\circ}{s}$
max. sideslip angle with OEI	7	$^\circ$
tail aspect ratio hor./vert.	4.5 / 2	-
tail volume coefficient hor./vert.	0.55 / 0.03	-
minimum battery state of charge	20%	-
target battery voltage	21.6	V
design load factor	$\pm$ 6	g
min. torsion eigenfrequency of wing/tail boom	10	Hz
min. bending frequency of wing	5	Hz

Table 4.2: Varied parameters

parameter	variable
aircraft configuration	n_{cfg}
cruise airspeed	v_c
stall airspeed at 45° bank	v_{stall}
wing aspect ratio	AR
airfoil	$n_{airfoil}$
distance of wing-tail aerodynamic centers	$\frac{d_{ac,w-ht}}{c}$
spanwise nacelle position	$\frac{2\ y}{b}$
rotor/propeller diameters	d_i[1]
pitch-to-diameter ratio of rotors/propellers	$\frac{p}{d}\Big\|_i$
relative motor rpm at maximum load	$\frac{rpm_{maxload}}{rpm_{idle}}\Big\|_i$
load share of all hover powertrains	$f_{Tshare,h} = \frac{T_{hpt}}{mg}$
control thrust overhead	$\frac{\Delta T_{ctrl,i}}{mg}$

[1] i = hpt, dmpt, cpt

- Optimization with Genetic Algorithm

  A genetic optimization algorithm generates new the parameter combinations based on the performance of previous parameter combinations. Evolutionary mechanisms like selection, recombination, mutation are used for that. For the nature of an aircraft optimization problem, genetic algorithms are well suited. MATLAB's built-in genetic algorithm (Goldberg 2012, Conn et al. 1991, 1997) is used. It allows to constrain parameter ranges and step widths. The fitness function serves as the performance metric. It may contain any combi-

nation of aircraft and mission properties. Within the studies here, either the maximization of cruise endurance/range or minimization of cost for a certain mission is used.

4.5 Wing and Tail Sizing

The wing's reference area S is sized to meet a prescribed stall speed at a prescribed bank angle ϕ in wing-borne flight at cruise altitude. Horizontal tail forces are not considered.

$$S = \frac{2\ m\ g\ n_z}{\rho\ c_{L,max}\ {v_{stall}}^2} \tag{4.1}$$

Singh (2017), Gudmundsson (2014) provide comparisons of low-fidelity wing lift coefficient estimation methods. For unswept, untwisted wings with moderate taper, as assumed in this aircraft design tool, the most simple eq. 4.2 (Finck 1978) appears sufficient. The maximum lift coefficient $c_{l,max}$ of the selected airfoil at present Reynolds number is extracted from the input airfoil polar data table and transferred to a maximum wing lift coefficient $c_{L,max}$ by a constant factor of 0.9.

$$c_{L,max} = 0.9\ c_{l,max} \tag{4.2}$$

For tractor powertrain arrangements that affect parts of the wing with their slipstream's overspeed $(1 + a_{ax})v_c$, the increased wing lift coefficient can be calculated using eq. 4.3 (Smelt & Davies 1937, Patterson 2016). The axial induction factor a_{ax} can be calculated by momentum theory under the assumption of a glide ratio.

$$\frac{c_{L,blown}}{c_L} = 1 + \frac{S_{blown}}{S} a_{ax} \tag{4.3}$$

The procedure of wing area determination requires a short iteration as the lift coefficient is depend on wing area via the Reynolds number. The applied procedure can only handle a wing with negligible twist, sweep and taper and a constant airfoil along the span. Its validity was checked on exemplary wings whose spanwise lift coefficient distribution was calculated by a lifting line method implemented in XFLR5 (Deperrois 2019). The implemented method turned out to lead to conservatively oversized wing areas.

The required polar data tables are generated with XFOIL (Drela 1989) for adequate ranges of lift coefficients, Reynolds numbers and deflections of an optional plain trailing edge flap. Envelope airfoil polars for each airfoil and Reynolds number summarize the polars of all flap deflections in one. These can then be handled like an unflapped airfoil. The flight controller therefore selects the flap deflection angle with the lowest drag coefficient for the present lift coefficient as it was demonstrated in Oberschwendtner (2016).

Horizontal and vertical tail geometries are defined by tail volume coefficients $c_{V,h},\ c_{V,v}$ and aspect ratios. Hence, tail areas are calculated using the tail lever arm $d_{ac,w-t}$ (distance between wing and

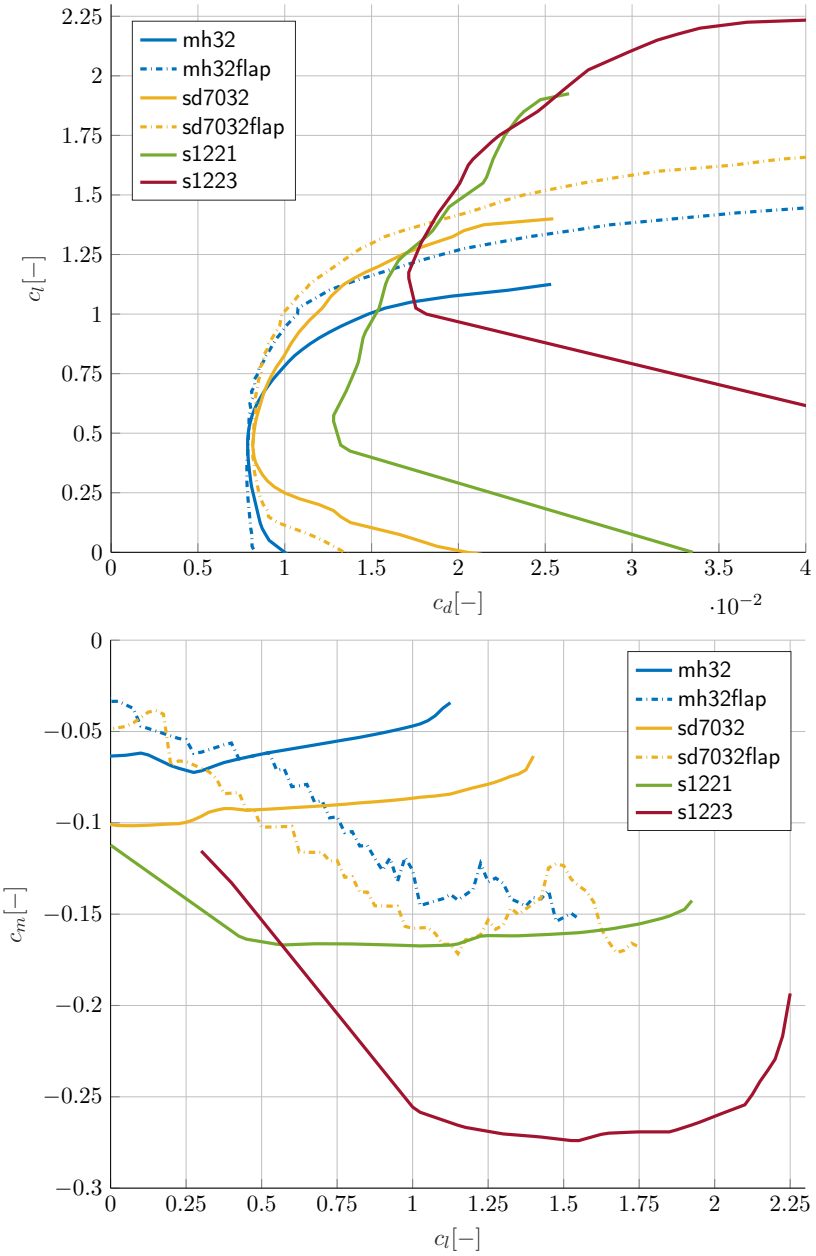

Figure 4.3: Polars of the considered wing airfoils at $Re = 2.5 \times 10^5$

tail aerodynamic center) as variation parameter. Tail lever arms of horizontal and vertical tail are assumed to be identical.

$$S_h = \frac{c_{V,h}\ c\ S}{d_{ac,w-t}} \tag{4.4}$$

$$S_v = \frac{c_{V,v}\ b\ S}{d_{ac,w-t}} \tag{4.5}$$

For twin-boom configurations, the span of the horizontal tail is prescribed by the tail boom distance. The aspect ratio requirement is omitted and the chord length adjusted for the required tail volume coefficient. For configurations like tAt_hpt or tVt, the tail lever arm is set by the pitch moment equilibrium in hover and hence depends on powertrain thrust share, wing and rotor geometry.

For both wing and tailplanes, a rectangular planform is used. This simplifying approach is conservative in forecasting structural mass and induced drag. It well approximates typical UAV wings with high outboard chord lengths due to Reynolds number criticality.

Aileron size is estimated based on an equilibrium of the wing's roll damping moment and the aileron's roll moment at the prescribed roll rate in cruise condition (Schlichting & Truckenbrodt 2001, p. 454). For tilt wingtips, the lift slope $\frac{\mathrm{d}c_L}{\mathrm{d}\alpha}$ of the isolated wingtip segment is used as a conservative assumption in sizing for roll authority. A flaperon option allows to have ailerons along the full wing span and checks if the desired roll rate can be achieved.

4.6 Fuselage and Nacelle Sizing

The term fuselage refers to the payload carrying center body, while nacelles carry motors and their propellers. Fuselage and nacelle geometries significantly depend on the aircraft configuration. The bodies consist of multiple strung trapezoid or cone segments. Their quadratic or circular cross sections derive from the surrounded components e.g. payload cross section or engine diameter. Fuselage segment lengths derive from rotor diameters, wing chord, maximum widening/constriction angles and empennage lever arm. The rearmost fuselage or nacelle segments that carry the empennage use a constant cross section. An iteration is required to perform a structural sizing of this rearmost tail boom segment. Also the battery which is housed by the center fuselage causes an iteration as its mass and size is left over as a residual at the end of the design loop. Avionics and control link are assumed to find place between payload, battery and engines, so that no dedicated space is preserved for them. Also, component locations are not iterated to realize the required CG. With battery and payload placed in the desired CG, the considered configurations inherently lead to close agreements of required and resultant CG. These deviations can be adjusted with minor battery shifts. For later use, the portion of the rotor disk area which is blocked by nacelles or fuselages is calculated. Several checks to guarantee sufficient clearance of rotors or propellers to fuselages and lifting surfaces are performed.

4.7 Landing Gear

The standard landing gear has three ground contact points in a taildragger layout. Configurations that cannot use the tail boom end or inverted vertical tail as rear contact point (e.g. qXc due to pusher propeller ground clearance) use a second landing gear bow. Each landing gear strut is considered to act as a tapered elastic beam with prescribed anhedral and material. The landing gear design must fulfill the following requirements:

- prescribed bank angle clearance between forward landing gear ground contact points and any rotor/propeller on the wing in hover and cruise position
- prescribed vertical clearance between ground and fuselage bottom when landing gear is fully suspended

- absorption of a prescribed free fall energy while not exceeding a maximum load factor and strut material strength

4.8 Aerodynamic Drag Build-Up

Aerodynamic drag is evaluated for the two flight conditions of cruise and fast cruise. Variations in lift or drag coefficients in the climb or descent segments are neglected due to the small altitude differences for this type of UAV. Aerodynamic drag coefficients are calculated for all relevant aircraft components and summed up by the weight of their reference surfaces $\frac{S_i}{S}$.

$$c_D = \sum_i c_{D,i} \frac{S_i}{S} \tag{4.6}$$

4.8.1 Wing

The drag estimation of the wing splits up in 2D airfoil drag and 3D drag effects. The wing lift coefficient c_L derives from the cruise flight state and is transformed to an average local airfoil lift coefficient c_l using the lift curve slope eq. 4.7. The lift contribution of the horizontal tail is neglected hereby. The airfoil drag coefficient is interpolated from a precalculated $c_l - c_d$ polar data table (see fig. 4.3). While maximum lift coefficient prediction is taken from XFOIL calculations without change, drag coefficients receive a margin of +15% on top of the prediction. This is to account for too optimistic XFOIL results and wing surface imperfections. As fuselage-wing or nacelle-wing intersections and propeller outflow trigger turbulent flow, a fixed airfoil drag coefficient increase is added in those areas. The drag coefficient $c_{D,AR=\infty}$ represents this corrected airfoil drag. An induced drag coefficient $c_{D,ind}$ that represents inviscid, 3D flow effects is added.

$$c_L = c_l \frac{AR}{2 + \sqrt{AR^2 + 4}} \tag{4.7}$$

$$c_{D,wing} = c_{D,AR=\infty} + c_{D,ind} \tag{4.8}$$

$$c_{D,ind} = \frac{{c_L}^2}{\pi \ AR \ e} \tag{4.9}$$

$$e = e_{taper} \ e_{fus/nac} \ e_{dihedral} \tag{4.10}$$

Equation 4.10 calculates the Oswald efficiency e that results from different sources of induced drag (Niță & Scholz 2012). Hoerner (1965, chap. 7-4, fig. 5) provides a function for the Oswald efficiency of unswept, trapezoidal wings based on taper and aspect ratio. The degradation of the Oswald efficiency by a fuselage or nacelle follows an approach after Kroo (2001) that penalizes the ratio between fuselage width and span. It as well provides a method for the dihedral influence.

4.8.2 Empennage and Trim Drag

The lift coefficient on the horizontal tail is derived from the pitch moment equilibrium of lifting surfaces. Powertrain pitch moments are neglected due to typically small pitch moment contributions

and for faster tool execution. The vertical tail is assumed to operate at zero lift during wing-borne flight. With the lift coefficient as input, the drag calculation follows the same approach as for the main wing. Fuselage and dihedral impact on Oswald efficiency are not considered. An interference factor on drag is multiplied.

4.8.3 Fuselages and Nacelles

Fuselages and nacelles are considered to generate minimum drag in the main flight condition of cruise. Their drag can then be estimated with a c_L-independent, zero-lift drag coefficient c_{D0} term. At angles of attack different from the design cruise flight state, this method underestimates the drag.

Wall shear stress coefficients $c_{\tau,i}$ acting on fuselage slices i are summed up to an integral surface friction coefficient c_f (eq. 4.13). This approach is used instead of the typical integral form of the friction coefficient due to the strong variation in fuselage cross section (wide forward body and slim tail boom). A transition point is predefined by the user and can be assumed to be located at propeller planes (due to turbulent downwash) as well as rotor, payload or wing mounting locations. Laminar and turbulent wall shear coefficients are calculated according to Hoerner (1965, chap. 2-4,2-5):

$$c_{\tau,lam} = \frac{0.664}{\sqrt{Re_x}} \tag{4.11}$$

$$c_{\tau,turb} = (2 \log Re_x - 0.65)^{-2.3} \tag{4.12}$$

$$c_f = \frac{1}{S_{fus}} \sum_i c_{\tau,i} \; S_i \tag{4.13}$$

A second drag component $c_{d,sep}$ are flow separations that can occur at blunt fuselage ends or rapid cross section reductions. If the constriction angle of a fuselage slice i exceeds a threshold, the projected frontal area of this annulus ΔA_i is assumed to exhibit a user defined drag coefficient of $c_d, base$.

$$c_{d,sep} = c_{d,base} \; \frac{\sum_i \Delta A_i}{A_{fus}} \tag{4.14}$$

$$c_{D,fus} = (c_f + c_{d,sep}) \; \frac{S_{fus}}{S_{ref}} \; f_{interf,fus} \tag{4.15}$$

The overall fuselage drag is multiplied with an interference factor as suggested by Raymer (1992).

4.8.4 Stopped Rotor

The majority of the investigated aircraft configurations feature hpt which are stopped during wing-borne flight. The sharp edges and blunt bodies of a large rotor system potentially mean a significant drag component for a fixed-wing VTOL aircraft. An accurate and reliable drag model is required. A straightforward approach is the drag build-up of the major involved components, as it is done

$$c_D A = \sum_{\substack{i=rotor,\\ shaft,\dots}} c_{D,i} A_i f_{interf,i} \tag{4.16}$$

Table 4.3: Stopped rotor drag modeling

	c_D or c_f [−]	A or S_{ref} [10^{-4} m^2]	f_{interf} [−]	$c_D A$ [10^{-4} m^2]	share of total [%]
rotor	0.0051	259.5	1	1.32	41
shaft	1.1	1.0	1	1.10	34
connector	0.75	1.1	1	0.84	26
total				3.26	100

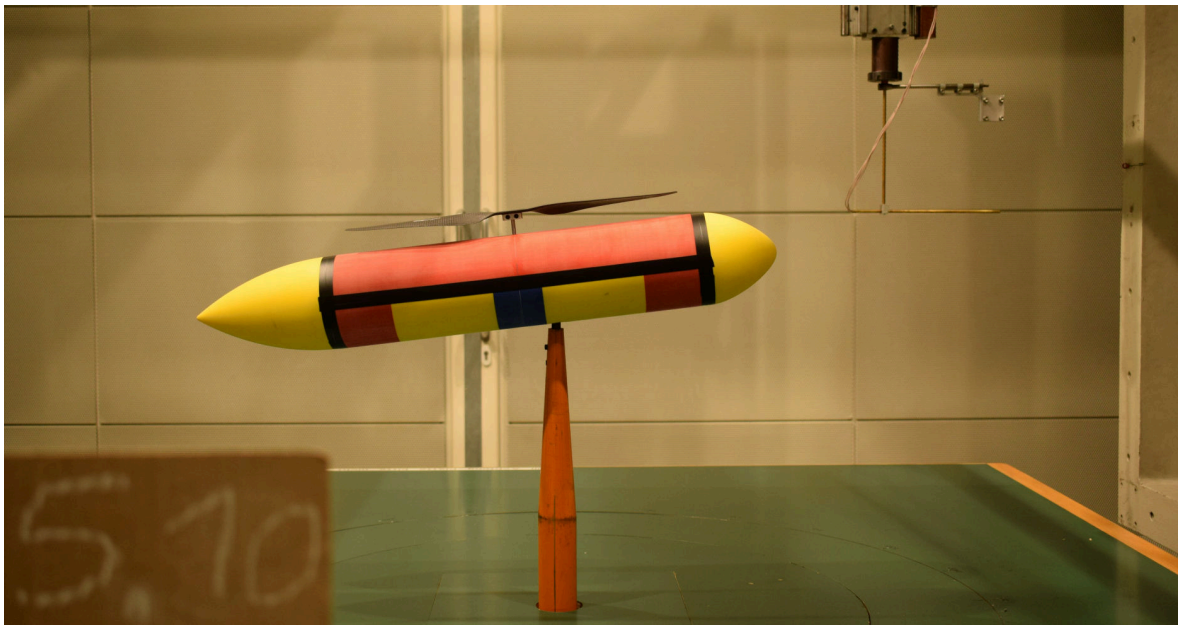

Figure 4.4: Model configuration #4 in the wind tunnel

in table 4.3 for the rotor system of section 3.2.3. It sums up the products of drag coefficient, corresponding area and interference factors for all contributions to the overall drag area $c_D A$. Rotor drag is modeled as pure turbulent surface friction (Hoerner 1965, chap. 2-5). Drag coefficients for the rotor-to-shaft connector and the shaft are taken from Hoerner (1965, chap. 3-11, 3-13). The interference factor is set to 1.

To back the presented model, wind tunnel measurements were performed in the wind tunnel B at the Chair of Aerodynamics and Fluid Mechanics at TUM (TUM AER 2020). The prototype for rotor retraction (see section 3.2.3) is therefore configured in different states (see axis labeling in fig. 4.5). For a rotor azimuth angle $\gamma = 0°$, the blade span direction is parallel to the airflow. The distance $d_{rot-nac}$ describes the minimal vertical spacing between rotor and nacelle body. Drag measurements are taken at the dynamic pressures $q = 225/900\,\text{Pa}$ and angles of attack $\alpha = 0/6°$.

Figure 4.5 shows the results of the drag measurements by means of the drag area $c_D A$. Therefore, the drag force measurements are offset with the drag of the clean cylindrical nacelle (without rotor

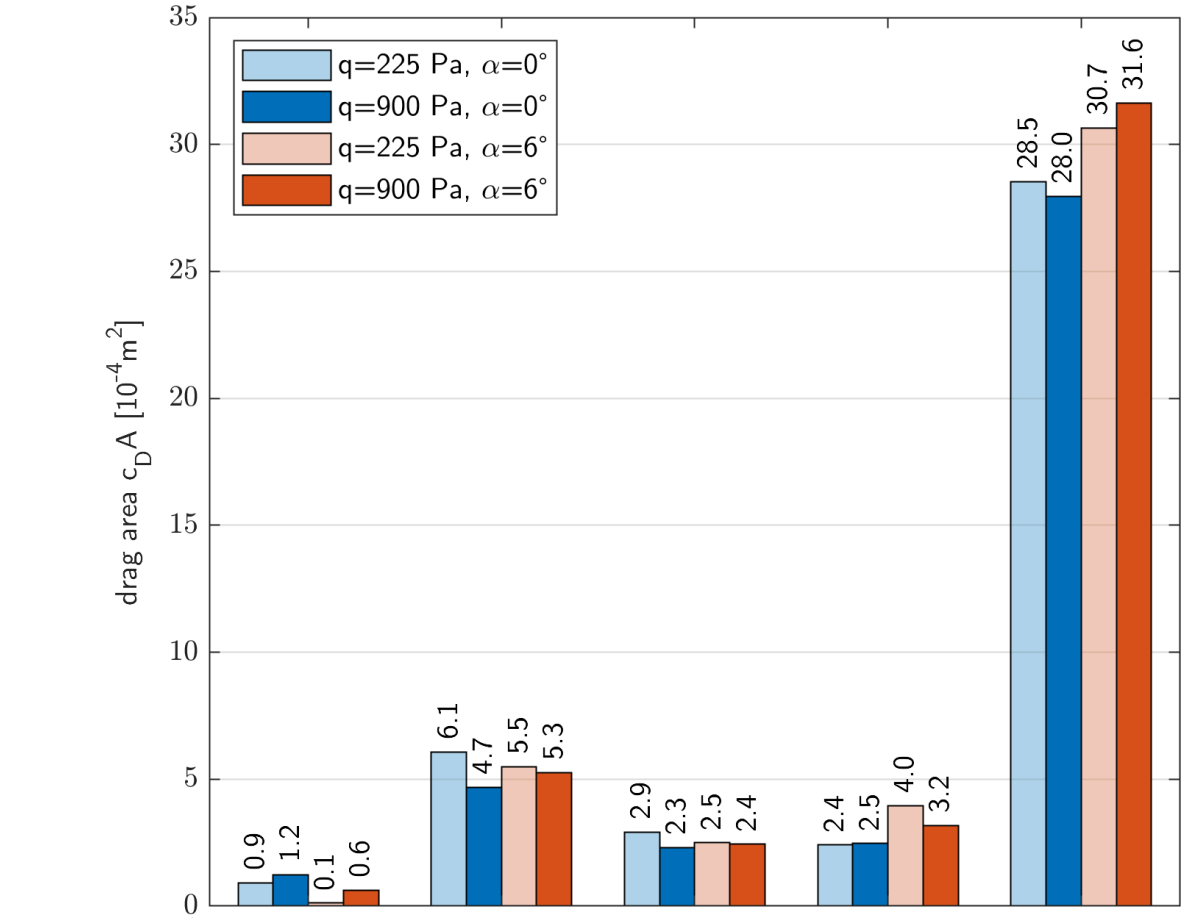

#	1	2	3	4	5
model	retraction sys	retraction sys	rotor on cyl	rotor on cyl	rotor on cyl
$d_{rot-nac}$ [mm]	retracted	extended	7	20	20
azimuth γ [°]	0	0	0	0	90

Figure 4.5: Results of the wind tunnel measurements on stopped rotor drag

and shaft) and normalized with the dynamic pressure q.

$$c_D A = \frac{D - D_{cyl,no\ rotor}}{q} \tag{4.17}$$

The slightly uneven surface of the retracted rotor (#1) causes only little more drag than the clean cylinder. A clear drag difference between retracted (#1) and extended (#2) rotor retraction system can be seen. The increased drag of the extended rotor retraction system (#2) over the rotor mounted to the cylinder (#4) can be associated with a wider shaft and the edges of the opened recess. The influence of the distance nacelle-rotor on the drag force is minimal (#3 vs. #4). The drag increase for the rotor perpendicular to the airflow (#5) is predominant. Investigations with a wool string probe indicate vortices behind the rotor-shaft-connector and the chord tapering towards the blade root. The trailing edge forward blade likely operates in stalled condition. Except for configuration #5, the influence of the angle of attack is insignificant. A possible explanation is the surface-parallel airflow close to the nacelle body. The estimated drag area of table 4.3 overestimates the measured drag of the configurations #3 and #4 by almost one third.

For the actually implemented stopped rotor drag model, it is refrained from a drag breakdown in rotor system components to reduce the number of required geometry input parameters. From the measurements #3, #4 and #5 at $\alpha = 0°$, drag coefficients $c_{d,rot,0}$ and $c_{d,rot,90}$ are derived which include shaft and hub drag. The rotor blade bottom surface is used as reference. A sinusoidal dependence is assumed in eq. 4.20 to interpolate the coefficients for azimuth angles γ between the available measurements of 0° and 90°. The drag of an unaligned rotor equals the drag of a randomly stopped rotor. Assuming equal stop probabilities for each azimuth angle, averaging eq. 4.20 within one rotor revolution yields the randomly stopped rotor drag coefficient $c_{d,rot,rand}$.

$$c_{d,rot,0} = 0.0194 \tag{4.18}$$

$$c_{d,rot,90} = 0.2177 \tag{4.19}$$

$$c_{d,rot}(\gamma) = c_{d,rot,0} + (c_{d,rot,90} - c_{d,rot,0}) \left|\sin\gamma\right| \tag{4.20}$$

$$c_{d,rot,rand} = \int_0^{2\pi} c_{d,rot}(\gamma) \frac{1}{2\pi}\, d\gamma = 0.1457 \tag{4.21}$$

A retracted rotor is assumed to generate no additional drag in cruise flight.
A skin friction method (Raymer 1992, p. 280) is used to calculate the drag of folded propellers as it is e.g. present at the tVt configuration.

4.8.5 Miscellaneous

Landing gear, antenna and payload drag are based on typical drag coefficients of their cross section shape. Leakage and protuberance drag is considered to be 7.5% of the total zero lift drag (Raymer 1992, p. 289).

4.9 Powertrain Sizing

One powertrain branch consists of the propeller or rotor, the electric motor, the electronic speed controller (ESC) and the connecting cables (see fig. 4.6). Multiple of those powertrain branches are installed in a fixed-wing VTOL aircraft. The battery is treated separately from the powertrain.

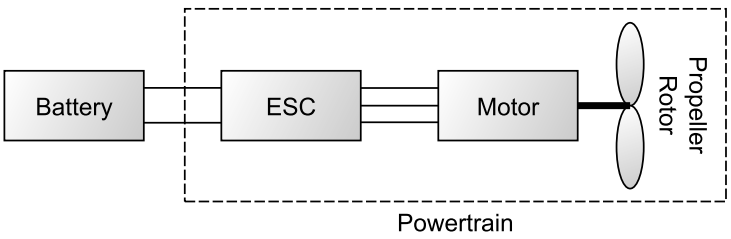

Figure 4.6: Powertrain components

4.9.1 Rotor and Propeller

The operating conditions for rotors or propellers in hover and cruise phases are considerably different due to the inflow airspeed. Hence, different methods are applied.

4.9.1.1 Hover Condition

Powertrain sizing starts at the thrust requirements for the powertrain types $i = hpt, dmpt$ and mission segments $j = h, hc, hd$. The total thrust requirement in hover in eq. 4.22 derives from an equilibrium of gravity force $m\,g$ and aerodynamic drag due to vertical motion $D_{vert,ij}$. The thrust share factor $f_{Tshare,i}$ represents the share of total thrust which the powertrain type i contributes. In order to obtain moment balance, the thrust share factor determines the ratio of geometric lever arms of hpt and dmpt to the CG for configurations like tAt or qXt. The control factor $f_{ctrl,i}$ adds thrust overhead on top of the hover climb thrust requirement to yield the maximum thrust requirement of all hover phases. Both the control factor and thrust share are given by the outer parameter variation framework (see table 4.2). The net thrust requirement is corrected for the thrust loss that is caused by blocking objects in the rotor slipstream. The blocking or thrust loss coefficient $k_{block,i}$ and blocked rotor disk portion $\frac{S_{block,i}}{A_{disk,i}}$ is further described in section 4.9.1.2. Finally, the gross thrust requirement for each powertrain is obtained.

$$T_{net,ij} = \frac{(m\ g + D_{vert,ij})\ f_{Tshare,i}}{n_{pwtr,i}} \tag{4.22}$$

$$D_{vert,ij} = \frac{\rho_j}{2}\ \dot{h}_j^2\ c_{D,vert}\ S_{proj} \tag{4.23}$$

$$T_{net,i,max} = T_{net,i,hc} + T_{net,i,h}\ f_{ctrl,i} \tag{4.24}$$

$$T_{gross,ij} = T_{net,ij}\ \frac{1}{1 - k_{block,i}\frac{S_{block,i}}{A_{disk,i}}} \tag{4.25}$$

Conventional momentum theory or actuator disk theory as explained in Leishman (2017, p. 81-88) is used in eqs. 4.26 and 4.27 to calculate the required ideal rotor shaft power in h, hc and hd. Case differentiations are made for climb and descent.

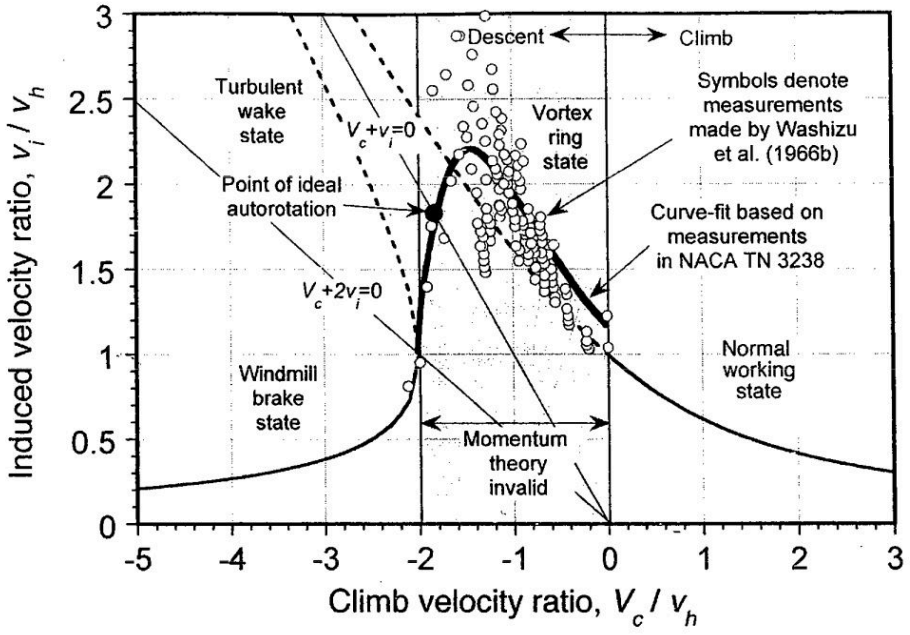

Figure 4.7: Induced velocities for different climb/descent states (Leishman 2017, fig. 2.18)

$$v_{h,ij} = \sqrt{\frac{DL_{ij}}{2\ \rho_j}} \tag{4.26}$$

$$v_{ind,ij} = \begin{cases} -\frac{\dot{h_j}}{2} + \sqrt{\frac{\dot{h_j}}{2}^2 + v_{h,ij}^2} & \text{for } \dot{h_j} \geq 0 \\ -\frac{\dot{h_j}}{2} - \sqrt{\frac{\dot{h_j}}{2}^2 - v_{h,ij}^2} & \text{for } \frac{\dot{h_j}}{v_{h,ij}} \leq -2 \\ v_{h,ij} \left(1\ (1.15) - 1.125\ \frac{\dot{h_j}}{v_{h,ij}} - 1.372\ \left(\frac{\dot{h_j}}{v_{h,ij}}\right)^2 \ldots \right. & \\ \left. \ldots - 1.718\ \left(\frac{\dot{h_j}}{v_{h,ij}}\right)^3 - 0.655\ \left(\frac{\dot{h_j}}{v_{h,ij}}\right)^4 \right) & \text{for } -2 \leq \frac{\dot{h_j}}{v_{h,ij}} \leq 0 \end{cases} \tag{4.27}$$

$$P_{ideal,ij} = T_{gross,ij}\ \left(\dot{h_j} + v_{ind,ij}\right) \tag{4.28}$$

$$P_{shaft,ij} = \frac{P_{ideal,ij}}{FM_i} \tag{4.29}$$

For the region between hover and windmill state, a semi-empirical approximation (Leishman 2017, p. 87, eq. 2.96) is used (see fig. 4.7). The validity of the approximation is poor for small negative values of $\frac{v_{climb}}{v_{ind,h}}$. To improve validity of the polynomial approximation for small negative values of $\frac{v_{climb}}{v_{ind,h}}$ (main operational region) and remove the unsteadiness at $\frac{v_{climb}}{v_{ind,h}} = 0$, the polynomial's constant is changed to 1.

The propeller measurement databases of Brandt et al. (2020) and Kolb (2018) are analyzed for a relationship between figure of merit FM and pitch-to-diameter ratio $\frac{p}{d}$ among adequate propeller

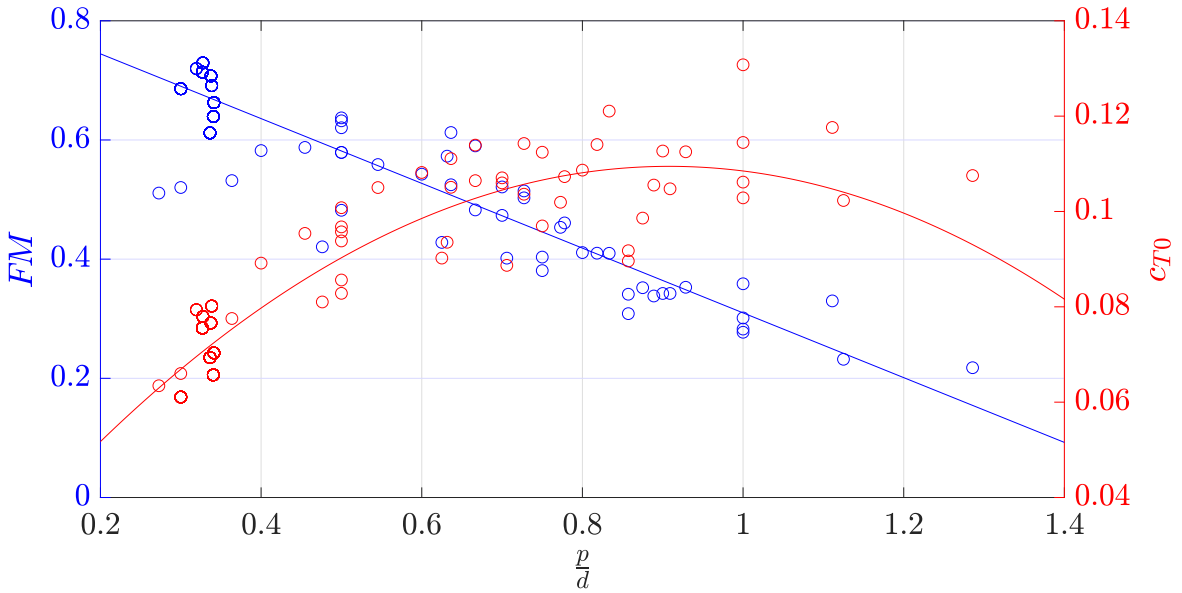

Figure 4.8: Fits of FM and c_{T0} to propeller measurement data of the brands *APC electric*, *APC sport*, *KDE* and *T-Motor*

$$FM = -0.5434\ \frac{p}{d} + 0.8532 \tag{4.30}$$

$$c_{T0} = -0.1151\ \left(\frac{p}{d}\right)^2 + 0.2091\ \frac{p}{d} + 0.01451 \tag{4.31}$$

makes. The same is performed for the static thrust coefficient c_{T0} (see fig. 4.8 and eqs. 4.30 and 4.31, consider the limited validity range). This procedure is inspired by Serokhvostov & Churkina (2011) who applied it for cruise propeller parameters.
Using the thrust coefficient c_{T0}, the rotational frequency of the rotor rps (unit 1/s) is calculated. Consequently, motor shaft torque Q and an approximate rotor tip speed v_{tip} are yielded. For a valid aircraft, the tip speed as a simple measure for rotor noise must not exceed a user-defined threshold value.

$$rps_{ij} = \sqrt{\frac{T_{gross,ij}}{\rho_j \; c_{T0,ij} \; {d_i}^4}} \tag{4.32}$$

$$Q_{shaft,ij} = \frac{P_{shaft,ij}}{2 \; \pi \; rps_{ij}} \tag{4.33}$$

$$v_{tip,ij} \approx rps_{ij} \; \pi \; d_i \tag{4.34}$$

4.9.1.2 Hover Thrust Loss due to Slipstream Blocking

Objects which are located in the slipstream of a rotor or propeller cause a reduction of the net static thrust. For VTOL aircraft, blocking objects are typically fuselages, nacelles, wings or horizontal tails that carry hover powertrains. For configurations like the qPt family whose fuselage blocks a significant portion of the rotor disk, the blocking effect may not be neglected.

A similar problem occurs on helicopter fuselages and tail rotor fins which has been addressed by Leishman (2017, pp. 307-309, 318-319), Johnson (2013, pp. 117-118, 149), Wilson (1975) as well as Lynn et al. (1970). A simple approach is to consider the parasitic aerodynamic drag of a body which is exposed to the flow field of a rotor with thrust T. The drag or thrust loss ΔT can then be calculated with eq. 4.35.

$$\frac{\Delta T}{T} = \frac{\frac{\rho}{2} \left(f_v v_{i,disk}\right)^2 c_D f_S S}{2 \rho A {v_{i,disk}}^2} = \frac{S}{A} \frac{{f_v}^2 c_D f_S}{4} = \frac{S}{A} \; k_{block} \tag{4.35}$$

$\frac{S}{A}$ describes the portion of the rotor disk area that is blocked. Therefore, the blocking body is orthogonally projected onto the rotor disk. c_D is the average drag coefficient of the blocking body. The factor f_v accounts for the airspeed variation with the radial and streamwise location in the slipstream. It can be calculated using momentum theory. f_v takes values < 1 (for positions on the rotor inflow side) up to values of 2 (for positions in the far wake). f_S alters the effective blocking area S of the blocking body as the slipstream constricts along the flow. For simplicity, the drag coefficient and velocity factor are summed up to a blocking or thrust loss coefficient k_{block}.

Rotor blocking measurements have been performed in the scope of this thesis to obtain data for the investigated types and sizes of VTOL UAV. Rieger (2017) and Linke (2019) contain a detailed documentation of the performed measurements. Parts of it were published in Stahl et al. (2019) and Stahl & Hornung (2020). For the experiment, an existing static thrust test stand (Speck et al.

Figure 4.9: Extension to the load cell to measure rotor thrust blocking with object pyr mounted

2015) is modified with an extension on which the blocking objects could be mounted in various distances to the rotor (see fig. 4.9). The blocking body extends along the rotor diameter and exceeds the tip radius. The presented results are attained using a two-blade T-Motor 17x5.8 inch UAV rotor. The following parameters are varied:

- shape of the blocking body

  cyl: cylinder

  cub: cuboid with constant quadratic cross section and rounded edges $\frac{r}{a} = 0.1$

  pyr: truncated pyramid with quadratic cross section and rounded edges $\frac{r}{a} = 0.24$

- $\frac{z}{R}$: distance of rotor plane to blocking object, normalized by rotor tip radius R, < 0 if the blocking body is on the inflow side of the rotor
- $DL = \frac{T}{A}$: disk loading by variation of rotor thrust

Even for the highest disk loading, the Reynolds numbers on the bodies stay below 10^5, meaning subcritical flow for the rounded bodies is present. As only one load cell is available at the base of the extension, unblocked reference measurements are performed. All test points are averaged over a 10 s recording interval and offset with the stopped rotor reading.

Figure 4.10 depicts the blocking coefficient dependent on the rotor-object spacing for the different

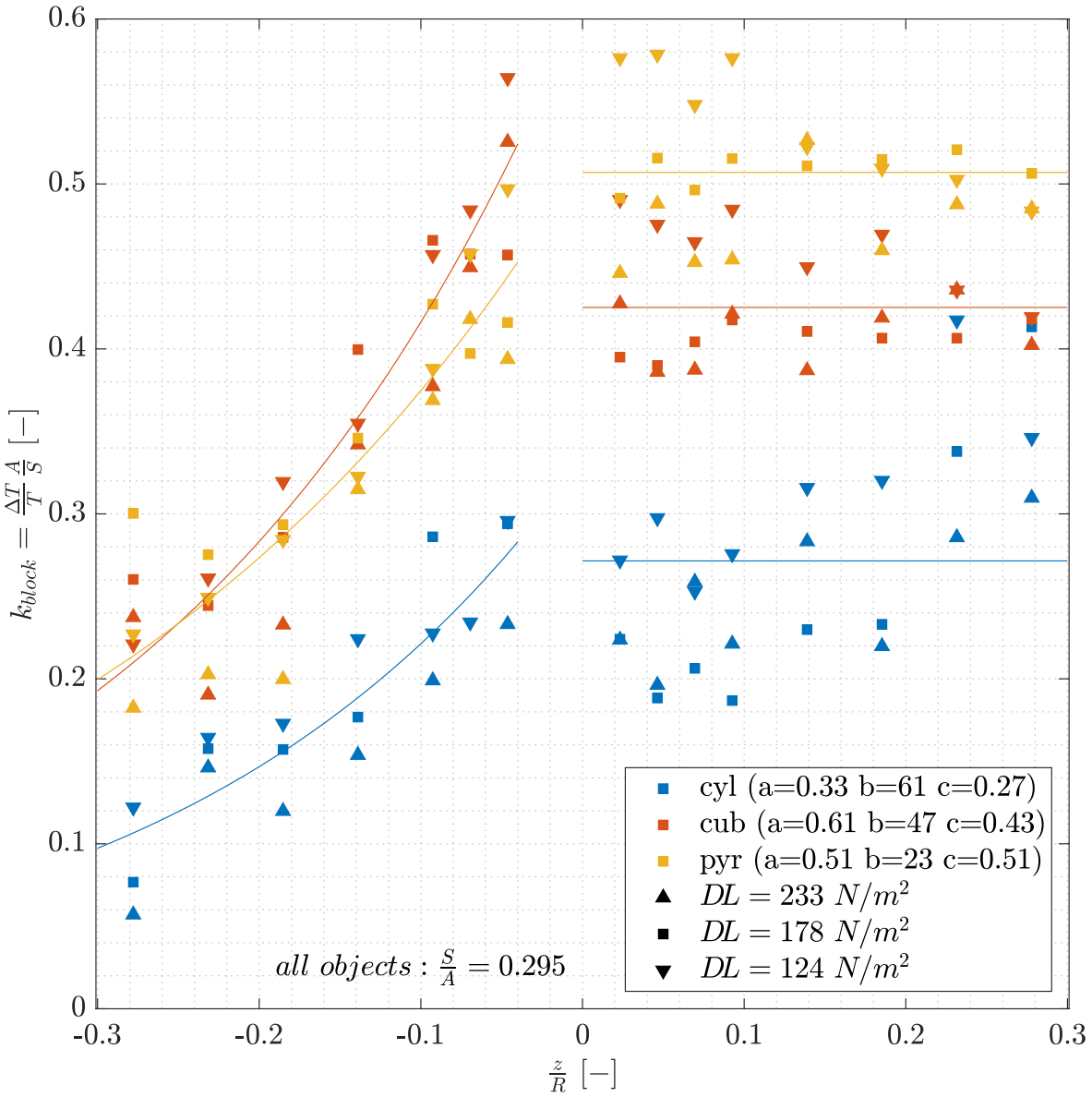

Figure 4.10: Measurement results on thrust loss due to rotor slipstream blocking.

$$\text{fitted model: } k_{block} = \begin{cases} ab^{\frac{|z|}{R}} & \text{for } \frac{z}{R} < 0 \\ c & \text{for } \frac{z}{R} > 0 \end{cases} \tag{4.36}$$

object shapes and disk loadings. Blocking downstream of the rotor is mostly independent of the spacing. This suggests that f_S- and f_v-effects mostly cancel each other. Only the cylinder data show an increase with spacing. A modeling independent of the spacing as proposed by Johnson (2013, pp. 149) seems reasonable. Equation 4.36 together with the coefficients in the legend of fig. 4.10 describe the empirical fit to the measurement data. Using eq. 4.35, the measurements agree with typical drag coefficients of $c_{D,cyl} \approx 1.1$ and $c_{D,cub/pyr} \approx 1.7$ (Hoerner 1965, chap. 3-13, fig. 23). For the pyramid, the blocking area increases along the rotor radius. The higher slipstream velocity at more outboard annuli cause the slightly higher blocking coefficient compared to the cuboid. The blocking coefficients for objects on the inflow side of the rotor significantly

decrease with spacing. The levels close to minimal possible spacing are equal or higher than for the tractor arrangement. A significant increase in rotor noise indicates pressure effects acting besides the parasitic drag. The f_v-reduction seems to dominate the f_S increase. Lower disk loading tends to result in higher blocking coefficients. Based on Hoerner (1965, chap. 3-8, fig. 10), this however should not be a Reynolds number effect. In general, the electric power consumption is not measurably influenced by slipstream blocking.
The installation degradation factors $\eta_{inst,hpt,h}$ and $\eta_{inst,dmpt,h}$ in fig. 5.7 show the remaining portion $1 - \frac{\Delta T}{T}$ of rotor thrust for exemplary configurations.

4.9.1.3 Cruise Condition

The thrust requirement for the cruise phases $i = c, cc, cd, fc$ calculates with

$$T_{ij} = \frac{D_j + m\ g\ \frac{\dot{h}_j}{v_j}}{n_{pwtr,i}}\ f_{Tshare,i} \tag{4.37}$$

$$D_j = \frac{\rho_j}{2}\ v_j^2\ c_{D,j}\ S \tag{4.38}$$

Thrust blocking is not considered in cruise, but installation losses due to non-uniform inflow. Mainly pusher arrangements behind wings or at the end of fuselages suffer from that. Table 4.4 gives the knock-down factors f_{inst}. Wilson (1942), Taylor (1968), Roskam & Lan (1997) provide measurements and notes on the impact of propeller efficiency in pusher arrangements. The low drag coefficient of UAV wing sections with long laminar flow and low chord lengths might mitigate fluctuations in propeller inflow and therefore tend to show lower knock-down factors than with the larger aircraft of the above references. Additionally, the minimum distance between propeller plane and trailing edge is set to 0.75 of the upstream wing chord which helps to even out wake buckets.

Table 4.4: Cruise efficiency knockdown factors due to propeller location

propeller location	knockdown factor f_{inst}
at end of fuselage	0.95
behind wing	0.97
at wingtip	0.985
upstream of fuselage or wing	1

Again, an approach close to Serokhvostov & Churkina (2011) is used to derive propeller coefficients from pitch and diameter. Unlike them, propeller efficiency is directly fitted instead of the power coefficient c_P to obtain better accuracy. Fits are made on an applicable excerpt (APC electric and APC sport propeller series) of the database of Brandt et al. (2020). The thrust coefficient c_T can be well modeled as linear for advance ratios J close to the advance ratio of zero thrust J_0 (see eqs. 4.43 and 4.44). Figure 4.11b shows that the region of good model agreement matches with the intended operating region of high propeller efficiency. For the investigated brands of propellers, a clear linear correlation between J_0 and the pitch-to-diameter ratio $\frac{p}{d}$ is evident (see

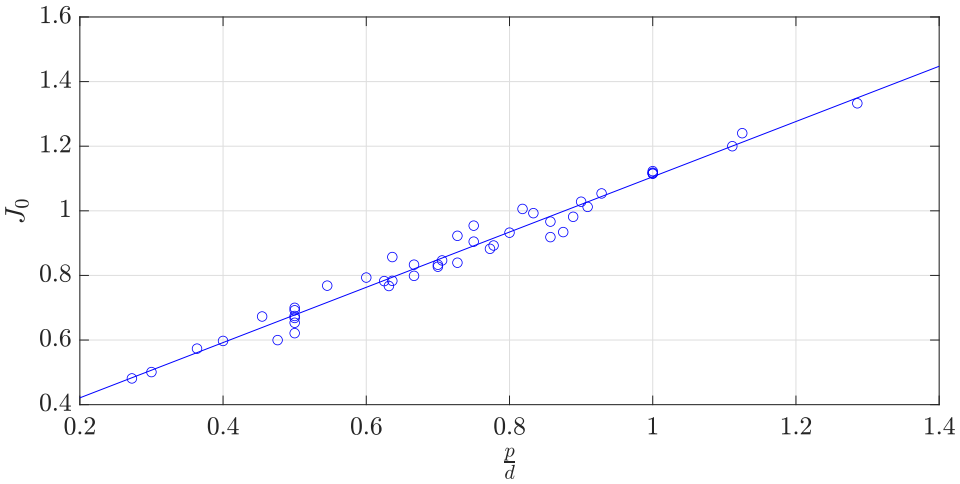

(a) Fit of zero thrust advance ratio J_0 vs. pitch-to-diameter ratio $\frac{p}{d}$

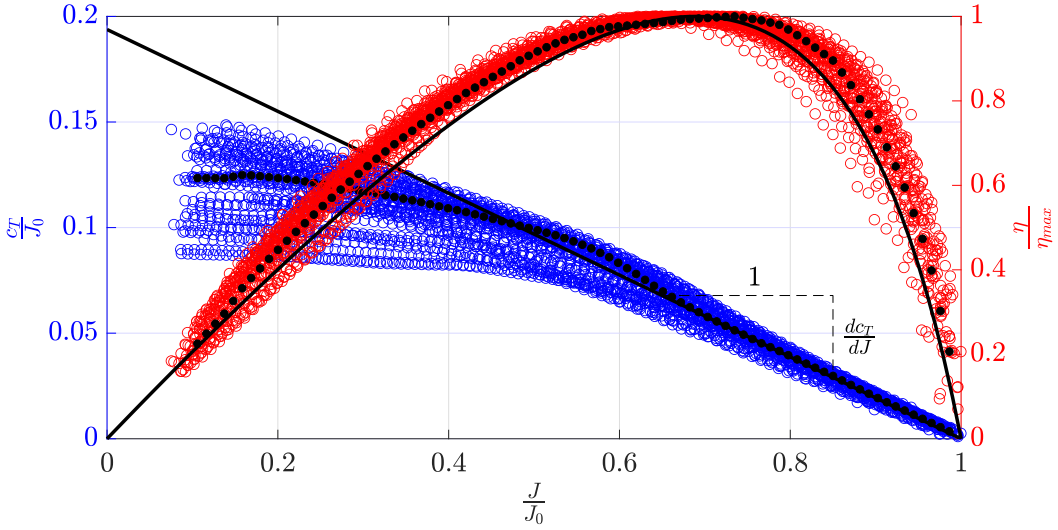

(b) Normalized measurements of thrust coefficient c_T and propeller efficiency η and their models. The black lines model the measurement data of an exemplary propeller (black dots).

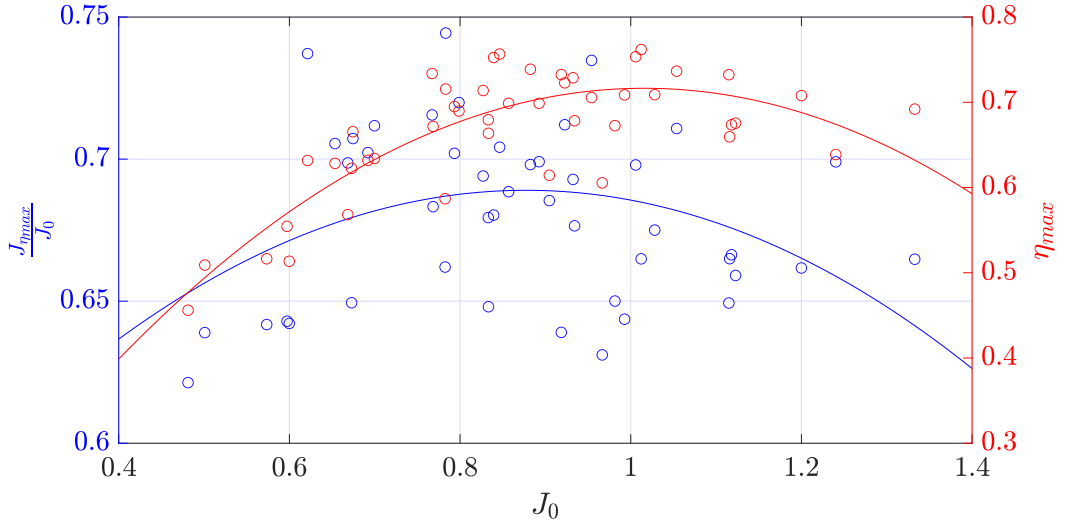

(c) Measurements and data fits for propeller efficiency modelling

Figure 4.11: Fits derived from propeller measurement data of the brands *APC electric* and *APC sport*

$$J_0 = 0.8553 \ \frac{p}{d} + 0.25 \tag{4.39}$$

$$\frac{\mathrm{d}c_T}{\mathrm{d}J} = -0.1938 \tag{4.40}$$

$$\frac{J_{eta,max}}{J_0} = -0.2297 \ J_0^2 + 0.4032 \ J_0 + 0.5121 \tag{4.41}$$

$$\eta_{max} = -0.8383 \ J_0^2 + 1.703 \ J_0 - 0.1483 \tag{4.42}$$

Figure 4.11: Fits derived from propeller measurement data of the brands *APC electric* and *APC sport*

fig. 4.11a). Only minor deviations among the investigated propeller brands occur due to their similarity in blade aspect ratio, solidity, twist/chord distributions and used airfoils. This may be an inherent result of optimization for efficiency under similar boundary conditions (e.g. materials, flight regimes). Figure 4.11b justifies that a single slope $\frac{\mathrm{d}c_T}{\mathrm{d}J}$ may represent the entire range of propeller data. Normalizing propeller efficiency η to η_{max} reveals a similar behavior throughout the entire database. The used shape function in eq. 4.45 (which is similar to the one used for electric motor efficiency modeling in section 4.9.2) requires the coordinates of the peak efficiency point $\frac{J_{eta,max}}{J_0}$ and η_{max}. Again, curve fits were generated in fig. 4.11c. Due to the scatter of data, a simple constant value for $\frac{J_{eta,max}}{J_0}$ may alternatively be considered instead of a polynomial. The black line (model) versus the black dots (measurement points) in fig. 4.11b illustrate the model quality for an exemplary propeller in the database.

$$J_{ij} = \frac{v_j}{n_{ij} \ d_i} \tag{4.43}$$

$$c_{T,ij} = \left.\frac{\mathrm{d}c_T}{\mathrm{d}J}\right|_i (J_{ij} - J_{0,i}) \tag{4.44}$$

$$\eta_{ij} = \frac{\left.\frac{J}{J_0}\right|_{ij}}{2 \ \left.\frac{J_{eta,max}}{J_0}\right|_i - 1 + \frac{\left(\left.\frac{J_{eta,max}}{J_0}\right|_i - 1\right)^2}{1 - \left.\frac{J}{J_0}\right|_{ij}}} \ \eta_{max,i} \tag{4.45}$$

$$\eta_{ij,inst} = f_{inst} \ \eta_{ij} \tag{4.46}$$

Measurement data analysis revealed the pitch-to-diameter ratio to be a meaningful parameter to derive propeller coefficients. The obtained propeller coefficients enable a more differentiated evaluation of operating points as well as powertrain component matching than simple momentum theory would. Also, the trade-off in propeller design for dual-mode powertrains, which have to operate in static thrust and high inflow airspeed velocities, can be covered. This raises the fidelity in powertrain efficiency prediction which is a crucial parameter for overall aircraft performance. The database fits form a model of a generic propeller family with arbitrary diameter and pitch and consistent efficiency levels. This removes discretization artifacts that disturb the comparison

of aircraft configurations. Accordingly, the approach is less suited for detailed aircraft design and even not capable of detailed propeller analysis. The averaging character of data fits lets the model tend to be conservative in terms of predicted efficiency. Real propellers that provide the assumed performance hence should be manufacturable. The amount of input data for the fits is low compared to propeller coefficient data tables or input datasets for blade element methods. With regard to computational effort, the presented propeller model settles between momentum theory and blade element methods (Leishman 2017, p. 115-170).

4.9.1.4 Wingtip Propulsion

The placement of a propeller inside the wingtip vortex can harvest performance benefits from flow interaction. Propeller swirl and wingtip vortex must roughly be concentric and have opposite direction of rotation. The following effects are considered to contribute to the performance benefit:

- The superposition of propeller swirl and the vortex system of the wing reduces the lift-induced downwash velocity. Induced drag is therefore decreased (Patterson & Bartlett 1987). This effect is applicable to both tractor and pusher configurations.
- The wing section behind the propeller experiences higher angles of attack due to the upwash of the inboard-up rotating propeller swirl. This rotates the resultant wing section force vector forward, such that a thrust component emerges in the wing's coordinate system (Veldhuis 2005, p. 38-41). This is commonly referred to as swirl recovery. If the wing is also affected by the swirl downwash of the outer propeller half, this effect is reduced. As no swirl is present in front of the propeller plane, this effect only applies to tractor arrangements.
- A propeller operating in a counter-rotating flow field, e.g. of a wingtip vortex, achieves the same thrust and torque at lower rotational frequency as in a flow field without rotation. This leads to a lower required shaft power for the same propulsive power. Patterson & Bartlett (1987) furthermore argues with a rotation of the blade force vector that increases the force component in the direction of thrust. To operate inside the wingtip vortex, the propeller must be arranged as pusher behind the wing.

Very insightful literature (Snyder 1967, Snyder & Zumwalt 1969, Dimchev 2012, Patterson & Bartlett 1987, Nootebos 2018, Stokkermans et al. 2019, Janus et al. 1996) can be found on wind tunnel measurements and CFD analysis. Borer et al. (2017) reviews approaches for aero-propulsive performance prediction in the course of the design of NASA's X-57 distributed electric propulsion aircraft. Miranda & Brennan (1986) use a vorticity tube model for the propeller that is incorporated in the evaluation of the overall induced flow field of the wing. Applying Munk's Stagger Theorem, they show that the efficiency benefit of wingtip propulsion is the same for pusher and tractor arrangement from a potential flow perspective. Stoll & Veble Mikic (2016) or Stahl & Hornung (2020) use simple semi-empirical approaches with minimal input requirements, but also low levels of fidelity and validation.

In the design tool chain, for each tractor and pusher arrangement, one model with applicability in early conceptual design is implemented. The goal is to get a rough indication about the benefit of wingtip propulsion with minimal input. Simplifications are extensively used. The proposed models must be considered as ideas upon more thorough validation.

For the tractor arrangement, the swirl recovery effect is implemented. The lift vectors dL on the wing section, which is wetted by the propeller slipstream, are considered to be rotated forward by the increased angle of attack α_{sw} (see fig. 4.12). Miranda & Brennan (1986) find that an elliptical span load distribution is close to the optimal span load distribution for wingtip propulsion. So, an easy-to-describe elliptic lift distribution can be used with good justification. Twist or changed airfoil camber is likely required to maintain this span load distribution despite the increase of axial airflow v_{ax} and angle of attack inside the propeller slipstream. Other force components are considered unchanged due to small-angle approximation. The swirl induced thrust component T_{sw} is bookkeeped as an increase in propeller efficiency. Scrubbing drag over the wingtip segment is considered in the wing drag calculation. In eq. 4.53, Patterson et al. (2016), Patterson (2016) provide a calculation approach for the swirl induction factor a_{tan} under the hypothesis of a constant axial velocity distribution at the propeller disk (which means a constant axial induction factor $a_{ax}(r)$).

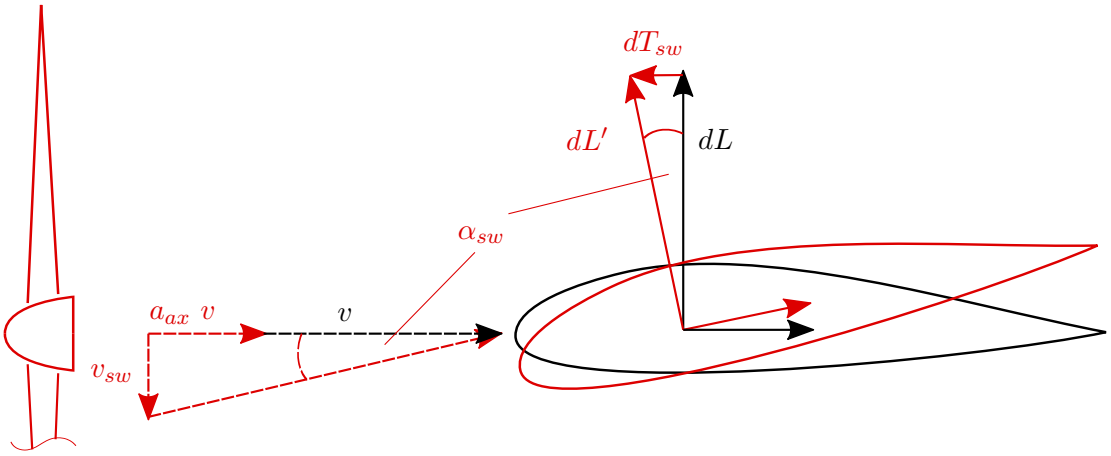

Figure 4.12: Wing section to illustrate swirl recovery with tractor wingtip propulsion (red color if affected by slipstream)

$$\frac{\eta_{sw}}{\eta} = \frac{T}{T - T_{sw}} \tag{4.47}$$

$$T_{sw} \approx 2 \int_{-r_{tip}}^{r_{hub}} \frac{\mathrm{d}L}{\mathrm{d}y}\ \alpha_{sw}\ dy \text{ with } \alpha_{sw} \approx \frac{v_{sw}}{v_{ax}} \tag{4.48}$$

$$\frac{\mathrm{d}L}{\mathrm{d}y} = \rho\ v\ \Gamma_0 \sqrt{1 - \left(\frac{2\ y}{b}\right)^2} \text{ with } \Gamma_0 = \frac{4\ m\ g}{\rho\ v\ b\ \pi} \tag{4.49}$$

$$v_{ax} = v\ \ (1 + a_{ax}) := \text{constant} \tag{4.50}$$

$$v_{sw} = 2\ \pi\ rps\ r\ a_{tan} \tag{4.51}$$

$$a_{ax} = \frac{v_{ind}}{v} = 0.5\sqrt{\frac{2\ DL}{\rho\ v^2} + 1} - 0.5 \tag{4.52}$$

$$a_{tan} = \frac{1 - \sqrt{1 - \frac{4\ v^2(1+a_{ax})\ a_{ax}}{(2\ \pi\ rps\ r)^2}}}{2} \quad \text{valid if } \mathrm{Im}(a_{tan}) = 0 \tag{4.53}$$

For the pusher arrangement, the counter-rotation of the propeller inflow is modeled. To avoid the necessity of a blade element method, a rigid body rotation around the propeller axis is considered for the inflow velocity field. Under this assumption, the turning frequency of the propeller rps_{prop} can be reduced by the turning frequency of the inflow rps_{in} while maintaining the same thrust and torque as without inflow rotation. The reduction in power scales with the reduction in the propeller's angular velocity, and so does the propeller efficiency.

$$rps_{prop} = rps_{eff} - rps_{in} \tag{4.54}$$

$$\frac{\eta'}{\eta} = \frac{\frac{T'\ v}{2\pi\ Q'\ rps'_{prop}}}{\frac{T\ v}{2\pi\ Q\ rps_{prop}}} = \frac{rps_{prop}}{rps'_{prop}} = \frac{rps_{eff}}{rps_{eff} - rps_{in}} \text{ with } Q' = Q,\ T' = T \tag{4.55}$$

$$v_{tan} = \frac{\Gamma}{2\ \pi\ r} \tag{4.56}$$

$$\Gamma = k_\Gamma \frac{L}{\rho\ v\ b} \tag{4.57}$$

$$rps_{in} = \frac{v_{tan}(k_R R)}{2\pi\ R} \tag{4.58}$$

$$\left(\frac{\eta'}{\eta}\right)^{-1} = \frac{P'_{shaft}}{P_{shaft}} = 1 - \frac{1}{\pi}\frac{k_\Gamma}{k_R}\frac{c_L}{AR}\frac{\lambda}{\delta} \text{ with } \delta = \frac{4R}{b},\ \lambda = \frac{v}{2\pi\ rps\ R} \tag{4.59}$$

A most simple representation of a wing's near field wake can be modeled with a single horseshoe vortex. Its vertical wake velocity components v_z is shown in fig. 4.13. If one neglects the influence of the opposite vortex filament (due to its rapid velocity decrease with distance), a tangential velocity v_{tan} within a potential vortex of circulation Γ and orthogonal distance r from the filament

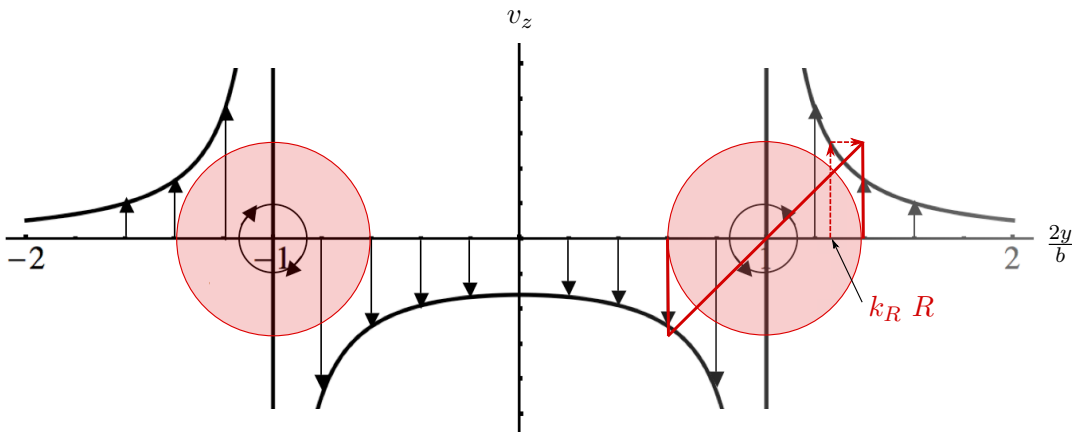

Figure 4.13: Wing flow field affecting the propeller inflow as present in a single horseshoe vortex model (view from behind the wing, propeller disks in red)

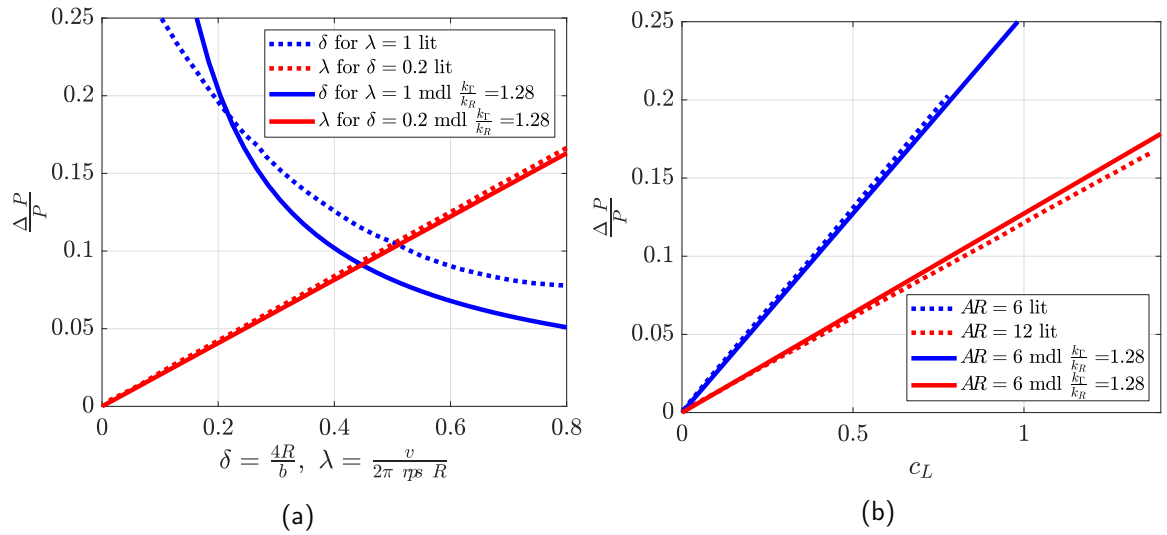

Figure 4.14: Validation and calibration of the derived model (mdl) for power savings due to wingtip pusher powertrains with data (lit) of Miranda & Brennan (1986)

is given by eq. 4.56. A location $r = k_R R$ must be selected to transform the vortex flow field into a rigid-body rotation which has an equivalent effect in terms of propeller performance. Therefore, the vortex's tangential velocity at the location $k_R R$ is considered to be present at the propeller tip radius and linearly decreases to zero towards the propeller center. For $k_R < 1$, the velocity differences of the rigid rotation and the potential vortex switch sign within the propeller radius. Hence, values of $k_R < 1$ are expected as overspeed and speed deficit cancel and lead to the same effect on the propeller rpm. The circulation Γ can be derived from wing lift and airflow conditions. k_Γ describes which portion of the horseshoe vortex circulation acts at the vortex that is used to describe the propeller inflow. Here, values of $k_\Gamma < 1$ are expected as the vortex circulation just behind the wingtip trailing edge should be smaller than the average circulation of the wing. Data from Miranda & Brennan (1986) is used in fig. 4.14 to validate the model and calibrate the factor $\frac{k_\Gamma}{k_R}$. With regard to its simplicity, the model shows good agreement. Deviations are conservative for $\delta > 0.2$. A value of $\frac{k_\Gamma}{k_R} = 1.28$ is within the expected range.

The propeller's counter-rotating swirl furthermore mitigates the intensity of the vortex system. The resultant reduction in induced drag is not considered in any of the presented methods.

4.9.2 Electric Motor

To calculate the efficiency η of the motor dependent on its operating condition with shaft torque Q and turning frequency $\eta ps = \frac{\omega}{2\pi}$, a discrete current motor model based on three motor parameters and the governing equations eqs. 4.60, 4.61 and 4.63 as presented in Faulhaber (2020), Drela (2005), Schenk (2014) is used. See fig. 4.15 for a normalized form of the motor model. For a fair comparison of aircraft configurations, their motors shall all exhibit similar quality. Therefore, the equations were inversely solved to calculate the motor parameters k_Q (torque constant), R (ohmic resistance) and $\mu = \frac{R}{k_Q^2} k_{fricf}$ (friction constant) from a common peak efficiency η_{max} and

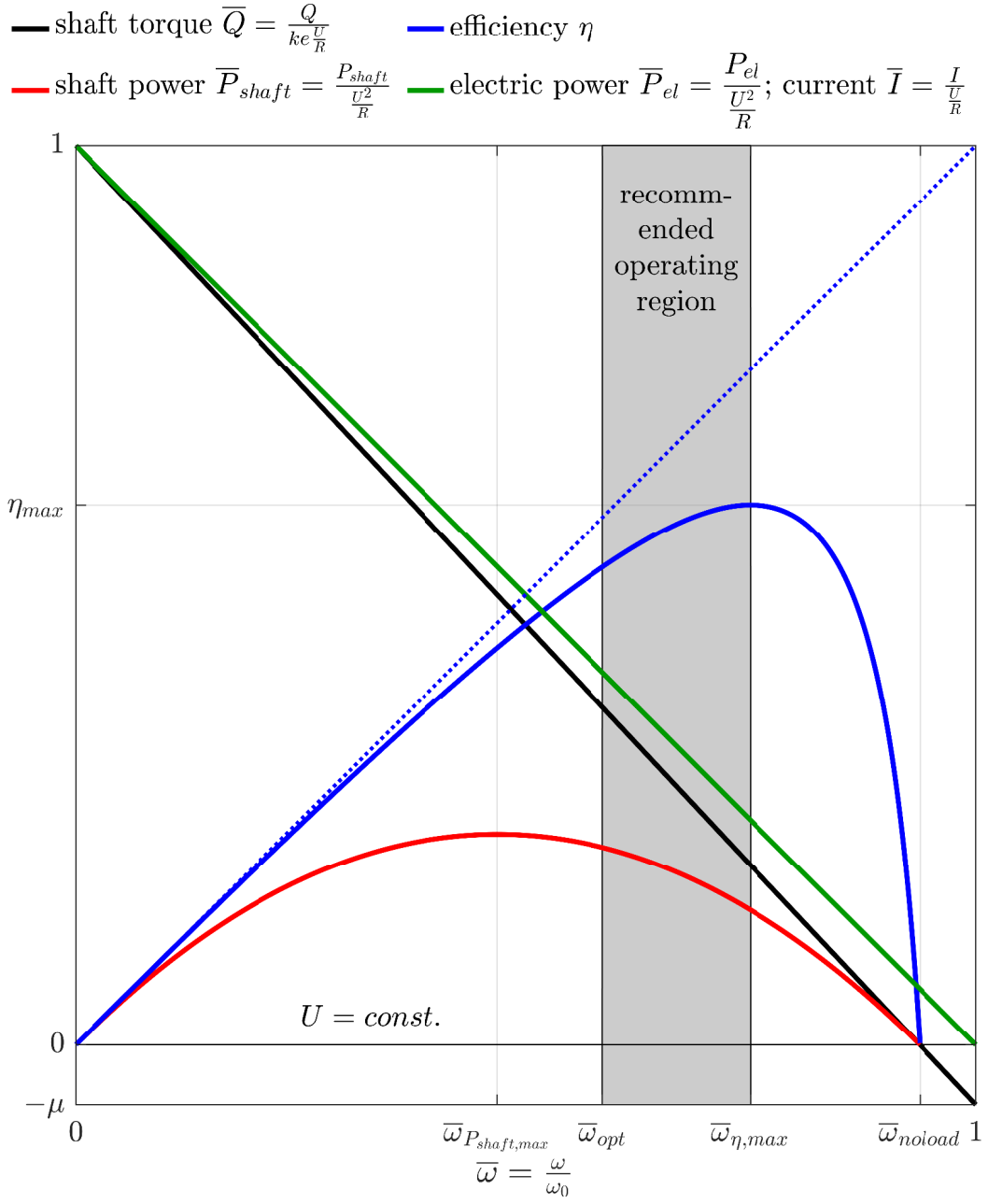

Figure 4.15: Normalized electric motor model

a minimum relative turning speed $\overline{\omega}_{min}$ (see eqs. 4.64 and 4.68) above which every operating point j shall take place. Note that the friction constant μ is defined slightly different from the usually used k_{frict}. The parameter $\overline{\omega}_{min}$ trades the efficiency at the operating conditions against the motor size. It is therefore open for optimization for each of the present powertrain types i. It is recommended to choose every operating point j between the so called optimal point $\overline{\omega}_{opt}$ (eq. 4.77) and the point of maximum efficiency $\overline{\omega}_{\eta,max}$ (eq. 4.76), but definitely not lower than the point of maximum shaft power $\overline{\omega}_{P_{shaft,max}}$ (eq. 4.79) (Schenk 2014, p. 13). δ is the ratio between the motor operating voltage U_{ij} provided by the electronic speed controller and the battery voltage U_{bat} (eq. 4.65). The $()_0$ subscript indicates the zero-load condition of the frictionless motor ($\mu = 0$).

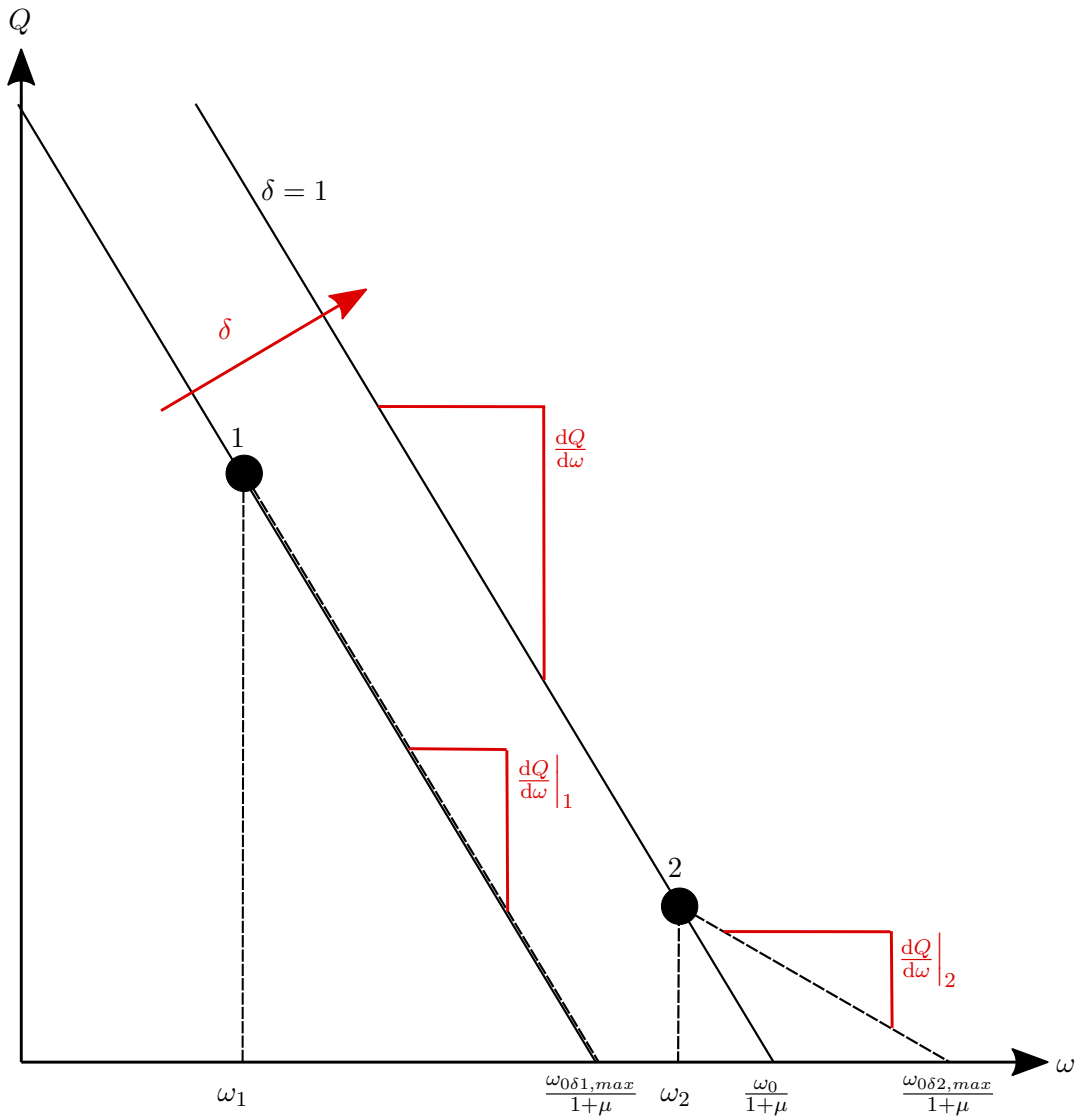

Figure 4.16: Diagram to explain the calculations on the electric motor model

$$U_{ij} = k_{Q,i}\omega_{ij} + R_i I_{ij} \tag{4.60}$$

$$Q_{ij} = k_{Q,i}\ I_{ij} - \mu_i \frac{k_{Q,i}^2}{R_i}\omega_{ij} \tag{4.61}$$

$$Q_{ij} = k_{Q,i}\frac{U_{ij}}{R_i} - \frac{k_{Q,i}^2}{R_i}\left(1+\mu_i\right)\omega_{ij} = \tag{4.62}$$

$$= k_{Q,i}\frac{U_{ij}}{R_i}\left(1-\left(1+\mu_i\right)\overline{\omega}_{ij}\right) \tag{4.63}$$

$$\overline{\omega}_{ij} = \frac{\omega_{ij}}{\omega_{0\delta ij}} \tag{4.64}$$

$$\delta_{ij} = \frac{U_{ij}}{U_{bat}} \tag{4.65}$$

$$\mu_i = \frac{\left(\eta_{max}-1\right)^2}{4\ \eta_{max}} \tag{4.66}$$

$$\overline{\omega}_{noload} = \frac{\overline{\omega}_{0\delta ij}}{1+\mu_i} \tag{4.67}$$

$$\overline{\omega}_{ij} \overset{!}{>} \overline{\omega}_{min,i} \tag{4.68}$$

$$\left.\frac{\mathrm{d}Q}{\mathrm{d}\omega}\right|_{ij} = -\frac{Q_{ij}}{\omega_{ij}\left(\frac{1}{\overline{\omega}_{min,i}(1+\mu_i)} - 1\right)} \tag{4.69}$$

$$\left.\frac{\mathrm{d}Q}{\mathrm{d}\omega}\right|_{i} = \min\left(\left.\frac{\mathrm{d}Q}{\mathrm{d}\omega}\right|_{ij}\right) \tag{4.70}$$

$$\omega_{0\delta ij} = \left(\omega_{ij} - \frac{Q_{ij}}{\left.\frac{\mathrm{d}Q}{\mathrm{d}\omega}\right|_{i}}\right)(1+\mu_i) \tag{4.71}$$

$$\omega_{0i} = \max\left(\omega_{0\delta ij}\right) \tag{4.72}$$

$$k_{Q,i} = \frac{U_{bat}}{\omega_{0,i}} \tag{4.73}$$

$$R_i = -\frac{k_{Q,i}^2}{\left.\frac{\mathrm{d}Q}{\mathrm{d}\omega}\right|_{i}}(1+\mu_i) \tag{4.74}$$

$$\eta_{ij} = \overline{\omega}_{ij}\left(1 - \frac{\mu_i\ \overline{\omega}_{ij}}{1-\overline{\omega}_{ij}}\right) \tag{4.75}$$

$$\overline{\omega}_{\eta_{max}} = \frac{-\sqrt{\mu_i^2+\mu_i} + \mu_i + 1}{\mu_i + 1} \tag{4.76}$$

$$\overline{\omega}_{opt} = \frac{0.625}{(1+\mu_i)} \tag{4.77}$$

$$P_{shaft,ij} = \frac{U_{ij}^2}{R_i}\overline{\omega}_{ij}\left(1 - \overline{\omega}_{ij}\left(1+\mu_i\right)\right) \tag{4.78}$$

$$\overline{\omega}_{P_{shaft,max}} = \frac{0.5}{(1+\mu_i)} \tag{4.79}$$

$$P_{el,ij} = \frac{U_{ij}^2}{R_i}\left(1 - \overline{\omega}_{ij}\right) \tag{4.80}$$

The sizing process starts at eq. 4.66 which calculates the friction constant μ directly from the maximum motor efficiency η_{max}. The condition in eq. 4.68 leads to a maximum ideal no load turning speed $\omega_{0\delta max}$ for each operating point, which in turn defines a minimum motor stiffness $\left|\frac{\mathrm{d}Q}{\mathrm{d}\omega}\right|_{min}$ (absolute values are used in the context of motor stiffness). To fulfill eq. 4.68 for all operating points with the same motor, the maximum motor stiffness must be chosen (which means a minimum for the negative slope $\frac{\mathrm{d}Q}{\mathrm{d}\omega}$ in eq. 4.70). Now, all idle turning frequencies, duty cycles, relative turning frequencies, operating efficiencies, electric input powers and motor constants can be calculated using the remaining equations. To provide the desired performance, the calculated motor constants must be present at the actual operating motor temperature. Based on a conservative user input for the motor temperature, the equivalent motor parameters at ambient temperature as given in data sheets can be calculated using linear temperature coefficient corrections for R and k_Q (Faulhaber 2020). The presented inverse design approach however assumes all operating conditions of one powertrain to take place at the same motor temperature. This certainly deviates from reality.

The advantages of this motor modeling approach are similar with those of the propeller or rotor. Motors are available in arbitrary sizes and peak efficiency is constant. Discretization artifacts do

not hamper the configuration evaluation by the choice of different motor individuals. Furthermore, only few and well perceptible input data are required. Nevertheless, the variation in efficiency of matched propeller-motor operating points is possible and improves the fidelity of the powertrain performance prediction.

The presented approach can also be used to preselect motors with similar motor constants from a database, in order to reduce the number of motor-propeller combinations put through the conventional try-and-error matching process.

4.9.3 Electric Speed Controller

There is no common practice in literature on how to model an ESC, as there is for the electric motor. Its behavior depends on too many product-specific parameters, such as hardware, software and motor interaction effects. Among many other, Gong et al. (2017), Green (2015), Lundström et al. (2010), Roessler (2012) performed measurements on the efficiency of electronic speed controllers. Gong et al. (2017), Green (2015) measure the electric in- and output power while Lundström et al. (2010), Roessler (2012) measure motor shaft power against ESC electric input power on motor-ESC drive trains under different input voltages and throttle settings. Their derived efficiencies include losses in the motor introduced by part throttle operation and may hence be more realistic. The wording 'drive train part throttle efficiency' might be more adequate. Both find a major, nearly linear dependence of the ESC efficiency on the throttle setting for the predominant operating

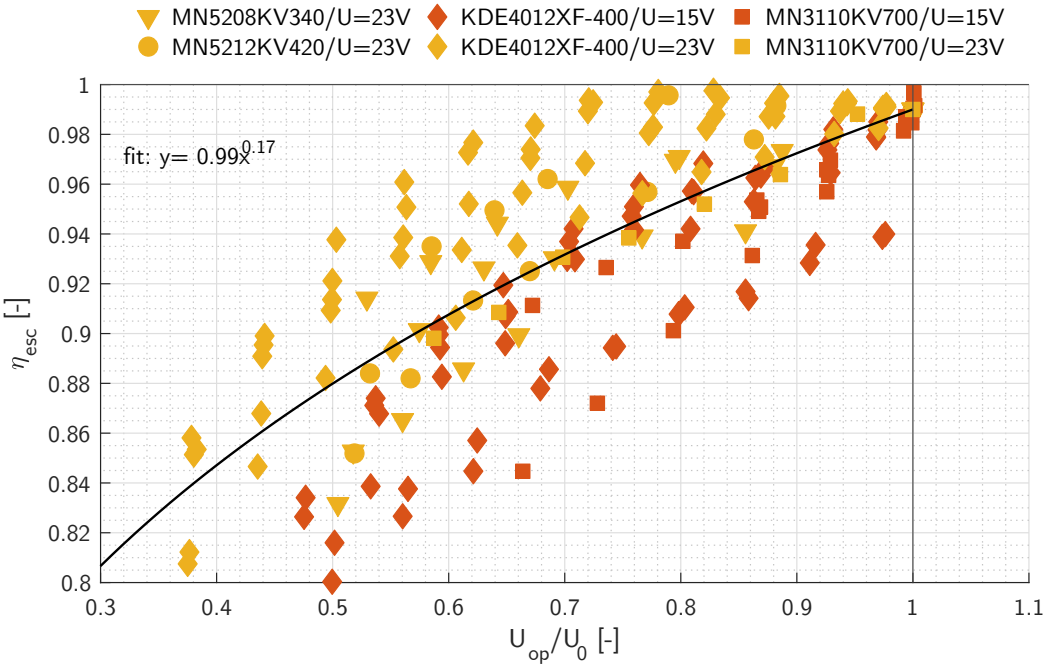

$$\eta_{ESC} = 0.99\ \delta^{0.17} \tag{4.81}$$

Figure 4.17: ESC model derived from dynamometer measurements on motor-ESC-combinations (excerpt of database)

conditions. Lundström et al. (2010) finds very similar part throttle efficiencies for various ESC and operating conditions on the same motor. A main factor that changes the part throttle efficiency curves is the attached motor. Roessler (2012)'s model uses ESC specific factors to describe the part throttle behavior. His model requires to calculate the full throttle powertrain efficiencies to obtain part throttle efficiencies. Both find individual ESC diverging significantly from their suggested models. Gong et al. (2017) uses a physics based modeling (Yao et al. 2013) to identify a shape function and fits it to experimental data with good success. The derived parameters however are inconsistent with the major forms of power loss he suspected and modeled. A validation of combined motor-ESC efficiency is not provided.

Based on manufacturer provided dynamometer measurements of 25 powertrains (KDE Direct 2020, T-Motor 2020) and the beforehand described motor model, an empirical part throttle efficiency model is derived. It considers the ESC as a voltage regulator whose efficiency depends on the voltage ratio between output and input voltage δ (eq. 4.65). The obtained model (eq. 4.81 and fig. 4.17) averages the part throttle efficiency throughout a variety of voltage, motor, ESC and load combinations. Its simplicity and generality is tailored to comparative conceptual aircraft design. It furthermore agrees with Lundström et al. (2010)'s findings in shape and magnitude.

4.10 Mass Calculation

Masses are calculated for major systems and components of a fixed-wing electric VTOL aircraft, such as

- wing, empennage, fuselage, nacelle and landing gear structures
- powertrain components
- actuators
- wire harness

Systems for control and communication, navigation and flight control computing together make up for a fixed mass fraction of 4% of the total aircraft mass. Another 4% is reserved for miscellaneous items. The applied methods are presented in the following.

4.10.1 Powertrain Components and Actuation

For UAV propellers and rotors, Tyan et al. (2017) provides an empirical mass estimation method. Motor and ESC masses can be estimated after Gundlach (2012, p. 193,212). From the compiled powertrain database, mass models specifically for the UAV size of this study are generated. Figure 4.18 illustrates the quality of the data fits. The motor mass is calculated based on torque density. For comparison, the motor's power density is as well depicted.
Using a constant power density for the ESC is justified by the database values.
Propeller and rotor mass for sUAS can be well modeled using only the diameter as input.

Wire harness mass is a relevant mass item for electric distributed propulsion aircraft. It is derived

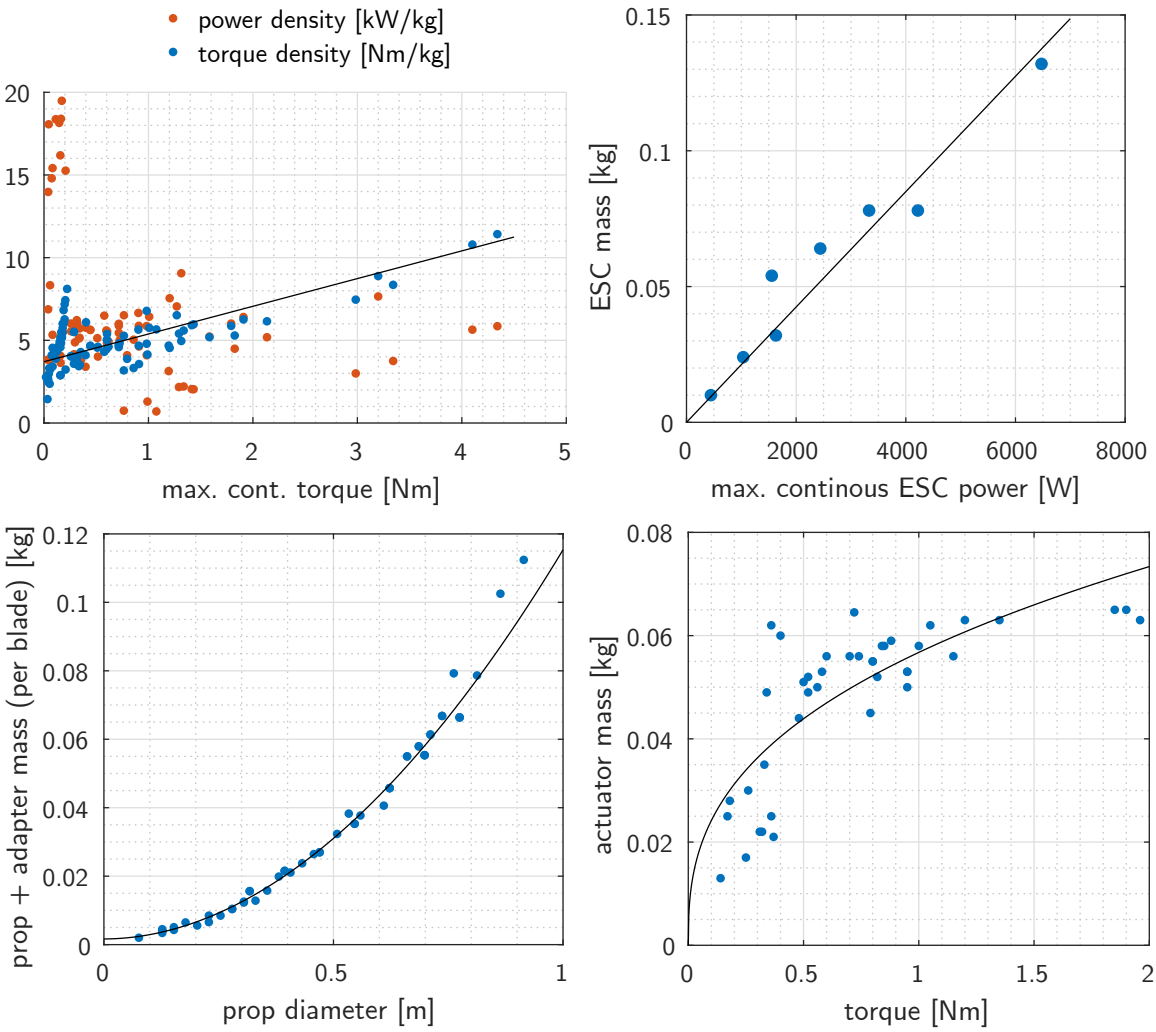

$$\frac{Q_{max}}{m_{motor}} = 3.707 \frac{\text{N m}}{\text{kg}} + 1.671 \frac{1}{\text{kg}} \, Q_{max} \tag{4.82}$$

$$m_{ESC} = f_{marg} \; 2.124 \times 10^{-5} \frac{\text{kg}}{\text{W}} \, P_{in,max,cont} \text{ with } f_{marg} = 1.3 \tag{4.83}$$

$$m_{prop,adapt} = n_{blades} \left(0.1137\,\text{kg} \left(\frac{d_{prop}}{1\,\text{m}} \right)^{1.952} + 0.001656\,\text{kg} \right) \tag{4.84}$$

$$m_{act} = f_{inst} \; 0.0568\,\text{kg} \left(\frac{Q_{act}}{1\,\text{N m}} \right)^{0.371} \text{ with } f_{inst} = 1.5 \tag{4.85}$$

Figure 4.18: Empirical powertrain and actuator mass models

from the individual lengths and wire gauges of the electrical connections for powertrains and actuators. Wire gauge and the mass per length are taken from Oberschwendtner (2019) based on the conducted current and installation situation. 15% mass overhead is considered for cable management and connectors.

Actuator masses m_{act} are calculated with the empirical equation eq. 4.85 based on the torque Q_{act} they need to provide to hold the aerodynamic control surface (Drela 2004) or rotor tilt mechanism. To estimate the mass of tilt mechanics, its components are sized based on the motor dimensions

and maximum thrust (e.g. as in Karpfinger (2018*a*)).

4.10.2 Structural Mass

All major structural components use common construction concepts for fiber reinforced composite materials. Their masses are generally calculated by their volume and density.

The wing and empennage are treated identically. Their structures are decomposed in the sandwich shell of the wing loft and the spar. The closed shell is considered to solely take all torsional loads from the pitching moments of the airfoil sections along the wing. With Bredt's Rule for thin-walled closed shell structures and a requirement for the maximum elastic tip twist at maximum design speed, the shell layup can be sized. The spar is considered to solely take all shear and bending caused by the lift force along the wingspan. For the definition of the load case, a mass-free wing is assumed to either provide a certain lift force (in case of the empennage surfaces) or load factor to the aircraft (in case of the wing). Euler-Bernoulli beam theory is used to size the components of the composite spar for fiber fracture. This approach is well tested on CTOL UAV (Roessler (2012) and many more projects at TUM Institute of Aircraft Design). The resulting wing layup is then simplified for improved manufacturability. Additionally, masses for paint, bonding, ribs, control surface reinforcement and wing connectors are considered based on the specific geometries and typical material densities.

The above, stiffness-neglecting method may lead to aeroelastic or servoelastic issues if heavy powertrains are attached to the wing. As a precaution, additional requirements have to be fulfilled during structural sizing:

- torsion deformation and spar strength under powertrain thrust load

  The above maximum wing twist and spar laminate strength criteria must also be fulfilled under the maximum torsion and bending load that can be generated by the powertrains. The powertrains as well as the wings are considered mass-free for this calculation. Aerodynamic and powertrain loads are checked individually. Superimposed load cases are not implemented.

- first bending mode and torsion mode eigenfrequency

  A simple and adequate method for early conceptual design is to size for natural structural eigenfrequencies. This requirement also tends to shift aeroelastic and servo elastic problems to higher onset speeds and excitation frequencies.

  The wing shell is modeled as a torsion spring up to the spanwise location of the nacelle y_{nac}. The inertia of the fully integrated nacelle $J_{nac,tot}$ is attached to the end of this torsion spring, while its root is considered fixed. Rearranging Hartog & Mesmer (1952, p. 407) allows to calculate the required thickness $t_{tor,freq}$ of the shell from the shear modulus G, chord length c and an airfoil cross-section factor k_{xsect}.

$$t_{tor,freq} = k_{xsect} \frac{\pi^2 \ f_{tor}^2 \ J_{nac,tot} \ y_{nac}}{G \ c^3} \tag{4.86}$$

To evaluate the first bending mode, a cantilever beam up to the spanwise location of the nacelle y_{nac} with height H, width B and Young's modulus E is considered. At the beam's tip, the mass of the fully integrated nacelle $m_{nac,tot}$ and the mass of the wing segment outside the nacelle position $m_{wing,out}$ is attached. The mass of the inner wing $m_{wing,in}$ is evenly distributed along the beam. The wing masses are estimated based on the already calculated sizing criteria. The total wing mass is updated after the bending frequency evaluation. An approximate formulation for the spar height between the top and bottom spar caps $h_{bend,freq}$ after Hartog & Mesmer (1952, p. 407) is

$$h_{bend,freq} = \sqrt[3]{H^3 - \frac{16\ \pi^2\ f_{bend,freq}^2\ y_{nac}^3\ \left(m_{nac,tot} + m_{wing,out} + 0.23\ m_{wing,in}\right)}{E\ B}} \tag{4.87}$$

If one of these requirements is not met, a reinforcement up to the spanwise position of the nacelle is made. The restriction to untapered wings is helpful as the related constant beam cross-section simplifies the equations.

Fuselage and nacelles are basically treated in an identical manner. Their masses build up from paint, composite layers, bonding overlaps and bonding adhesive as well as bulkheads which are sized in an empirical way based on the local fuselage diameter. Fuselages are split in a forward and a rear/tail boom section based on a threshold diameter. The cross-section and monolithic layup in the tail boom section is constant. No bulkheads are used here. As the layup of the fuselage is driven by robustness and stability, the user needs to input an adequate shell thickness. To avoid aeroelastic and servoelastic problems caused by heavy and powerful powertrains mounted to slender fuselage structures, the tail boom is checked to fulfill the following structural requirements:

- allowable bending stress under maximum aerodynamic empennage force, powertrain thrust or landing gear load
- allowed deflection angle at tail boom end due to bending under maximum aerodynamic or powertrain load
- allowable torsion stress under maximum aerodynamic or powertrain load
- allowed twist angle at tail boom end due to torsion under maximum aerodynamic or powertrain load
- minimum torsion eigenfrequency under powertrain, nacelle and tilt mechanism inertia

Bending loads are considered to be taken by unidirectional 0° laminates while torsional loads are taken by ±45° fabrics. The thickness of these two laminates is sized for the above mentioned requirements. The areal weight of the forward fuselage and nacelle layup is a fixed, experience-based value. The nacelle structure is checked to meet the required bending frequency.

4.11 Battery and Endurance Evaluation

The battery is one of the most performance driving systems for electric VTOL aircraft. The following models try to find a good balance of fidelity and effort for the context of conceptual aircraft design.

The implemented battery modeling methods were prepublished in Stahl & Hornung (2020).

4.11.1 Constant Voltage

A basic simplification is to consider the battery as constant voltage source. The voltage at 20% state of charge (SoC) is assumed. This equals the minimum voltage within a discharge cycle in typical operation. Consequently, the voltage drop under increased load (Gundlach 2012, p. 325) is neglected due to this assumption. Correspondingly, the maximum continuous power capability of a battery at 20% SoC is used in the battery model. This ensures that all performance requirements of the aircraft can be fulfilled by the battery at the end of the discharge cycle.

4.11.2 Energy-Power-Trade

As already outlined in section 2.2, the trade between energy density and power density as well as the battery mass fraction are key design drivers. Consequently, a range of battery cell types (see fig. 3.18 and table 4.5) is used to represent the energy-to-power trade that is inherently linked to battery design (Lain et al. 2019). While battery type 1 is still in the prototype phase, the rest is commercially available to date.

Table 4.5: Specifications of implemented battery types (on cell level)

number	-	1	2	3	4	5
category	-	Future High Energy LiS	High Energy LiIon	Intermediate LiIon	High Power LiIon	High Power LiPo
representative	-	Oxis Energy POA000412	Panasonic NCR18650GA	Sony US18650VTC6	Sony US18650VTC5	generic LiPo 40C
mass	g	85	47	46	44	any, in steps of 10
capacity	A h	14.7	3.5	3	2.6	any, in steps of 0.35
nominal voltage	V	2.1	3.6	3.6	3.6	3.7
energy density	$\frac{\text{W h}}{\text{kg}}$	400	260	240	215	135
power density[1]	$\frac{\text{W}}{\text{kg}}$	325	655	1030	1700	4950
reference	-	OxisEnergy (2019)	Panasonic (2020)	Sony (2020*b*)	Sony (2020*a*)	Chanan (2017)

[1] at 20% SoC

The usable energy density of one battery cell type depends on the power drain. Therefore, the battery efficiency η_{bat} relates the usable battery energy due to high power drain with the nominal

battery energy for the hypothetical zero power drain case.

$$\eta_{bat} = \frac{E_{bat}(P)}{E_{bat}(P \to 0)} \tag{4.88}$$

The losses in usable energy are mainly caused by the internal resistance of the battery. Modeling as ohmic losses (Gundlach 2012) or using Peukert's Law (Peukert 1897) is common. Here however, battery efficiencies are derived from discharge curves to cover battery specific characteristics. The applied model uses power drain instead of the usual current drain as the source of usable battery energy degradation. Dependent on the state of charge voltage, the same power can be provided at different currents and affect energy degradation differently. This inaccuracy is compensated by calculating a mean battery efficiency which represents the complete battery discharge cycle.

4.11.3 Discrete Cell Sizing

In the presented conceptual aircraft design tool chain, the battery mass budget $m_{bat,max}$ remains as a residual after subtracting powertrain, system, structural and payload mass items from the total aircraft mass. This budget must be exploited to a best possible extent to maximize onboard energy. Due to the high mass of best-performing battery cells in relation to the battery mass budget of small unmanned aircraft, a battery pack only consists of few parallel cell strings. For example, a representative 5 kg fixed-wing VTOL uses a battery pack in 6s4p configuration. The next bigger 6s5p battery pack means a +25% increase in energy and mass. The feasible steps for the battery mass fraction $\frac{m_{bat}}{m}$ are in the order of 7-8%. A discretization problem with significant impact on the aircraft performance arises. Using cells of smaller unit mass would mitigate this problem. They however tend to have less performance as they show a worse mass ratio of active material and experienced less development progress than more popular battery formats. Additionally, a low nominal cell voltage compared to the powertrain voltage level supports this effect. Conclusively, the batteries are discretely sized respecting possible cell interconnections. Although the popular 'rubber sizing' method (with arbitrarily small steps in battery size) can lead to significant mistakes for the real aircraft, it avoids discretization distortion in an aircraft concept comparison. It is therefore as well implemented for these purposes.

$$m_{bat,max} = m - m_{pyld} - m_{pwtr} - m_{sys} - m_{struct} \tag{4.89}$$

4.11.4 Overpower Capability

Batteries can provide more than their continuous power rating for a limited amount of time. This mitigates an oversizing of the battery for short flight phases like hover climb. An overpower factor f_{ovp} is introduced. One conservative profile for all battery types is derived in fig. 4.19 from distributor specifications (EnerCig 2020*a*,*b*). Overpower capability is mainly driven by temperature and heating rates. Full performance can be harvested using temperature monitoring and battery

type specific overpower profiles.

$$f_{ovp} = \frac{P_{ovp}(\Delta t_{ovp})}{P_{cont}} \tag{4.90}$$

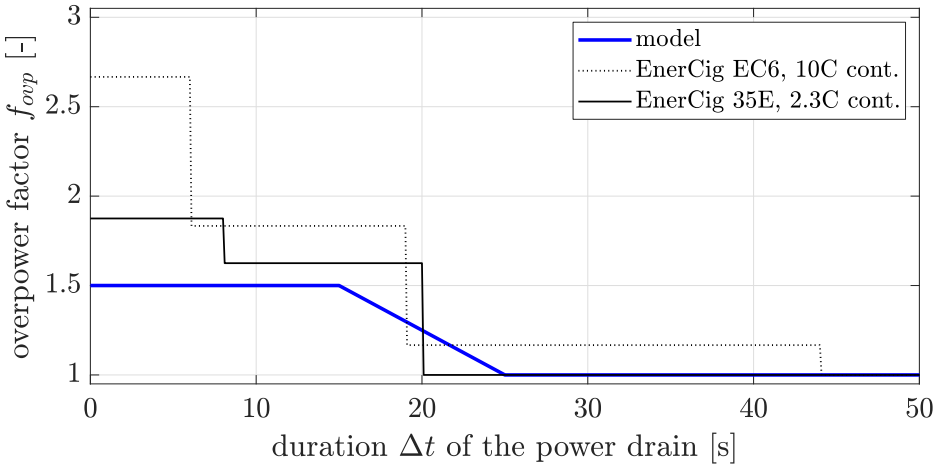

Figure 4.19: Overpower capability of battery cells

4.11.5 Battery Architecture Modeling

The battery architectures presented in section 3.3 are all treated with a similar framework that allows to

- assign different power consumptions to each battery
- share power consumptions among the batteries
- enable and disable energy crossfeed
- insert efficiencies of devices like switches or battery power managements systems

for each mission phase j. Due to the shape of the problem, a 'try and error' approach is used. This means that the discrete combinations of the two batteries $k = 1, 2$ are calculated and checked later for their validity. To reduce the number of battery combinations to be calculated, only parallel cell counts $n_{p,k}$ that fit within the total battery mass budget $m_{bat,max}$ and only reasonable combinations of cell types are considered. For example, battery type 1 must have a higher energy density than battery type 2. Battery masses m_k, nominal battery energy E_k and maximum power capability $P_{max,kj}$ are calculated using

$$m_k = n_{s,k}\ n_{p,k}\ m_{cell,mk}\ f_{pack} \tag{4.91}$$

$$E_k = m_k \frac{e_{cell,mk}}{f_{pack}} \tag{4.92}$$

$$P_{max,kj} = m_k \frac{p_{cell,mk}}{f_{pack}}\ f_{ovp,kj} \tag{4.93}$$

The serial cell count $n_{s,k}$ derives from a predefined powertrain voltage. The factor f_{pack} considers the mass increase for the battery pack assembly. E.g. values of $f_{pack} \approx 1.1 - 1.15$ are adequate for RC hobby grade and manned electric glider battery packs (Thiede et al. 2012).
Table 4.6 assigns which powertrain drains which battery in which flight phase j. As a power limiting system is involved in the architectures BPMS BAT 1/2, it has to be differentiated between two cases with an if-else statement. Here, all powertrains are always connected to the battery system and generate the power drain P_{all}. If the battery architecture allows for a crossfeed, unused energy in battery 2 can be used for cruise as well.

Table 4.6: Assignment of powertrains to battery power drain for each flight phase (valid for aircraft configurations of section 3.1)

	P_{1j}		P_{2j}		cross-feed?
	hc, hd, hres	c, cc, cd	hc, hd, hres	c, cc, cd	
SGL BAT	all	all	-	-	no
SPRT BAT	dmpt	dmpt, cpt	hpt	-	no
BAT MUX	dmpt	dmpt, cpt	hpt	c: dmpt, cpt cc, cd: -	yes
BPMS BAT 1					
$if\ P_{all,j} < \eta\ P_{max,1}$	$\frac{P_{all,j}}{\eta}$		0		yes
$else$	$P_{max,1}$		$P_{all,j} - \eta\ P_{max,1}$		
BPMS BAT 2					
$if\ P_{all,j} < P_{max,1}$	$P_{all,j}$		0		yes
$else$	$P_{max,1}$		$\frac{P_{all,j} - P_{max,1}}{\eta}$		

The required energies E_{kj} are calculated in eq. 4.94 using the predefined duration t_j for all phases except cruise. The batteries' remaining energies $E_{k,c}$ can be spent on the cruise phase. For battery life extension, the battery energy is not used to its full extent (typ. $SoC_{min} = 20\%$).

$$E_{kj} = \frac{P_{kj}\ t_j}{\eta_{bat,kj}} \tag{4.94}$$

$$E_{k,c} = (1 - SoC_{min})\ \ E_k - \sum_{j \neq c} E_{kj} \text{ with } E_{2c} = 0 \text{ if no crossfeed} \tag{4.95}$$

$$t_{k,c} = \frac{E_{k,c}\ \eta_{bat,k,c}}{P_{k,c}} \tag{4.96}$$

$$t_c = t_{1,c} + t_{2,c} \tag{4.97}$$

Several validity checks are performed on each of the battery system options e.g. that their energy and power capabilities are sufficient. Among these valid battery systems, the one providing the highest cruise endurance t_c is selected.

4.12 Controllability Evaluation

The design of aerodynamic control surfaces for good controllability and maneuverability of fixed-wing aircraft is well understood. Decent control authority must also be satisfied for the hover and transition flight phases. Although these flight phases are supported by flight stability augmentation without exception, the basis is a proper geometric layout and thrust sizing of the distributed powertrains. The latter design features have a considerable impact on vehicle performance through aerodynamic drag, powertrain mass, battery type selection, etc. These dependencies between control layout and overall aircraft design are significantly stronger than for fixed-wing aircraft. Conclusively, the evaluation of vehicle controllability already in an early VTOL design phase appears necessary.

4.12.1 Cruise Flight

Experience shows that an aircraft which is controllable for a human pilot is usually also controllable for a flight control computer. Therefore, conventional controllability and stability criteria are used. As presented in section 4.5, in wing-borne forward flight, the design for lateral and longitudinal stability and control relies on the prescription of tail volume coefficients. The increase in pitch and yaw inertia by distributed powertrain masses can be counteracted by a general increase of these coefficients over the historic values, the employment of computed stability augmentation or all moving control surfaces. Raymer (1992, p. 112) provides corresponding data and correction factors.

Roll control can be well reduced to the evaluation of roll rate. Its analysis is possible based on geometrical parameters (Schlichting & Truckenbrodt 2001, p. 454). A sizing of respective control surfaces (ailerons, flaperons, elevons) is hence included in the tool chain.

Also associated with wing-borne controllability is the scenario of one engine inoperative (OEI). For aircraft using a pair of spanwise off-centered powertrains for cruise propulsion, the sideslip angle β_{OEI} for level flight with only one remaining engine is estimated in a simplified manner. If the sideslip allowable $\beta_{OEI,max}$ of 7° is not exceeded, the aircraft is considered to be capable of OEI flight.

$$\beta_{OEI} = \frac{c_{D,OEI}\ y_{nac}}{\left.\frac{\mathrm{d}c_Y}{\mathrm{d}\beta}\right|_v\ c_{V,v}\ b} < \beta_{OEI,max} \tag{4.98}$$

Hereby, the drag coefficient of the aircraft in OEI flight condition $c_{D,OEI}$ is assumed to be 15% higher than the nominal drag coefficient at the desired OEI threshold airspeed.

4.12.2 Hover Flight

In hover flight, control augmentation by a flight control computer is required. To maintain the simplicity in conceptual aircraft design, flight control laws shall not be incorporated in the controllability evaluation. It is therefore limited to quasi-static maneuvers and flight conditions for which the minimum required physical control authority is calculated. Powertrain dynamics, control

allocations and moment couplings are widely neglected.
The following criteria are checked by comparing the required moments against the available control moments.

- pitch, roll and yaw rate acceleration
  Rate accelerations are crucial to perform the desired maneuvers e.g. a change in bank angle within a given time frame. Aircraft inertia necessary for this evaluation are built up from the components with considerable inertia contribution (fuselage and nacelles, lifting surfaces, powertrains, tilt mechanism, cables, actuators, payload, landing gear, battery). Components with comparably small dimensions (e.g. powertrains components, actuators) are treated as point masses. The required control moments derive from the multiplication of rate accelerations with the rotational inertia tensor.
- pitch, roll and yaw rate
  Besides rate accelerations, the feasibility of quasi-static rates is important for maneuverability. Rate damping moments calculate from the aerodynamic drag which wing, tail surfaces or fuselages generate when rotated like paddles around the aircraft CG.
- static roll moment to compensate an asymmetric vertical gust
  A quasi-static helical gust is considered to act on the lifting surfaces and disturb the roll attitude. This gust owns axial and rotational speed components and hits the aircraft parallel and concentric to the center fuselage. The gust increases the AoA on the one wing half while it reduces the AoA on the other. The gust's roll moment must be counteracted by the powertrains. It can be treated similar to a roll damping moment in wing-borne flight.
- static yaw moment to sustain a crosswind component
  Although VTOL vehicles often align their heading with strong winds, it is necessary to maintain a certain sideslip angle off the wind vector e.g. during takeoff or landing. For simplicity, only the yaw moment generated by the vertical tail is evaluated.
- static pitch moment to represent non-ideal CG locations
  The aircraft's CG can deviate from its ideal design location e.g. due to a variable payload mass and position. The worst-case deviation of the CG in pitch direction is checked to be trimable in static hover.
- positive vertical acceleration
  This ensures that the aircraft's descent rate can be reduced to zero within a certain altitude loss.

Control moments can origin from thrust components over their respective distance to the CG and direct moments (torque of rotors). For yaw control on e.g. qXw and qXc configurations, the hpt are slightly tilted around the x-axis to augment the small direct rotor moments with a force-by-lever component. In case of the roll gust criterion, control moments can also be generated with

aerodynamic control surfaces.

Control thrust overheads on top of the static thrust requirements are planned individually for each powertrain type $i = hpt, dmpt$ by the control thrust factor $f_{ctrl,i}$. The control thrust factor is an optimization parameter.

$$\Delta T_{net,i,ctrl} = T_{net,i,h}\ f_{ctrl,i} \tag{4.99}$$

The suitability of the proposed criteria to ensure sufficient aircraft controllability in hover must be proven. Likewise, adequate input values for these requirements must be found. The approach will however already now highlight the differences between aircraft configurations.

4.12.3 Transition Flight

The evaluation of the moment household in transition flight is complex. Rotors e.g. produce airspeed-dependent moments and their slipstreams act on wings and elevators under constantly changing angles of attack. With regard to controllability, the transition flight phases hence remain unconsidered in this design tool chain.

4.13 Cost Analysis

The analysis of various cost components within an aircraft life cycle enables a better evaluation of the aircraft in its actual application: a profit-oriented business case. Mission performance, size or the implementation of certain features can be weighed against each other using cost as a common metric. The outputs are cost per mission, cost per traveled distance, cost per survey area or total system acquisition cost. Those can be incorporated in the target function of the aircraft optimization.

Various sources of aircraft life cycle cost modeling are available (Raymer 1992, Gundlach 2012, Stoll & Veble Mikic 2016). Top-down approaches are used that break down the different kinds of cost into rates (per-time, per-area, per-mass, per-unit, per-power, ...) that can be multiplied with

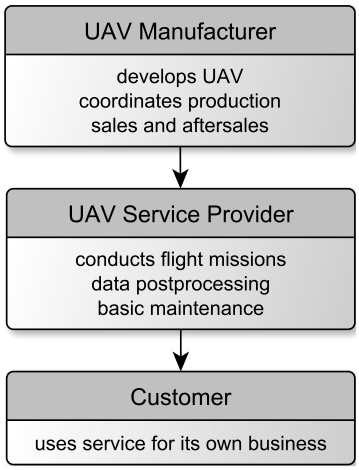

Figure 4.20: Assumed business relations for cost modeling

Table 4.7: Exemplary cost assumptions

	value	unit	multiplicand
Production			
powertrain parts purchase	0.35	$\frac{€}{W}$	power of powertrains
time for paint, layup, assembly	28	$\frac{h}{m^2}$	surface area of composite parts
time to integrate one tilt mech.	0.58	h	no of tilt mechanisms
production labor rate	56	$\frac{€}{h}$	production labor time
Development and Engineering			
	3	pmo[1]	no of powertrains
system development effort	3	pmo	no of tilt mechanisms
	1.5	pmo	no of control surfaces
general development effort	6	$\frac{pmo}{kg}$	mass of ac w/o payload
cost multiplier for prototype	3	-	cost of serial product
engineering labor rate	12000	$\frac{€}{pmo}$	development labor time
no of ac to share develop. cost	500	-	-
Acquisition and Depreciation			
battery purchase and disposal	0.83	$\frac{€}{Wh}$	battery energy
battery cycles at end of life	300	-	-
factor to add admin/sales cost	1.35	-	manuf/prod cost
factor to add profit	1.5	-	company prime cost
depreciation time of aircraft	2	yr	-
missions per year	150	$\frac{1}{yr}$	-
Maintenance			
time btw small/big overhaul	10/50	h	-
time for powertrain check/overhaul	0.08/0.5	h	no of powertrains
Electricity			
electricity cost	0.29	$\frac{€}{kWh}$	used energy for flight mission
charging efficiency	0.95	-	used energy for flight mission
Operating Personnel			
duration preflight check	5	s	no of act, pwtr, ctrl surf, etc.
duration post-processing	1.5	h	-
operator labor rate	60	$\frac{€}{h}$	operator labor time
Insurance and Permissions			
insurance rate	2.5%	$\frac{1}{yr}$	ac system purchase cost
permissions	150	$\frac{€}{yr}$	-
Crash			
MTBF act/pwtr	100/150	h	-
cost of crash event (beyond ac damage)	500	€	probability of crash event

[1] person month

properties known from conceptual design. The major challenge is to choose appropriate values for these cost rates dependent on the scale and complexity of the aircraft. Table 4.7 gives an insight into the cost rates used in this thesis. The below presented cost analysis has been prepublished in Stahl et al. (2019).

To establish a simple, though meaningful cost analysis, the cost components of development, manufacturing, operation and maintenance are incorporated. Figure 4.20 depicts the underlying business relations. The 'UAV Company' develops the aircraft and sells it to a 'UAV Service Provider' that conducts flight missions to gather e.g. imagery data or transport a good for the 'Customer'.

4.13.1 Production

Production cost of an aircraft sums up from tooling, component and raw material cost as well as labor cost for production, integration, setup, checks and flight test. Wherever possible the raw material or component cost relate to the number of components and their properties like dimensions or power capability. To estimate labor cost, durations of production steps are defined and scale with the number of step repetitions (e.g. integration of powertrains, systems, actuators) or size of parts (e.g. composite layup, milling and finishing of molds). Manufacturing labor rate includes workshop environment and overhead cost.

4.13.2 Development and Engineering

Development and engineering cost is made up based on the time to develop system units, their frequency and the labor rate. A component of general development effort scales with the aircraft mass without payload. Cost for several prototypes (derived from aircraft production cost) add on top of the labor cost. This total cost is shared by the estimated number of produced aircraft. Development and engineering cost is likely the most vague and least predictable cost component of the ones presented here. Company data on development program cost is hardly accessible and poorly traced.

4.13.3 Acquisition and Depreciation

Cost for the complete aircraft system purchase add up from development, production, ground control station, payload and transportation/turnaround equipment. Overhead factors for administration and sales departments multiply on top as well as potential interest cost and profit margins. A simple linear depreciation model divides the above cost by the applicable operation hours or number of missions until end of life.

The purchase and disposal cost of the battery are linked to its energy and depreciates linearly with the number of charge-discharge cycles until it has to be renewed. One cycle per mission is assumed.

4.13.4 Maintenance, Repair, Overhaul

A simple maintenance, repair and overhaul (MRO) schedule is set up consisting of two types of checks with different time effort, replacement cost and intervals. While the 'small' check is limited to thorough visual checks, cleaning and lubrication, the 'big' check involves the exchange of wear prone components like actuator gears or engine bearings. Cost is again made up from time for single work steps, repetition of work steps (e.g. number of systems to inspect) and labor rate plus replacement part cost.

4.13.5 Electricity

The cost of electricity to recharge the battery depends on the energy used within a flight mission, the charging efficiency and the electricity price.

4.13.6 Operating Personnel

Cost for personnel to conduct the actual flight mission builds up from the number of personnel required for a subtask, time to conduct a subtask and the personnel's labor rate. Subtasks involve installation of the payload, transportation to/from the takeoff site, rigging/derigging of the aircraft, exchange of the battery, flight trajectory definition, preflight checks, monitoring the actual flight and post-processing to make the collected data usable for the customer.

4.13.7 Insurance and Permissions

Yearly insurance cost for the aircraft and the payload are a certain percentage of the purchase price. Insurance against damage to third parties and flight permissions use fixed yearly rates. Yearly cost are allocated by the amount of missions per year.

4.13.8 Cost of Aircraft Crash

Under certain circumstances like operation over unpopulated areas in low altitudes, small UAV are allowed to operate under significantly higher risk of critical system failure than manned aviation does. Although legitimate and non-hazardous for third parties, a simple, failure-prone system architecture does not necessarily mean an economic optimum when considering the cost of a crash. These can not only mean cost for the repair or replacement of the aircraft, but moreover the cost for the damaged payload, recovery, non-availability for further missions, follow-up paperwork and bad reputation. Weighting those costs with the probability of the corresponding failure scenario to occur during a mission yields a cost component that can be used to indicate appropriate system architectures and redundancies.

Gundlach (2012, p. 763) includes cost of aircraft loss during flight testing, training and wartime with fixed loss rates and cost, but does not link them to the system architecture.

In this thesis, the implementation of the crash cost component respectively the evaluation of failure probabilities must still be considered experimental and therefore uses strong simplifications (e.g. linearization of the exponential failure probability function, neglect of higher order probabilities

$p^2 << p$, independence of failure events).

In this exemplary case, a failure condition that prohibits the propelled wing-borne flight is classified as a crash. Hover and transition flight phases are hence not considered. Their small time shares (typically 2-3% of wing-borne segments) would anyway result in negligibly low failure probabilities. Only the following failure events are assumed to cause a crash of the aircraft.

- function *pitch control*: failure of all elevator actuators $n_{fail} = n_{sys}$
- function *roll control*: failure of all aileron actuators $n_{fail} = n_{sys}$
- function *cruise propulsion*
  - if OEI flight is not possible: failure of at least one powertrain $n_{fail} = 1, ..., n_{sys}$
  - if OEI flight is possible: failure of at least two powertrains $n_{fail} = 2, ..., n_{sys}$

n_{sys} is the number of systems associated with one function and is limited to $n_{sys,max} = 2$ for the presented analysis. n_{fail} is the number of failed systems within one function that leads to the crash condition. Mean times between failures (MTBF) for powertrains and actuators (Sarson-Lawrence et al. 2014) are assumed to calculate the crash scenario probabilities and expected crash cost.

$$p_{crash,mission} = \sum_{funct.} \sum_{n_{fail}} \binom{n_{sys}}{n_{fail}} \left(\frac{t_c + t_{cc} + t_{cd}}{MTBF} \right)^{n_{fail}} \tag{4.100}$$

$$c_{crash,mission} = p_{crash,mission}\ c_{crash,event} \tag{4.101}$$

The configuration tVt represents a special case. Its probability for a crash caused by powertrain failure is approximated with 0, as its tiltable hpt can be engaged if the dmpt fails.

4.13.9 Cost for Customer

Overheads for administration, sales and profit are added on top of the internal cost for the service provider. The cost for a land survey needs to assume parameters like swath width and track overlap of the optical payload to relate the trajectory length with the surveyed area.

5 Design Studies

Different runs of the design tool chain are performed to give insights into the general design drivers and sensitivities of a fixed-wing VTOL UAV and the strength and weaknesses of different aircraft configurations.
The main relevant input variables can be taken from tables 4.1 and 4.7.

5.1 Optimized Configurations

By varying the parameters of table 4.2 with a genetic algorithm, each of the configurations is optimized for each of the targets

- minimum survey mission cost per survey area
- maximum range
- maximum endurance

Although none of the resultant aircraft represents a 'best' aircraft in terms of the multidimensional requirements of a real-life application case, these straightforward targets facilitate isolating the effects of design choices. The nature of a genetic algorithm can not guarantee to really find the global optimum. Sufficiently large population sizes as well as different start populations have been chosen however to increase the chance of finding it or come close.

In this study, survey mission cost derives from a survey project performed by one operator with one aircraft on a total survey area of 68 km^2. The survey project extends over several days which requires multiple transports to the deployment site. For all optimizations the cruise airspeed is limited to between 17 and 30 $\frac{\mathrm{m}}{\mathrm{s}}$. The upper airspeed limit is defined by the imaging, storage or data transmission rate of the electro-optical payload. The stall margin (difference between level stall airspeed and design cruise airspeed) is limited to between 3 and 5 $\frac{\mathrm{m}}{\mathrm{s}}$. It is open to the algorithm to choose the usage of a hpt alignment system (not retraction) or redundant elevator actuation. The tractor arrangement of the hpt is prescribed. All optimizations use a continuous battery sizing in both mass and energy-to-power capability to reduce discontinuities in the results ('rubber sizing', fig. 2.2).

While in appendix A all aircraft top views, main performance numbers, breakdowns of mass, drag, energy and cost as well as controllability figures are listed for all optimization targets, only the range optimization results are used for a representative presentation of the effects in this chapter.

All figures show the best aircraft in terms of the optimization target in the far left column with decreasing performance to the right. Shares in bar plots below 6% do not carry numbers for better readability. Figure 5.1 lists the aircraft in decreasing performance in western reading direction. Dotted outlines of propellers show a pusher arrangement. A red elevator marks its redundant actuation. Cost figures are given as internal cost for the service provider, hence without the multiplication of administration and profit overheads.

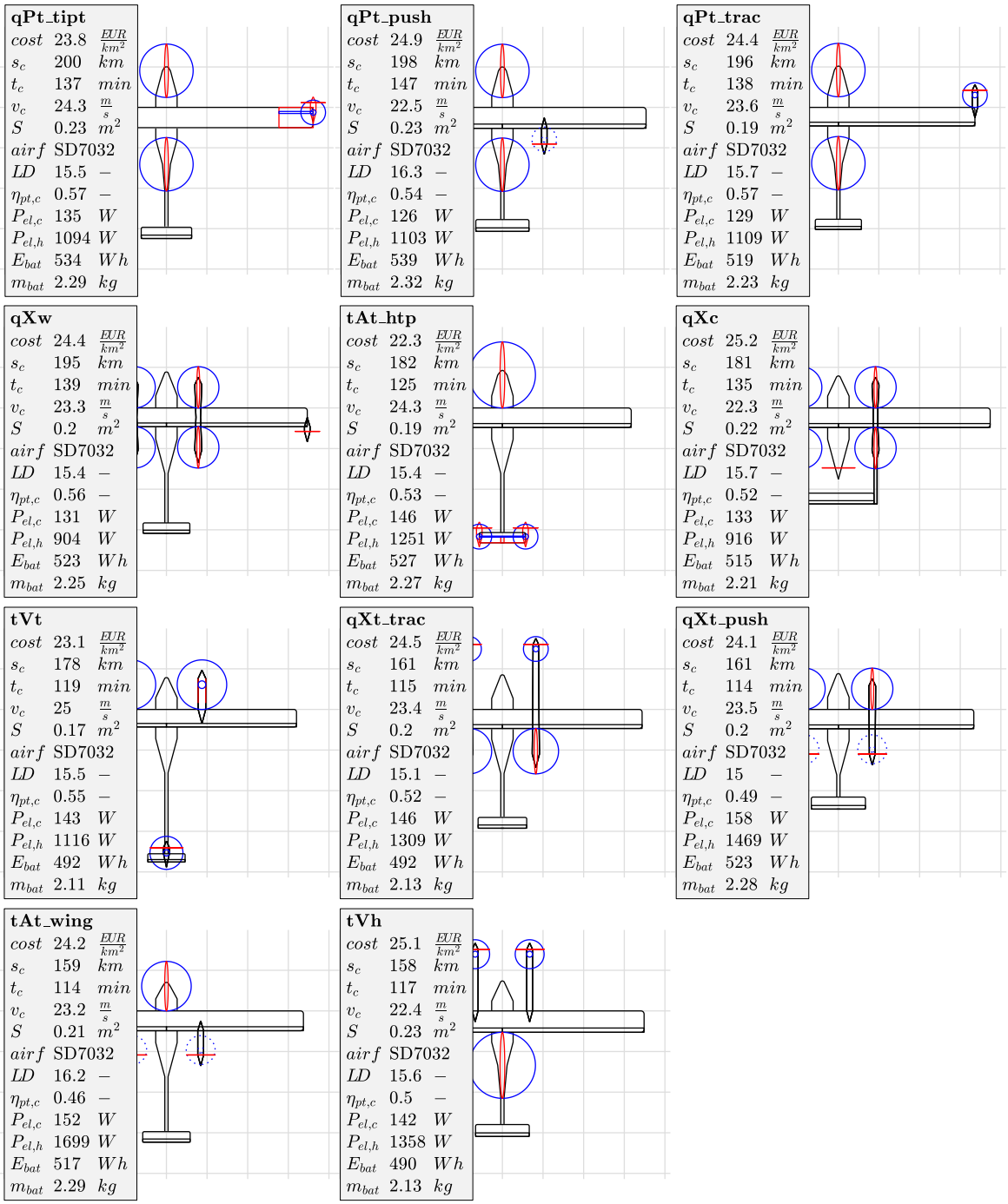

Figure 5.1: Aircraft top views for range-optimized configurations

The qPt family ranks best in terms of maximum range. Only minor differences occur due to the different types of tilt-aileron coupling and dmpt positioning. The spanwise portion of qPt_tipt's tilt wingtip sections is significant. If the design cruise airspeed is further reduced as e.g. for the endurance optimum, flaperons are added and the spanwise extension of the tilt wingtip is reduced to the minimum (see fig. A.3). Eye-catching are the long nacelles/fuselages of qXt, tAt and tVh. The driver behind this choice is to reduce the hover thrust load on the dmpt and at the same time optimize the propeller more towards cruise efficiency. The gains overcompensate increased

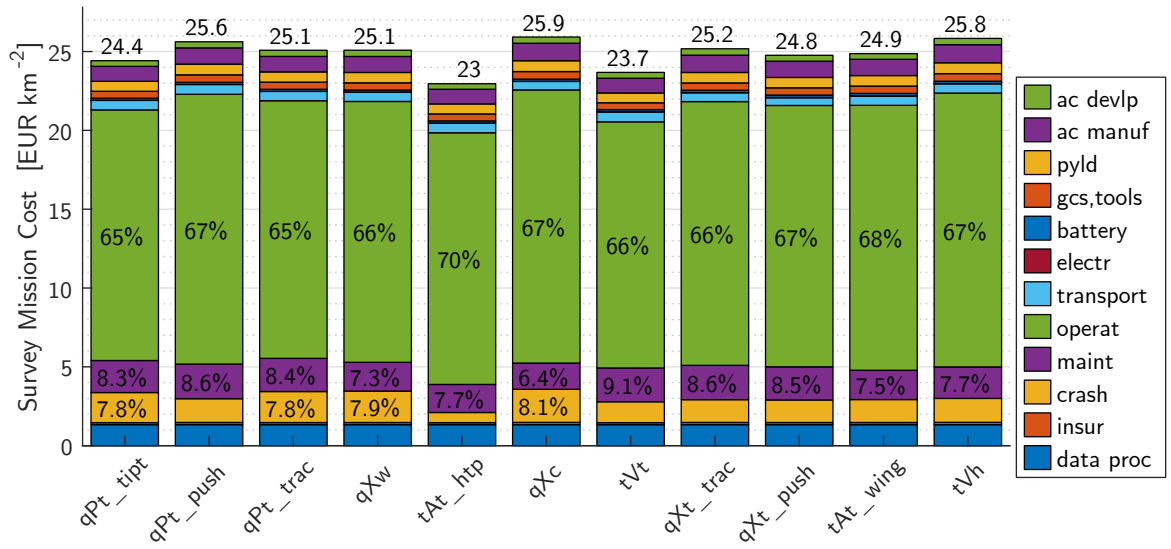

Figure 5.2: Cost breakdown for range-optimized configurations

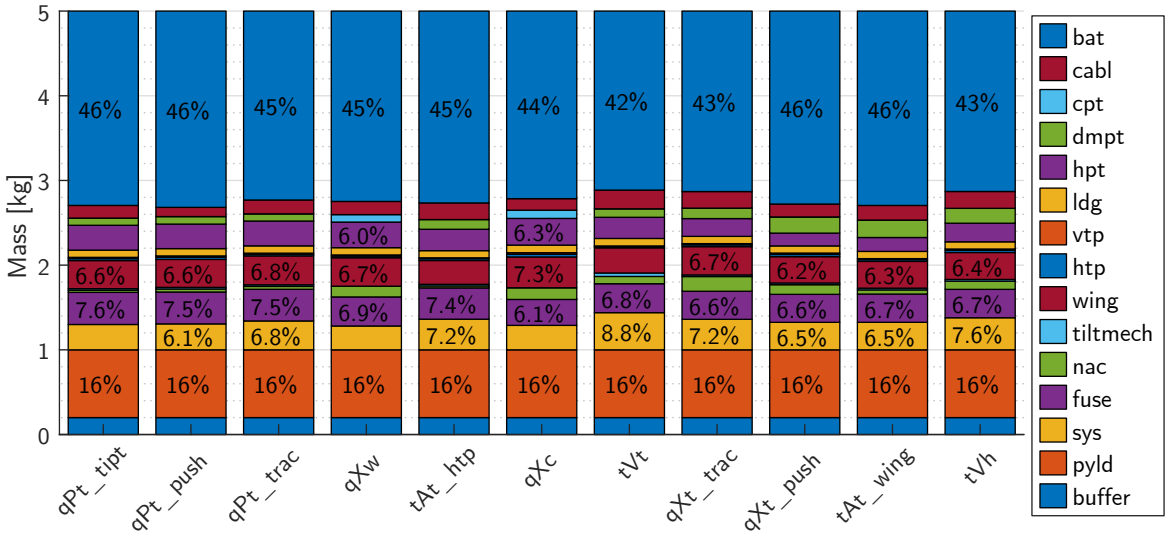

Figure 5.3: Mass breakdown for range-optimized configurations

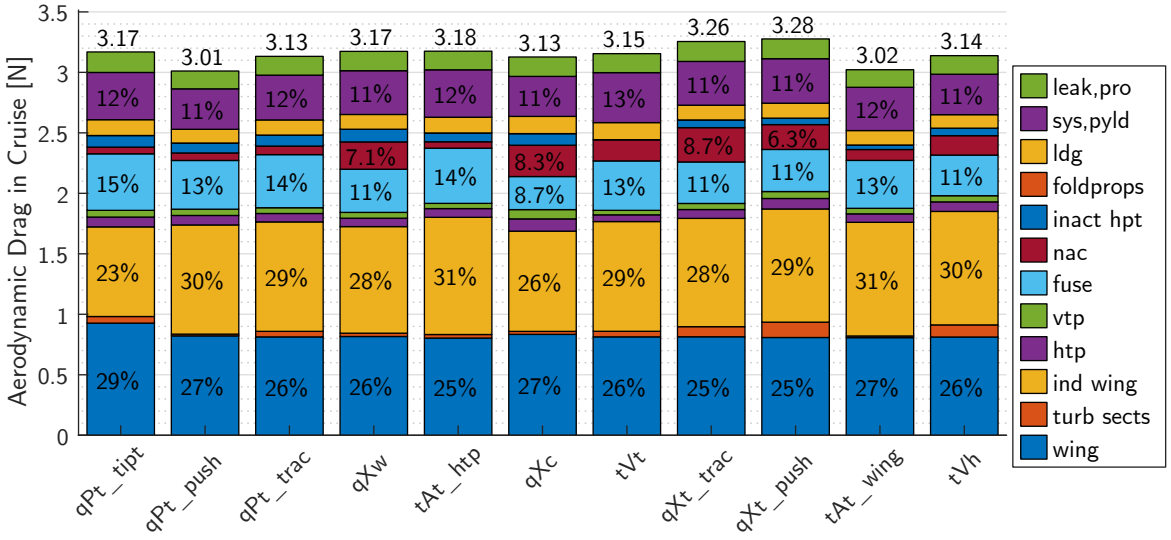

Figure 5.4: Drag breakdown for range-optimized configurations

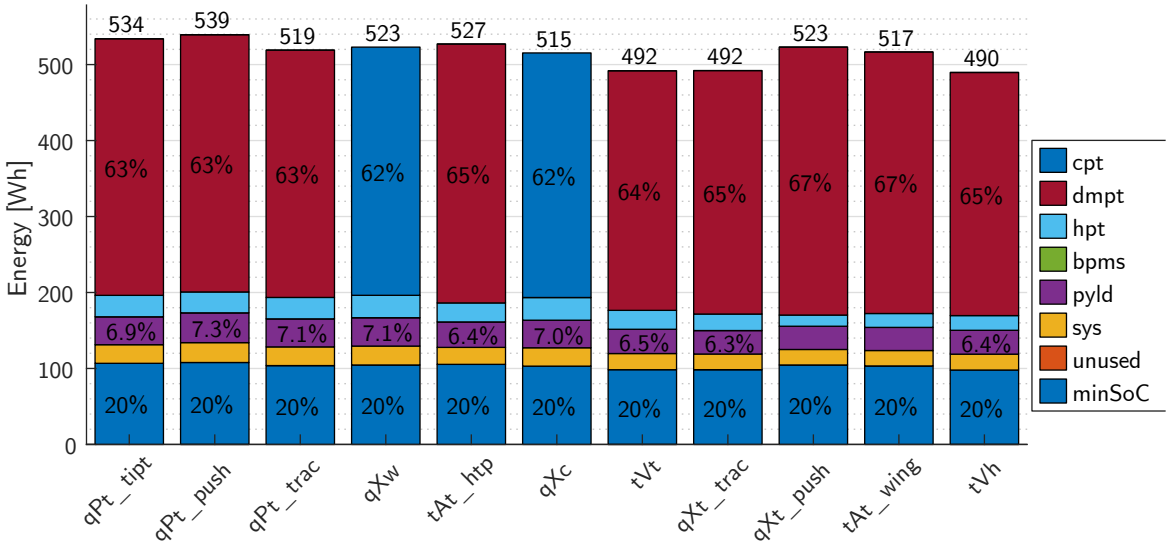

Figure 5.5: System energy breakdown for range-optimized configurations

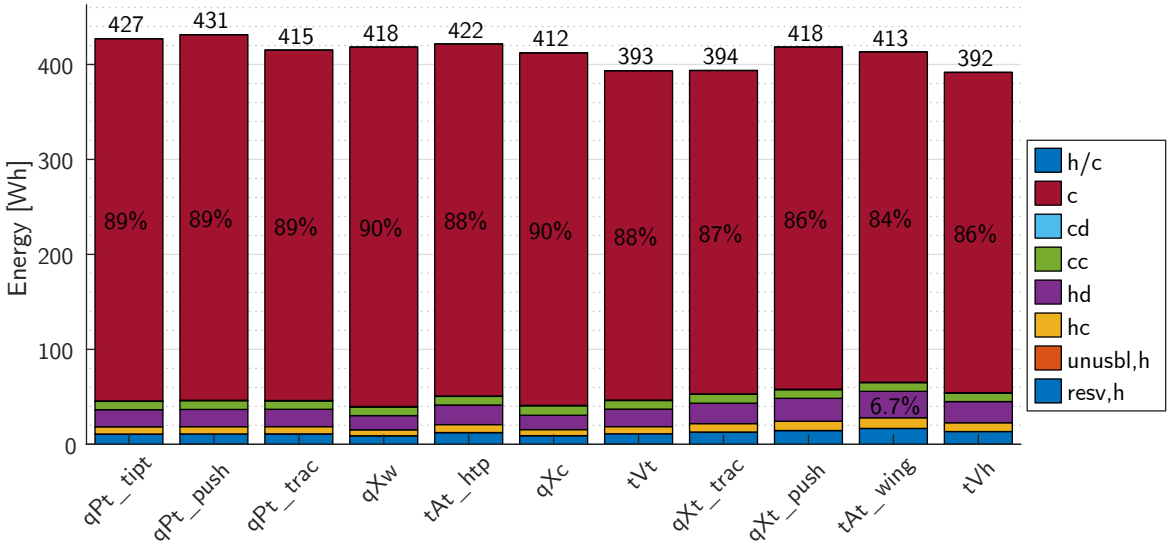

Figure 5.6: Phase energy breakdown for range-optimized configurations

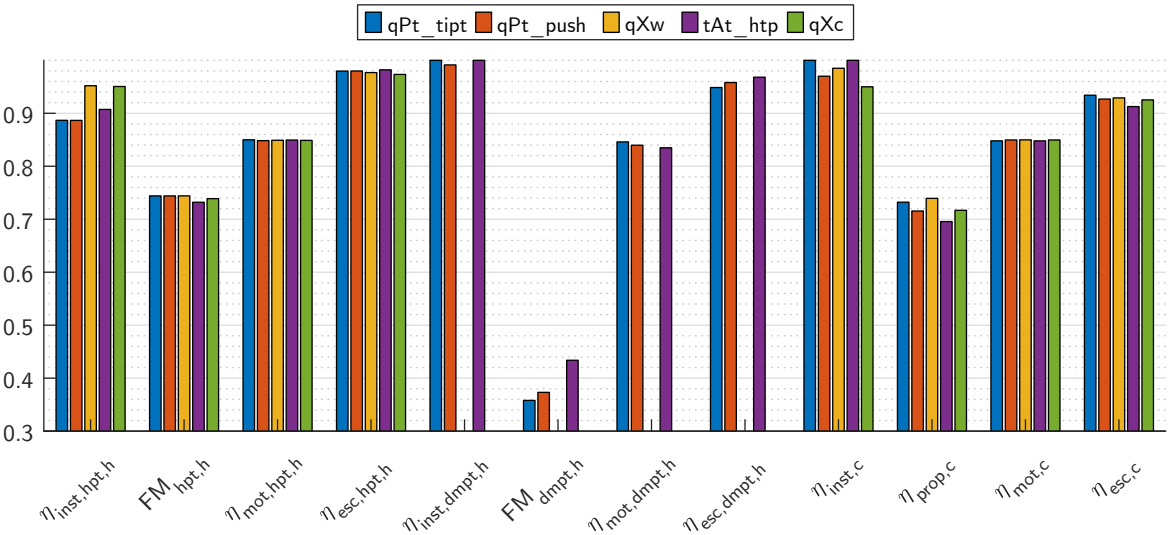

Figure 5.7: Powertrain efficiency breakdown for range-optimized configurations

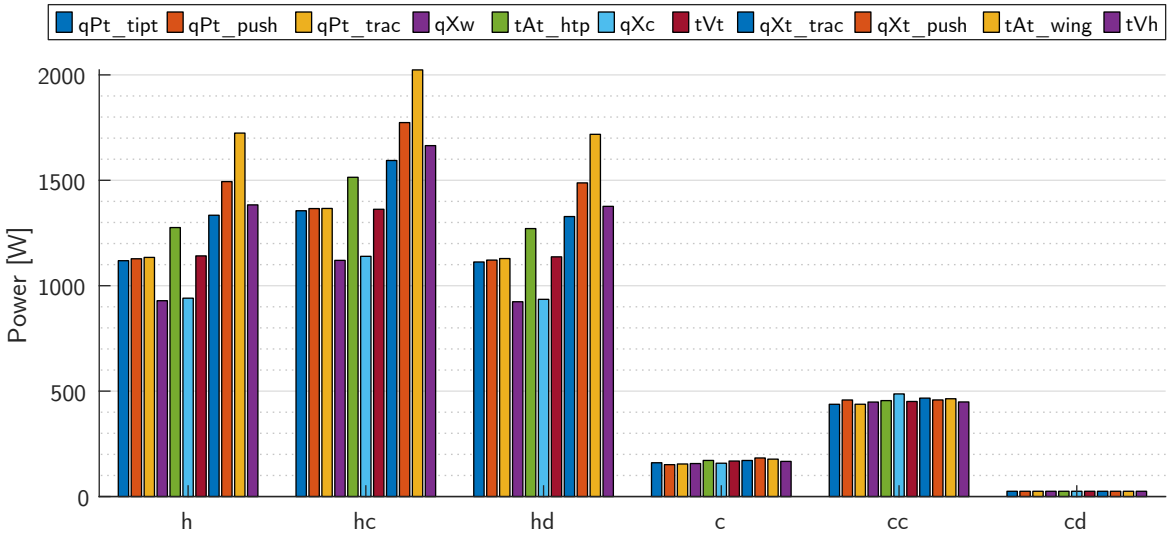

Figure 5.8: Power breakdown for range-optimized configurations

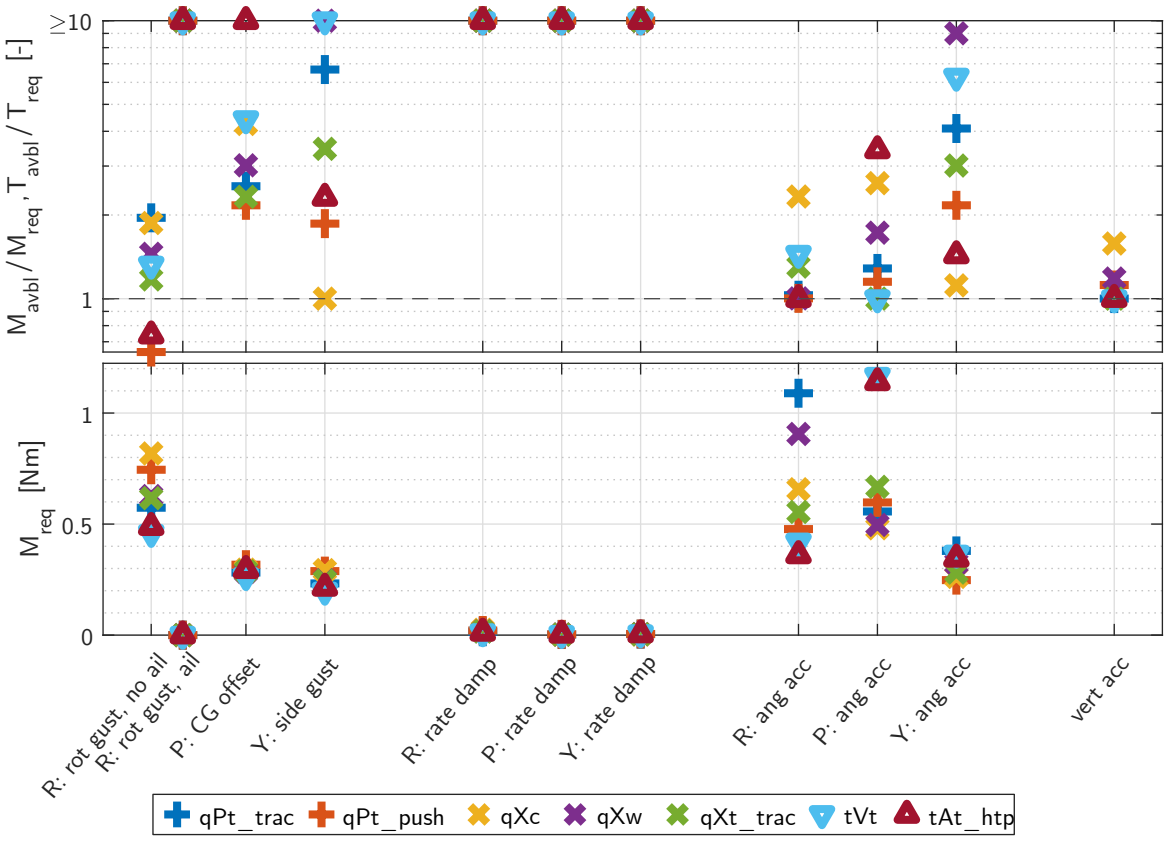

Figure 5.9: Hover control figures for exemplary range-optimized configurations

structural masses.

Remarkable in the cost breakdown in fig. 5.2 is the relatively small variance in total cost. This is even less for the cost optimized configurations (see fig. A.4). The main reason is the high share of operator labor cost. Higher flight speed is the main measure to reduce this cost item as only shorter flight durations have to be attended by an operator. Hence, all aircraft use the upper airspeed limit when optimized for minimum cost (see fig. A.1). Different payload setups or better operational techniques like multiple aircraft supervision would be other effective cost savers. The

second biggest item is maintenance cost. Considering the dominance of operator cost, the number and kind of systems can not achieve a significant cost impact. Remarkable is the cost share of a crash event. Redundancy of systems plays a key role as can be seen at the elevators in fig. A.1 which are all chosen to be actuated redundantly (evident from the red color). Also for the reason of crash avoidance, OEI capability is enabled by moving the dmpt of the qPt_trac inwards (compare cost-optimized to range-optimized version).

qPt_push and qPt_tipt reach the lowest system masses among configurations with tilt powertrains (see fig. 5.3). The coupling of tilt actuators with control surfaces enables this. The qPt family and tAt_hpt configurations use the fuselage for hpt powertrain installation and rank among the highest fuselage mass shares. This is because geometric relations require the foremost fuselage section to lengthen with rotor diameter. Nevertheless, very small nacelle masses widely make up for this. tAt_htp achieves the lowest wing mass as it combines a small wing area with a powertrain-free wing without reinforcements. The mass for power distribution/cabling must not be condemned for remote powertrain locations. Given a payload mass fraction of 16%, battery mass fractions of up to 46% are achieved.

The highest shares in aerodynamic drag are the wing's parasitic and induced drag (fig. 5.4). Fuselage and nacelle drag are lowest with the qPt family as both scales primarily with surface area. Stopped rotor drag accounts with up to 5%. As it basically scales with "stopped" rotor disk area, the differences between qPt and qX family are minor.

Around two thirds of the battery energy is used by the systems that propel cruise (see figs. 5.5 and 5.6). Less than 6% is used by the hpt. Energy for hover descent is higher than the hover climb due to the smaller absolute vertical speed respectively higher duration of the hover descent phase. The qPt_push and qPt_tipt configurations have the highest energy available.

Figure 5.7 lists installation degradation, figure of merit respectively propeller efficiency as well as combined motor-ESC (part throttle) efficiency for the involved powertrain types. Installation losses occur due to rotor blocking in hover and non-uniform propeller inflow (pusher behind wing/fuselage) in cruise. Attaching the hover rotor to the fuselage instead of nacelles leads to significantly increased installation degradation. The figures of merit of the dmpt are only about half of those of the hpt. Operation behind the fuselage is assigned with higher losses than behind the wing due to the smaller affected propeller area and thinner boundary layer. Wingtip propulsion effects are bookkeeped to the propeller efficiency which gives qPt_tipt and qXw superior cruise propeller efficiencies. tAt_htp's propeller efficiency in cruise suffers from the high thrust share of its dmpt in hover. This requires a compromise between hover and cruise efficiency (see also increased figure of merit). Its powertrain must also be throttled down further in cruise which negatively affects ESC/part throttle efficiency.

Figure 5.8 shows that the cruise climb power only is around one third of the hover climb power. By tendency, both hover power and cruise power consumption rise with decreasing range (from

left to right). The lowest hover power is achieved by the separated lift/cruise configurations. On average, tricopters tend to show higher hover power consumption than quadrocopters.

Markers just above the dashed line in the top figure of fig. 5.9 indicate driving requirements for control in hover flight. Maintaining a level bank angle in a roll gust gets a critical criterion for multiple aircraft configurations if ailerons are not supporting the roll moment generated by the powertrains. This requirements gets harder to fulfill if wing area or aspect ratio increases as e.g. with endurance optimized aircraft (see fig. A.27). Other critical sizing requirements are roll and pitch rate acceleration as well as vertical acceleration. qXc configurations generally suffer from poor yaw authority. This is despite a 10° tilted installation of thrust vectors around the x-axis for those configurations. This poor yaw control effectiveness is a performance barrier for qXc configurations as the high control thrust overhead drives powertrain mass. Also tAt_htp only slightly surpassed several requirements - an evidence for a narrow design space to satisfy both good performance and controllability. The lower figure displays the absolute control moments. Remarkable are the high moments required for angular acceleration which can be directly ascribed to high inertia. This is the case for all wingtip mounted powertrains for the roll axis and tail mounted powertrains for the pitch axis.

The matrix plot in fig. 5.10 reveals the dependencies of different input variables and main aircraft describing properties and performances. Aircraft configurations are color and marker-shape coded by their families. Included are the best aircraft of the three optimization targets. It must be differentiated if a direct or indirect effect is visible in the plots. Explanations on these effects are given in the following sections.

5.1.1 Cruise Airspeed

Optimal cruise airspeeds v_c are higher for maximum range s_c than for maximum endurance t_c. The qPt family clearly shows superior performance for both these performances.

Areal survey mission cost almost linearly decreases with increasing cruise airspeed. As visible in the cost breakdown in fig. 5.2, operator labor cost are the key factor. Those cost scale with the flight time in first order. Flight time is reduced by increased cruise airspeed. Accordingly, all cost optimized configurations choose the upper airspeed bound of 30 $\frac{\mathrm{m}}{\mathrm{s}}$.

Cruise powertrain efficiency $\eta_{pwtr,c}$ slightly increases with cruise airspeed as the thrust and inflow speed conditions of cruise approach the fast cruise and climb conditions. The narrower operational band yields efficiency benefits.

Battery mass fraction $f_{m,bat}$ increases with increasing cruise airspeed. The reason is the reduction in structural mass $f_{m,struct}$ associated with smaller wing areas.

The lift coefficient of the wing $c_{L,c}$ slightly increases with airspeed. This is mainly an effect of using the optimal point of the drag polar and an absolute, constant margin between airspeed and stall speed: Wing area shrinks with increasing airspeed respectively stall speed (not shown in fig. 5.10,

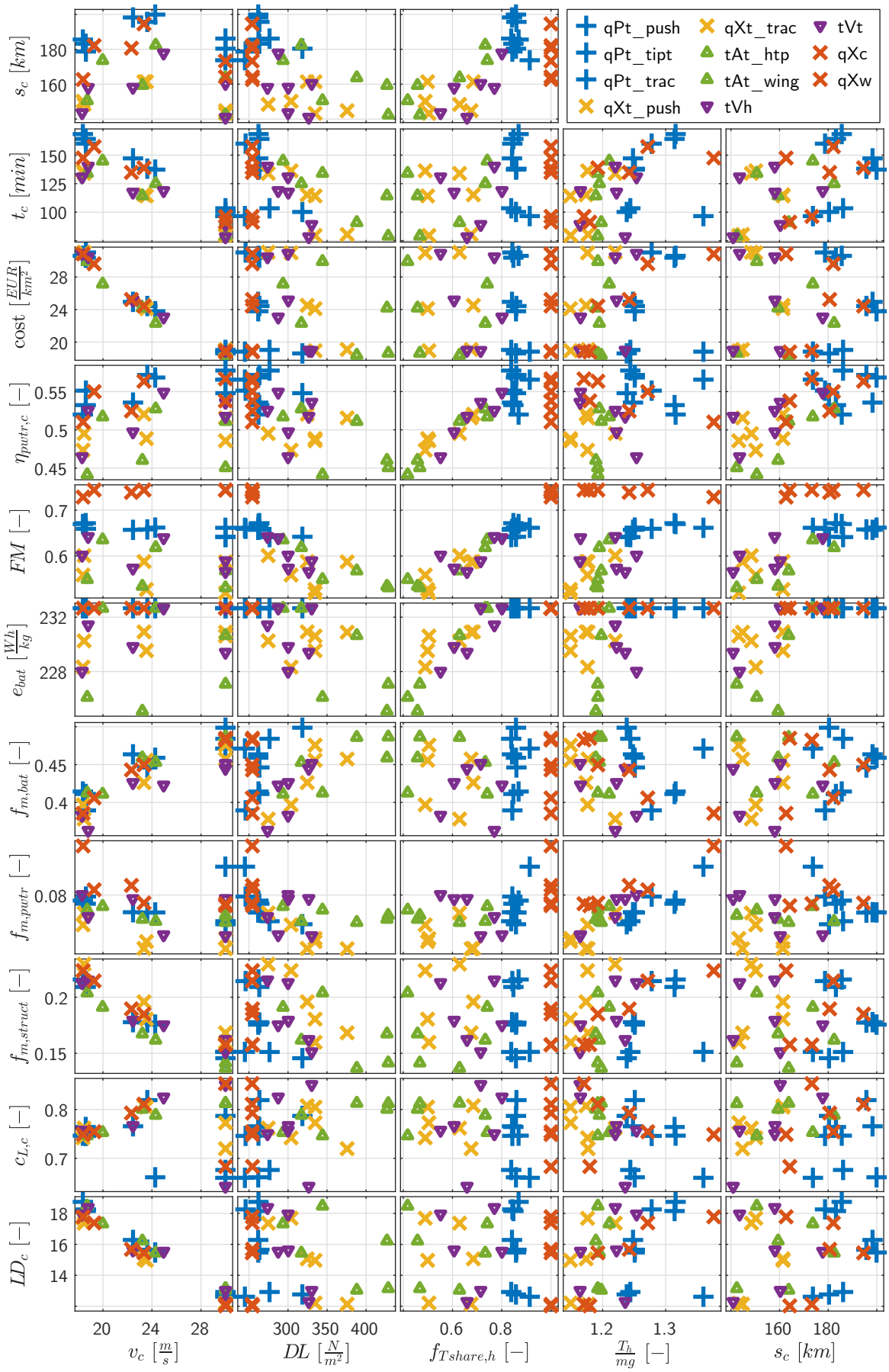

Figure 5.10: Matrix plot relating important input value to key aircraft and performance figures

but visible in the legends of figs. A.1 to A.3). An identical payload needs to be housed by the fuselage with almost constant surface. This means an increase in drag coefficient when referenced to the reduced wing size. As a consequence aerodynamic efficiency LD_c decreases. But also the optimal point of the drag polar shifts to higher lift coefficients if parasitic drag increases. With increasing airspeed and due to cost optimization, flaps are used less frequent (see figs. A.1 to A.3 and $c_{L,c}$ scatter for highest cruise airspeeds) e.g. as airfoil drag advantages decrease when cruise speed approaches fast cruise speed. Without flaps, the maximum lift coefficient is reduced (same baseline airfoils assumed) which simultaneously reduces the cruise lift coefficient to maintain the required stall margin. Reynolds numbers stay relatively constant for all airspeeds as reduced wing size compensates the airspeed increase.

5.1.2 Average Disk Loading

Low disk loading DL is an indirect prerequisite for high range and endurance. This is related to the battery energy density via the hover power consumption.

For configurations whose dimensions are strongly driven by rotor size (all except qPt and qX family), the structural mass decreases with increasing disk load. If the diameter of the hpt is reduced (disk loading rises), the hpt powertrain location can move closer to the CG. This is also the case for the dmpt. Fuselage and nacelle dimensions can shrink and cause less structural mass.

Powertrain mass is slightly decreased with higher disk load respectively smaller rotor diameters. Despite a higher power consumption, the lower rotor diameters require less motor torque which in turn results in lighter motors. The lowest disk loading is chosen by the qX and qP family.

5.1.3 Thrust Share of the Hover-Only Powertrain

For configurations with dmpt, range clearly increases with higher thrust share of the hpt $f_{Tshare,h}$. The contradiction between hover and cruise design conditions is mitigated, the lesser hover load the dmpt has to carry. This is visible in the rise of the figure of merit and powertrain efficiency in cruise.

Powertrain mass seems widely unaffected up to thrust shares of 0.8. Beyond that, which relates to the qX family with separate hover and cruise powertrains, the powertrain mass rises.

Battery energy density continuously profits from lesser power for hover thrust generation until no battery type with higher energy density is available.

For the structural mass, a clear trend can not be identified as different effects likely compensate each other. Fuselage and nacelle masses, especially of tricopters, increase with higher thrust share as the pitch moment equilibrium requires higher lever arms. Empennage mass decreases due to the smaller surface accompanied with higher lever arm. Tilt actuator masses reduce with increasing hpt thrust share due to less loading. Those exemplary structural mass dependencies are however not visible in the matrix plot.

Thrust shares around 0.85 seem optimal for range optimized aircraft. The qPt family is able to realize such high hpt thrust shares as it can choose the thrust share free from geometrical lever arm ratio constraints.

While the best figure of merit is reached by configurations with completely separated hover and cruise powertrain (qX family), cruise powertrain efficiencies do not rank best. The reason is the installation penalty of pusher propellers (either behind wingtip or fuselage).

5.1.4 Hover Thrust-to-Weight Ratio

Thrust-to-weight ratio $\frac{T_h}{mg}$ is not a direct input variable, it however can be regarded as an intermediate result of the hover control authority evaluation. The majority of configurations get along with thrust-to-weight ratios between 1.15 and 1.3. This is less than the values around 1.4 used by VTOL design tool chains that do not explicitly evaluate control authority (Stahl, Roessler & Hornung 2018, Karpfinger 2018*a*). All qXc configurations in the plot use a fixed tilt of the hpt thrust vector to support yaw moment generation. Without that tilted hpt mount (not depicted in the plot), the thrust-to-weight ratio of the qXc configurations would exceed 1.5.

Obviously, the thrust-to-weight ratio also correlates with powertrain mass. For the interpretation of correlations to endurance, lift coefficient, glide ratio, structural mass, etc., one must be aware that the hover thrust-to-weight ratio is driven by aircraft size and corresponding vehicle inertia.

5.1.5 Range

Also interesting is the correlation between relevant aircraft figures and the range performance. While all configurations reach similar minimum cost numbers, the qPt family provides the highest range at this cost magnitude. The dependency of increasing range with increasing cruise powertrain efficiencies, battery energy densities and battery mass fraction is confirmed. Low aerodynamic efficiency can be compensated by other means to still achieve good range.

5.1.6 Other Notes

The best cruise powertrain efficiencies are reached by the qPt_trac configuration by combining the wingtip propulsion benefit, high hpt thrust share and undisturbed propeller inflow (see fig. 5.1).

The tAt_htp and qPt family reach the best battery mass fractions. A contributor certainly are the mass savings from the dual use of actuator systems for tilt and wing-borne control surfaces and the mounting of powertrains to the main fuselage structure.

The best aerodynamic efficiency is reached by the endurance optimized qPt_push configuration (see fig. A.12). Especially at low airspeeds, the inactive rotor drag is no major disadvantage. Very low drag is also achieved by the tVt configuration which folds its hover rotors to the nacelles. Tilting the hover powertrains horizontally is however associated with a mass penalty of the required tilt actuators.

5.2 Impact of Subsystems

By imposing certain design choices and comparing them to a reference, an idea about a subsystem's benefit can be gained. Maximum range is chosen as the optimization target.

5.2.1 Rotor Alignment, Rotor Retraction, Pusher Rotors, Wingtip Propulsion and Flaps

The design tool chain is executed with the following enforced features:

- disabled htp rotor alignment system
- enabled hpt rotor retraction system
- pusher arrangement for hpt rotors
- disabled wingtip propulsion benefit (by neglecting the model for it)
- ban of full-span flaps

The results of these optimization runs are normalized with the range of a reference aircraft. The best of each range-optimized configuration of section 5.1 serves as this reference aircraft. Again, different start populations and multiple optimization runs are used to minimize the potential error introduced by the genetic algorithm. The modeling of the features and corresponding experiments can be found in chapters 3 and 4.

Figure 5.11 illustrates the results for all aircraft configurations. Figure 5.12 plots the corresponding aircraft top views for three exemplary aircraft configurations. Note that each configuration and its derivatives are depicted in one column and are not sorted for best range.

The alignment of stopped hover rotors has a major impact. The significant addition of aerodynamic drag can reduce range by more than 15%. Obviously, configurations with large or many stopped rotors are more affected.

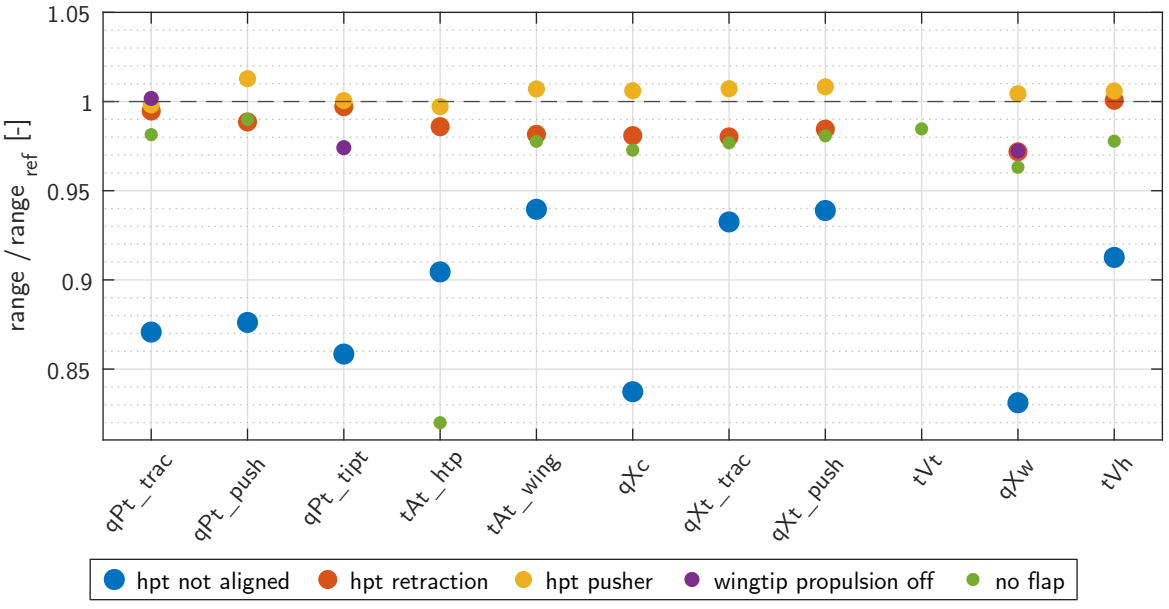

Figure 5.11: Impact of the certain features or subsystems on range

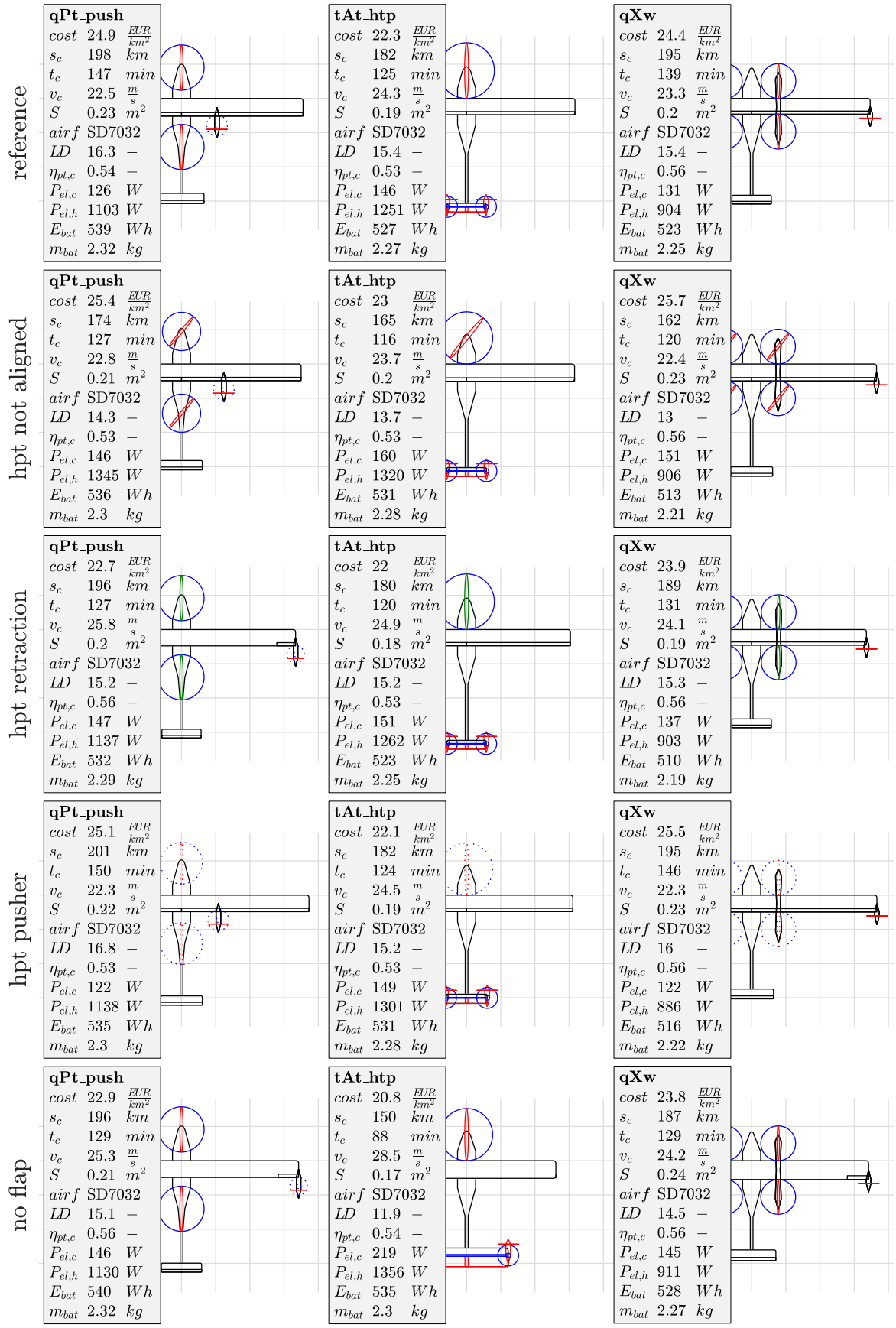

Figure 5.12: Top views of aircraft with enforced features or subsystems

Rotor retraction, to completely eliminate the drag of stopped rotors, comes at cost of additional system mass. No configuration can gain range compared to the reference aircraft that just align their rotors.

The usage of a pusher arrangement on the hover powertrain affects range within $\pm 1.5\%$. The lower power consumption which results from mitigated downwash blocking effects is e.g. traded against the additional mass of a higher landing gear. The results are however likely within the repeatability error of the optimization algorithm.

Disabling the wingtip propulsion effect decreases range by almost 3% for qPt_tipt and qXw configurations. qPt_trac moves the dmpt to a more inboard position and increases the wingspan if the wingtip propulsion benefit is disabled (no aircraft top view printed). Such it achieves similar range.

The ban of full span plain trailing edge flaps costs up to 3.5% in range for configurations except tAt_htp. For the qPt_push configuration, it changes the best location for the dmpt to the wingtip. Here both a coupling of the aileron with the tilt actuator and harvesting wingtip propulsion benefits is possible. tAt_htp loses 18% in range as the elevator has to be significantly increased to satisfy the control requirements. Range loss due to the ban of flaps will be pronounced for endurance optimized aircraft. The velocity range is increased here due to a slower optimal cruise speed, but constant fast cruise speed. The full span flaps help to widen the drag polar and obtain favorable drag coefficients in both flight conditions.

5.2.2 Battery Architectures

The following evaluation addresses the impact of the different battery architectures (as presented in section 3.3) and discrete battery mass sizing.
The range optimized configurations from section 5.1 serve as baseline. Their rubber-sized (continuous choice of battery mass and energy-power density trade-off) single battery is exchanged with battery systems of different architectures. The parameters of the battery architectures are chosen to maximize the range of the aircraft. The aircraft geometries, its powertrains, etc. remain constant. Short-time overpower capability is disabled. Battery types are explained in table 4.5.

Figure 5.13 breaks down masses, powers and energies of the battery systems for the qPt_push configuration.

The top subplot shows that the usage of the battery mass budget is generally high (>97%). This is even the case for SGL BAT using battery type 3 (as stated in the white box at the bottom of the column). For this battery type, the feasible steps in battery mass are large (6s x 46 g/cell x assembly overhead = 14% of battery mass budget) which makes it usually difficult to completely fill up the battery mass budget. The equally heavy but more energy dense battery type 2 is not up for selection as it cannot provide enough power due to its $\approx$ 40% lower power density. This can be evaluated in the bottom subplot. Here, the white bar represents the battery's maximum

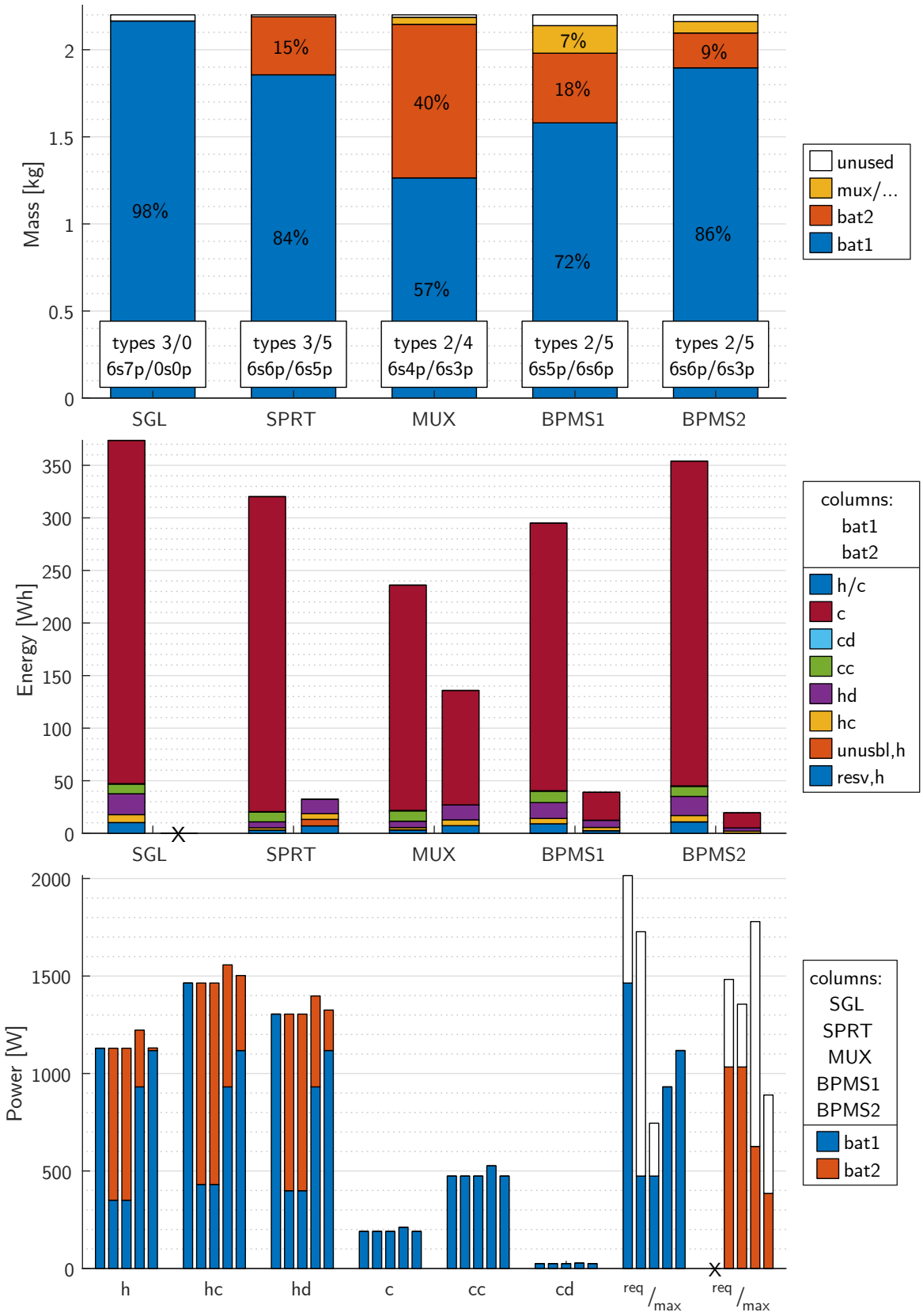

Figure 5.13: Breakdowns for masses, power drain and energy share for the different battery architectures, qPt_push configuration, 0.8 kg payload, discrete cell mass sizing, no future bat (settings as in fig. 5.14)

power capability. The blue bar indicates the maximum power requirement of the battery. All other battery architectures can use battery type 5 with very small mass steps of 10 g/cell to tightly fill up the mass budget. MUX finds a solution to even use a more energy dense battery as secondary battery bat2. BPMS1 and BPMS2 generally suffer from the mass of the battery power management system as it does not carry energy. It indeed wastes energy due to its conversion efficiency (see higher power drains from those batteries in the bottom subplot). MUX, BPMS1 and BPMS2 enable the usage of the more energy dense battery type 2 in the primary battery bat1. The energy bars (see middle subplot) visualize the dominant share of energy used for the cruise phase. Secondary batteries only need to contain little energy (see right columns of each battery architecture) as they primarily provide hover power. SPRT contains unusable energy in the secondary battery as the cruise powertrains cannot access this energy. The origin is a mismatch in required power-to-energy compared to what the available cell types provide. Also visible is that due to the dmpt of qPt_push, hover energy is stored in the more energy dense primary battery. That would not be possible for separated hover and cruise configurations (qXw, qXc) with SPRT and MUX architectures. For MUX, energy of the secondary battery is used for cruise. This explains the higher energy density battery type choice for the secondary battery. The power bar plots of both BPMS architectures confirm the full usage of the primary batteries' power capability (as regulated by the BPMS devices). The power requirement of the secondary battery is relieved and a maximum of hover energy is stored in the primary battery with favorable high energy density - independent of the powertrain architecture. The difference in BPMS mass between BPMS1 and BPMS2 can be explained by the power conducted through these devices. With BPMS1, the power drain from the larger primary battery is higher than the power drain from the secondary battery with BPMS2.

For further investigations, the battery mass budget is varied by a corresponding variation of the payload mass. The 'useful payload' mass (battery plus payload mass) and, with that, the total aircraft mass remains constant. While for fig. 5.14 the actual cell masses are used, the subsequent figures assume battery cells to be available in an arbitrary size/capacity/mass (mass-rubber sizing). Figure 5.16 runs the analysis of fig. 5.15 for a different aircraft configuration: the qXw configuration with separated hover and cruise powertrains. Figure 5.17 extends the state-of-the-art range of battery types by a super-high-energy-density battery type with very low power capability (bat type 1).

Figure 5.14 to fig. 5.16 all use the following identical plot layouts. The far left figure gives the relative range improvement over the SGL battery architecture. The middle figure describes the battery budget usage. Only the mass of the batteries, no multiplexer or battery power management systems, is considered for this. It hence represents the energy-carrying mass fraction. The far right figure indicates the battery type choice. The syntax is <primary battery type> 'dot' <secondary battery type>. Obviously, only one battery type is assigned for the SGL architecture. Only battery

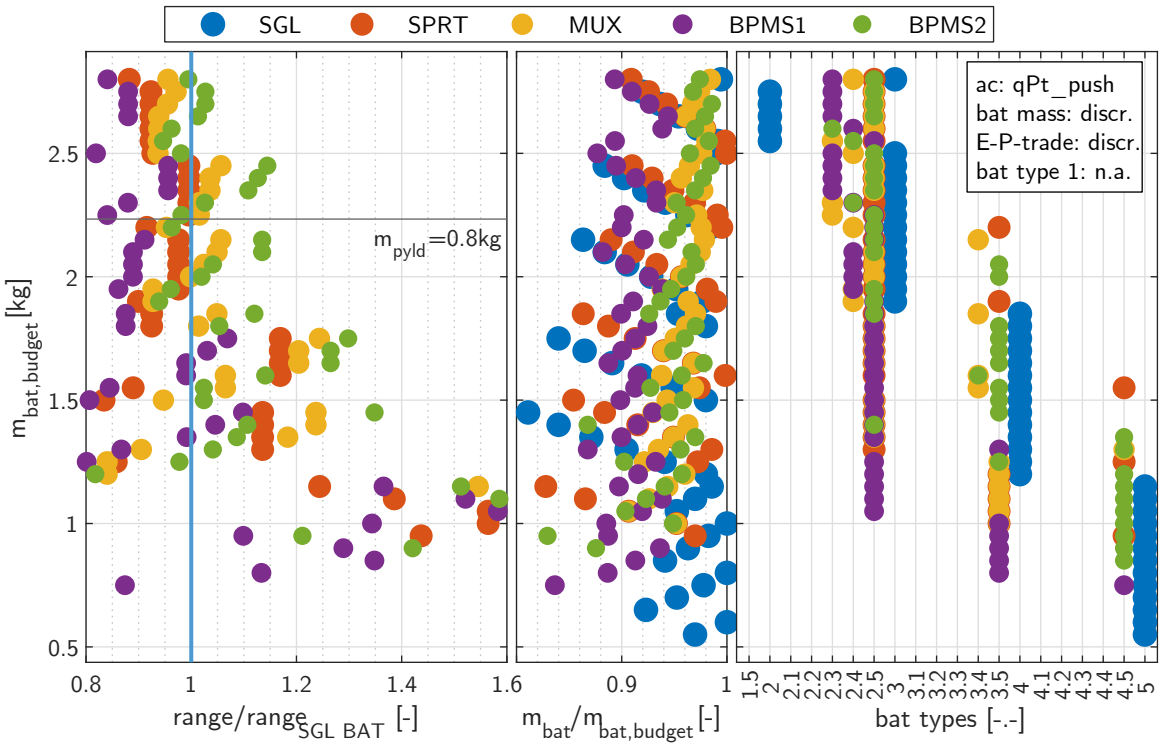

Figure 5.14: Battery mass budget variation for qPt_push, discrete sizing, no future battery

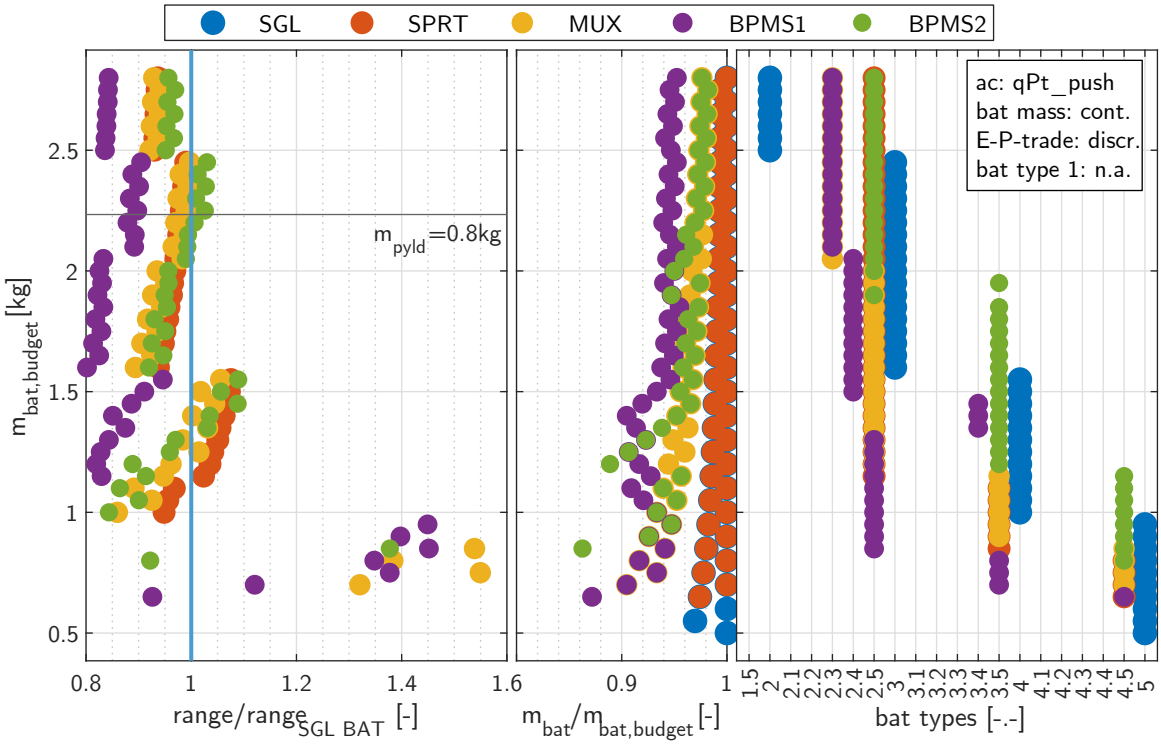

Figure 5.15: Battery mass budget variation for qPt_push, quasi-rubber sizing, no future battery

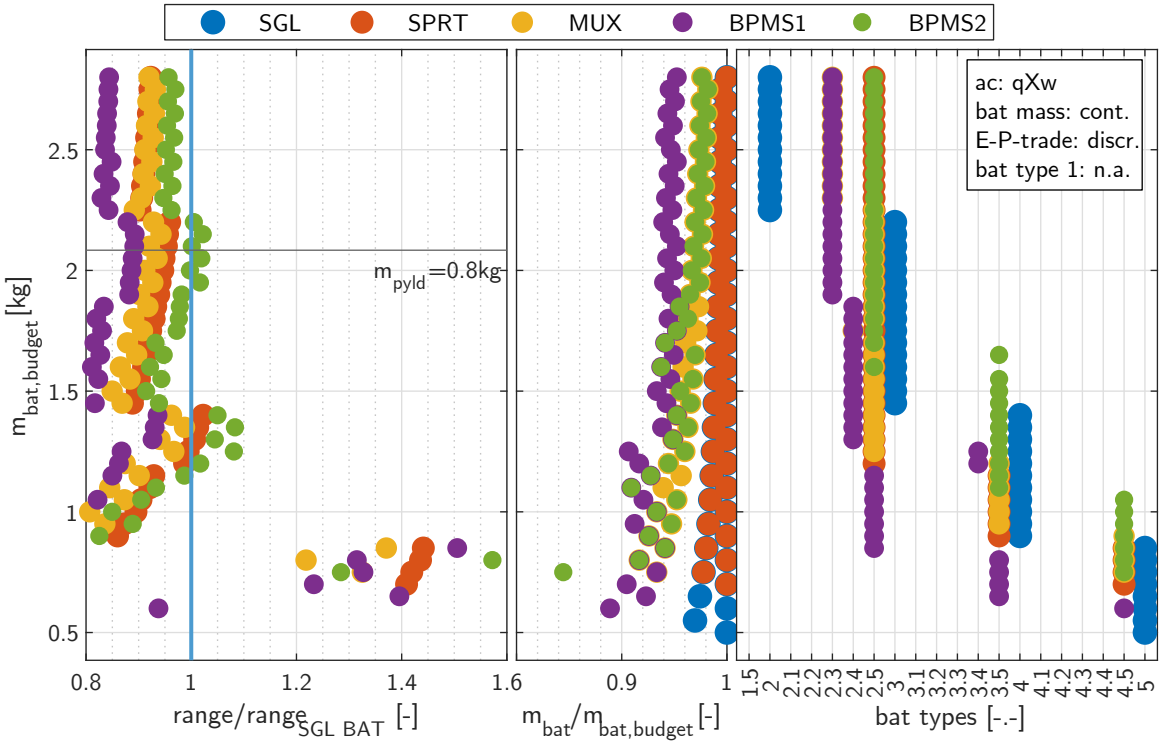

Figure 5.16: Battery mass budget variation for qXw, quasi-rubber sizing, no future battery

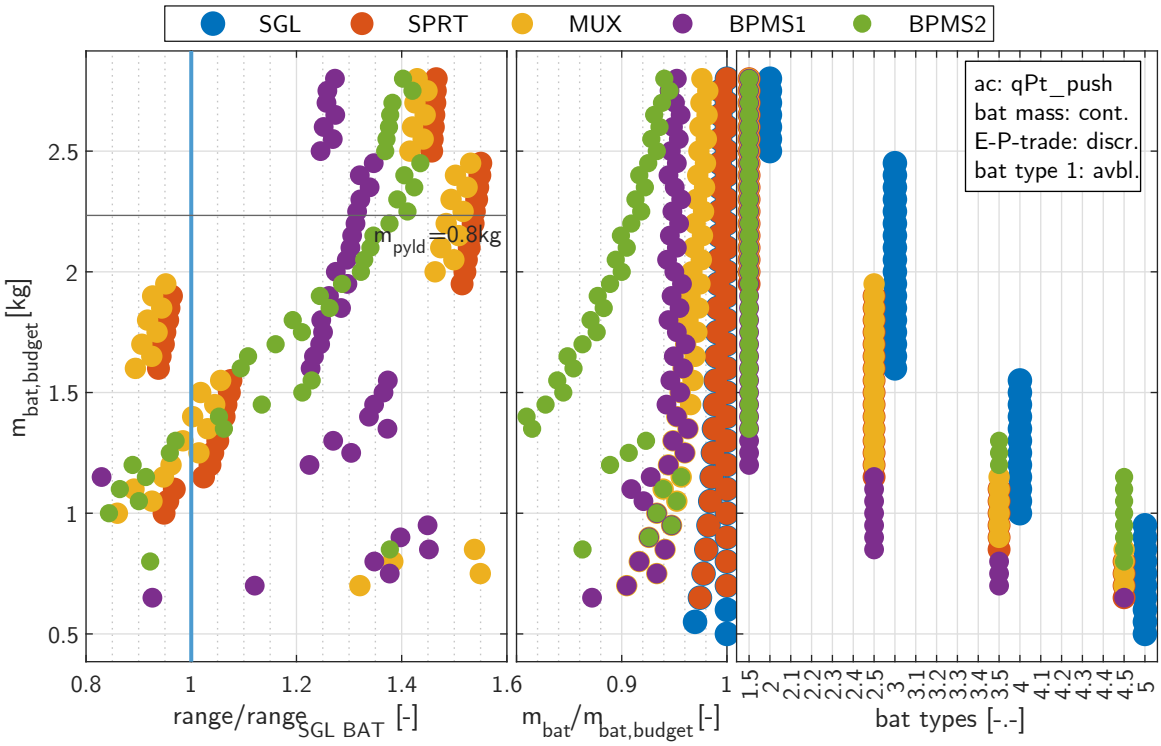

Figure 5.17: Battery mass budget variation for qPt_push, quasi-rubber sizing, future battery available

type combinations are investigated in which the primary battery type has a lower number (means lower power density) than the secondary battery type. On the vertical axis, the battery mass budget in kg is plotted. Battery mass is exchanged with payload mass such that the total aircraft mass remains the same. A horizontal line marks the typical payload mass of 0.8 kg which is used in the other studies. Due to identical geometries and powertrains for all considered aircraft in one plot, the maximum power requirements are constant. Correspondingly, the power density requirement tends to decrease with increasing battery mass budget. As can be seen in the right figures, this leads to a common shift towards higher energy density battery types as the battery mass budget is increased.

Clearly visible in the upper two thirds of the center subplot in fig. 5.14 are the high mass steps for the SGL battery (blue dots). Between the jumps in the battery budget usage factor, a gradual reduction takes place. Jumps happen when a further parallel battery string fits inside the battery budget. In between, more and more of the battery budget is left unused as it cannot be filled up by batteries. This behavior also leads to a jump in the relative range improvement for the other battery architectures (left subplot) as they have the SGL architecture's range as reference in their denominator. The jump width decreases with increasing battery mass, as the relative mass of one parallel cell string reduces. The behavior changes to a certain extent for low battery mass budgets (lower third of subplots) where the SGL battery architecture uses battery type 5 with very small cell mass increments.
Generally, hybrid battery architectures harvest two possible advantages. Firstly, if the combination of the high power and high energy battery types together achieves a better power-to-energy ratio than what the battery technology benchmark line provides (consider fitted line in fig. 2.2 as technology benchmark). Secondly, if gaps in the available power-to-energy ratios are large, the hybrid batteries can make a better fit to the requirements. This both is the case for high power density requirements. Hybrid battery architectures hence may mitigate the disadvantages of aircraft configurations with high hover power consumption or small battery budget. The maximum range improvements in fig. 5.14 vary from 3 to 60%. In the region of the 0.8 kg reference payload mass, almost 15% range improvement seem possible with BPMS2.

To remove battery mass step effects for evaluation purposes, mass rubber sizing is introduced in fig. 5.15. Accordingly, the SGL and SPRT battery mass fractions are close to one. Range improvements now solely origin from combined battery technology advantage and flexible matching to power-to-energy requirements. Larger range improvements are still evident for low battery mass budgets. The best range improvements for the reference payload mass reduce to around 3% for BPMS2. For qPt_push as a representative for dmpt architectures, simple SPRT and MUX battery architectures can reach the performance of BPMS2 for intermediate battery mass budgets where the mass and efficiency penalty of the BPMS device weighs heavier.

Figure 5.16 provides the same plot for the qXw configuration which owns a lower hover power

consumption. This shifts the plot down towards lower battery mass budgets (to yield a comparable power density requirement of the battery as with the qPt_push configuration). SPRT and MUX show less range improvement compared to the qPt configuration as they do not allow to store hover energy in the primary battery due to the separated hover and cruise powertrain architecture. BPMS2 is not affected by this and yields range improvements similar to the qPt configuration.

A possible scenario for a trend in future battery development is underlying fig. 5.17: the availability of a very high energy density battery type with low power density as it is demanded by the high volume consumer electronics industry. Even for high battery mass budgets, this battery type would provide range improvements in the order of 55% for simple SPRT architectures. The SGL architecture cannot make use of this battery type due to its low power density. It must however be pointed out that this superior hybrid battery architecture performance only holds true as long as no higher power density battery type on an equivalent technology level is available.

As the plots originate from a hybrid battery system retrofit to an existing airframe, a full optimization of aircraft and battery system together may release another minor range improvement. Beyond range improvements, other aspects like supply chain, fast-charge, battery failure and mission flexibility must be taken into account.
Different voltage levels of primary and secondary battery were not investigated, but could also lead to minor range improvements.

6 Configuration and Tool Validation

Prototypes of the qPt_push and tAt_htp configurations were built and test flown to demonstrate the general feasibility of the aircraft concepts and to learn about their in-flight characteristics. The qPt_push prototype is instrumented to deliver flight performance data for the validation of the beforehand presented design tool. The prototypes do not follow the requirements or optimal parameters of the previous chapters.

6.1 Prototypes and Their Design Tool Representations

6.1.1 Prototype Implementation and Control

Figures 6.1 to 6.3 and table 6.1 give insight in the make and properties of the prototype aircraft. Both prototypes are based on identical wings, fuselage, actuators, control/communication system and powertrain components. This common baseline is extended by the configuration-specific parts like tilt-aileron coupling (see fig. 3.6) or tilt-elevators (see fig. 3.11). Materials and construction methods are selected with rapid prototyping in mind. For the purpose of flight performance data measurements and better predictability, the qPt_push prototype is equipped with rotor alignment and a fabric-covered fuselage.

OpenAeroVTOL (Thompson 2013) is used as primary flight control software. Its architecture allows to configure almost arbitrary aircraft layouts and perform manually piloted hover, transition and wing-borne flight. To compensate its missing capability of flight data recording and automated trajectory flying, ArduPlane (ArduPilot 2020) is used on a secondary flight controller running on Pixhawk hardware. For automatic trajectory flying, the command source is switched to the secondary flight control computer with a signal multiplexer once fully wing-borne. Au-

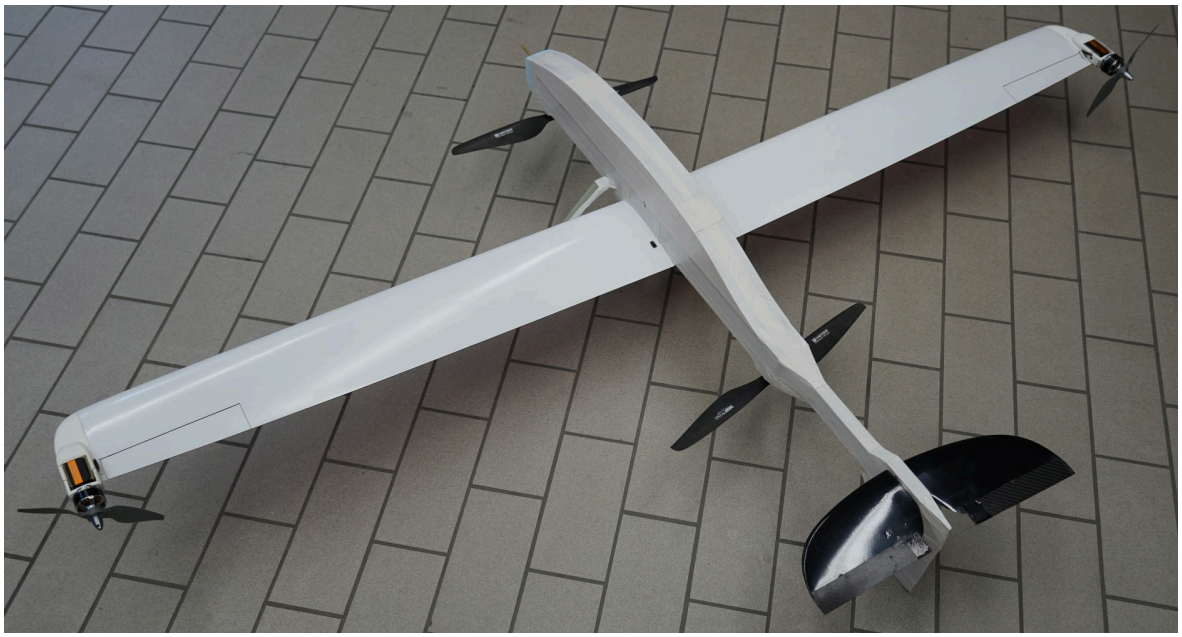

Figure 6.1: qPt_push prototype

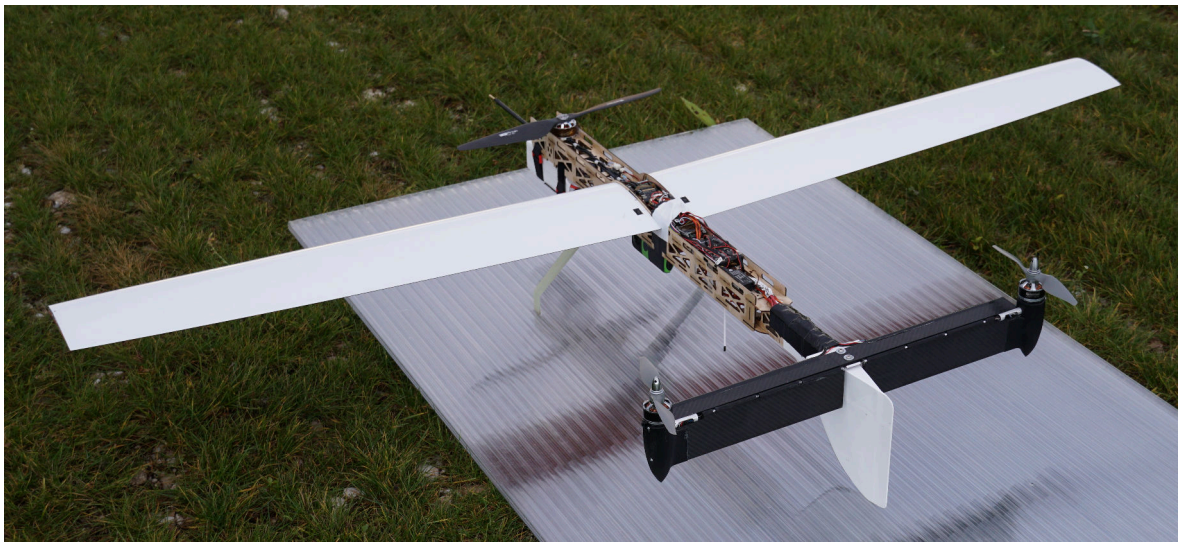

Figure 6.2: tAt_htp prototype

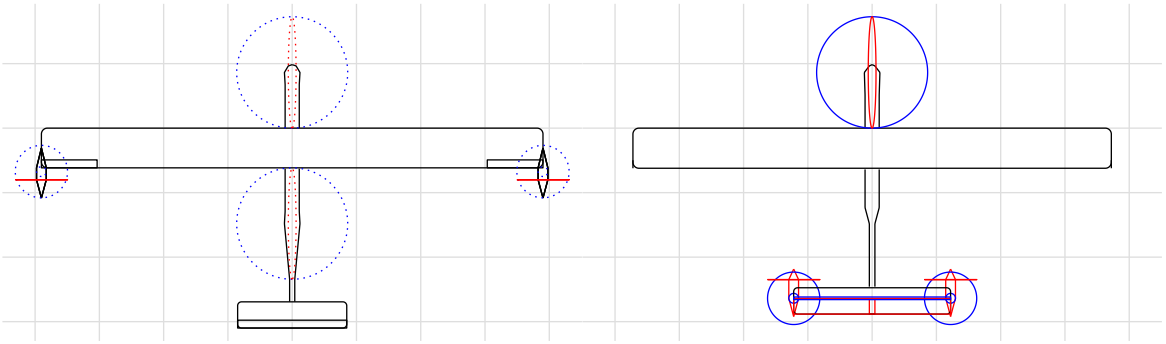

Figure 6.3: Top views of the prototypes as modeled in the design tool

Table 6.1: Data of qPt_push and tAt_htp prototypes

	qPt_push	**tAt_htp**	
mass	3.87	3.43	kg
wing span	1.95	1.86	m
wing area	0.30	0.29	m^2
wing aspect ratio	12.7	12.0	-
wing airfoil	SD7032		-
wing loading	127	116	$\frac{N}{m^2}$
htp span	0.42	0.61	m
htp area ratio	0.14	0.22	-
horiz. tail volume coefficient	0.62	0.84	-
hpt rotor size	17 x 5.8		in
dmpt propeller size	8 x 6		in
hpt thrust share in hover	0.93	0.64	-
average hover disk loading	106	159	$\frac{N}{m^2}$

tomatic trajectory flying is just implemented on the qPt_push prototype to increase the quality and repeatability of the performance measurements. IMU/INS data, airspeed, barometric altitude, battery voltage and battery current are recorded using Pixhawk standard sensors.

Table 6.2 summarizes the control mapping. Five channels (2x two axis sticks, 1x three position switch) are required for the control inputs of the pilot. The mapping of control inputs to vehicle reaction uses a consistent attitude reaction as rationale. The throttle channel is used to control the throttle setting of vertical, respectively horizontal powertrains. Its mapping is changed when entering and leaving the wing-borne flight state. This mapping is tailored to pilots which are already familiar with the manual piloting of fixed-wing aircraft and multicopters. The three manual flight phases hover, (outbound) transition and wing-borne flight are selected by a three position switch. The (outbound) transition switch setting contains a time-controlled ramp for tilting and throttling up the dmpt as the pilot manually controls the throttle setting of the hpt. A dedicated inbound transition phase is not used. For inbound transition, the pilot directly switches from wing-borne to hover flight mode. In wing-borne flight, another switch is used to multiplex the control signal source between OpenAeroVTOL (manual) and ArduPilot (automatic) flight modes.

Table 6.2: Control mapping for qPt_push and tAt_htp prototypes

mode switch setting	throttle channel	roll channel	pitch channel	yaw channel	tilt offset	throttle horiz. pwtr
hover	throttle vert. pwtr	roll attitude	pitch attitude	yaw rate	vert.	0%
transition	throttle vert. pwtr	roll rate	pitch attitude	yaw rate	ramp vert. to horiz.	ramp 0 to 100%
wing-borne	throttle horiz. pwtr	roll rate	pitch attitude	yaw rate	horiz.	throttle channel

6.1.2 Prototype Models in the Design Tool

The layout of the design tool chain as *conceptual design* tool poses restrictions to the analysis of existing aircraft. The correct input parameter set to match the prototypes' properties has to be found partly iterative. The planforms of the lifting surfaces are restricted to rectangular shapes. The parameters of fuselage geometry are set to match lever arm relations and the vertical projection. Top views of the prototypes as they are modeled in the design tool are presented in fig. 6.3. Other changes include:

- addition of center fuselage surface to match the real prototypes' wetted area
- implementation of a loiter trajectory to match the test flight trajectory
- 10% drag increase of the center fuselage for higher surface roughness and protuberance

- 32% drag increase of the wingtip nacelles due to uncovered tilt mechanism
- drag of missing dmpt spinners, partly exposed hpt motors and its larger rotor adapters, belly-mounted camera, stopped dmpt propellers in gliding flight

As the prototypes' structural materials and construction methods significantly differ from what is implemented in the design tool chain, the masses of these airframe parts are not used for validation.

6.2 Test Flight Approach

6.2.1 Test Flight Stages

After passing various ground tests to ensure the correct setup, functionality, integrity and durability of the aircraft and its subsystems, tethered hover is the initial flight test step. Flight controller settings are tuned until a reliable attitude stabilization and sufficient maneuverability are achieved. The following free hover flights test the behavior at successively increasing lateral and vertical speeds. The ability to recover from high speeds and steep attitudes is further validated to qualify the hover mode as an emergency recovery mode. In safe altitude, transition attempts are aborted at successively higher forward speed to familiarize with the transition sequence and the required control inputs. Once confident, the transition is fully performed by proceeding to the wing-borne flight mode. Control authority, stability and stall recovery behavior under different throttle settings and airspeeds are checked to clear the intended flight envelope.

A CTOL test phase to investigate wing-borne flight before transition can be beneficial, however turned out to be associated with significant challenges and effort if the aircraft is not designed for CTOL (e.g. high stall speed, qPt's inverted vtp/ground AoA limit, wingtip propeller clearance when tilted horizontal).

6.2.2 Recovery Aids

As a last resort, the engagement of the reliable hover flight control law was used to recover non-hardware failures like unusual attitudes or stall. This control law can be tested thoroughly and at low risk in tethered and low altitude hover over impact-absorbing high vegetation.

A spring-ejected parachute recovery system was mounted on the back of the aircraft for parts of the test flight program and could avoid a total loss in one out of two deployments. The system is widely ineffective during failures causing high rotational rates or at low altitudes. The retrofit of the unit led to significantly increased aerodynamic drag.

6.2.3 Flight Performance Data Capture

The goal is to capture in-flight performance data to validate the predictions of the aircraft design tool chain under the limitations of the given off-the-shelf measurement equipment and airspace restrictions (e.g. VLOS, lateral margins to infrastructure).

From the measurements of

- electric power consumption in hover (via voltage and current measurement at battery ter-

minals)

- electric power consumption at three wing-borne airspeeds
- descent rates in unpowered gliding flight at various airspeeds

key aircraft performance figures can be derived. Using eqs. 2.1 and 2.2, the overall figure of merit FM (averaging all involved powertrains and the complete efficiency chain from rotor to battery) and the product of glide ratio and cruise powertrain efficiency $LD\eta_{pwtr}$ can be determined. A drag polar can be calculated from the descent rate measurements and allows to isolate the cruise powertrain efficiency η_{pwtr} for the measured wing-borne flight states.

Based on energy conservation, the target values can be related with the measurement values and atmospheric conditions. This is done exemplarily for the measurement of $LD\eta_{pwtr}$.

$$\Delta E_{bat}\eta_{pwtr} + \cancel{\Delta E_{pot}} + \cancel{\Delta E_{kin}} = W_{air} + W_{wind,h} + W_{wind,v} \tag{6.1}$$

$$LD\eta_{pwtr} = \frac{\left(n_z + \frac{w_h}{v}\right) mgv}{UI + mgw_v} \tag{6.2}$$

$$e_{LD\eta_{pwtr}} = \frac{1}{1 + \frac{w_h}{v\ n_z}} \left(e_{n_z} + e_v\right) + \frac{1}{1 + \frac{mgw_v}{UI}} \left(e_U + e_I\right) + \frac{1}{1 + \frac{v\ n_z}{w_h}} e_{w_h} + \frac{1}{1 + \frac{UI}{mgw_v}} e_{w_v} \tag{6.3}$$

$$v = \sqrt{2RT}\sqrt{\frac{q}{p}} \tag{6.4}$$

$$e_v = \frac{1}{2}\left(e_q + e_p\right) \tag{6.5}$$

The work W_{air} required to overcome aerodynamic drag together with the work to correct horizontal and vertical wind drift equals the change in state and battery energy. The factor η_{pwtr} accounts for the conversion losses between electric and propulsive energy. In eq. 6.2, the change in state energy is neglected as altitude and velocity are assumed to be equal at the beginning and end of the measurement period. Equation 6.3 uses linear error propagation (Taylor 1988) to show the effects of atmospheric disturbances and sensor errors on the target value error. e_i represents the relative errors (absolute error normalized by the measured value).

The impact of an imprecisely measured or neglected horizontal wind w_h is reduced with higher airspeed v or load factor n_z. The impact of vertical atmospheric motion w_v reduces with high power consumption at low aircraft mass - in other words, if the aircraft flies fast, has a low glide ratio or an inefficient powertrain ($\frac{UI}{mg} = \frac{v}{LD\eta_{pwtr}}$). As rather the opposite is true for the investigated aircraft, a generally low atmospheric motion is desired. To mitigate the impact of short period atmospheric disturbances (gusts, thermals), a long measurement duration is helpful as it reduces the average horizontal and vertical wind speed. While the uncertainty about the horizontal wind velocity can be reduced by a conventional wind measurement (offset-calibration), the vertical air motion is hard to capture when the aircraft efficiency is still unknown. The test flights therefore took place at a day with low lateral wind (1.5 $\frac{\mathrm{m}}{\mathrm{s}}$ average), starting 2 h after sunrise when solar radiation only had little time to activate thermal convection. As thermal updraft and lateral wind

speed often increase at higher altitudes, the flight was conducted at safety minimum altitude.
To keep a constant flight state over the duration of the measurement within the limited airspace, the flight controller maintains a circular trajectory, constant airspeed and altitude. The quality of trajectory and airspeed tracking as well as the duration of the test segments (gray background) can be seen in fig. 6.4.
The load factor n_z is derived from the trajectory radius and velocity. Accelerometer and bank angle measurements are considered as too transient, biased and noisy. For simplicity and equation readability, the load factor is assumed independent of the airspeed for the error propagation calculation.
Airspeed measurement uses a pitot tube to probe dynamic pressure q (sensor: MS4525DO), a barometer inside the FCC (sensor: MS5611) to measure static pressure p and the relation in eq. 6.4. Using eq. 6.5, the resulting velocity error can be estimated to $e_v \approx \pm 4\%$ at 20 $\frac{\mathrm{m}}{\mathrm{s}}$ airspeed and test altitude. A GNSS-based calibration of the airspeed measurement is performed.
The shunt-based total battery current measurement is offset by an average systems current to obtain the powertrain current. The systems current is measured during powerless flight. Using a single sensor that is rated for the high currents of e.g. hover climb comes at cost of less accuracy when measuring the low currents of the wing-borne flight phase. A calibration of the current and voltage sensor has been performed over the entire measurement range. The highest current errors will reach around $e_I \approx \pm 10\%$ at the low speed, low power test conditions.
Although errors must often be estimated due to missing sensor information, a summation of just the known errors reveals the overall low precision of the test setup. This is caused by the general approach of an inflight measurement on a slow, efficient aircraft and the low quality of sensors available with ArduPlane at that time.
Besides three airspeeds (20, 23 and 29 $\frac{\mathrm{m}}{\mathrm{s}}$), the wing-borne power consumption tests are performed with both inboard up and inboard down rotation of the wingtip propellers. A difference in the measurements would in theory indicate the presence of a wingtip propulsion benefit. The given measurement accuracy will however not allow a reliable statement.

The stated measurement problems are mitigated for the hover performance testing due to the irrelevance of airspeed and load factor measurement, less atmospheric disturbances at lower altitude and higher power consumption. The aircraft can be controlled sufficiently precise by manual pilot inputs. The altitude is chosen to exclude ground effect influences. The available rpm measurement together with the wind tunnel data of the propeller is used to identify the thrust share of hpt and dmpt. It is then fed into the prototype calculation model.

Sink rate tests are performed with stopped or slightly rotating wingtip propellers (<1 Hz). Straight glide legs are maintained as long as the airspace restrictions allow. Airspeed is kept constant by a pitch angle command throughout one glide leg. Glides are performed at different pitch angles. Airspeed and sink rate are measured. Karpfinger (2018*b*) performs an error estimation for the

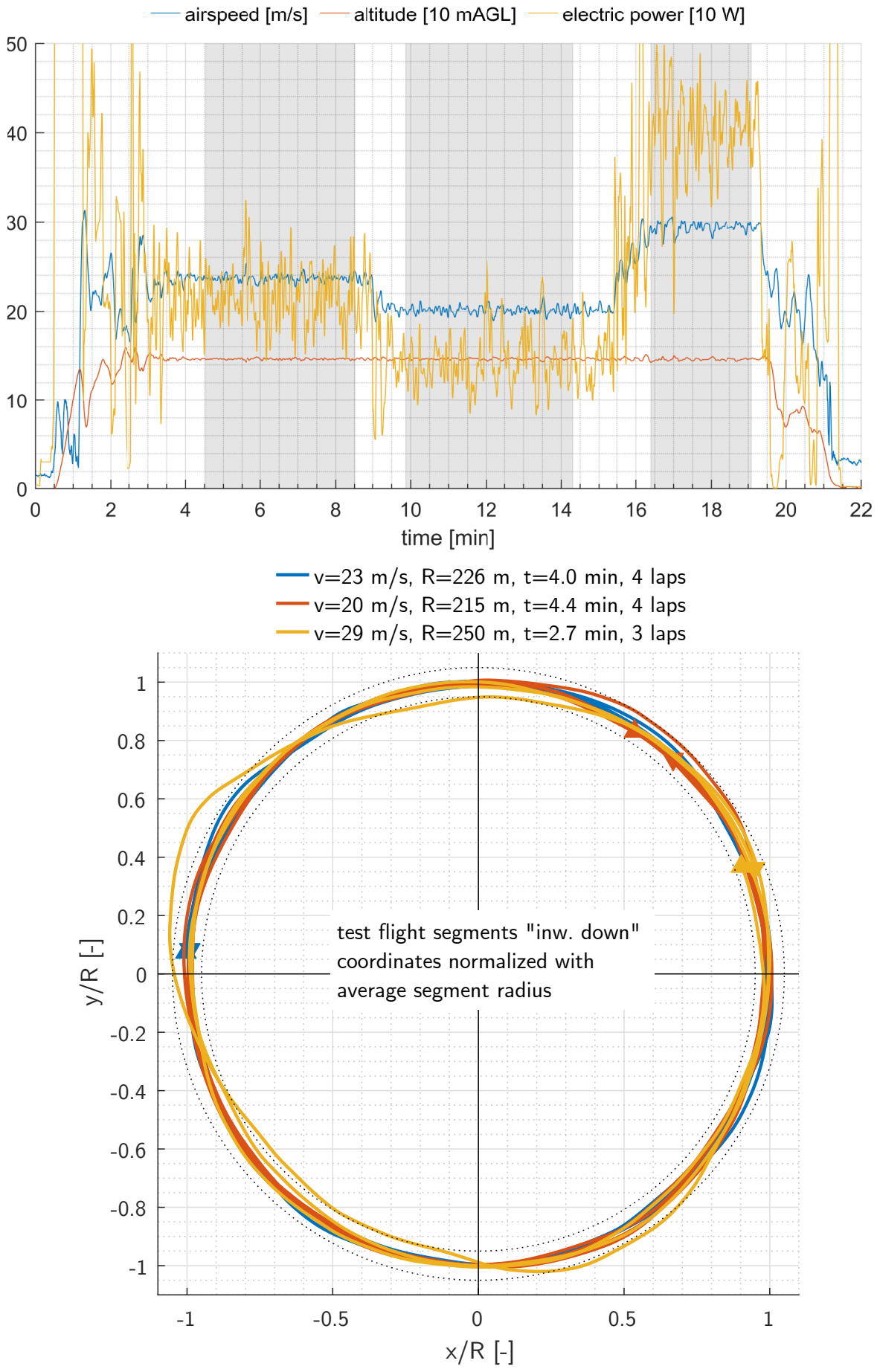

Figure 6.4: Exemplary data and trajectories of the power consumption flight test

employed test approach and for a comparable aircraft. He finds similar dependencies as stated for the wing-borne power consumption test. His overall error estimation for the glide ratio is $e_{LD} = \pm 63\%$.

Segments of the captured data in which the desired flight condition is maintained within certain thresholds are selected for further evaluation. Additionally, time derivatives of the signals and minimum segment durations are used as quality measures. The data of each segment is averaged and yields one point in the diagrams of section 6.3.2.

6.3 Test Flight Results and Validation

In this chapter, qualitative and quantitative flight test results are presented and used for validation. Wherever flight test data is not an adequate or reliable source of validation, alternative data is consulted. The main priority in validation is given to the major performance sensitive properties like mass, aerodynamic and powertrain efficiency.

6.3.1 Inflight Characteristics

The manual control of the aircraft allows for a pilot feedback on handling qualities. A rather qualitative description shall highlight the most notably handling characteristics of the prototype aircraft.

6.3.1.1 qPt_push

The qPt_push prototype exhibits sufficient control authority in hover to achieve accelerations, rates and moments for agile flying and gust handling. Roll and pitch axes are very responsive, yaw is significantly slower in reaction. Obvious reasons are the high inertia and small horizontal force components of the tilted powertrains. A coupling of pitch rate acceleration into yaw due to the differential torque of the large rotors is well compensated by the flight controller. Symmetric tilt allows to maintain pitch level in headwind or forward/rearward acceleration and minimize undesired wing forces. While high vertical climb velocities are unproblematic, fast vertical descent excites vibration, probably due to the aircraft entering its own rotor vortices. It can be mitigated by maintaining forward airspeed or reducing descent rate.

In a standard outbound transition, the dmpt are slowly tilted forward and throttle is increased. This provides an increase in airspeed and, with that, an increase in aileron effectiveness when the powertrains' roll authority vanishes. The tilting of the dmpt to horizontal was tested up to the tilt actuators' highest speed. Even then, due to the low thrust share of the dmpt, the sudden loss in vertical lift can be compensated by the main rotors. No relevant altitude loss is evident. Roll control is sluggish with horizontally tilted dmpt at full throttle in the first moment of transition. The short time period until ailerons gain effectiveness by increasing airspeed can be covered well. A pitch-up moment arises with increasing airspeed. Three main sources are proposed:

- Transverse flow effect of the hpt rotors: the rotor induces downwash to its rear section which

reduces the thrust there and generates a pitch up moment

- The flow field induced by the wing's lift: upwash in front of the wing increases thrust on the front rotor, downwash behind the wing decreases thrust on the rear rotor. The result is a pitch-up moment.
- The rear rotor's slipstream deflects with increasing airspeed. The elevator operates more and more in the downwash of the rear rotor and produces a pitch-up moment.

Differential thrust on the hpt and the deflection of the all-moving elevator is however sufficient to counter this pitch moment. To reduce the intensity of pitch-up effects, the inbound transition should be initiated at lowest possible airspeed. Due to the complexity of occurring effects, manually piloted transitions without pitch attitude stabilization are not possible. On the roll and yaw channels however, rate dampers are sufficient.

In wing-borne flight, special behavior is present with pitch and yaw. The elevator has less effectiveness as it is placed outside the propeller slipstream. Also the vertical placement of the wingtip powertrains below the CG causes a coupling of horizontal thrust on pitch. This means trim effort and drag. Both effects however reduce the pitch control margin and can get critical at low airspeed flight conditions like stall recovery or forward transition.
In normal operation, the computer controlled differential thrust of the wingtip powertrains supports yaw rate damping and provides the rudder function. In OEI failure events however, the high lever arms of the powertrains lead to yaw moments that initiate an immediate spin.
Roll control is not noticeably affected when stopping the dmpt.

The design tool predicted no violation of any controllability requirement for the qPt_prototype which conforms with the general good control authority in real flight.

6.3.1.2 tAt_htp

Pitch and roll authority in hover are well sufficient with the tAt_htp prototype. Pitch control required tuning the commanded ratio between htp and dmpt thrust to avoid vertical acceleration. Roll moments lead to a visible torsion of the fuselage tail boom. Aggressive roll control gains even caused a servoelastic torsion oscillation. Yaw authority is noticeably reduced compared to the qPt_push prototype. The shorter lever arm (elevator span) can not be compensated by the higher thrust loading of the dmpt and lower yaw inertia. A coupling of yaw to forward motion results from the asymmetric tilt deflections of the dmpt. This was however accepted to increase yaw authority. Hover without wings required no retuning of control gains.

For outbound transitions, a simple but tuning intensive time-controlled tilt and thrust increase is used for the dmpt. Although transitions are feasible with that, maintaining the desired heading and altitude is hardly possible. The pilot struggles with the changing sensitivities and control allocations dependent on the progress of the transition. E.g. at the beginning of transition, the throttle lever controls both hpt and dmpt vertical thrust. At the end of transition, only hpt vertical

thrust is controlled as the dmpt is in horizontal position already. A vertical thrust stick input then affects the pitch motion. The limits of the simple flight control software seem to be reached. A tendency to roll to the right during transition can be explained with the hpt rotor's asymmetric lift under forward airspeed. The abrupt engagement of hover mode for inbound transition leads to a slight pitch down and gain in altitude.

While sufficient pitch control authority is not an issue for the tAt_htp neither in transition nor in wing-borne flight, roll authority is considered insufficient for manual, RC-like piloting. Average bank-to-bank roll rates of around $p = 20\,\frac{^\circ}{\mathrm{s}}$ respectively $\overline{p} = \frac{pb}{2v_c} = 0.017$ were achieved using elevons only. The design tool indicates this poor roll authority with $\overline{p} = 0.0093$ and a violation of the related controllability requirement. Adding yaw input increased the roll rates by around 50%. This increased roll rate is sufficient for foresighted manual piloting within VLOS. Stopping the dmpt leads to a slight reduction in roll rate as the thrust vector contribution is missing then. Differential thrust together with the vertical tail fin provides decent yaw control and stability.

6.3.2 Flight Performance Data Comparison

Figures 6.5 to 6.7 plot relevant performance figures of the flight test against the prediction of the design tool.

Both inward up and inward down wingtip propeller rotations are included. The percent numbers in the plots give the deviation of the design tool prediction to the average of both inflight measurements (normalized by the latter).

Hover power consumption is overestimated by +5%, which leads to a corresponding underestimation of the overall figure of merit FM (see fig. 6.5a). Using rpm information of the dmpt and test stand data, the static thrust coefficient $c_{T0,dmpt}$ and dmpt propeller figure of merit $FM_{prop,dmpt}$ can be compared. While the measured and modeled $c_{T0,dmpt}$ show good agreement, $FM_{prop,dmpt}$ deviates significantly. This error is attributed to the fitted propeller coefficient model which does not cover well the used propeller's figure of merit based on its pitch-to-diameter ratio. Due to the low thrust share of the dmpt in hover (<7%), this error's bias on the total hover power consumption remains small.

Figure 6.5b shows an increasing underestimation of the wing-borne power consumption, respectively overprediction of $LD\eta_{pwtr}$ with airspeed. The good repeatability between measurements with opposite propeller directions increases the trustworthiness of the measurements. The insignificant difference in opposite propeller directions further aligns with the tool prediction of <2% power reduction due to wingtip propulsion. The sink rate polars in fig. 6.5c suggest drag modeling as the source for the tool's underprediction of wing-borne power consumption. Data fits based on simple quadratic $c_L - c_D$ polars as shape functions show a difference in the zero drag coefficient. This conforms with the airspeed dependent growth of the prediction error. The tool does not consider fuselage and nacelle drag increase due to a changed AoA. Also a minor misalignment

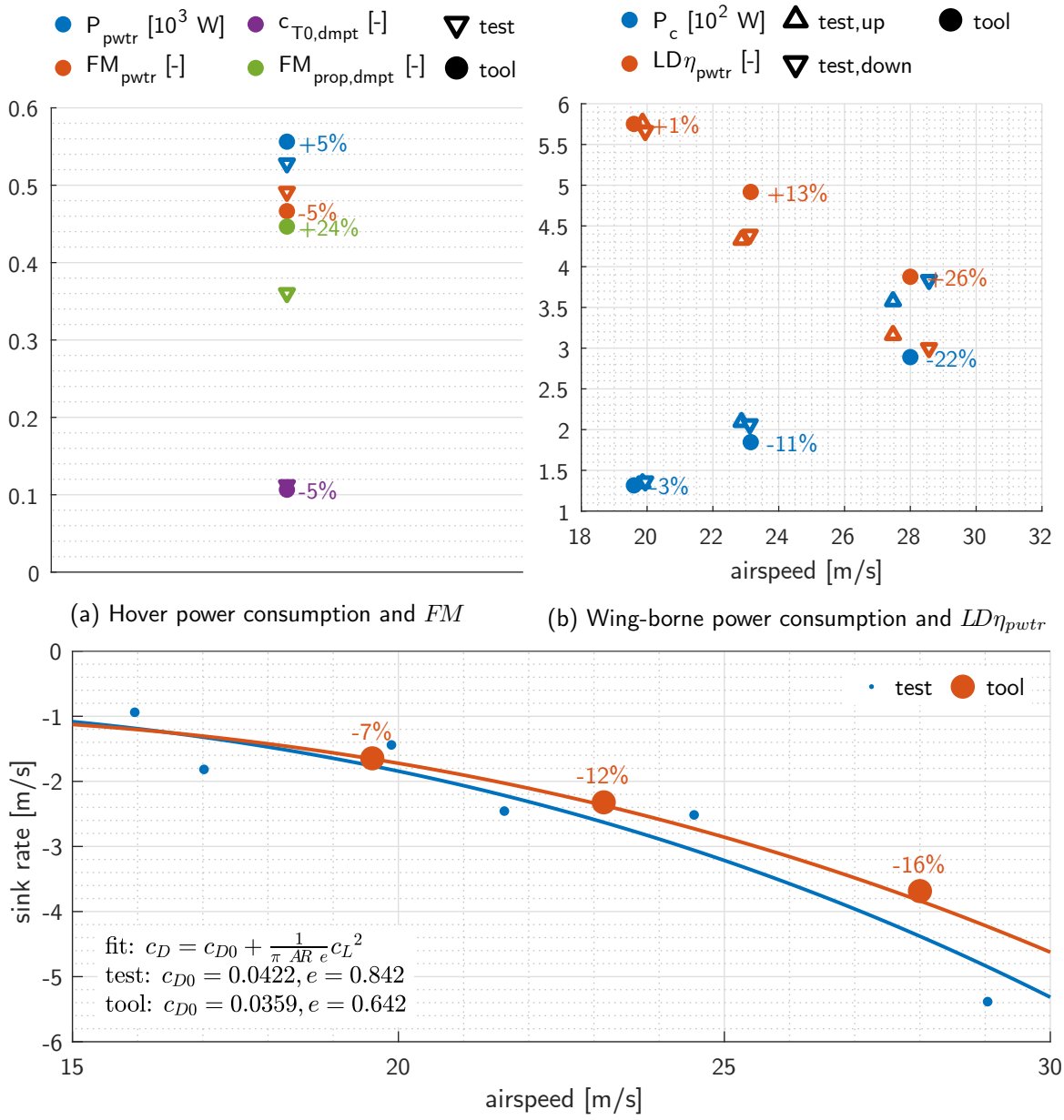

(a) Hover power consumption and FM

(b) Wing-borne power consumption and $LD\eta_{pwtr}$

(c) Wing-borne drag polar

Figure 6.5: Flight test segment average values and tool predictions for hover, powered and powerless wing-borne flight of the qPt_push prototype

of the hover rotors is visible in some flight test videos. Generally, the non-streamlined shape of the prototype fuselage provides several sources of too optimistic drag assessment. The deviation in Oswald efficiency e may be attributed to the limited flexibility of the chosen drag polar shape function and the minor share of induced drag at the considered airspeeds.

For figs. 6.6a and 6.6b, the measurements of $LD\eta_{pwtr}$ and sink rate are combined with propeller wind tunnel data to isolate the efficiencies of powertrain components. Therefore, the glide ratio LD for every flight state is calculated from the previously fitted $c_L - c_D$ drag polar and divided from $LD\eta_{pwtr}$. In correspondence to the sink rate polar, the glide ratio is constantly overestimated by the tool by roughly 10%. In total, the overall powertrain efficiencies match reasonably well. Instead

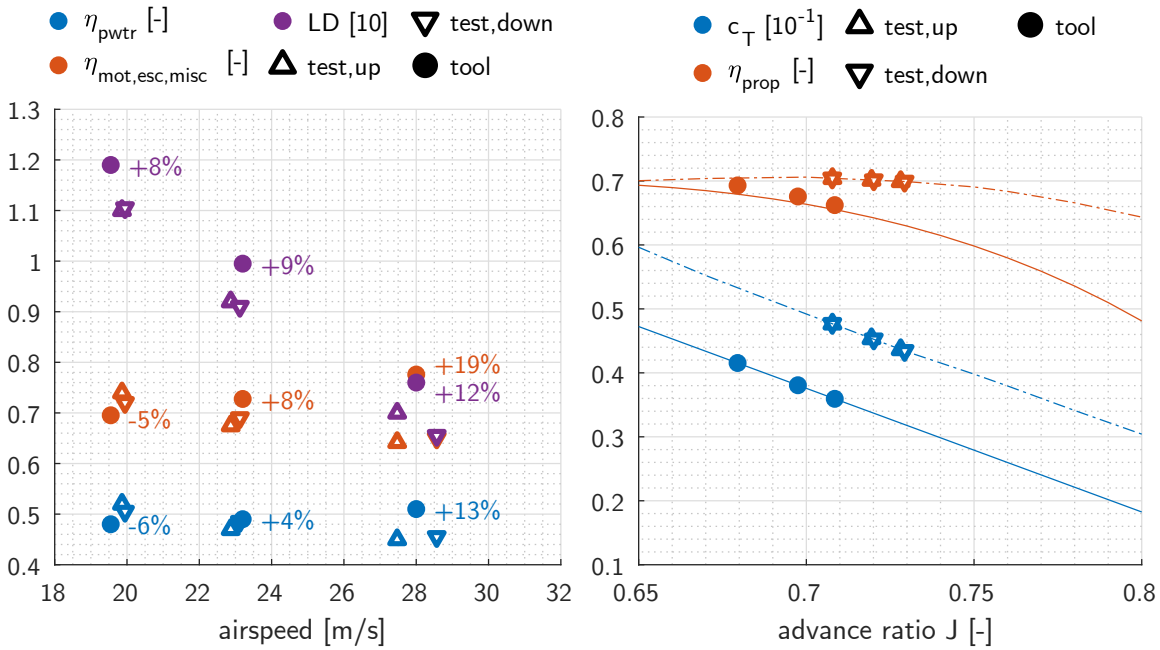

(a) Wing-borne powertrain efficiencies and LD

(b) Wing-borne propeller operating points

Figure 6.6: Further derived validation figures for powered wing-borne flight of the qPt_push prototype

of the tool's prediction of a slight efficiency improvement with airspeed, the measurements indicate an opposite trend. Figure 6.6b compares propeller efficiency and thrust coefficient as predicted by the tool against wind tunnel data. The advance ratio of zero thrust J_0 which is assigned to the model based on the propellers pitch-to-diameter ratio is significantly smaller than the wind tunnel value. The propeller in the tool behaves like a propeller with lower pitch. It however needs to operate at only marginally higher rpm (which can be seen in the lower advance ratios) as the tool's thrust requirement is smaller than in reality (see LD). The propeller efficiencies generally differ only little as the operating points lie in a region of the efficiency curves with low slope. It must be kept in mind, that using the drag polar fit and propeller wind tunnel data for the latter calculations further increases the error level.

Figure 6.7 visualizes the motor operating points for the two powertrain types hpt and dmpt in their different flight conditions as the tool calculates. The angular velocities Ω are normalized with the angular velocity under zero load. For the hpt, all operating conditions use a narrow band in angular velocity. Motor efficiency is high as the motor is operated under relatively light loading. This makes sense as the motors were selected based on a maximum aircraft mass of 5 kg compared to the actual mass of 3.87 kg. The dmpt operates at a significantly wider range of angular velocities and lower torque than the hpt. The angular velocities of most operating points are higher than what is required for maximum efficiency. Due to the steep slope in this region, slightly shifted operating points can mean a noticeable efficiency variation.

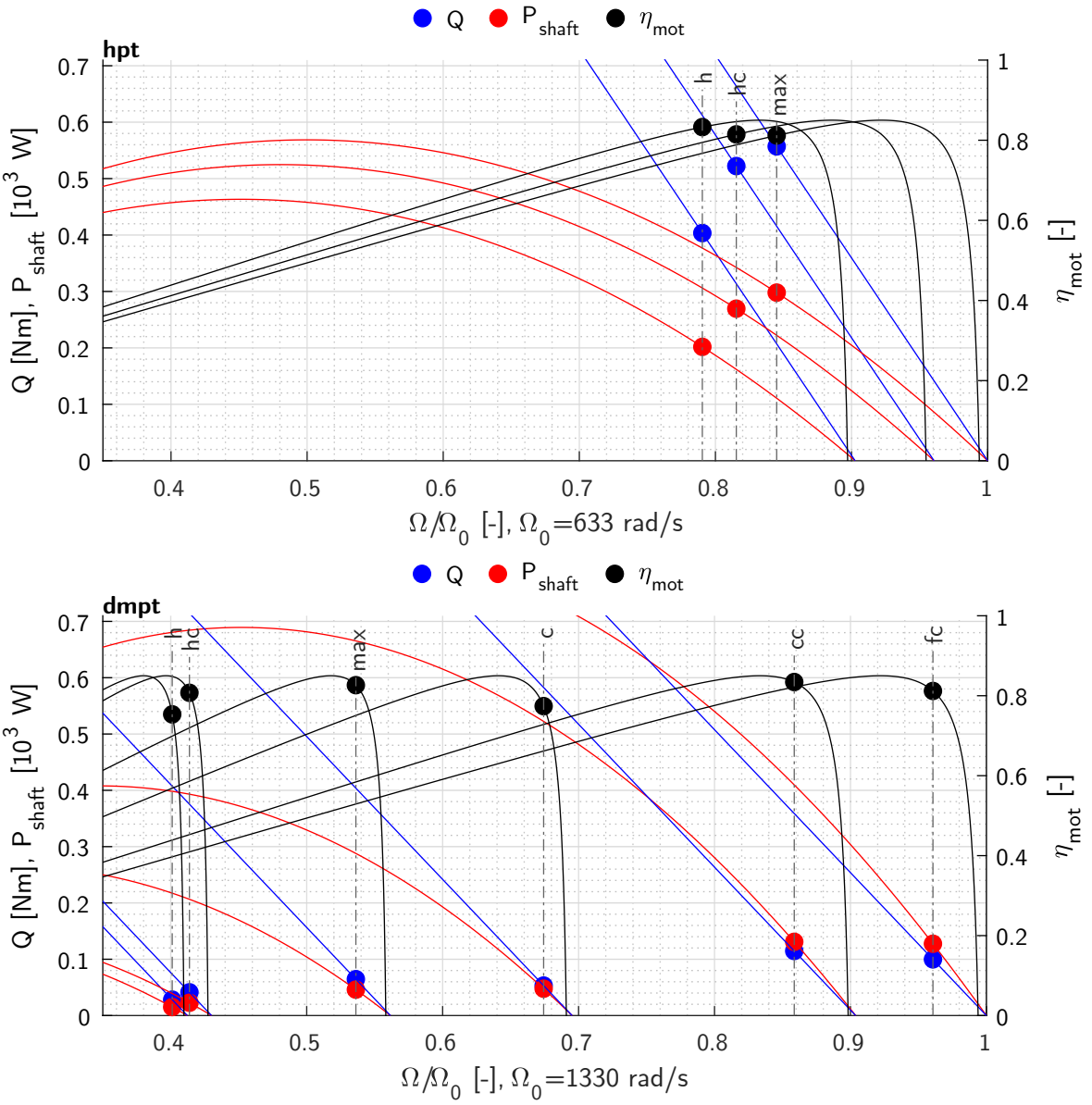

Figure 6.7: Tool prediction of qPt_push prototype's motor operating points for hpt and dmpt

6.3.3 Mass Validation

The high sensitivity of aircraft performance on battery mass fraction requires a precise prediction of all other mass components. In particular, items with high mass shares shall be validated.

The consistency of the empirical powertrain and actuator mass model is presented in section 4.10.1.

The prototype's structural construction differs too much from the tool implementation. Consequently, a database of structural masses of commercially available unmanned aircraft is compiled and used as validation basis (see fig. 6.8). The consulted aircraft are predominantly radio-controlled soaring competition aircraft of competition classes F3F, F3B, F3J (Gavrylko 2020, Rondel 2020). Their design load cases can be considered close to what is required for a fixed-wing VTOL UAV. Due to the extremely slim fuselage cross sections and missing fuselage geometry, the database only contains structural masses of lifting surfaces. The structural mass data of the range optimized

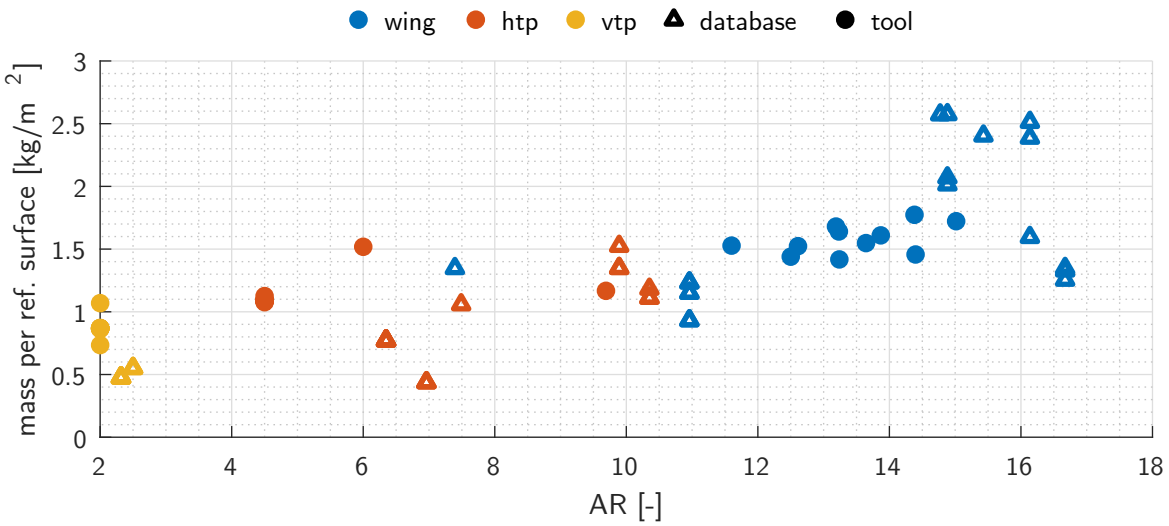

Figure 6.8: Validation of lifting surfaces' structural mass of range-optimized configurations (see section 5.1) against a commercial product database

fixed-wing VTOL aircraft of section 5.1 fit to the database values very well. Empennage surface masses tend to be overestimated by the tool.

6.3.4 Motor and ESC Performance Validation

Due to the limited fidelity level of the data derived from inflight measurements in section 6.3.2, the combined motor and ESC performance is validated using dynamometer test stand measurements.

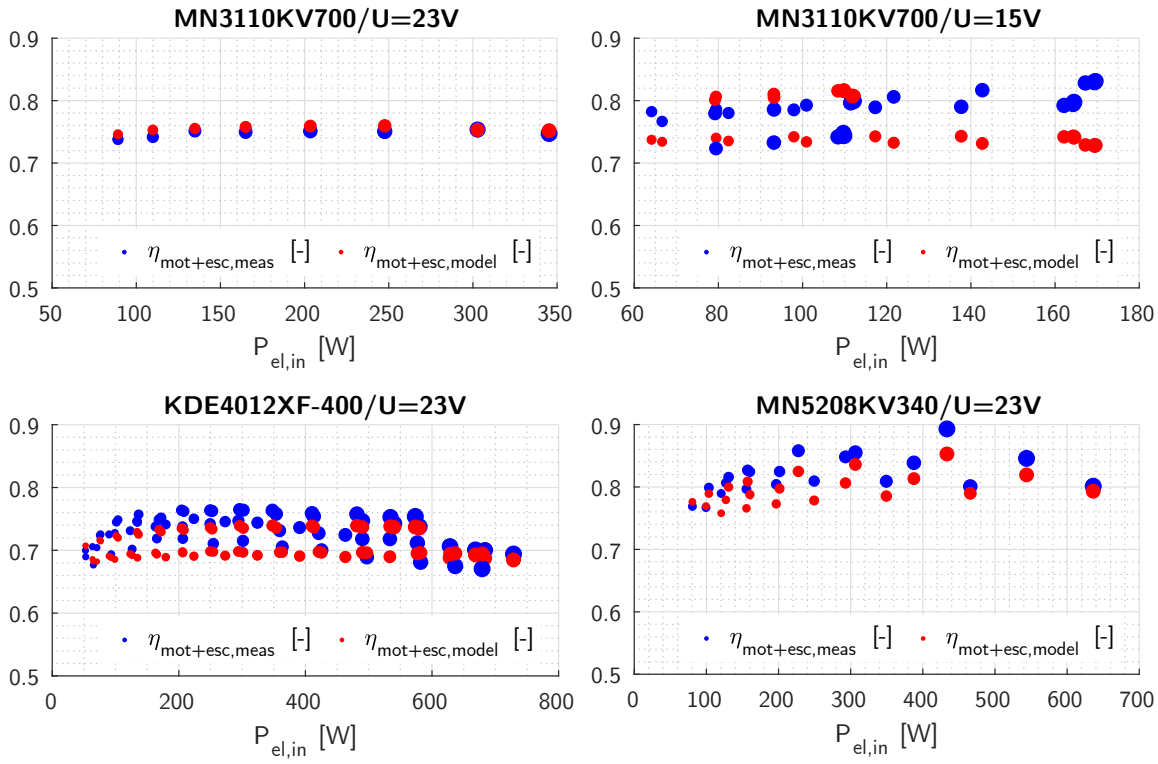

Figure 6.9: Validation of electric motor and ESC efficiency model against propulsion test stand data

The measurement data is obtained from manufacturers (KDE Direct 2020, T-Motor 2020) and own test campaigns. After validity checks, the database contains 25 motor-ESC combinations, each under at least one load curve and one voltage level.

Figure 6.9 illustrates the agreement of combined motor and ESC efficiency between test data and model for some of the motors in the database. Inconsistent disagreement is for example present for the MN3110 motor. Despite similar parameters, the good agreement under 23 V is not evident for 15 V operating voltage.

7 Conclusion

This chapter recapitulates the main achievements and findings of this thesis. It furthermore proposes fields of further research which emerged during the presented investigations.

7.1 Key Findings and Scientific Contribution

Answering the central research question

How is the flight performance and economy of small fixed-wing electric VTOL UAV affected by overall aircraft layout and specific subsystems?

breaks down in the following subjects:

What are key drivers for the flight performance and economy?

A simple initial sensitivity study as well as the evaluation of a conceptual aircraft design study identify the following factors to have a significant impact on range. Range serves as one metric for flight performance.

- The battery's fraction in total aircraft mass influences the amount of energy that can be spent to propel the aircraft in two ways. It obviously represents the amount of aircraft mass that carries energy. Furthermore, if the power demand of the aircraft is distributed over more battery mass, battery types with higher energy per mass can be used in theory. Higher battery mass fractions can be achieved if structural, powertrain or systems masses can be reduced.
- How much gain in battery energy density can be realized, if less specific battery power capability is required, depends on the range and specifications of the battery cells the aircraft designer can choose from. Also the selected battery architecture plays a role.
- The aerodynamic glide ratio, cruise powertrain efficiency and the reference energy density of the considered battery technology level all show a similar, proportional impact on range.
- A low disk loading and high figure of merit of the hover powertrain reduce the power demand in hover, and by that slightly improve the wing-borne range. On the one hand, the reduced energy consumption in the hover flight phase leaves more energy to the wing-borne flight and, on the other hand, allows to choose a battery type with higher energy density. The range increase is evident although a reduction in disk loading means larger rotors which generate higher aerodynamic drag when stopped for wing-borne flight.
- Both hover figure of merit and cruise powertrain efficiency degrade if the same powertrain needs to be designed for operation in hover and cruise condition. These dual-mode or tilt powertrains however can achieve an advantage in powertrain mass compared to the usage of separate powertrains for hover and cruise propulsion. For the studied exemplary survey mission, a range optimum is reached if around 80 to 85% of the total required hover thrust is provided by hover-only powertrains and the rest is contributed by a dual-mode powertrain.

The cost per area for a survey mission is used as a measure for the economy. The predominant design parameter here is cruise velocity. It determines the duration of a mission and thus the major cost component of operator salary. That cost item constitutes around two thirds of the total survey cost. The second biggest cost component is maintenance.

Which aircraft configurations can address and mitigate these sensitivities?
Two aircraft configurations are proposed, built and test flown in the course of this thesis.

- The qPt configuration (and their derivatives) features two hover-only rotors mounted on the back of the fuselage and one tilt powertrain is located on each of the left and right wing. As no nacelles are required to mount the rotors, the surface friction drag and structural mass are low. The pairwise powertrain arrangement on the longitudinal and lateral aircraft axis allows to establish the optimal ratio of hover thrust contribution for the tilt powertrains independent of geometric lever arm ratio restrictions. The actuators of the tilt powertrains are used to move the ailerons in order to save system mass.
- The tAt_htp configuration uses one hover-only powertrain at the fuselage nose and one tilt powertrain at each tip of the horizontal tailplane. The tilt actuators also move the elevon control surfaces. Ailerons on the wing can be omitted if the aircraft cruises at high airspeed. The primary goal of this configuration is to minimize the number of powertrains and actuators for a maintenance cost advantage.

Which aircraft subsystems address and contribute to mitigate these sensitivities?

- The majority of the considered aircraft configurations feature hover-only powertrains. If their rotors stop in random positions for wing-borne flight, they cause significant aerodynamic drag. Three different approaches are developed that aim to minimize the range penalty of these stopped rotors. Commercially available systems which address this problem are still very rare to date.

  A first approach aligns the rotor with the fuselage in a low drag position by a precisely timed braking of the motor. This system can be retrofit to off-the-shelf and widely used RC-type electronic speed controllers at minimal cost.

  The second system aligns and additionally retracts the rotor into a recess on the back of the fuselage. The additional drag saving can not compensate the higher mass and system complexity.

  In a third approach, the stopped rotor blades passively fold to the rear due to their aerodynamic drag force. For larger rotors, a vibration problem occurs from the lead-lag degree of freedom which the rotor blades require to fold.

  Among the three system approaches, the first yields the highest vehicle range at moderate system complexity and low cost.

- Several architectures to connect one high-power and one high-energy battery to the different

powertrains of a fixed-wing VTOL aircraft are proposed. The intention is to increase the overall energy density of the battery system if the short high power demand of vertical flight is mainly provided by a small high-power battery, while a large energy dense battery can be used to supply wing-borne flight.

How is a fair comparison and performance assessment of different aircraft configurations and subsystems performed?

A conceptual aircraft design tool chain is used for this purpose. The following points are considered especially important for its implementation:

- The methods within this tool chain are chosen to consider the individual characteristics of the aircraft configurations as much as possible. One main difference is the type and arrangement of the powertrains. That is why, for example, the structural mass of lifting surfaces, nacelles and fuselages is analytically sized to account for the influence of the powertrain location, thrust and mass. Unlike the current state of the art, the powertrains are further sized for several hover maneuverability requirements that consider the vehicle geometry, inertia and powertrain layout. Installed rotor thrust is penalized dependent on the geometry of the support structure inside the slipstream. As literature data was not available, the aerodynamic drag of stopped rotors is assessed in a wind tunnel experiment and modeled correspondingly.
- A matching of powertrain components is required to cover the impact of the widely different operating points of tilt powertrains. Usually manufacturer data sets of individual powertrain components are used within the corresponding methods. An undesired bias can however be introduced to the configuration comparison as the individual components can have different technology levels, manufacturing quality or data errors. Therefore, generalized models for the powertrain components are developed. The rotor and propeller coefficients are modeled based on their pitch-to-diameter ratio. The model is derived from regressions of wind tunnel data. A simple efficiency model for the electronic speed controller is calibrated from dynamometer measurements. A common electric motor model is reformulated to exhibit equal peak efficiencies.
- To ensure the correctness and trustworthiness of the results, the individual models and the tool chain as a whole are validated wherever possible. For the latter, the two implemented configurations are used to gather test flight data which is compared against the tool chain predictions. Hereby, hover power consumption is overestimated by 5%. Dependent on the flight state, cruise power consumption is underestimated by between 3 and 22%. Controllability deficits of one prototype are correctly indicated by the design tool.
- To enhance the fairness in comparison, all aircraft and subsystems are optimized for the corresponding target function by a genetic algorithm. This approach is supported by the time-efficient computational methods of conceptual design.

- A meaningful and practice oriented evaluation metric must be chosen. Range and endurance are selected as usual performance metric, they however widely neglect the interests of a commercial aircraft operator. Therefore, the cost for a standard survey mission is calculated. It better weighs relevant aspects like physical aircraft performance, labor times, infrastructure cost and system complexity. Experimental cost components like the stochastically expected cost of an aircraft crash extends common cost modeling and can give indications for an optimal redundancy architecture. Here as well, the goal is to address the differences between the configurations.

What is the quantitative performance benefit caused by the choice of aircraft configuration or usage of the above-mentioned subsystems?

Comparative design studies with 11 different aircraft configurations are performed using the previously described design tool chain. Each of the 5 kg aircraft carries a 0.8 kg payload and is optimized for each of the target functions minimal cost for an exemplary survey mission, maximum range and maximum endurance.

The cost optimization drives all cruise airspeeds to the upper limit to reduce the mission time and related dominant labor cost. Survey mission cost ranges in a narrow band of 18.4 to 19.1 $\frac{EUR}{km^2}$. The lowest cost are achieved by tAt_htp, qPt_push, tAt_wing and the twin-boom lift+cruise configuration qXc (order with increasing cost).

Range and endurance show significantly wider variances (158-200 km, 131-168 min). In both cases, the three variants of the qPt family perform best. The next best qXw configuration, a lift+cruise aircraft with wingtip powertrains, still achieves 195 km range and 157 min endurance.

Not aligning, but letting the hover-only rotor stop in a random position reduces the range of the lift+cruise configurations qXc and qXw to around 83%. The range of the qPt family degrades to around 87%. All other configurations maintain ranges above 90%. Aligning and additionally retracting the rotors leads to range reductions between 0 and 2%.

The impact of different battery architectures is studied for the qPt_push and qXc configuration. Simply connecting the high power battery to the hover-only powertrain and the high energy battery to the tilt respectively cruise powertrain only yields range improvements for battery mass fractions <35%. The qPt configuration can then realize range improvements close to 10%, while the qXc configuration only reaches around 3% at best. A scenario, in which future battery technology realizes higher energy density at the price of lower power density, enables range improvements beyond 50% over single battery architectures, even for similar and higher battery mass fractions.

7.2 Outlook

From the experience gained with the design, implementation and operation of small unmanned electric fixed-wing VTOL aircraft, the following improvements to the design procedure can be suggested:

- The proposed model for propeller coefficients can likely be improved by the addition of input parameters like e.g. solidity and a better choice of the shape functions for the regressions.
- In this design tool chain, only rough estimates are used to cover the cruise propeller efficiency degradation due to their installation at the end of a fuselage or behind the trailing edge of the main wing. As these locations are especially interesting when distributing powertrains on a VTOL aircraft, installation penalty models for these powertrain locations are required.
- Partly unsatisfactory discrepancies between predicted and measured aerodynamic drag are present. The suspected sources for this deviation need to be checked systematically.
- A dedicated validation of the consulted control evaluation criteria is still open. Further, effects like flight control law and system dynamics are not yet represented. Also, the distinction between controllability driven steady-state thrust requirements (e.g. off-center CG) and short term, overpower thrust requirements (e.g. gust compensation) have a significant influence on powertrain size.
- The transition flight phases are mostly unconsidered. The introduction of a transition distance limit however could impact powertrain sizing or even configuration choice.
- For applications like cargo transport, that need heavier aircraft to operate in noise sensitive environments, noise models suitable for conceptual design are required. These ideally also address the above mentioned powertrain installation close to aircraft structure.
- The cost model requires a larger validation basis. Also making an effort to include hard-to-quantify aspects like practicability, handling characteristics, robustness, customer preferences and market trends could lead to a better, more holistic real-world target function for aircraft design optimization.

Removing the limitations made at the beginning of this thesis are likewise points to follow up on. Although increasing the system complexity considerably, variable pitch propellers and a battery/gasoline or battery/hydrogen hybrid energy supply have the potential to improve flight performance.

This thesis could not only theoretically propose and benchmark performance-promoting and cost-reducing overall vehicle layouts and subsystems for small fixed-wing VTOL aircraft, also their practical feasibility is demonstrated. This contribution to the advancement of this aircraft class helps to make drone services more capable, more affordable and thus more widely applicable.

A Appendix

Further Design Tool Results

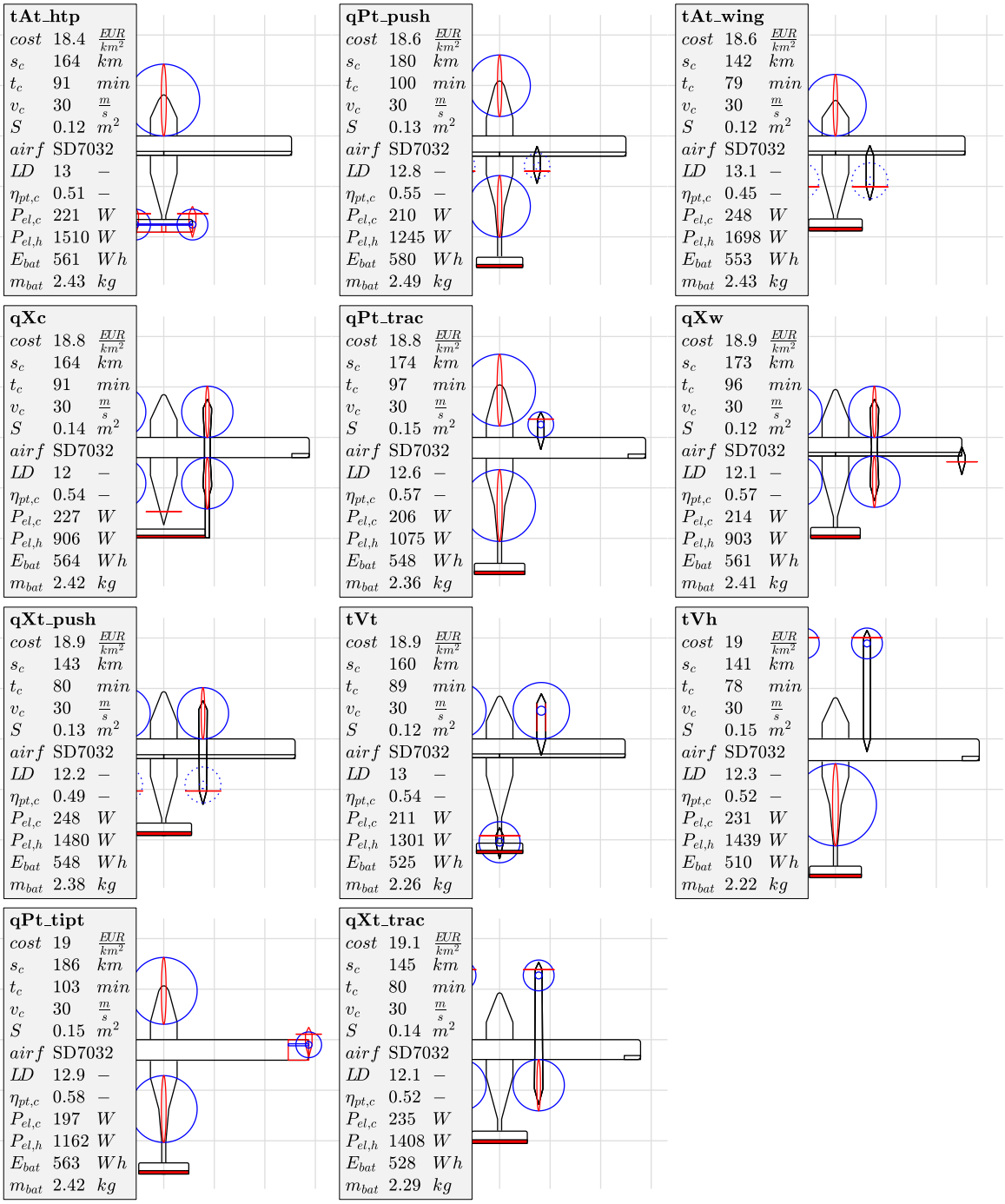

Figure A.1: Aircraft top views for cost-optimized configurations (worse in reading direction, green hpt means retracted, red elevator means redundant actuation, dotted hpt means pusher arrangement, length unit is 0.25m)

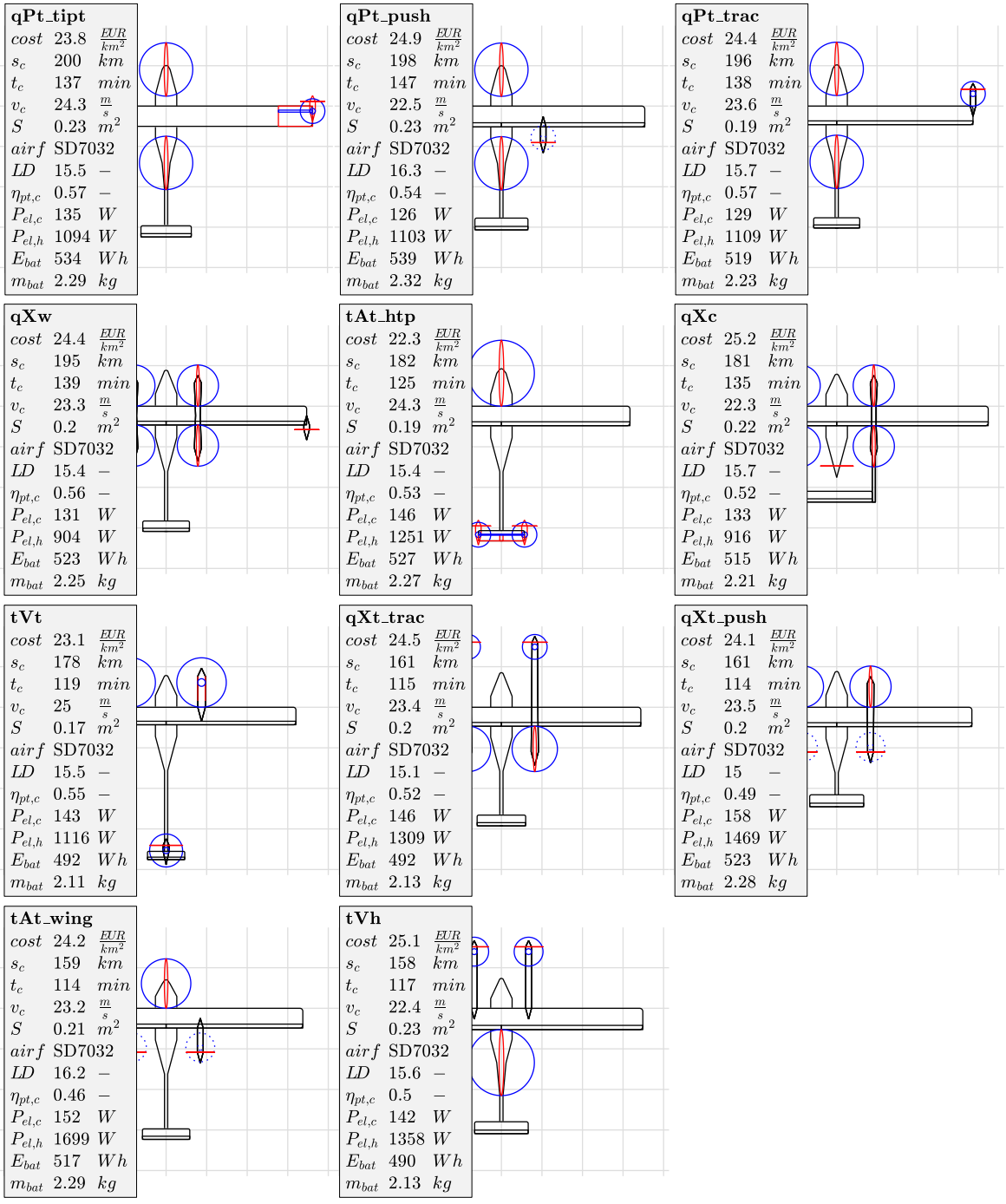

Figure A.2: Aircraft top views for range-optimized configurations (worse in reading direction, green hpt means retracted, red elevator means redundant actuation, dotted hpt means pusher arrangement, length unit is 0.25m)

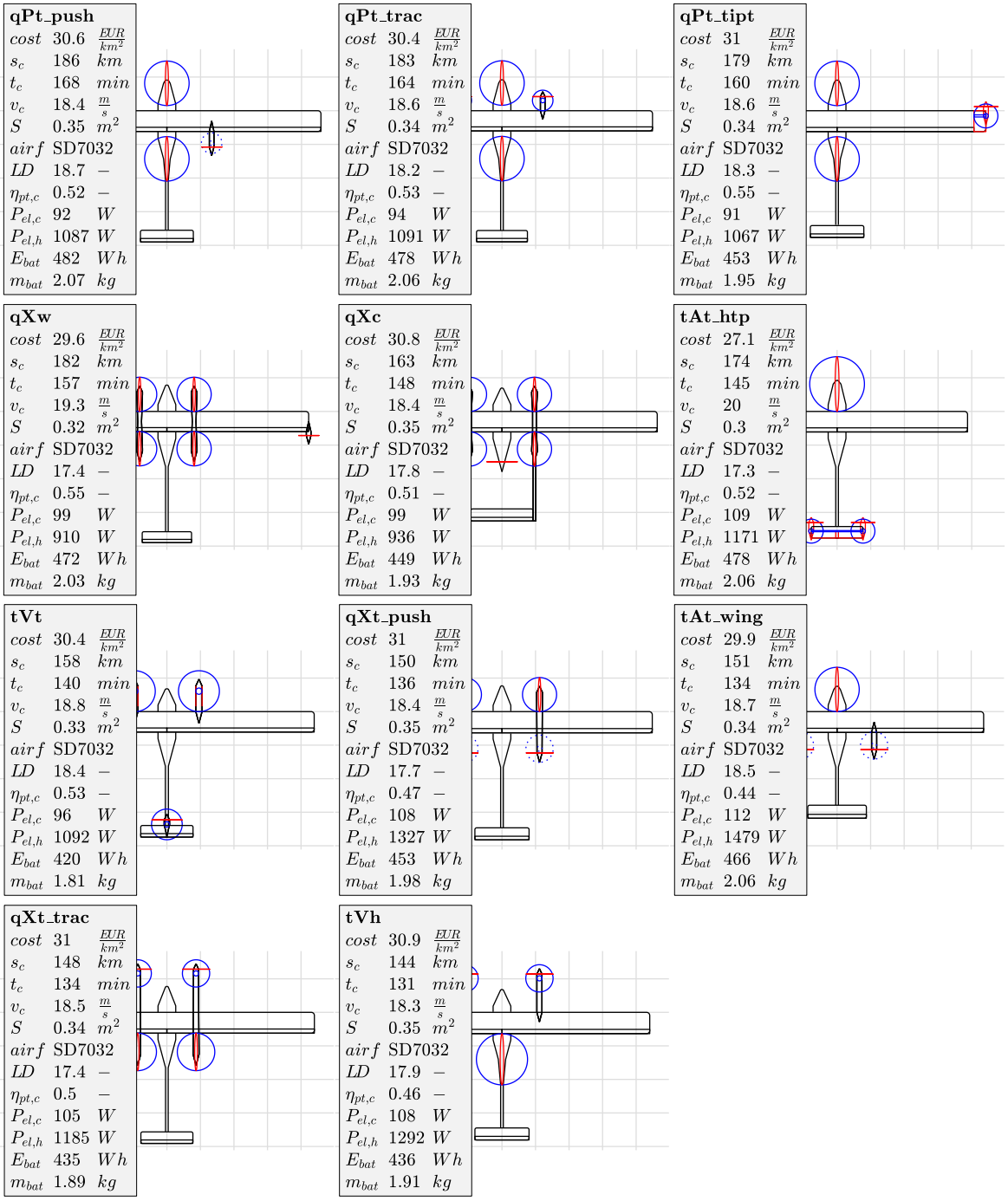

Figure A.3: Aircraft top views for endurance-optimized configurations (worse in reading direction, green hpt means retracted, red elevator means redundant actuation, dotted hpt means pusher arrangement, length unit is 0.25m)

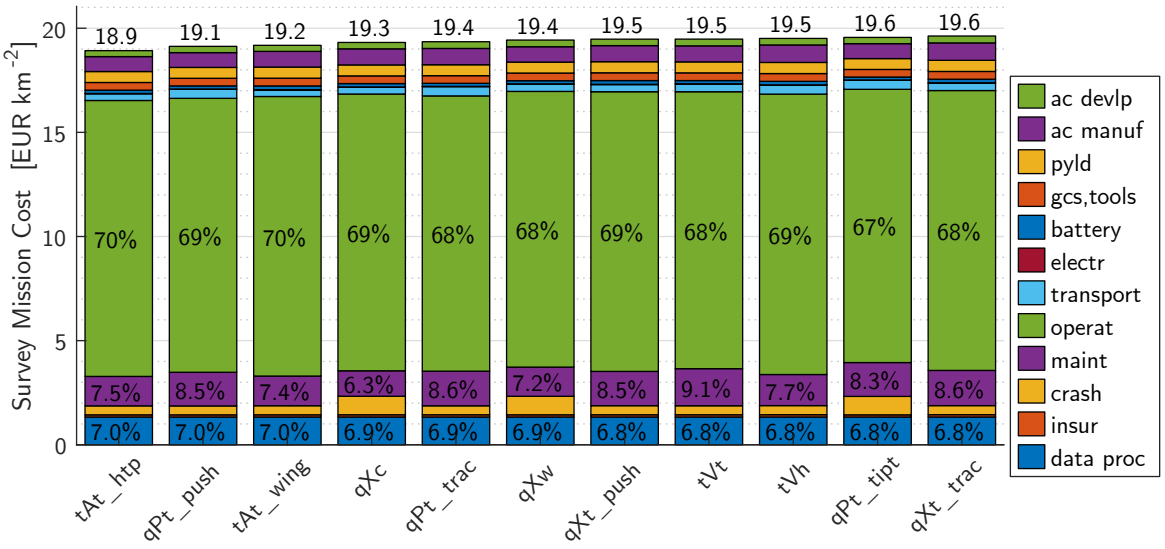

Figure A.4: Cost breakdown for cost-optimized configurations (leftmost is best)

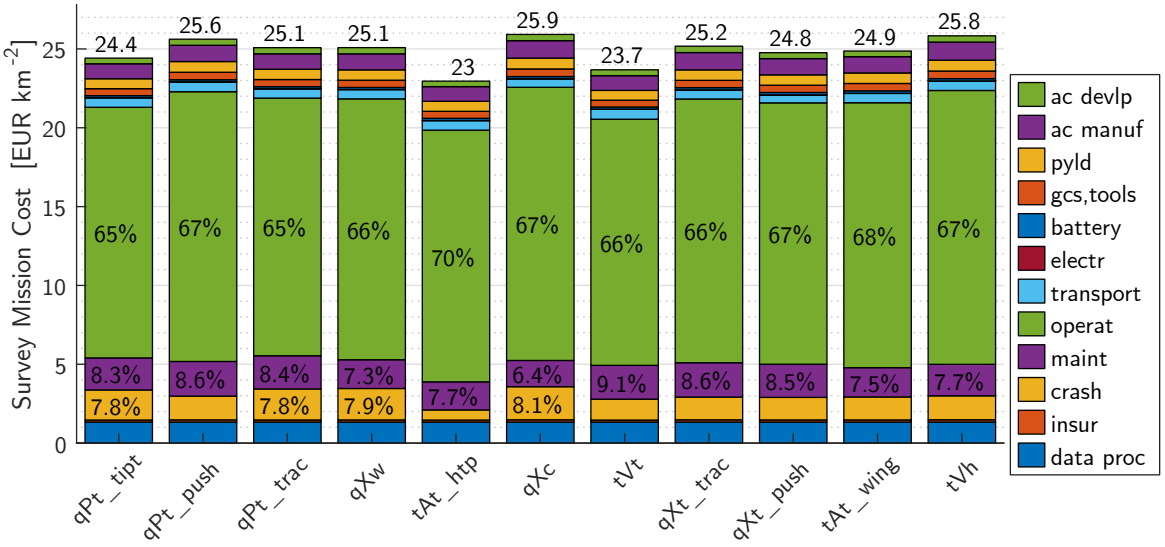

Figure A.5: Cost breakdown for range-optimized configurations (leftmost is best)

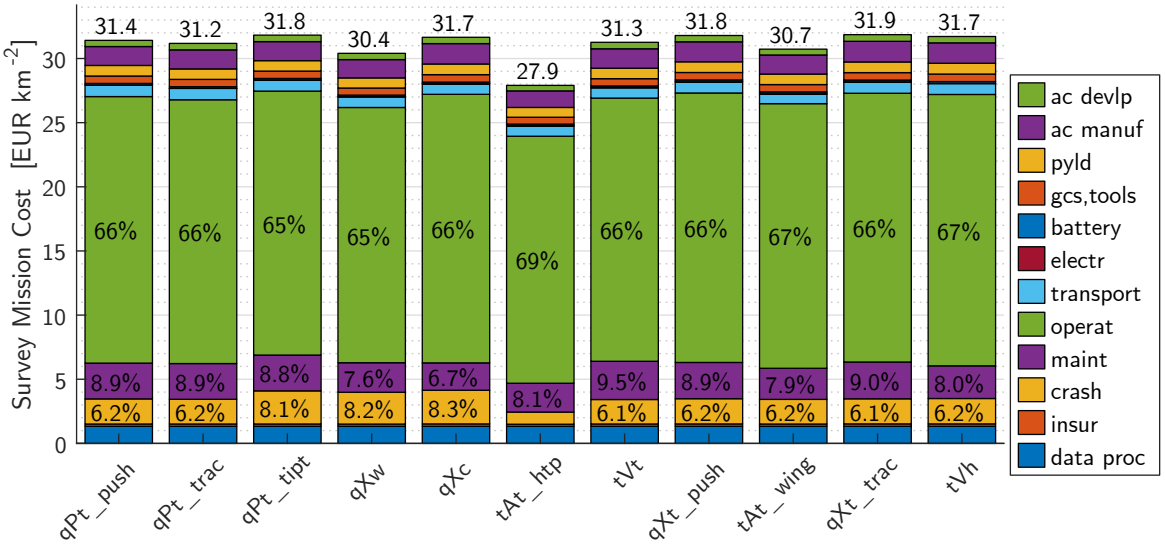

Figure A.6: Cost breakdown for endurance-optimized configurations (leftmost is best)

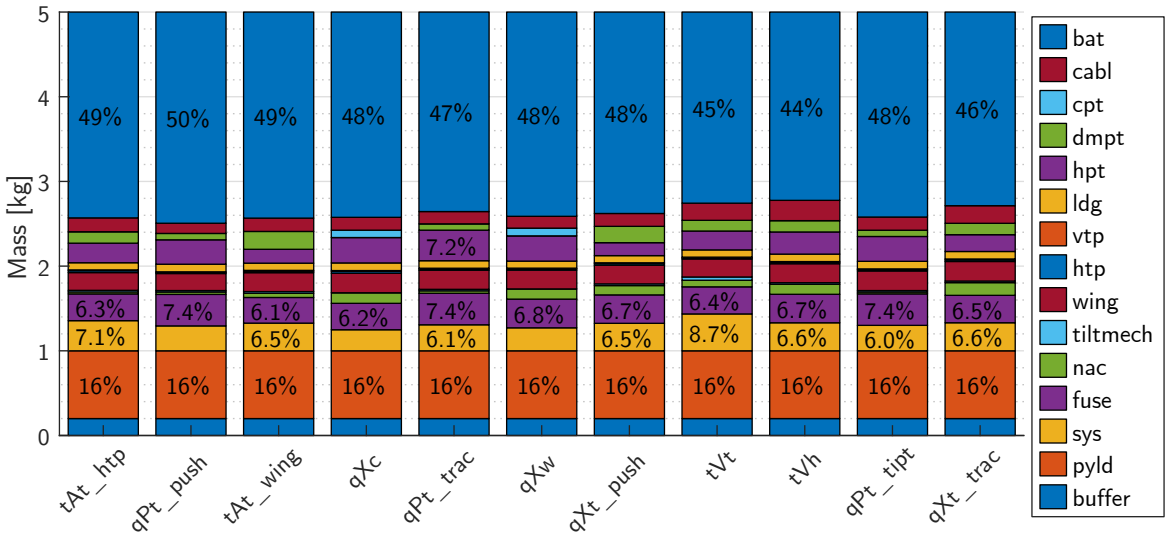

Figure A.7: Mass breakdown for cost-optimized configurations (leftmost is best)

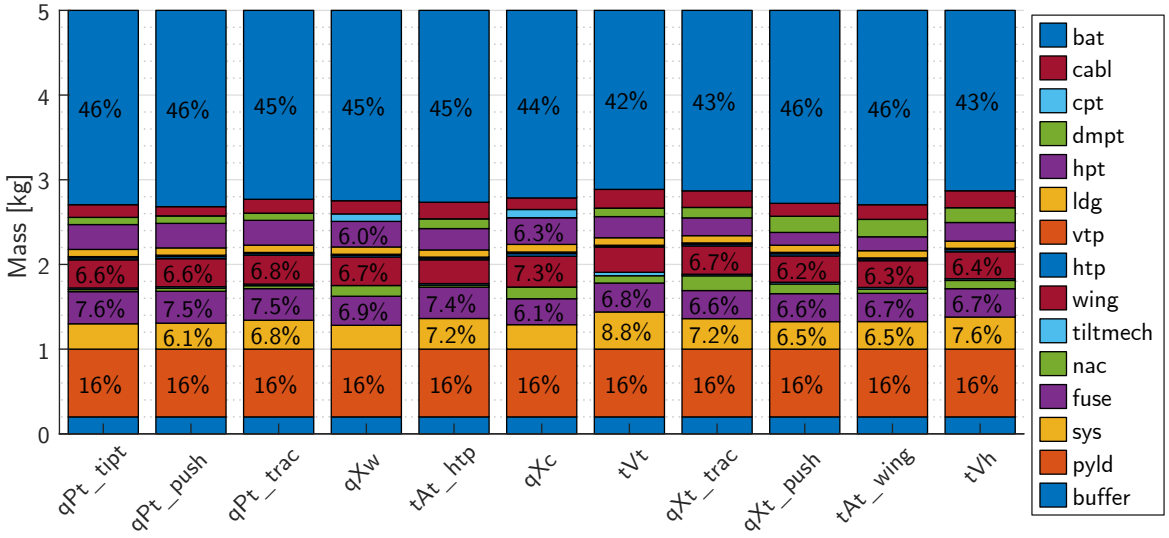

Figure A.8: Mass breakdown for range-optimized configurations (leftmost is best)

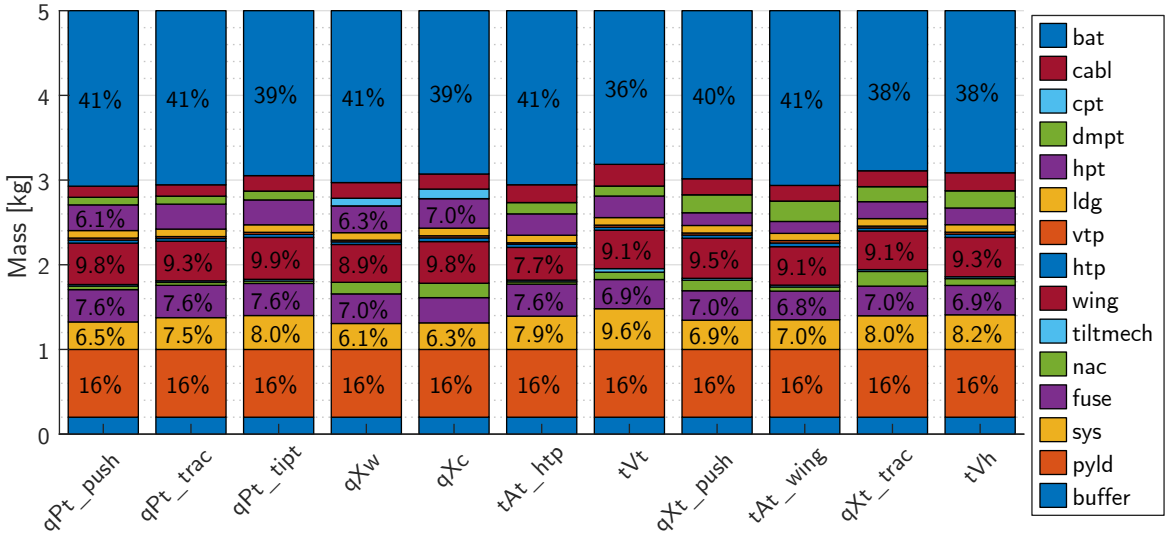

Figure A.9: Mass breakdown for endurance-optimized configurations (leftmost is best)

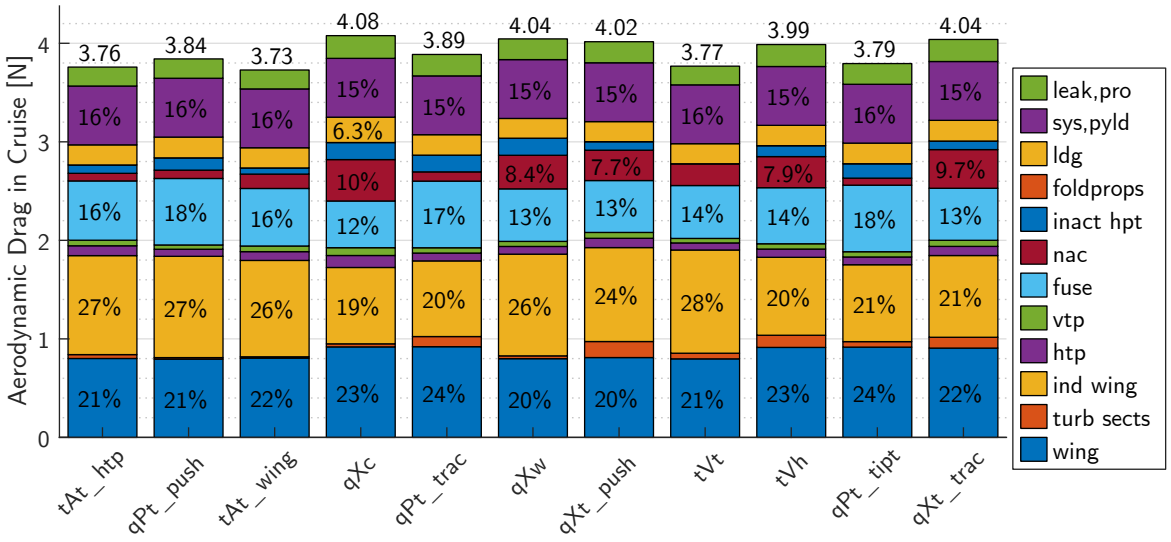

Figure A.10: Drag breakdown for cost-optimized configurations (leftmost is best)

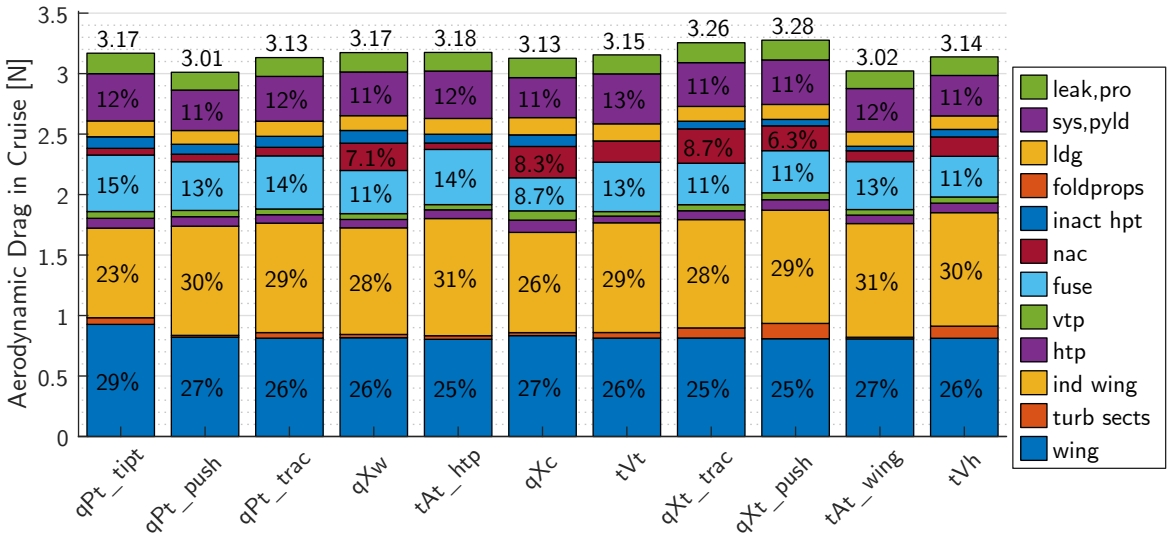

Figure A.11: Drag breakdown for range-optimized configurations (leftmost is best)

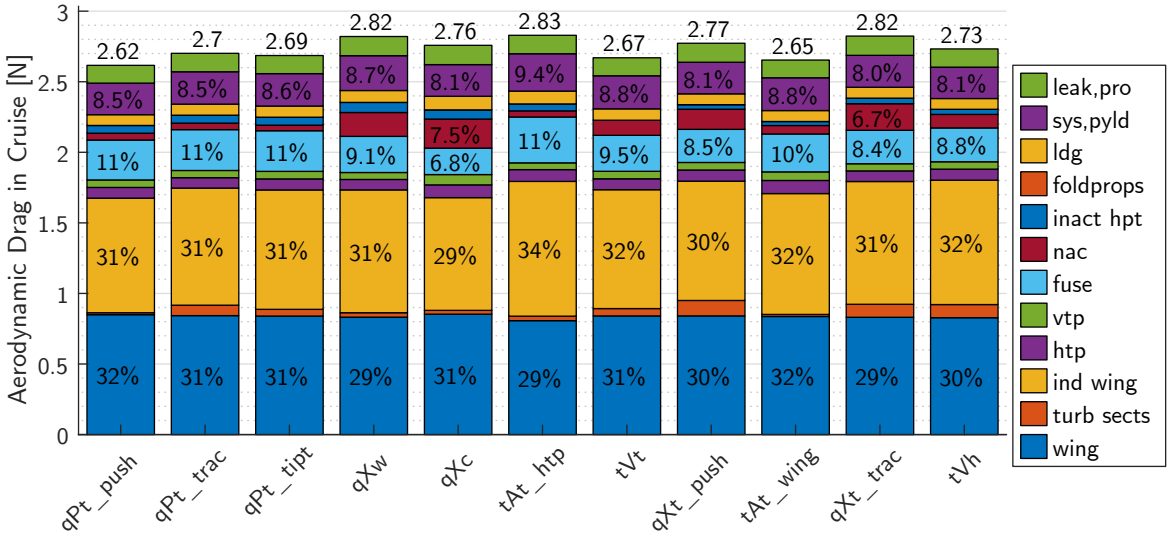

Figure A.12: Drag breakdown for endurance-optimized configurations (leftmost is best)

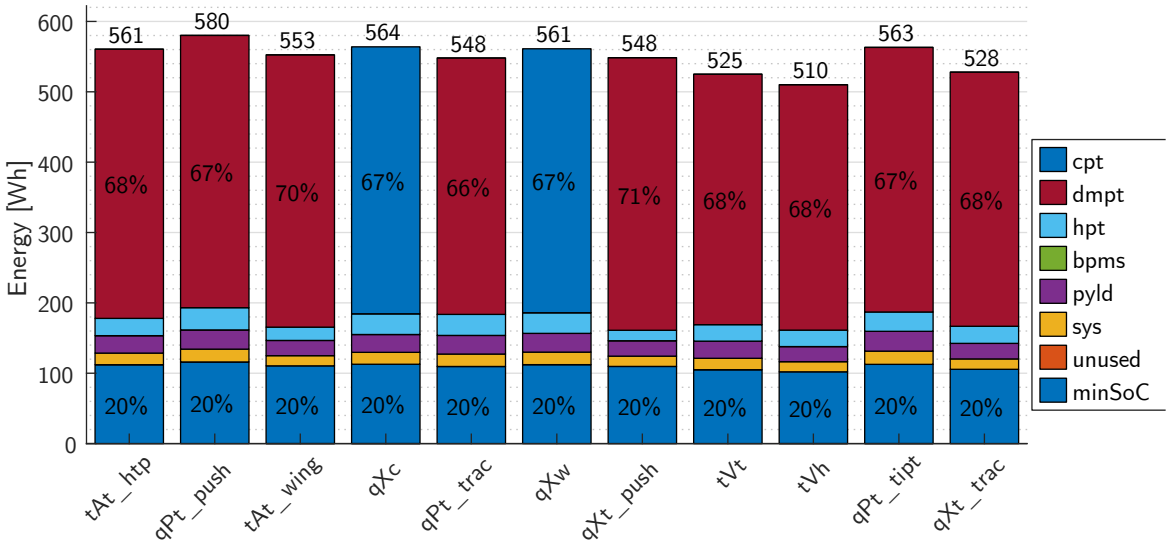

Figure A.13: System energy breakdown for cost-optimized configurations (leftmost is best)

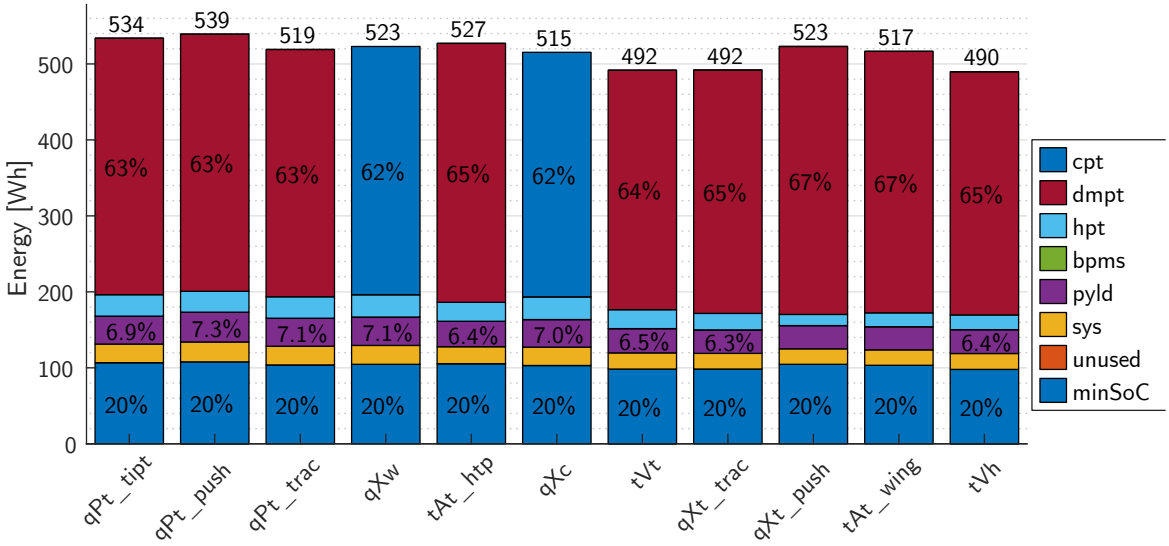

Figure A.14: System energy breakdown for range-optimized configurations (leftmost is best)

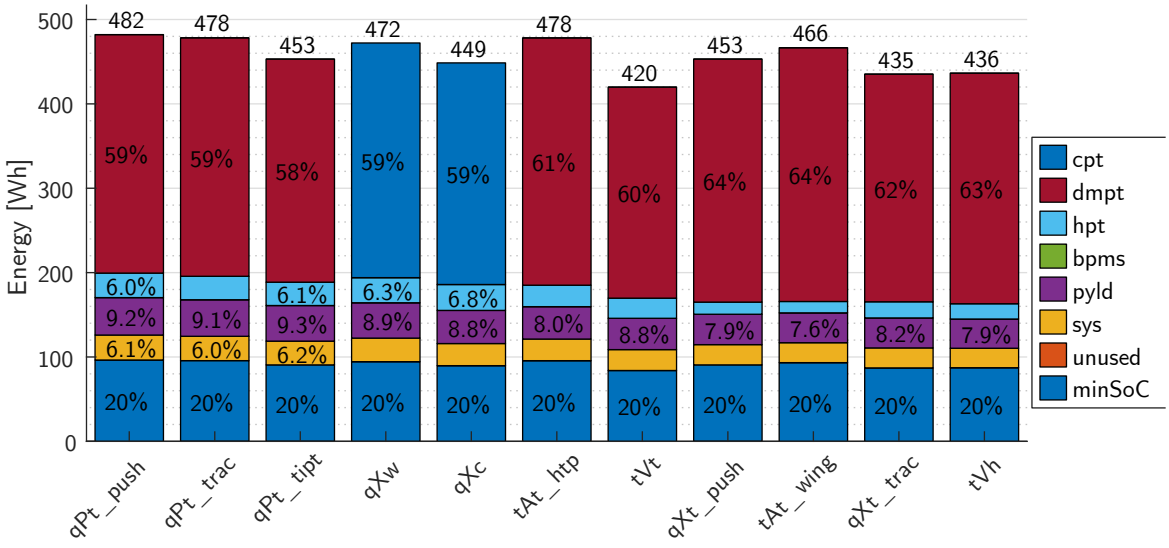

Figure A.15: System energy breakdown for endurance-optimized configurations (leftmost is best)

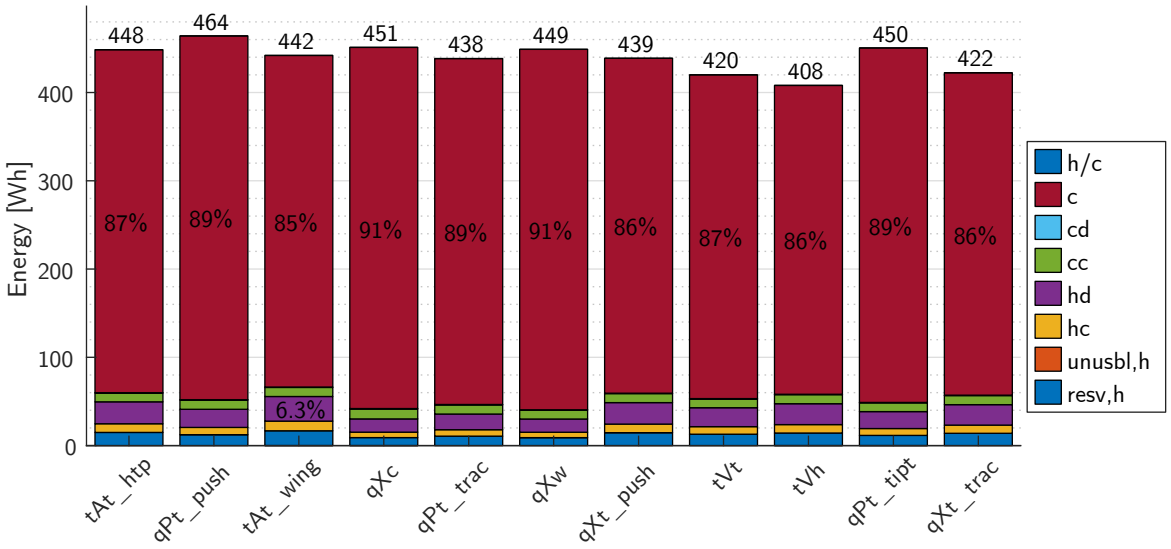

Figure A.16: Phase energy breakdown for cost-optimized configurations (leftmost is best)

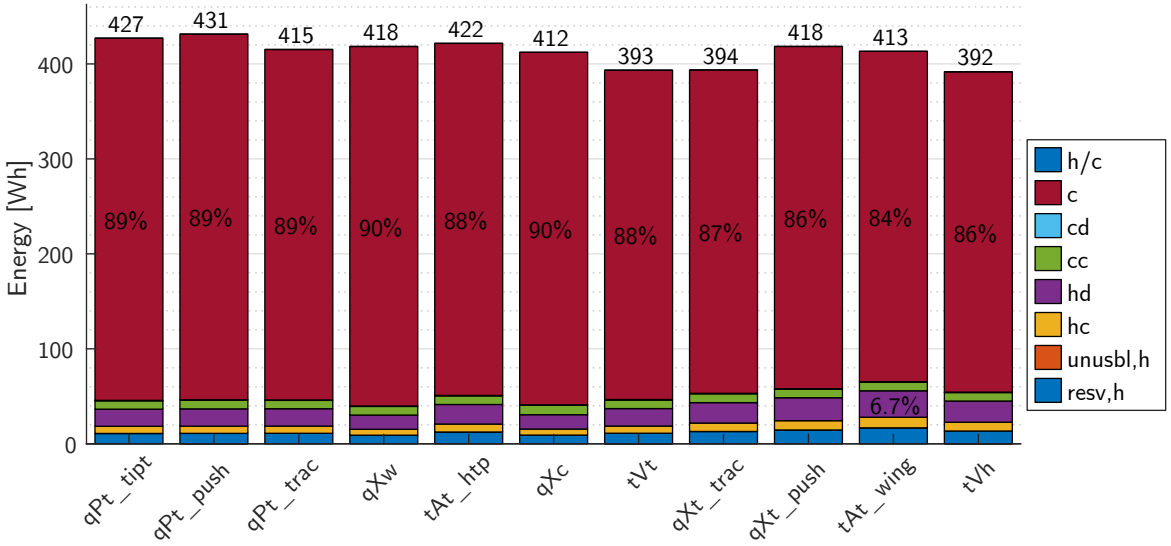

Figure A.17: Phase energy breakdown for range-optimized configurations (leftmost is best)

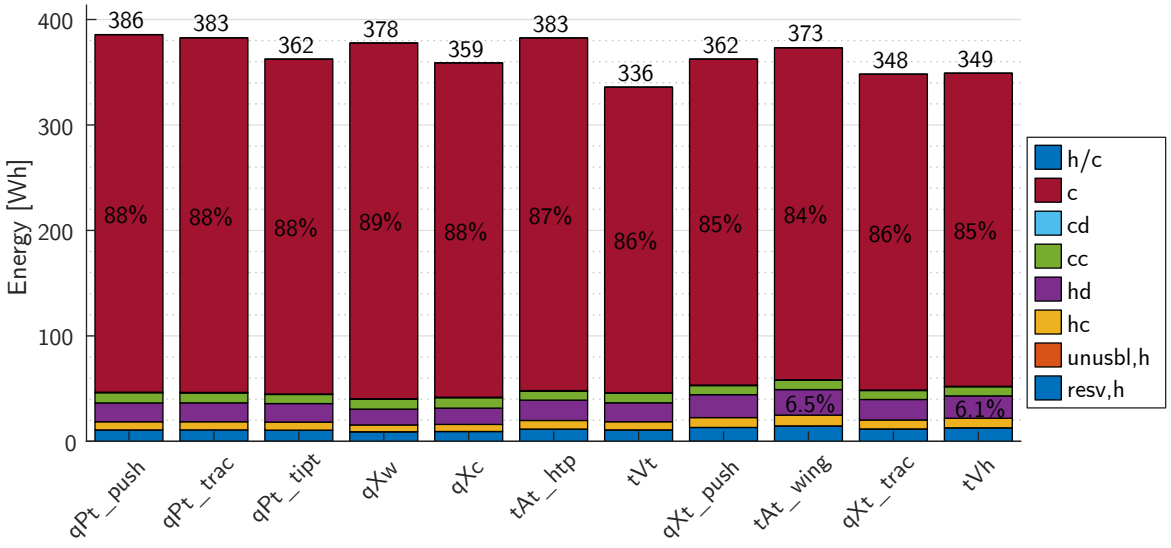

Figure A.18: Phase energy breakdown for endurance-optimized configurations (leftmost is best)

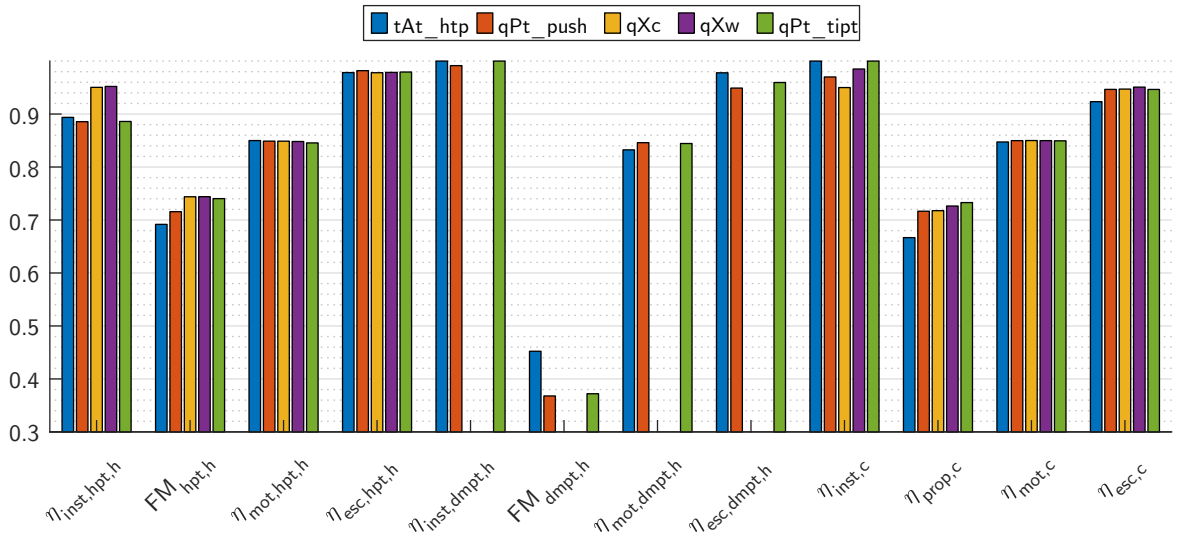

Figure A.19: Powertrain efficiency breakdown for cost-optimized configurations (leftmost is best)

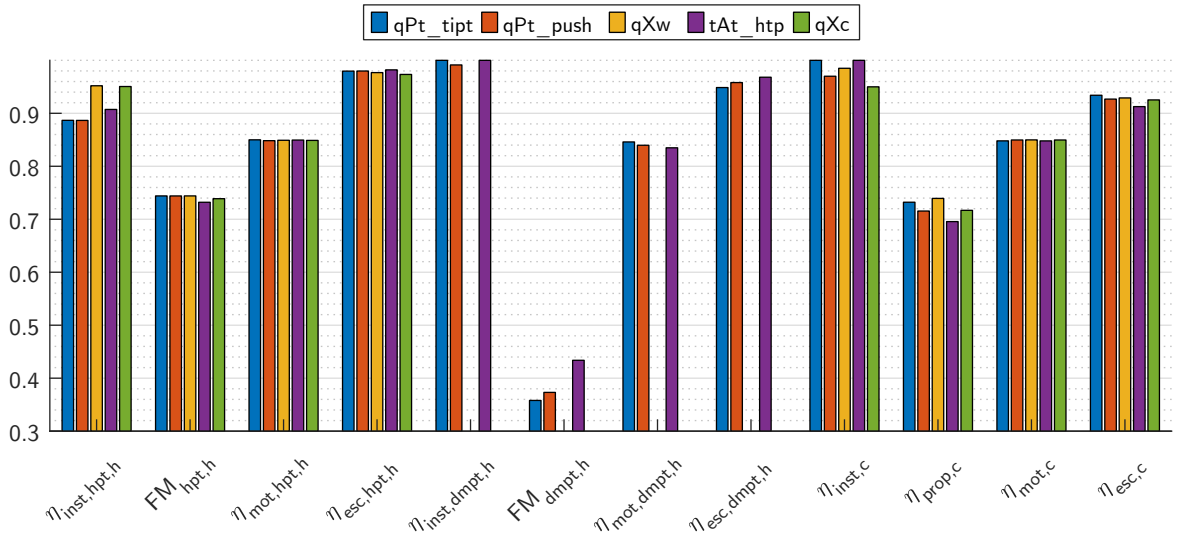

Figure A.20: Powertrain efficiency breakdown for range-optimized configurations (leftmost is best)

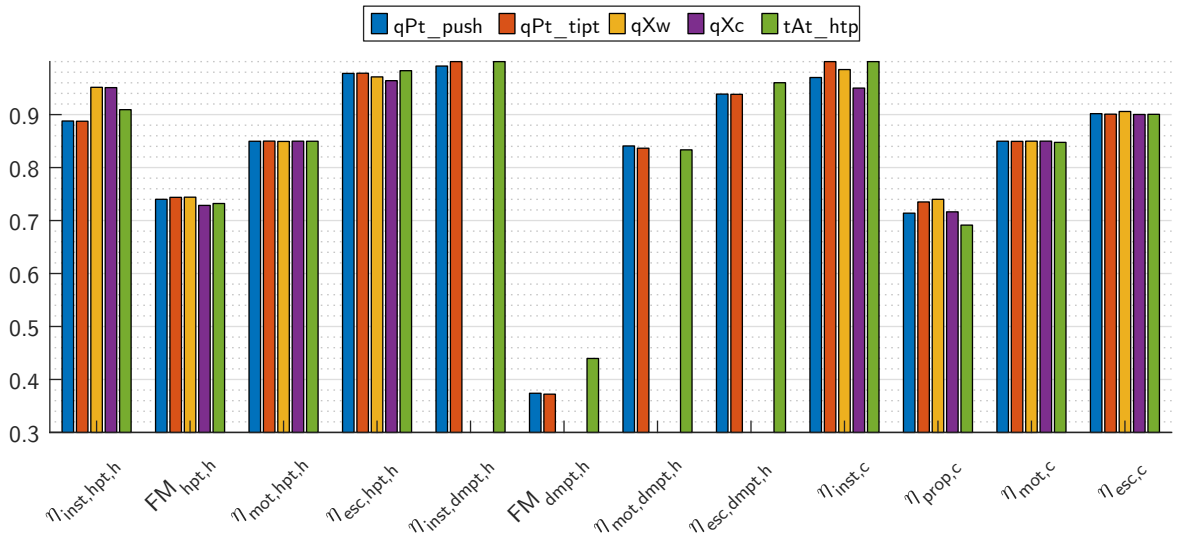

Figure A.21: Powertrain efficiency breakdown for endurance-optimized configurations (leftmost is best)

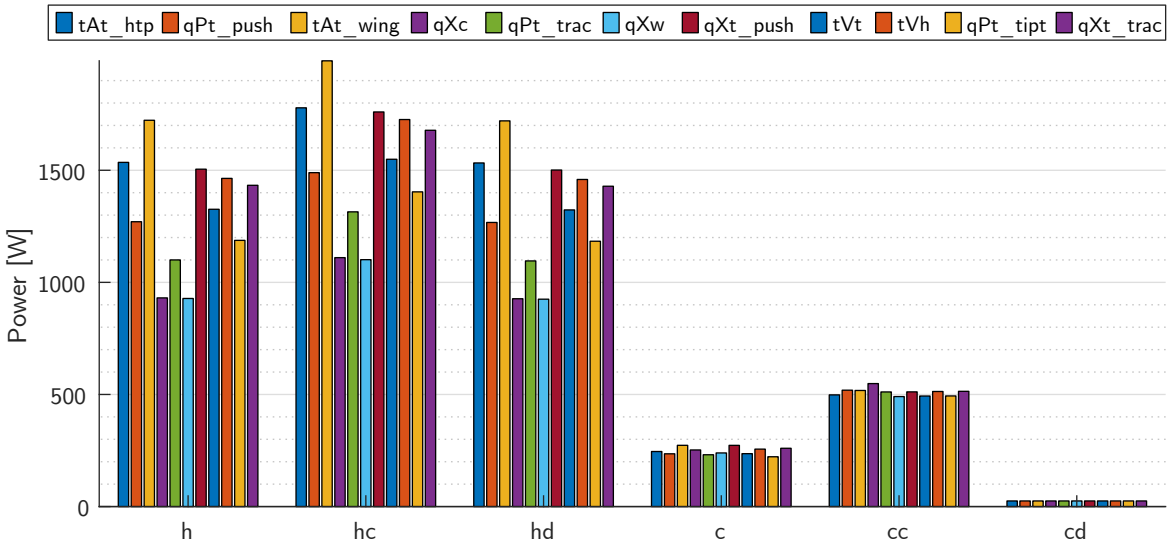

Figure A.22: Power breakdown for cost-optimized configurations (leftmost is best)

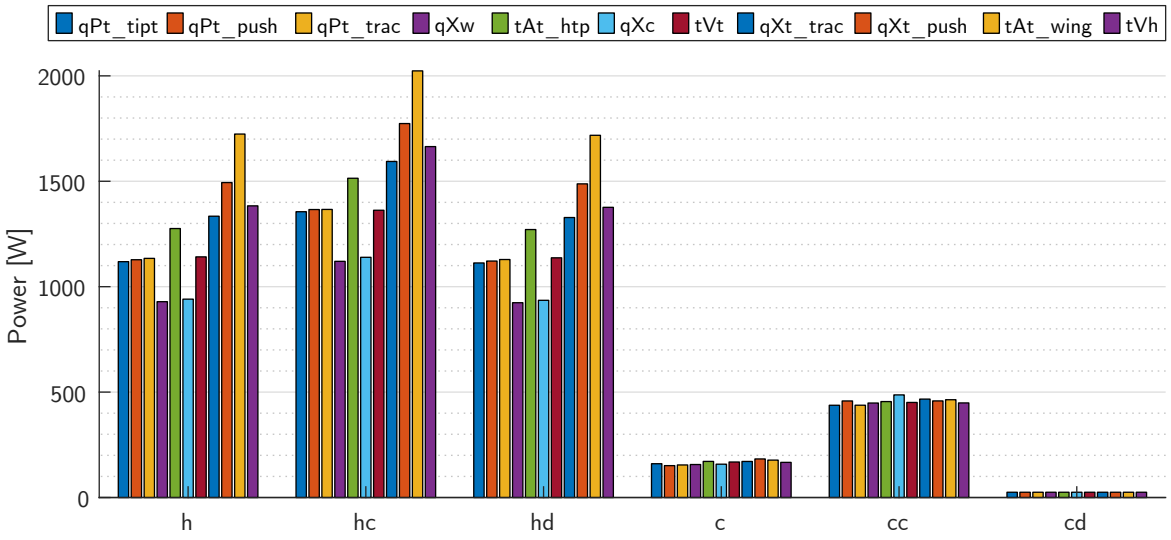

Figure A.23: Power breakdown for range-optimized configurations (leftmost is best)

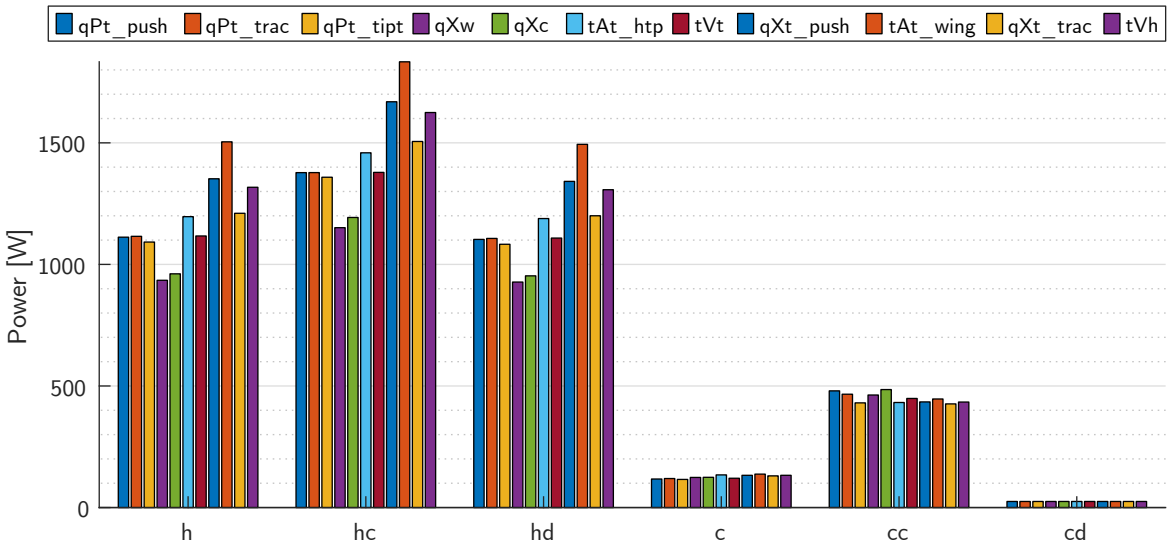

Figure A.24: Power breakdown for endurance-optimized configurations (leftmost is best)

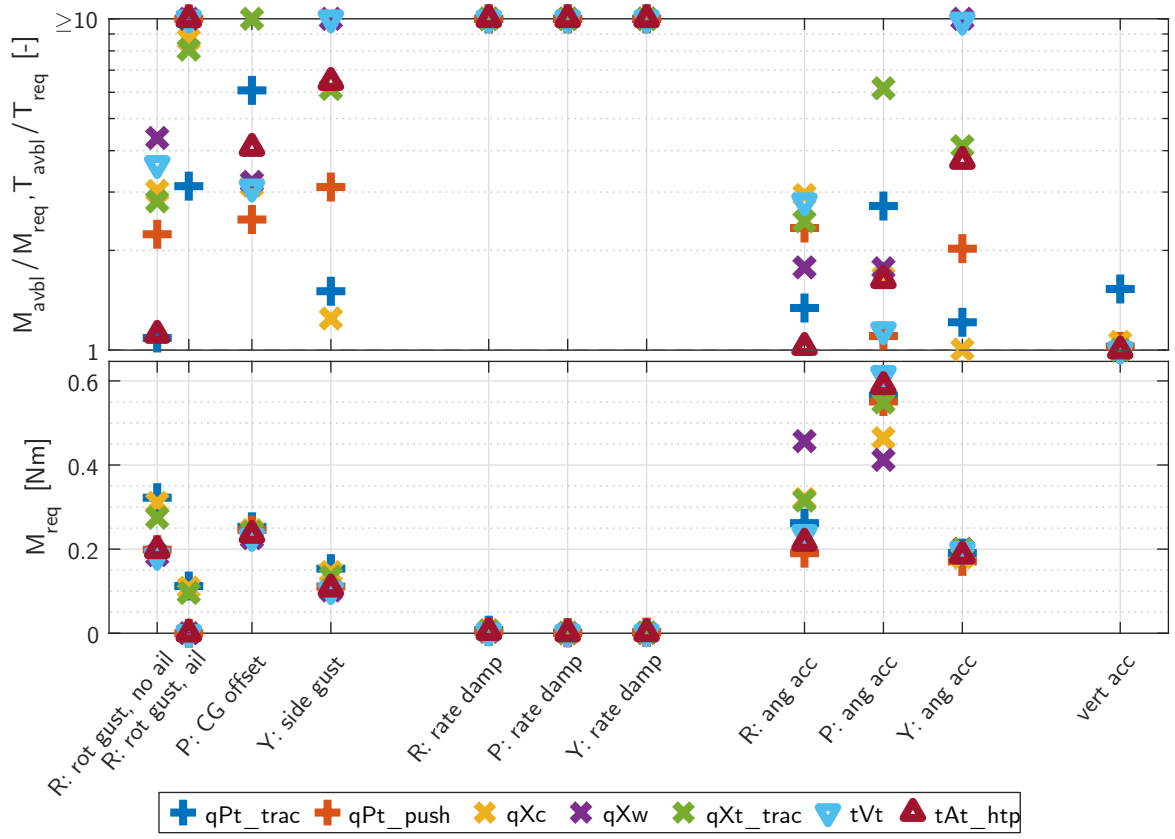

Figure A.25: Hover control figures for exemplary cost-optimized configurations

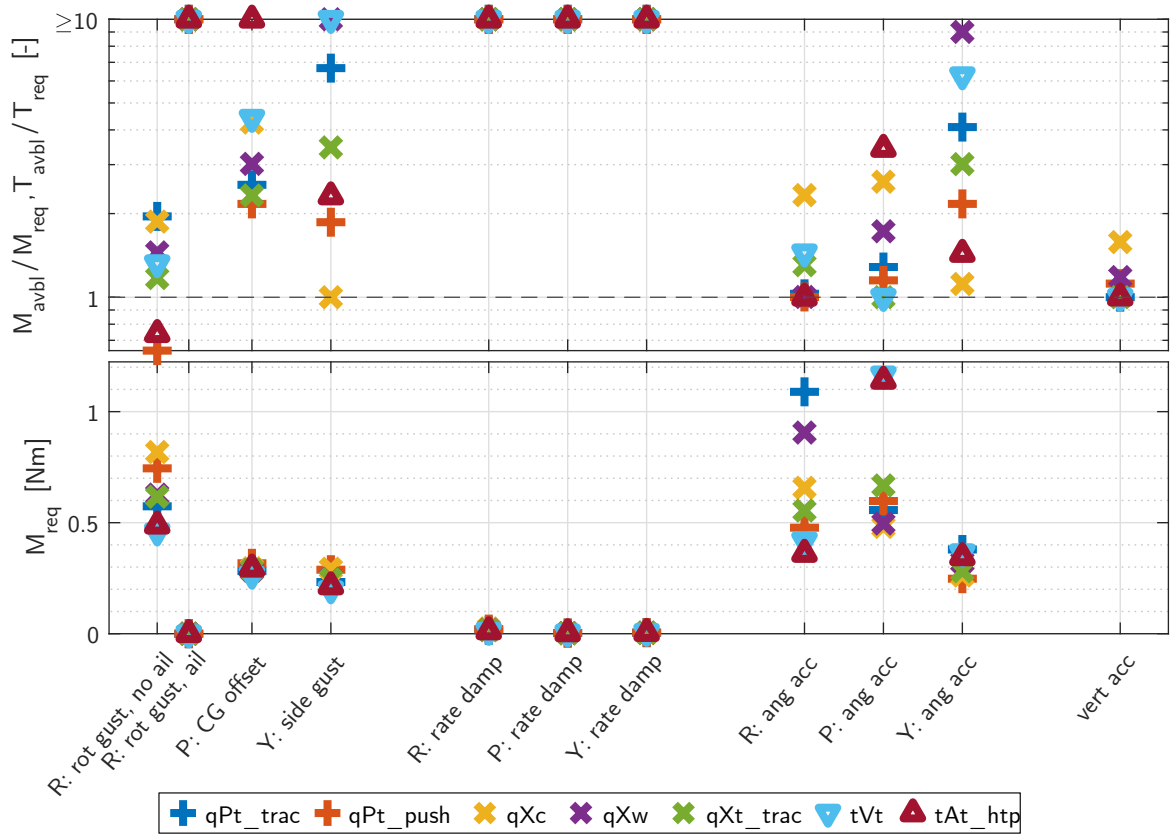

Figure A.26: Hover control figures for exemplary range-optimized configurations

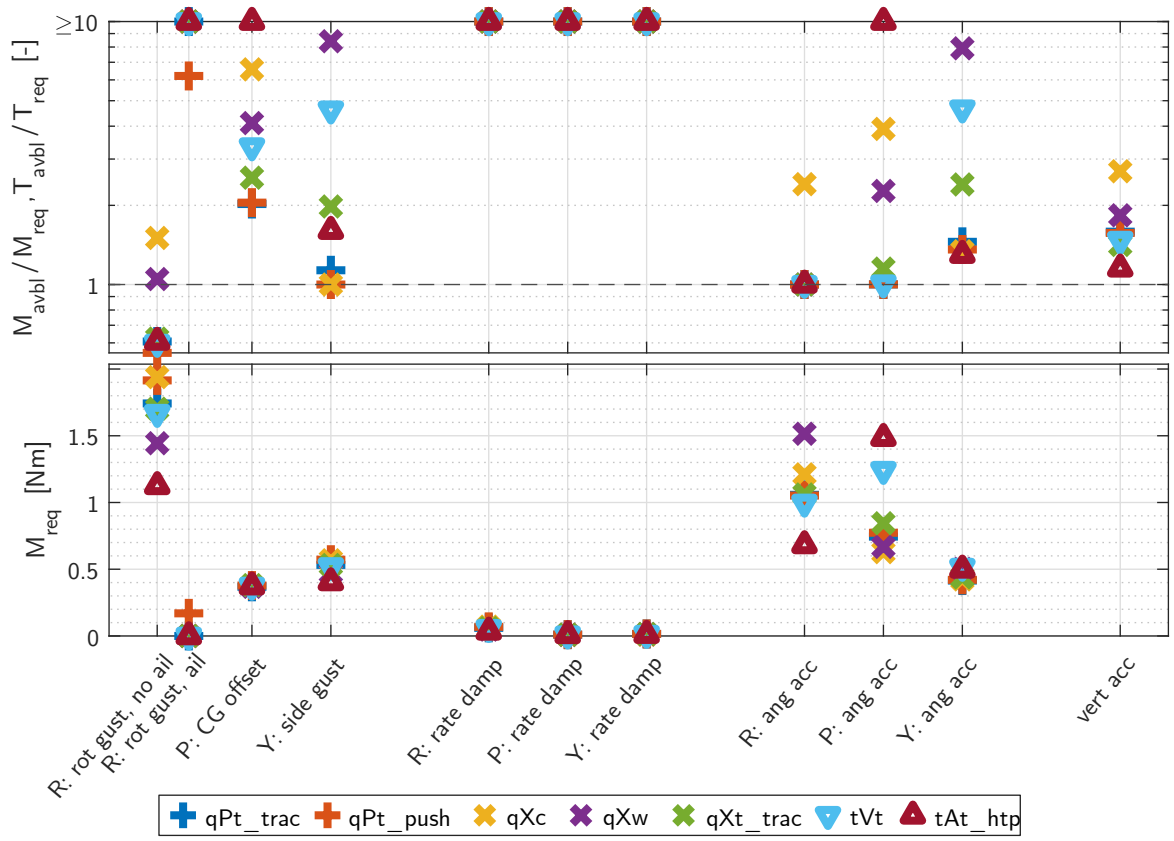

Figure A.27: Hover control figures for exemplary endurance-optimized configurations

References

AHS (2017), 'The V/STOL Wheel: V/STOL Aircraft and Propulsion Concepts'.
URL: https://vertipedia-legacy.vtol.org/vstol/wheel.htm

Akaflieg Berlin (2020), 'B13e'.
URL: https://b13e.akaflieg-berlin.de/bestandteile/

ALTIUAS (2020), 'ALTI - The world's best endurance VTOL unmanned aircraft fleet'.
URL: https://www.altiuas.com/

Amazon (2016), 'Amazon Prime Air'.
URL: https://www.amazon.com/Amazon-Prime-Air/b?ie=UTF8&node=8037720011

ArcturusUAV (2017), 'JUMP 20'.
URL: https://arcturus-uav.com/product/jump-20

ArduPilot (2020), 'ArduPilot Documentation'.
URL: https://ardupilot.org/ardupilot/

Bacchini, A. & Cestino, E. (2019), 'Electric VTOL Configurations Comparison', *MDPI Aerospace* **6**(3), 26.

Bacchini, A., Cestino, E., van Magill, B. & Verstraete, D. (2021), 'Impact of lift propeller drag on the performance of eVTOL lift+cruise aircraft', *Aerospace Science and Technology* **109**, 106429.

Becker, J., Nemeth, T., Wegmann, R. & Sauer, D. (2018), 'Dimensioning and Optimization of Hybrid Li-Ion Battery Systems for EVs', *World Electric Vehicle Journal* **9**(2), 19.

Blaim, T. (2017), Entwicklung eines Mechanismus zur Reduktion des aerodynamischen Widerstands der inaktiven Rotoren am 5TOL UAV, Bachelor Thesis, Institute of Aircraft Design, Technical University of Munich, Munich.

Borer, N. K., Derlaga, J. M., Deere, K. A., Carter, M. B., Viken, S., Patterson, M. D., Litherland, B. & Stoll, A. (2017), Comparison of Aero-Propulsive Performance Predictions for Distributed Propulsion Configurations, *in* 'AIAA SciTech 2017 Forum'.
URL: https://ntrs.nasa.gov/citations/20170001218

Brandt, J. B., Deters, R. W., Ananda, G. K. & Selig, M. S. (2020), 'UIUC Propeller Database'.
URL: http://m-selig.ae.illinois.edu/props/propDB.html

Chanan (2017), 'e-Bike Battery Discharge Rate: 4C vs. 3C', *LaBatteria* .
URL: https://www.labatteria.co.il/en/e-bike-battery-discharge-rate-4c-vs-3c/

Channa, V. V. (2015), Sensitivity of Pusher Propeller Performance and Noise Emissions to the Upstream Wake Characteristics: An Experimental and Numerical Study, Master Thesis, Delft University of Technology, Delft.
URL: http://resolver.tudelft.nl/uuid:e32f84f1-21da-4a5a-a541-2f15b041ede5

CompositAirplanes (2020), 'Viva Motor Glider'.
URL: https://www.compositairplanes.cz/our-products

Conn, A. R., Gould, N. I. M. & Toint, P. (1991), 'A Globally Convergent Augmented Lagrangian Algorithm for Optimization with General Constraints and Simple Bounds', *SIAM Journal on Numerical Analysis* **28**(2), 545–572.

Conn, A. R., Gould, N. & Toint, P. L. (1997), 'A globally convergent Lagrangian barrier algorithm for optimization with general inequality constraints and simple bounds', *Mathematics of Computation* **66**(217), 261–289.

Deperrois, A. (2019), 'XFLR5 v6.47'.
URL: http://www.xflr5.tech/xflr5.htm

DHL (2016), 'Einbindung des DHL-Paketkopters in die Logistikkette erfolgreich getestet'.
URL: https://www.dpdhl.com/de/presse/pressemitteilungen/2016/einbindung-dhl-paketkopter-logistikkette-erfolgreich-getestet.html

Dimchev, M. (2012), Experimental and numerical study on wingtip mounted propellers for low aspect ratio UAV design, Master Thesis, Delft University of Technology, Delft.
URL: http://resolver.tudelft.nl/uuid:3a71cddb-b1b1-446c-9656-c4f686f688c7

Drela, M. (1989), XFOIL: An Analysis and Design System for Low Reynolds Number Airfoils, *in* C. A. Brebbia, S. A. Orszag, J. H. Seinfeld, P. Spanos, A. S. Cakmak, P. Silvester, C. S. Desai, G. Pinder, R. McCrory, S. Yip, F. A. Leckie, A. R. S. Ponter, K.-P. Holz, K.-J. Bathe, J. Connor, W. Wunderlich, J. Argyris & T. J. Mueller, eds, 'Low Reynolds Number Aerodynamics', Vol. 54 of *Lecture Notes in Engineering*, Springer Berlin Heidelberg, Berlin, Heidelberg, pp. 1–12.

Drela, M. (2004), 'Quick Servo Moment Prediction'.
URL: https://www.rcgroups.com/forums/showpost.php?p=2517672&postcount=2

Drela, M. (2005), 'DC Motor / Propeller Matching: Lab 5 Lecture Notes'.
URL: http://web.mit.edu/drela/Public/web/qprop/motorprop.pdf

Drone Industry Insights (2020), 'The Drone Market Report 2020-2025'.
URL: https://droneii.com/the-drone-market-size-2020-2025-5-key-takeaways

EASA (2020), 'EASA publishes regulatory framework for drone service deliveries'.
URL: https://www.easa.europa.eu/newsroom-and-events/press-releases/easa-publishes-regulatory-framework-drone-service-deliveries

EnerCig (2020*a*), 'Datasheet EnerCig EC-35E: Li-ion rechargeable cylindrical battery 18650'.
URL: https://enercig.com/wp-content/uploads/2017/05/EC-35E.pdf

EnerCig (2020*b*), 'Datasheet EnerCig EC-C6: Li-ion cylindrical battery specification'.
URL: https://enercig.com/wp-content/uploads/2018/09/Technical-Specifications_EC-C6_EN.pdf

Faulhaber (2020), 'Motor Calculations for Coreless Brush DC Motors: Faulhaber Whitepaper'.
URL: https://www.faulhaber.com/en/support/technical-support/motors/tutorials/dc-motor-tutorial-dc-motor-calculation/

Finck, R. D. (1978), 'USAF (United States Air Force) Stability and Control DATCOM (Data Compendium)'.
URL: https://apps.dtic.mil/sti/citations/ADB072483

FlightWave (2019), 'Edge -130 Bundle'.
URL: https://www.flightwave.aero/product/edge-130-bundle/

Foxtech (2018), 'Dual Battery Swapping Board'.
URL: https://www.foxtechfpv.com/pg20-dual-battery-swapping-board.html

Foxtech (2020), 'NimbusVTOL UAV for mapping, survey and long range inspection'.
URL: https://www.foxtechfpv.com/foxtech-nimbus-vtol-v2.html

Fröhlich, F. (2017), Development of a 3D Printed Wing Tip and Engine Tilt Mechanism for a VTOL UAV, Master Thesis, Institute of Aircraft Design, Technical University of Munich, Munich.

Gao, L., Dougal, R. A. & Liu, S. (2005), 'Power Enhancement of an Actively Controlled Battery/Ultracapacitor Hybrid', *IEEE Transactions on Power Electronics* **20**(1), 236–243.

Gavrylko, V. (2020), 'Vladimir's Model Specifications'.
URL: http://f3j.in.ua/

Goldberg, D. E. (2012), *Genetic algorithms in search, optimization, and machine learning*, 30th edn, Addison-Wesley, Boston.

Gong, A., MacNeill, R. & Verstraete, D. (2018), Performance Testing and Modeling of a Brushless DC Motor, Electronic Speed Controller and Propeller for a Small UAV Application, *in* 'Joint Propulsion Conference 2018', American Institute of Aeronautics and Astronautics, [S.l.].

Gong, A., Maunder, H. & Verstraete, D. (2017), Development of an in-flight thrust measurement system for UAVs, *in* '53rd AIAA/SAE/ASEE Joint Propulsion Conference 2017', American Institute of Aeronautics and Astronautics, Reston, Virginia.

Green, C. (2015), Modeling and Test of the Efficiency of Electronic Speed Controllers for Brushless DC Motors, Master Thesis, California Polytechnic State University, San Luis Obispo.

Gudmundsson, S. (2014), *General aviation aircraft design: Applied methods and procedures*, 1st edn, Butterworth-Heinemann, Oxford, UK.

Gundlach, J. (2012), *Designing Unmanned Aircraft Systems: A Comprehensive Approach*, American Institute of Aeronautics and Astronautics, Reston, VA.

Harmon, H. N. (1941), 'Wind-Tunnel Tests of Several Model Tractor-Propeller and Pusher-Propeller Wing Extension-Shaft Arrangements, Special Report'.
URL: https://ntrs.nasa.gov/search.jsp?R=20090016321

Hartog, J. P. & Mesmer, G. (1952), *Mechanische Schwingungen*, 2nd edn, Springer Berlin Heidelberg, Berlin, Heidelberg and s.l.

Hirschberg, M. (2018), 'The Electric VTOL Revolution'.
URL: https://evtol.news/__media/PDFs/Hirschberg-eVTOL-19Sep2018-ERF.pdf

Hoerner, S. F. (1965), *Fluid-dynamic drag: Practical information on aerodynamic drag and hydrodynamic resistance*, 2nd ed. edn, Hoerner Fluid Dynamics, Bakersfield.

HORYZN (2020), 'HORYZN - Prototyping the Aerospace of Tomorrow'.
URL: https://horyzn.org/

Janus, J. M., Chatterjee, A. & Cave, C. (1996), 'Computational analysis of a wingtip-mounted pusher turboprop', *Journal of Aircraft* **33**(2), 441–444.

JARUS (2019), 'JARUS guidelines on Specific Operations Risk Assessment (SORA): Executive Summary'.
URL: http://jarus-rpas.org/sites/jarus-rpas.org/files/jar_doc_06_jjarus_sora_executive_summary.pdf

Johnson, W. (2013), *Rotorcraft Aeromechanics*, Cambridge University Press, Cambridge, United Kingdom.

JOUAV (2020), 'CW-100'.
URL: http://www.jouav.com/flightSystem/CW-100.html

Kapetair (2020), 'Kapetair – VTOL UAV Systems'.
URL: http://kapetair.com/

Karpfinger, J. (2018*a*), Entwicklung eines MATLAB-Programms für den Vorentwurf von unbemannten senkrechtstartfähigen Flächenflugzeugen, Master Thesis, Institute of Aircraft Design, Technical University of Munich, Munich.

Karpfinger, J. (2018*b*), Entwicklung und Untersuchung von Methoden zur Flugleistungsuntersuchung von sUAVs durch den Einsatz von sUAVinternen Miniatursensoren, Midterm Thesis, Institute of Aircraft Design, Technical University of Munich, Munich.

KDE Direct (2020), 'KDE Direct | ENGINEERING THE UNSEEN'.
URL: https://www.kdedirect.com/

Kolb, T. (2018), Implementation of a MATLAB Tool to Design the Electric Hover Powertrain of a Vertical Take-Off and Landing Unmanned Aerial Vehicle, Master Thesis, Institute of Aircraft Design, Technical University of Munich, Munich.

Kortas, M., Friebe, R., Rzegotta, I. & von Ammon, C. (2019), 'Analyse des deutschen Drohnenmarktes'.
URL: https://www.bdl.aero/wp-content/uploads/2019/02/VUL-Markststudie_Deutsch_final.pdf

Kroo, I. (2001), 'Drag due to lift: Concepts for Prediction and Reduction', *Annual Review of Fluid Mechanics* **33**(1), 587–617.

Krossblade Aerospace (2020), 'SkyCruiser'.
URL: https://www.krossblade.com/skycruiser-1

Lain, Brandon & Kendrick (2019), 'Design Strategies for High Power vs. High Energy Lithium Ion Cells', *Batteries* **5**(4), 64.

Leishman, J. G. (2017), *Principles of helicopter aerodynamics*, Cambridge aerospace series, second edition edn, Cambridge University Press, Cambridge, United Kingdom.

Linke, T. (2019), Experimental Analysis of Thrust Loss due to Rotor-Fuselage Interaction, Research Internship Report, Technical University of Munich.

Litherland, B. L., Patterson, M. D., Derlaga, J. M. & Borer, N. K. (2017), A Method for Designing Conforming Folding Propellers, *in* '17th AIAA Aviation Technology, Integration, and Operations Conference 2017', American Institute of Aeronautics and Astronautics, Reston, Virginia.

Lundström, D., Amadori, K. & Krus, P. (2010), Validation of Models for Small Scale Electric Propulsion Systems, *in* '48th AIAA Aerospace Sciences Meeting 2010', American Institute of Aeronautics and Astronautics, Reston, Virigina.

Lynn, R. R., Robinson, F. D., Batra, N. N. & Duhon, J. M. (1970), 'Tail Rotor Design Part I: Aerodynamics', *Journal of the American Helicopter Society* **15**(4), 2–15.

LZ Design (2020), 'Front Electric Sustainer'.
URL: `http://www.front-electric-sustainer.com/`

Matternet (2020), 'Matternet Homepage'.
URL: `https://mttr.net/company`

McDonald, R. (2018), 'eVTOL Analysis Tools & Frameworks'.
URL: `https://vtol.org/files/dmfile/2-TVF2018-MacDonald-Uber-Jan191.pdf`

Miranda, L. R. & Brennan, J. E. (1986), Aerodynamic effects of wingtip-mounted propellers and turbines, *in* '4th Applied Aerodynamics Conference 1986', American Institute of Aeronautics and Astronautics, Reston, Virigina.

Nagel, L. (2020), 'Unterstützung bei der Entwicklung und Erprobung eines unbemann- ten, senkrechtstartfähigen Starrflügelflugzeugs: Simulation von Batteriearchitekturen: Research Report'.

Nakayama, A. (1985), 'Characteristics of the flow around conventional and supercritical airfoils', *Journal of Fluid Mechanics* **160**, 155–179.

Newman, D. I., Lacy, R. W., Preator, R. M., Gianopulos, E. N. & Ziegenbein, P. (2015), 'EU Patent EP 2 927 122 A1: Vertically landing aircraft'.

Niță, M. & Scholz, D. (2012), Estimating the Oswald Factor from Basic Aircraft Geometrical Parameters, *in* 'Deutscher Luft- und Raumfahrtkongress 2012', Deutsche Gesellschaft für Luft- und Raumfahrt - Lilienthal-Oberth e.V, Bonn.
URL: https://www.dglr.de/publikationen/2012/281424.pdf

Nootebos, S. (2018), Aerodynamic analysis and optimisation of wingtip-mounted pusher propellers, Master Thesis, Delft University of Technology.
URL: http://resolver.tudelft.nl/uuid:83c88c41-3fa0-4ddb-9cc2-b5e574d0cd6a

North, D. D., Aull, M. J., Fredericks, W. J., Moore, M. D., Rothhaar, P. M., Hodges, W. T. & Johns, Z. R. (2018), 'Patent US 10,071,801 B2: Tri-Rotor Aircraft Capable Of Vertical Takeoff And Landing and Transitioning To Forward Flight'.

Oberschwendtner, S. (2016), Entwurf einer elektronischen Wölbklappensteuerung für unbemannte Fluggeräte, Bachelor Thesis, Institute of Aircraft Design, Technical University of Munich, Munich.

Oberschwendtner, S. (2019), Multi Objective Optimization of Wiring Harnesses for Overall System Performance of Electric Fixed Wing VTOL UAVs, *in* 'Conference Proceedings of the 8th Biennial Autonomous VTOL Technical Meeting & 6th Annual Electric VTOL Symposium 2019'.

OxisEnergy (2019), 'Ultra LightUltra Light Lithium Sulfur Pouch Cell'.
URL: https://45uevg34gwlltnbsf2plyua1-wpengine.netdna-ssl.com/wp-content/uploads/2019/07/OXIS-Li-S-Ultra-Light-Cell-spec-sheet-v4.2.pdf

Ozdemir, U., Aktas, Y. O., Vuruskan, A., Dereli, Y., Tarhan, A. F., Demirbag, K., Erdem, A., Kalaycioglu, G. D., Ozkol, I. & Inalhan, G. (2014), 'Design of a Commercial Hybrid VTOL UAV System', *Journal of Intelligent & Robotic Systems* **74**(1-2), 371–393.

Palaia, G., Abu Salem, K., Cipolla, V., Binante, V. & Zanetti, D. (2021), 'A Conceptual Design Methodology for e-VTOL Aircraft for Urban Air Mobility', *Applied Sciences* **11**(22), 10815.

Panasonic (2020), 'Specifications for NCR18650GA'.
URL: https://www.orbtronic.com/content/Datasheet-specs-Sanyo-Panasonic-NCR18650GA-3500mah.pdf

Patterson, J. C. & Bartlett, G. R. (1987), 'Evaluation of installed performance of a wing-tip-

mounted pusher turboprop on a semispan wing'.
URL: https://ntrs.nasa.gov/citations/19870016608

Patterson, M. D. (2016), Conceptual Design of High-Lift Propeller Systems for Small Electric Aircraft, PhD Thesis, Georgia Institute of Technology, Atlanta, GA.

Patterson, M. D., Borer, N. K. & German, B. (2016), 'A Simple Method for High-Lift Propeller Conceptual Design'.

Pätzold, F. (2014), 'Results of Flight Performance Determination of the Lak–17a FES (S5–3117)'.

Peukert, W. (1897), 'Über die Abhängigkeit der Kapazität von der Entladestromstärke bei Bleiakkumulatoren', *Elektrotechnische Zeitschrift (ETZ)* **18**, 287–288.

PhoenixWings (2020), 'Phoenix-Wings – Take Off. Next Level'.
URL: https://phoenix-wings.de/

Pifer, E. A. & Bramesfeld, G. (2012), 'Measuring Wing Profile Drag using an Integrating Wake Rake', *Technical Soaring* **Vol. 36, No. 3**.
URL: http://journals.sfu.ca/ts/index.php/ts/article/view/289

Quantum Systems (2020), 'VECTOR and SCORPION eVTOL Fixed-Wing Drones'.
URL: https://www.quantum-systems.com/download/222221/

Raymer, D. P. (1992), *Aircraft design: A conceptual approach*, AIAA, Washington, D.C.

Rieger, C. (2017), Experimental Investigation of the Effects of Objects in the In- and Outflow of Propellers on Multirotor UAV, Semester Thesis, Institute of Aircraft Design, Technical University of Munich, Munich.

Roessler, C. (2012), *Conceptual Design of Unmanned Aircraft with Fuel Cell Propulsion System: Zugl.: München, Techn. Univ., Diss., 2012*, Luftfahrt, 1. aufl. edn, Dr. Hut, München.

Rondel, P. (2020), 'Planet-Soaring: Aircraft Reviews'.
URL: https://planet-soaring.blogspot.com/p/reviews.html

Roskam, J. & Lan, C.-T. E. (1997), *Airplane Aerodynamics and Performance*, Darkorporation, Lawrence, Kan.

Sarson-Lawrence, J., Sabatini, R., Clothier, R. & Gardi, A. (2014), 'Experimental Determination of

Low-Cost Servomotor Reliability for Small Unmanned Aircraft Applications', *Applied Mechanics and Materials* **629**, 202–207.

Schempp Hirth (2020), 'Ventus'.
URL: https://www.schempp-hirth.com/flugzeuge/ventus

Schenk, H. (2014), 'Motormodellierung/Theorie'.
URL: https://www.rcgroups.com/forums/showatt.php?attachmentid=10325233

Schlichting, H. & Truckenbrodt, E. (2001), *Aerodynamik des Flugzeuges: Zweiter Band: Aerodynamik des Tragflügels (Teil II), des Rumpfes, der Flügel-Rumpf-Anordnung und der Leitwerke*, Klassiker der Technik, 3rd edn, Springer Berlin Heidelberg, Berlin, Heidelberg.

Schwank, M. (2016), Erstellung eines Flugzeugentwurfsprogramms für das Praktikum Flugzeugentwurf, Bachelor Thesis, Institute of Aircraft Design, Technical University of Munich, Munich.

Seren, T. (2017), Developement of a Design Tool for Vertical Take Off and Landing Unmanned Aerial Vehicles, Semester Thesis, Institute of Aircraft Design, Technical University of Munich, Munich.

Seren, T. (2018), Development of a MATLAB Tool for the design of electric Propulsion Systems for fixed wing unmanned Vertical takeoff Aircraft and integration into a design Tool, Master Thesis, Institute of Aircraft Design, Technical University of Munich, Munich.

Seren, T., Roessler, C. & Hornung, M. (2019), Comparative eVTOL UAV Design Optimization, *in* 'Conference Proceedings of the 8th Biennial Autonomous VTOL Technical Meeting & 6th Annual Electric VTOL Symposium 2019'.

Serokhvostov, S. V. & Churkina, T. E. (2011), One useful propeller mathematical model for MAV, *in* G. de Croon & M. Amelink, eds, 'Proceedings of the International Micro Air Vehicle Conference and Flight Competition 2011 Summer Edition', 't Harde, the Netherlands, pp. 111–117.

Serrano, A. R. (2018), 'Design methodology for hybrid (vtol + fixed wing) unmanned aerial vehicles', *Aeronautics and Aerospace Open Access Journal* **2**(3).

Singh, B. (2017), A Medium-Fidelity Method for Rapid Maximum Lift Estimation, Bachelor Thesis, Delft University of Technology, Delft.
URL: https://repository.tudelft.nl/islandora/object/uuid%3A193f8b1e-ea0c-4a6c-afa4-f49c14ba80e6

Skaug (2020), 'BLHeli32'.
URL: https://github.com/bitdump/BLHeli

Smelt, R. & Davies, H. (1937), 'Estimation of Increase in Lift Due to Slipstream: Reports and Memoranda 1788'.

Snyder, M. H. (1967), Effects of a Wingtip-mounted Propeller on Wing Lift, Induced Drag, and Shed Vortex Pattern, PhD Thesis, Oklahoma State University.

Snyder, M. H. & Zumwalt, G. W. (1969), 'Effects of wingtip-mounted propellers on wing lift and induced drag', *Journal of Aircraft* **6**(5), 392–397.

Sony (2020*a*), 'US18650VTC5: Lithium Ion Rechargeable Battery Technical Information'.
URL: https://www.powerstream.com/p/us18650vtc5-vtc5.pdf

Sony (2020*b*), 'US18650VTC6: Lithium Ion Rechargeable Battery Technical Information'.
URL: https://www.kronium.cz/uploads/SONY_US18650VTC6.pdf

Speck, S., Herbst, S., Kim, H., Stein, F.-G. & Hornung, M. (2015), Development, Startup Operations and Tests of a Propeller Wind Tunnel Test Rig, *in* '15th AIAA Aviation Technology, Integration, and Operations Conference 2015', American Institute of Aeronautics and Astronautics, Reston, VA.

Stahl, P. & Hornung, M. (2020), 'Proposal of a Fixed-Wing Tricopter VTOL Configuration with Minimal Number of Control Systems'.

Stahl, P., Roessler, C. & Hornung, M. (2018), Benefit Analysis and System Design Considerations for Drag Reduction of Inactive Hover Rotors on Electric Fixed-Wing VTOL Vehicles, *in* '18th AIAA Aviation Technology, Integration, and Operations Conference 2018', Curran Associates Inc, Red Hook, NY.

Stahl, P., Roessler, C. & Hornung, M. (2019), Configuration Redesign and Prototype Flight Testing of an Unmanned Fixed-Wing eVTOL Aircraft with Under-Fuselage Hover Lift and Pusher Wingtip Propulsion System, *in* 'Conference Proceedings of the 8th Biennial Autonomous VTOL Technical Meeting & 6th Annual Electric VTOL Symposium 2019'.

Stahl, P., Seren, T., Roessler, C. & Hornung, M. (2018), Development and Performance Comparison of Optimized Electric Fixed-Wing VTOL UAV Configurations, *in* '31st Congress of the International Council of the Aeronautical Sciences 2018', The International Council of the Aeronautical Sciences c/o Deutsche Gesellschaft für Luft- und Raumfahrt, Bonn.

URL: https://www.icas.org/ICAS_ARCHIVE/ICAS2018/data/papers/ICAS2018_0169_paper.pdf

Stokkermans, T. C., Nootebos, S. & Veldhuis, L. L. (2019), Analysis and Design of a Small-Scale Wingtip-Mounted Pusher Propeller, *in* 'AIAA Aviation 2019 Forum', American Institute of Aeronautics and Astronautics, Reston, Virginia.

Stoll, A. M. & Veble Mikic, G. (2016), Design Studies of Thin-Haul Commuter Aircraft with Distributed Electric Propulsion, *in* '16th AIAA Aviation Technology, Integration, and Operations Conference 2016', American Institute of Aeronautics and Astronautics, Reston, VA.

T-Motor (2020), 'T-MOTOR The Safer Propulsion System'.
URL: https://uav-en.tmotor.com/

Taylor, J. R. (1988), *Fehleranalyse: Eine Einführung in die Untersuchung von Unsicherheiten in physikalischen Messungen*, 1. aufl. edn, VCH, Weinheim.

Taylor, M. B. (1968), 'Pusher Propeller Efficiency and Problems', *Sport Aviation* .
URL: http://acversailles.free.fr/documentation/08~Documentation_Generale_M_Suire/Conception/Formules_speciales/Pusher/Pusher_propeller_efficiency_and_problems.pdf

Thiede, F., Kaufmann, M. & Stütz, P. (2012), *Auslegungsverfahren für elektrische Hilfsantriebe im Segelflug*, Deutsche Gesellschaft für Luft- und Raumfahrt - Lilienthal-Oberth e.V., Bonn.
URL: https://www.dglr.de/publikationen/2012/281255.pdf

Thompson, D. (2013), 'OpenAeroVTOL'.
URL: https://www.rcgroups.com/forums/showthread.php?1972686-OpenAeroVTOL-with-transitional-mixers-%28perfect-for-VTOLs%29

Tiesler, J. (2019*a*), Development, Assembly and Testing of a Powertrain and Stabilizer Tilt Mechanism for an Unmanned Fixed-Wing Vertical Take-Off and Landing Aircraft, Bachelor Thesis, Institute of Aircraft Design, Technical University of Munich, Munich.

Tiesler, J. (2019*b*), 'Unterstützung bei der Entwicklung und Erprobung eines unbemannten, senkrechtstartfähigen Starrflügelflugzeugs: TUM MSE Forschungspraktikum'.

TUM AER (2020), 'Windkanal B - Lehrstuhl für Aerodynamik und Strömungsmechanik'.
URL: https://www.mw.tum.de/aer/windkanaele/windkanal-b/

Tyan, M., van Nguyen, N., Kim, S. & Lee, J.-W. (2017), 'Comprehensive preliminary sizing/resizing

method for a fixed wing – VTOL electric UAV', *Aerospace Science and Technology* **71**, 30–41.
URL: http://www.sciencedirect.com/science/article/pii/S1270963817300871

UPS (2019), 'UPS Drone Delivery Service | UPS - United States'.
URL: https://www.ups.com/us/en/services/shipping-services/flight-forward-drones.page

Veldhuis, L. L. M. (2005), Propeller wing aerodynamic interference, PhD Thesis, Delft University of Technology, Delft.
URL: http://resolver.tudelft.nl/uuid:8ffbde9c-b483-40de-90e0-97095202fbe3

Vertical Aerospace (2020), 'VA-1X'.
URL: https://www.vertical-aerospace.com/

VFS (2017), 'eVTOL Aircraft Directory'.
URL: https://evtol.news/aircraft/

Wilson, H. A. (1942), 'Full-Scale-Tunnel Investigation of a Multiengine Pusher-Propeller Installation'.
URL: https://ntrs.nasa.gov/citations/19930093006

Wilson, J. C. (1975), Rotorcraft low-speed download drag definition and its reduction, *in* American Helicopter Society, ed., 'Forum 31'.
URL: https://ntrs.nasa.gov/citations/19750053523

Yao, Y., Lu, D. C. & Verstraete, D. (2013), Power loss modelling of MOSFET inverter for low-power permanent magnet synchronous motor drive, *in* '1st International Future Energy Electronics Conference 2013', IEEE, Piscataway, NJ, pp. 849–854.

Zimmermann, T., Keil, P., Hofmann, M., Horsche, M. F., Pichlmaier, S. & Jossen, A. (2016), 'Review of system topologies for hybrid electrical energy storage systems', *Journal of Energy Storage* **8**, 78–90.

Vita

Philipp Stahl was born and raised in southern Germany. He earned both a Bachelor's and Master's Degree in Aerospace Engineering from Technical University of Munich. In 2015, he started as a PhD student at the Institute of Aircraft Design at Technical University of Munich.
In the EU-funded research project *FLEXOP*, he was involved in the conceptual and detailed design of an unmanned demonstrator aircraft to investigate active flutter suppression and load alleviation techniques. In 2016, he switched to a research project with *AUTEL Robotics* to support the design of an unmanned fixed-wing VTOL aircraft. Within this cooperation, two vehicles of 5 and 15 kg takeoff weight were taken from scratch to maiden flight. Ultimately, the topic of his PhD thesis is derived from this.
In 2020, he started as lead aircraft design engineer at Phoenix Wings to develop fixed-wing VTOL UAV for cargo applications.
Since teenage, he is enthusiastic about RC model aircraft - especially about those without a motor. With the start of his studies, he got active member of AkaModell Munich, a student club for RC airplane design at Technical University of Munich. He also owns a manned glider pilot license. In a sailplane, he enjoys long distance cross-country flights the most.